Dynamics of epithelial monolayers assessed by acoustic and impedimetric whole cell biosensors

Quartz crystal microbalance (QCM) and electrical cell-substrate impedance sensing (ECIS) as novel tools to address cell motility and nanocytotoxicity

Dissertation
zur Erlangung des Grades
"Doktor der Naturwissenschaften"

am Fachbereich
Chemie, Pharmazie und Geowissenschaften
der Johannes Gutenberg-Universität Mainz

vorgelegt von
Marco Tarantola
geboren in Wiesbaden

Mainz 2010

Meinen Eltern und meiner Familie

Dosis sola venenum facit

Paracelsus (1493-1541)

Abstract

The central aim of this work was focused on scrutinizing migration dynamics of epithelial monolayers by two novel *in vitro* biosensors: electrical cell-substrate impedance sensing (ECIS) and quartz crystal microbalance (QCM). Both proved to be suitable to address cell motility and nanocytotoxicity.

The first focus was put on fingerprinting cancer cells by their cell body dynamics and the generated electrical or acoustic fluctuations in ECIS and QCM (termed F-QCM) readouts. Here, the classical cancer cell motility *in-vitro* assays for migration and invasion relying on Boyden chambers are compared to real-time biosensors that analyze the dynamic properties of adherent cells with a time resolution in the order of seconds. Signatures of long-memory correlations in motility as well as fractal, self-similarity and collective motion were analyzed by variance determination, power density estimation and detrended fluctuation analysis. Long-memory stochastic processes were found to govern the response of the adherent cells displayed in both F-QCM and ECIS micromotion measurements, with variance analysis of QCM frequency fluctuations providing the strongest correlation to classical Boyden invasion assays. Furthermore, we studied the impact of small molecule inhibitors on the dynamics of the cytoskeleton: effects of cytochalasin D, phalloidin and blebbistatin as well as taxol, nocodazol and colchicin were quantified by detecting changes in the noise pattern. We were able to identify actin-polymerization as well as microtubule depolymerization to be the main contributors of viscoelastic or impedimetric fluctuations.

As a second project, a comprehensive interfacial analysis enabled us to record both adhesion and desorption processes and cell-cell contacts degradation upon nanoparticles application. We followed cell-substrate dynamics via micromotility and viscoelastic fluctuations as a measure for nanotoxicity, related to shape, functionalization, intracellular stability and charge of particles.

In summary, the novel real time biosensor approach based on fluctuation analysis of acoustic and impedimetric readouts of F-QCM and ECIS displays a high cellular specifity and sensitivity for the dynamics of the cellular cytoskeleton and may serve also as a very sensitive measure for cellular viability.

Table of contents

List of figures

List of tables

Introduction: Molecular biology of cell motility

Actin

Microtubles

Intermediate filaments

Cytoskeletal filaments[1]

INTRODUCTION

Cell motility is a relevant process in plenty of biological processes including development, homeostasis or pathologies like cancer. Understanding the molecular basis on cytoskeletal level is as urgent as to assess single cell- or whole monolayer migration *in vitro*. The *chapters* 3 and 4 will emphasize on the application novel biosensors for the detection of epithelial cell monolayer motility.

Cell death, whether accidental or controlled, plays a decisive role in the same processes mentioned before. It is a necessary criterion to exclude possible cell death promoters in toxicological studies outlining risks of new developed drug carriers or user products in the nanoscale regime. Cell motility was revealed to be a subtle measure for toxicity of reagents. *Chapters* 5 and 6 will focus on cytotoxicity of carrier systems in the nano-regime.

The present chapter outlines the essential biological processes involved in cell motility: we present cytoskeleton and cellular adhesion basics as well as fundamentals

of whole cell migration. Finally, a short overview on motility regulation via small rho-GTPases is given.

1.1 CYTOSKELETON: CELLULAR COMPONENTS DETERMINING MOTILITY

1.1.1 Actin

The actin-molecule is ubiquitous (up to 200 µM or 15-60% of the total cell protein amount) and participates in cellular motility and cytoskeleton functions like (intra)cellular transport, muscle contraction, cytokinesis and stabilization of cell shape, i.e. through protrusions like microvilli or filopodia, cell-cell contacts like tight junctions or cell-substrate contacts like focal contacts and the connected stress fibres. Cellular motility is thereby supported in twofold ways: by actomyosin movements on actin or by dynamical rearrangements of actin in close proximity to the membrane, powering shape changes and protrusions. In contrast to microtubules, actin fibres sustain tension better than compression and do not present microtubules` rapid fluctuation in length (dynamic instability).

The monomeric G-actin is found in six human isoforms, whereby non-muscle cells express only the β and γ form. Additionally, actin-related proteins (ARPs) are known, with ARP2 and 3 participating in branched (or barbed)-actin filament initiation in the cell cortex. The monomer possesses an ATP-or ADP- and a bivalent cation (mostly Mg^{2+})-binding groove and provokes polarity of whole fibres. Polymers present a barbed end mentioned above (named after myosin projecting from the surface) and an opposed pointed end. Unpolymerized G-actin monomers are ATP-associated, following their high affinity for ATP and high intracellular ATP-concentration. However, actin trimers are the nucleus of polymer growth, which is only realised with the help of associated proteins. The structure of the longitudinal actin-polymer, named F-actin, with a diameter of 7 nm, is of a double-helix, where at both ends addition or loss of subunits occurs, often resulting in treadmiling (higher association rate: barbed end; dissociation rate: dependent on the nucleotide bound). Hydrolysis of ATP to ADP and a phosphate occurs upon assembly, whereupon ADP-actin resembles the core of most filaments.

The dynamic nature of actin is rendered possible by actin-modulation proteins, which prevent copolymerization of isoforms and control cytoplasmic localization: up to seven classes (and 60 families) can be distinguished by their action: actin-binding proteins capture monomers (1), sever (2), cross-link (3) (inter-actin, with membrane, microtubules or intermediate filaments), cap (4), stabilize (5), nucleate (6) or move along
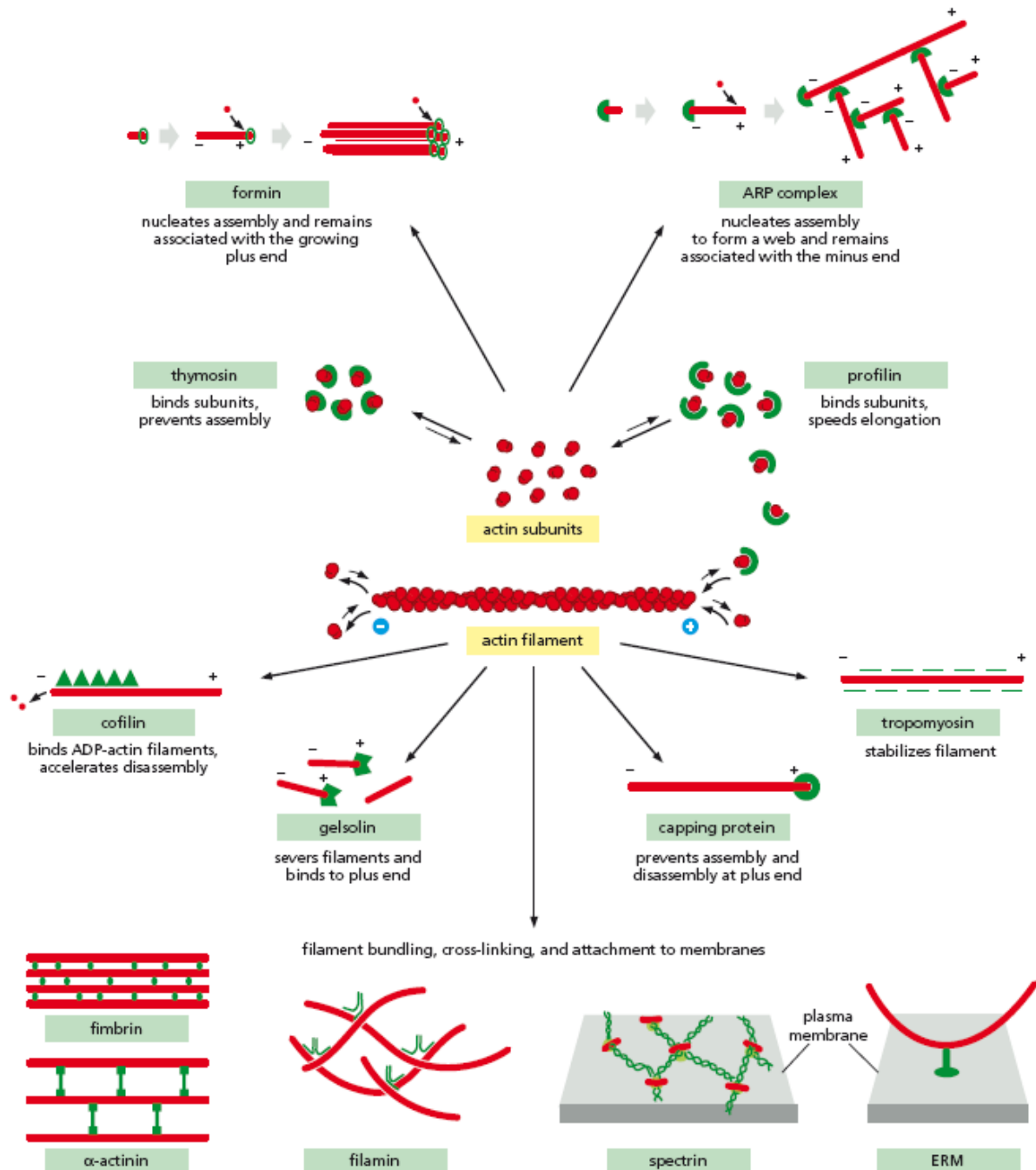
Figure 1.1 Major families of actin binding proteins (without motors): Monomer-binders with nucleotide specifity (ATP-actin: profilin and thymosin-β$_4$; ADP-actin: ADF/cofilins), severing proteins (gelsolin, fragmin), cross-linkers (filamin, spectin, ERM: ezrin, radixin, moesin). Capping/stabilizing proteins (barbed: gelsolin; pointed: tropomodulin/tropomyosin or Arp2/3 complex), nucleating agents (formin, Arp 2/3).[1]

(7) (motor proteins) these biopolymers. They often act in groups, have overlapping functions and are often Ca^{2+}-dependent (see overview in *figure* 1.1).

For example, stabilizing proteins include tropomyosin and caldesmon for the increase of tensile strength (first) or the regulation of action-myosin interaction (latter), whiles cross-linking ones are, i.e. α-actinin, fimbrin, filamin/spectrin, ezrin or WASp: the first one is found in the cortex and at adhesion plaques, while the second one stabilizes microvilli-actin-bundles; filamin/spectrin and ezrin anchor the actin filaments to the plasma membrane via integral proteins or polyphosphoinositides and WASp/Scar are multidomain adaptor proteins linking actin growth to signaling pathways, i.e. via Rho-familiy GTPases, mainly rhoA, RAC1 or CDC42. Different actin-aggregation states fulfil manifold stability criteria: the cortical actin ring (mainly composed of β-actin) bans organelles, fixates integral proteins and stabilizes the plasma membrane. Cross-linking of actin slows organelle-diffusion and allows external forces to be transmitted. Deformation of cellular structures is avoided via counteracting stress fibres, mainly containing γ-actin. Recently, functions of nuclear located actin are being studied.[2, 3]

1.1.2 Microtubules

Microtubules are built up by GTP- or GDP-binding heterodimers of α and β-subunits forming long and hollow, cylindrical biopolymers. The α-tubulin subunit binds GTP at a protected binding site; while the β-subunit-bound GTP or GDP is hydrolysed upon microtubule assembly. Terminal as- and dissotiation of subunits produces 4 nm longitudinal, helical repeats (protofilament); thereof, usually 13 form one microtubule. In addition, γ- as well as δ- and ϵ-tubulin isoforms are found at the tubules` nucleation spots. Microtubules are more rigid than actin or intermediate filaments and serve as routes for the transport of cell organelles by motor proteins dynein and kinesin. Furthermore, microtubule-associated proteins (MAPs), -/+TIP (minus or plus end tracking proteins), stathmin (assembly inhibitor), katanin (severing protein) or accessory proteins (tau, MAP2, plectin) fulfil manifold regulatory aspects (see overview in *figure* 1.2).

Microtubule biopolymers possess a polarity: associated motor proteins have different preference for the respective ends (dynein -, kinesin +). The plus end (β-tubulin- terminated) is usually growing, the minus either anchored or collapsing,
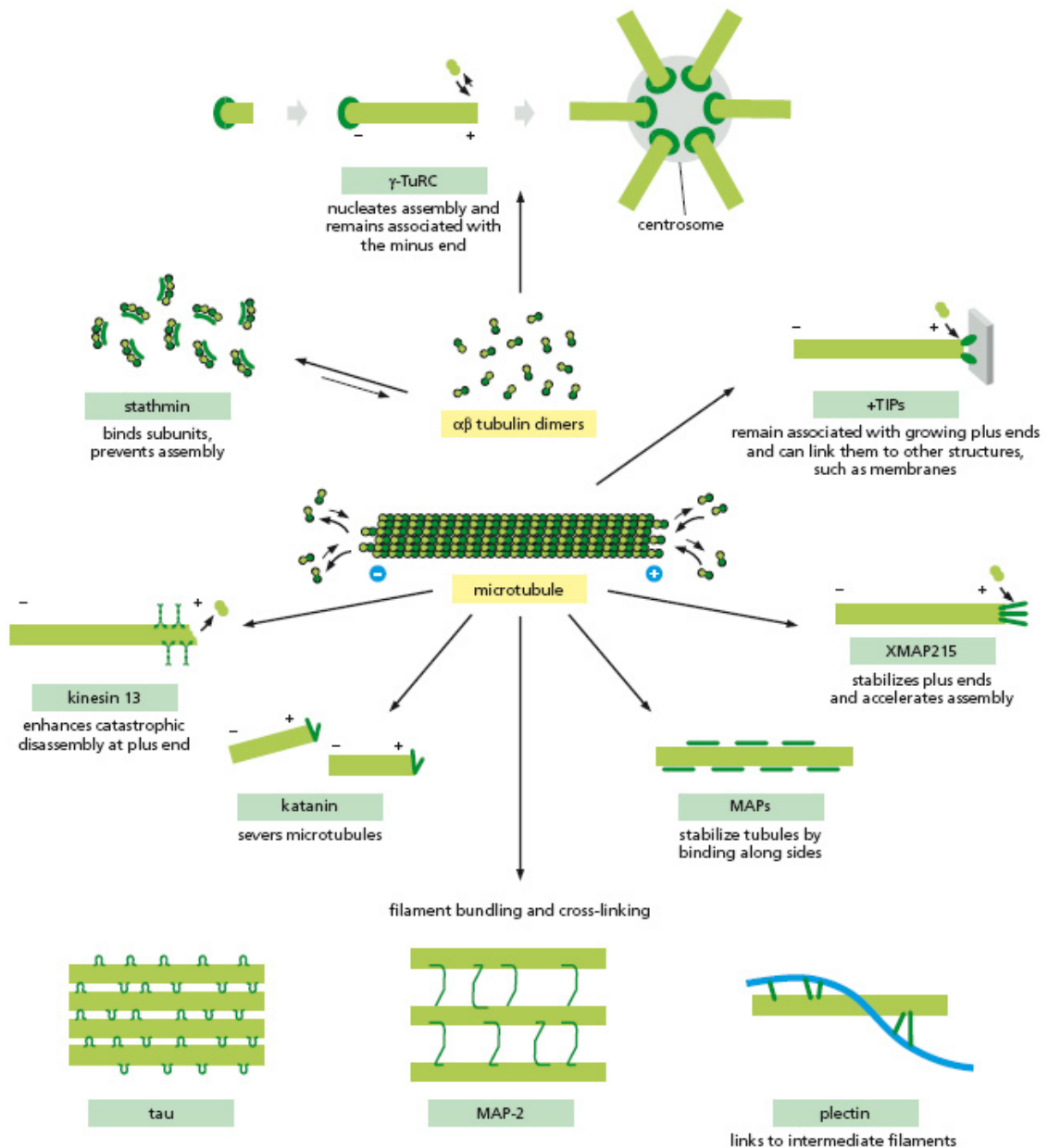
Figure 1.2 Major families of microtubules binding proteins: stabilizing proteins (- end: γ-tubulin ring complex γTuRC; side binding tau, actin crosslinker MAP-2 and plectin; + end binding TIPs) and destabilizing proteins (dimer binding stathmin, depolymerizing kinesin-13 and severing katanin).

dependent on the concentration of GTP-bound tubulin-dimers. Microtubules therefore possess an unstable core of GDP-subunits capped with less dynamic GTP-tubulin-ends and therefore present a randomly occuring dynamic instability. Segments of protofilaments are thereby rapidly peeling of the plus ends and filaments shortening. Rescue before complete degradation may occur. This instability accounts for their

dynamic functions (i.e. spindle formation, chromosome segregation, transport of TIPs to the actin-cortex/focal cotacts[4], interaction with actin in filopodia and lamellipodia).[1]

Their nucleation spot, termed a MTOC (microtubule-organizing center) or centrosome, is a non-membrane bound organelle consisting two interlinked centrioles, each composed of nine microtubules triplets, the PCM (pericentriolar matrix) and the site of microtubule formation, the γ-tubulin ring complex (γTuRC). The MTOC links microtubule dynamics to the cell-cycle and cytokinesis, but looses significance in differentiated G_0-phase cells, where the polymers also may detach from the centrosome and contribute to the specialized shape of cells (usually a radial distribution, in some epithelial cells also oriented along the cells` longitudinal axis). Microtubules have a diameter of 25 nm and can reach up to an intracellular length of 20 μm and usually present a 10-20 μM cellular concentration.

1.1.3 Intermediate filaments

A third group of apolar cytoskeletal biopolymers, named corresponding to their size of 7-11 nm, which is in between the actin- and microtubules thickness. They form rope-like fibres and constitute a heterogeneous group not involved directly in motility,[5] therefore not described in great detail here. They are, however, necessary for the mechanical support of cells and tissues due to their high tensile strength and flexibility. Four classes of cytoplasmic and two classes of nuclear intermediate filaments (IF) are distinguished, based on domain sequences of a central coiled-coil-core, but specialized cells usually express only one or two cytoplasmic polymers; due to their specifity, filament type description is often a convenient approach to differentiate tumors.

One example for this specialization are the keratines of epithelial cells, spanning the whole cytoplasm in between desmosomes. As far as associated proteins are concerned, connections to the nuclear- or plasma membrane are found and the plakins arrange linkage to microtubules, actin, cadherin and other desmosome-proteins (via desmoplakin) and even hemidesmosomal integrin subunits (via plectin).

No nucleation site or terminus is needed for growth, which occurs slowly at both fibril ends: assembly dynamics are controlled by terminal kinase-phosphorylation and stability against temperature, salt, detergents or most chemicals is found. Furthermore, no motor proteins are known to move along these filaments.

1.1.4 Motor proteins and intracellular motility

Besides cytoskeletal biopolymers, motor proteins may produce forces of the amount necessary to determine the shape of cells, when transduced by the associated, polarised fibres of actin and microtubules. Three categories of motor proteins interact with the cytoskeleton: myosin, kinesin and dynein, the first two ones being related to Ras family GTPase, the latter being an AAA-ATPase. Their usual configuration is made up by a motor domain with ATP-hydrolysis function and a tail for dimerisation or specific cargo association, depending on the local environment allowing an anchoring. Here, only a short focus on myosin and an introduction to non-muscle (NM) myosin II will be given, as the other motors are not of relevance in the present study.

A myosin molecule possesses a heavy chain, which may anchor two adjacent subunits, and two light chains (which, by phosphorylation, Ca^{2+}-interaction or folding, control the assembly), the so called essential and regulatory components. The cytoplasmic myosin II (see *figure* 1.3) is made up by two heads linked through a long tail of α-helical coiled-coil design; a β-sheet surrounded by two α-helices forms the nucleotide-binding site and is connected to the globular catalytic domain. Various isoforms have overlapping and sometimes specialized functions: myosin I has only one head and a short tail, but cross-linking actin binding sequences (multiple heads have to
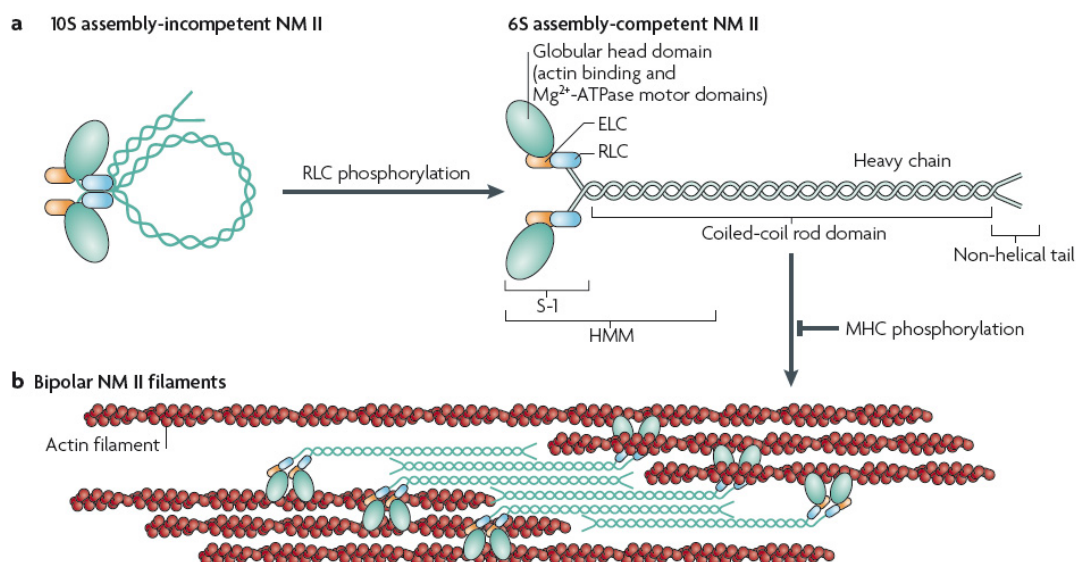
Figure 1.3 Three organization level of NMII a) Inactive form (10 s) with head to tail interaction, RLC unphosphorylated, Assembly-competent form (6 s) after RLC-phosphorylation: Heavy meromyosin (HMM) fragment contains motor domain, neck and rod to effect dimerization. b) Bipolar filaments bind to actin through head domains and the ATPase cycle of the head enables a conformational change that moves actin filaments in an anti-parallel manner.[6]
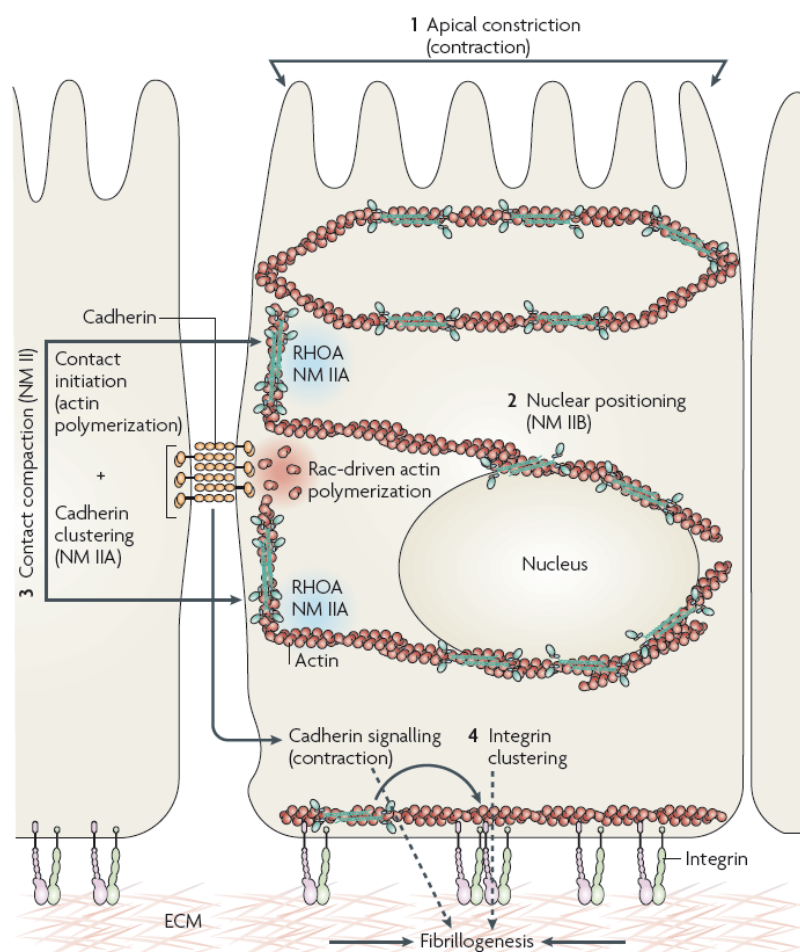
Figure 1.4 Major roles of non-muscle myosin II in epithelial cells: 1.Apical constricition; 2. Nuclear positioning; 3. Contact compaction; 4. ECM and integrin reorganization.[6]

work together) and participates in phago- and macropinocytosis and microvilli-plasma membrane anchoring. Cytoplasmic myosin II has two heads and a coiled-coil tail forming filaments, which interact with opposite polarized actin-fibres, i.e. during cytokinesis (NM) or also in muscles. Myosin V has two heads and a long tail enabling it to take giant steps and relocate cargos on tracks of microtubules. Myosin VI (with two heads) transports endocytotic vesicles and collaborates in Golgi organisation. In the ATPase cycle of actomyosin, an ADP and P_i-associated head binds actin and phosphate dissociation as well as light chain rotation occurs. The conformational change drives a strong stroke of the light chain towards the barbed end and tension is transmitted to the elastic elements of the heavy chain. Finally, ADP dissociation occurs, followed by an unbinding of myosin and by renewed ATP-binding and it`s hydrolysis. The motor proteins kinesin and dynein allow bidirectional transport on microtubules, while all myosin superfamily members, besides myosin VI, participate in barbed-end directed transport. Although long-term transport is achieved along microtubules between the centrosome and the cell periphery, for short distances, i.e. in the cortex region, actin-myosin complexes often take over cargoes.

Non-muscle myosin II (NMII) has a central integration function in (epithelial) cell migration, cell-cell and cell-matrix adhesion (see *figure* 1.4). Besides bundling of actin

and providing contractility, it represents a connection platform to Rho-GTPase signalling pathways controlling cell motility (see *chapter* 1.2.4).The NMIIA isoform is, in combination with rhoA GTPase, involved in apical contractions during embryo- and morphogenesis, while isoform NMIIB regulates nuclear positioning. Additionally, after RAC1 GTPase controlled actin-polymerization creates nascent adherens junction, cadherine clustering and stabilization through actin-crosslinking is accomplished by rhoA and NMIIA. NMII is further involved in ECM remodelling (fibrillogenesis), i.e. upon wound healing and integrin clustering in early as well as mature focal adhesions (see *chapter* 1.2.2).If ensemble integrity of epithelial sheets is lost, NMII may also function as master integrator of the switch from apico-basal to posterior-anterior polarity.

In general, the network of cytoskeletal polymers and the motor proteins associated allow a variety of intracellular movements, which are especially necessary for active transport of bigger molecules, which cannot diffuse freely through the 50 nm pores of the cytoskeleton. Examples for microtubules include: a) bidirectional axonal transport, b) polymerization driven, intermittent movements of secretory vesicles from plasma membrane to golgi apparatus c) distribution of the ER, bound to microtubules tips. In the case of actin, dispersed cargoes may be retracted on microtubule-motors (MyoV), budding of endocytotic vesicles controlled (NMII) or actin-polymerization driven bacterial movement occur, i.e. listeria.

1.2. CELL ADHESION AND -MOTILITY

1.2.1 Extracellular matrix

The extracellular matrix is assembled as mixture of five classes of macromolecules: protein filaments of collagens (1) and elastic fibres (2) as well as glycosaminoglycans (3) and proteoglycans (4) for stabilization and additional adhesive glycoproteins (5); it is needed, i.e. for intestines, ligaments, tendons, cartilage or blood vessel walls. The hydrated gel embedding ECM-proteins is made from glycosaminoglycans (GAG) and proteoglycans, often representing elastic space fillers. They are selectively secreted by cells, serve as co-receptors retaining growth factors or water to regulates diffusion and microorganism passage. 16 different collagenes, grouped in three families, are known,
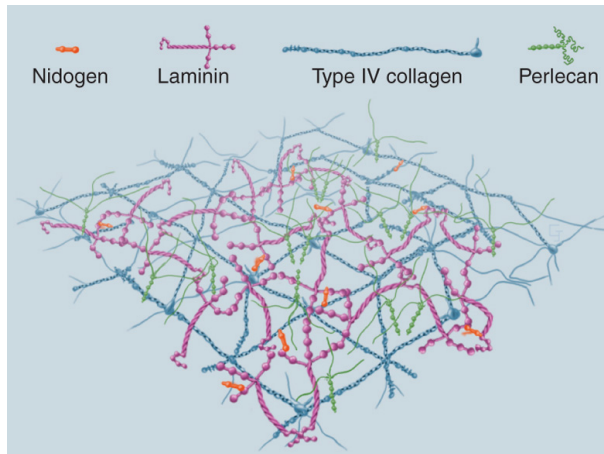
Figure 1.5 Molecular composition of the basal lamina with main components and three-dimensional arrangement[7].

with the family of sheet-forming collagens surrounding epithelia, where they forms hexagonal or spider-like nets. Elastic fibres also reinforce cross-linking and allow extension and recoiling. Adhesive glycoproteins mediate specific interactions of cells to cells (fibrinogen-aggregation), cells with the ECM (fibronectin: collagen adhesion) or the basal lamina (laminin). Adhesive glycoproteins bind elastic fibres like fibrin, collagen and GAGs and contain RGD sequences; they also influence intracellular actin stress fiber arrangement.

Mainly of interest for this work is the simple ECM called basal lamina (see *figure* 1.5), underlying and secreted by epithelial cells (as well as muscles and neurons) as self-functionalization of the underlying electrode surface of ECIS and QCM biosensors. It is a specialized, planar ECM which possesses specific porosity and therefore permeability, dependent on the cooperativity of ECM components and the underlying connective tissue. It is composed of laminin and smaller adhesive glycoproteins (nidogen), cross-linking collagen IV or anchoring collagen VII (*basement membrane*) and the proteoglycan perlecan. Laminin anchors the epithelia cells to the basal lamina, which additionally possesses the function to filter blood plasma to urine in the glomerula and tubules of the kidney and inhibits microorganism and fibroblast trespass.

The basal lamina confines the existence area of epithelial cells. Neoplasis must occur together with metalloprotease activity to free tumor cells from their site of origin.[8] Often, invadopodia (actin/phosphotyrosine-rich membrane protrusions, with a high extracellular matrix degrading capacity)[9, 10] produce these protease (found *only* in connective/inflammatory/epithelial cells, *figure* 1.6), usually necessary for controlled degradation/remodelling of ECM as i.e. during development or for cleaving of biological active components of cell surface or ECM proteins. Three classes of metalloproteases exist: matrix (MMPS), disintegrin (ADAMS) and thrombospondin (ADAMTS). MMPS usually contain a zinc protease and adhesive glycoprotein domain in
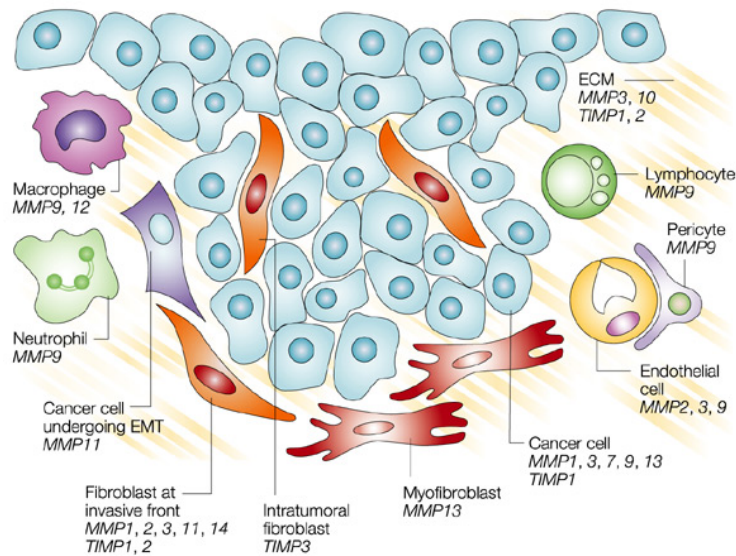
Figure 1.6 Matrix metalloproteases categorized by synthesizing cells and cancer cells. Exemplary shown for breast tumor growth (stromal cells of connective tissue in blue).[11]

the catalytic center and are secreted specifically by cells; seldom, transmembrane C-terminal segments may occur for non-secreted MMPs. ADAMS are usually membrane anchored and cleave cell surface proteins to produce signaling molecules like TNF or TGF -α. ADAMTS are secreted and cleave signal molecules out of the ECM-components, i.e. necessary for osteoblasts ECM generation. Regulation of all three classes occurs through auto-inhibition and site-specific secretion of growth factors, cytokines or TIMPs (tissue inhibitors of MMPs). Activity of metalloproteases can be quantified by invasion assays based on Boyden-chambers, as discussed in *chapter 3*.

1.2.2 Cell-substrate adhesion

Since a considerable amount of the cell shape fluctuations presented in this work are based on forming and decomposing of cell-substrate adhesions in confluent epithelial cell layers, we will have a short glance at cell adhesion. Intercellular adhesion as well as cell-ECM adhesion determine i.e. organ architecture, embryonic development or immune system cell migration and are therefore either of permanent or transient nature. All cell adhesion molecules (CAMs) are transmembrane adaptor proteins with extracellular domains determining the family or class and a cytoplasmic tail for actin-/intermediate filament-binding or activation of signaling cascades, whereby mechanical continuity and response to chemical/physical stimuli is achieved. Selective expression of CAMs is necessary for cell specifity, but often overlapping receptor sensitivity and high reversibility of the bond is found. Therefore, cooperativity and time patterning is necessary to strengthen multiple weak bonds. We discriminate between five families of cell - adhesion - molecules (see *figure* 1.7) : immunoglobulin class (IgCAMs, 1),
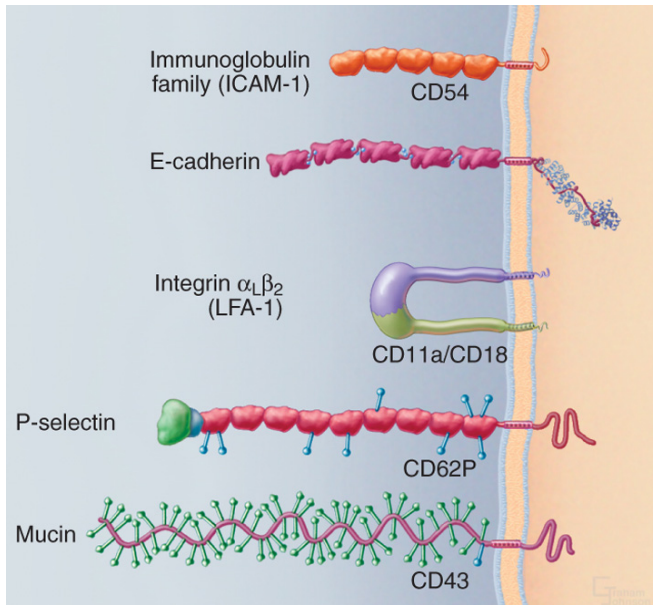
the biggest family with hundreds of members, selectin-cell adhesion molecules (2), mucin glycoproteins and connexins/dystroglycans (3), integrins (4) and cadherines (5).

Mainly relevant for this work are the last two families, shortly presented in more detail: the cadherin class has Ca^{2+} binding extracellular domains (CAD-domains) that produce usually rigid, rod-like homodimers with cadherines of neighbouring cells or on the same cell. Intracellular, they are linked via β-catenin to actin (trough α-catenin in adherens junction, γ-catenin in desmosomes or formins upon de-novo junction synthesis) or IF-filaments (desmoplakin mediated). Additionally, they may have tyrosin-kinase domains for signalling amplification. In the present work, their contribution to epithelial contact inhibition is of relevance (*figure* 1.8). E-cadherines, produced upon adherens junction formation, signal confluence, whereupon proliferation, migration and differentiation is blocked: this is achieved by capturing free β-catenin in equilibrium with binding sites on cadherines,
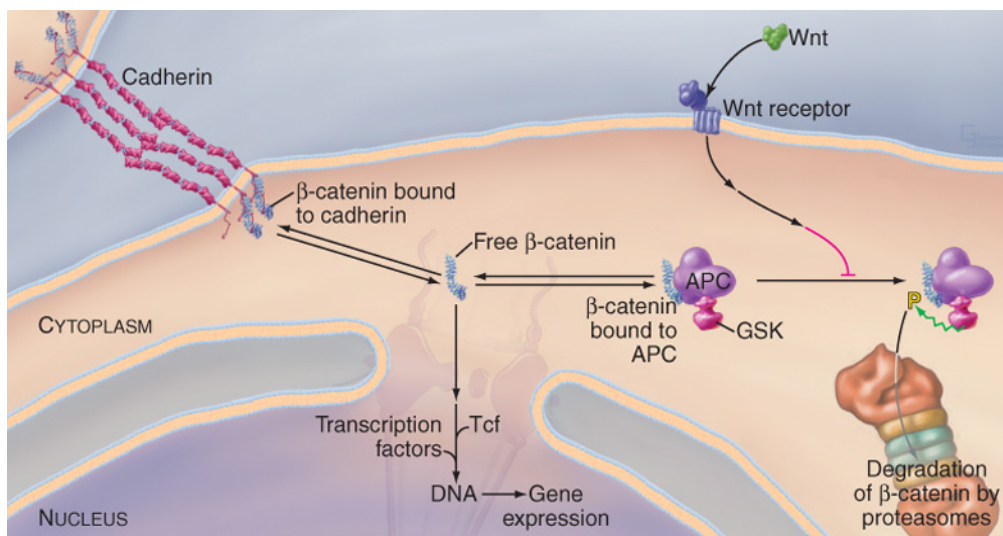
Figure 1.8 Wnt signaling through ß catenin, APC/GSK-3ß and the mediated epithelial gene expression[12], respectively contact inhibition triggered by e-cadherines. Tcf, T-cell factor.[7]

the APC/GSK3ß protein complex (adenomatous polyposis coli/ glycogen synthase kinase) or on transcription factors. APC/GSK3ß drives β-catenin degradation through phosphorylation by GSK3ß (which may be blocked by Wnt-signalling) and degradation rate determines the free β-catenin amount. Free β-catenin may diffuse into the nucleus, bind TCF/LEF-1 and activate genes promoting differentiation and cellular growth.

The integrin family is built up by heterodimers of α (16 isoforms) and β (8 isoforms) subunits, combined to 24 known isoforms.[13, 14] For epithelial cells, $\alpha_2\beta_1$, $\alpha_6\beta_4$, $\alpha_5\beta_3$, $\alpha_6\beta_1$, and $\alpha_7\beta_1$ are most common, the first two binding laminin, the third vitronectin and fibronectin and the latter collagen. In general, RGD-sequences (arginine-glycine-aspartic acid) form common binding motifs and therefore explain overlapping ligand activity. They bind ECM, all other CAMs and growth factors to control motility and organ integrity, transmit forces and allow cell-cell-adhesion (platelets to each other, sperm to egg cell, leucocytes to endothelium). As far as molecule architecture is concerned, heterodimeric binding produces a globular head on 16 nm legs, fixated by transmembrane segments, with each chain binding to (at least) two ligand sites, but both weakly. Conformational state (activated ex- and intrinsically) additionally influences binding ability (low affinity closed state with head being bent over the legs).

As far as cytoplasmic integrin tails are concerned, they are located in adhesion plaques, which are split up into three categories: nascent focal complexes(1), found in the lamellipodium, mature focal adhesions in the cell periphery (lamellum and the trailing edge, 2) or fibrillar adhesions (3), loosely found in central regions of the cell. Focal adhesions (or contacts, *figure* 1.9) are the most frequent adhesion plaques in epithelial cells and discussed here briefly: they have oval appearance, are 2.5 μm big and associated with stress fibres and α_5 integrin clusters. In the cytoplasm, β-integrins binds to dimeric talin, which is also interacting with phoshpoinositide-bound vinculin, with cross-linking α-actinin, with LIM-kinase (a cofilin deactivator) activating zyxin and with Arp2/3 capped, NMII bundled actin polymers. Regulation occurs through an interaction of the integrin with paxillin as adapter to downstream molecules like tensin, Src-kinase, or Crk/Cas, which is mediated by focal adhesion tyrosin-kinase FAK. FAK couples focal adhesions to cell migration via small GTPase signaling: while RAC1 is activating ARP2/3
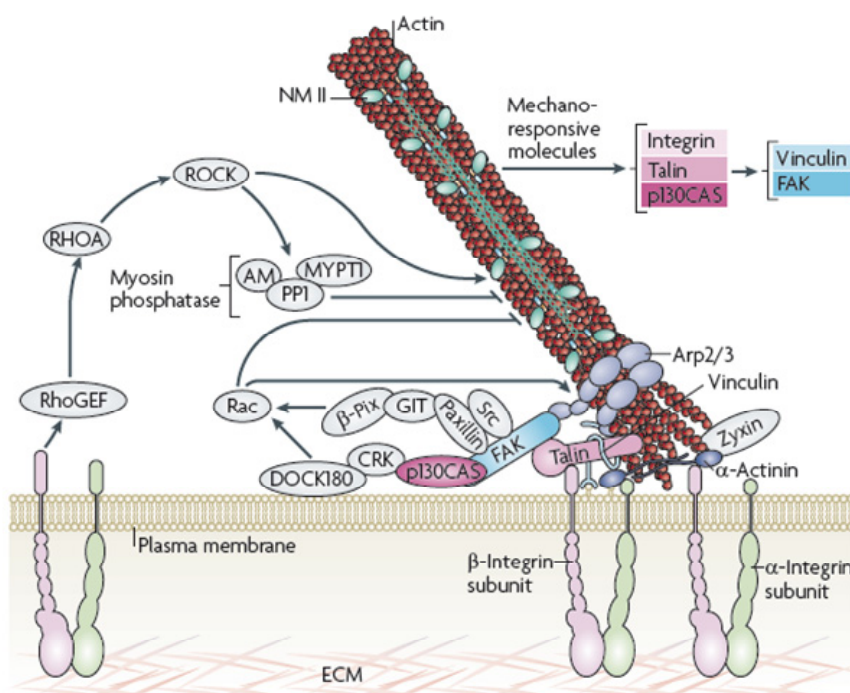
Figure 1.9 Molecular composition of integrins and focal contacts of epithelial cells (detailed in the text). NMII contractions trigger changes in conformation (pink) or clustering (blue) of adhesion molecules.[6] and therefore actin branching in focal adhesion, rhoA activates NMII through ROCK and therefore initializes focal contact maturation. Both pathways are spatially and temporally regulated.

Finally, integrins are necessary for another, epithelia cell connected aspect: $\beta_1/\beta_3/\beta_4$ integrins provide basal lamina anchorage, which, when not present, as in case of suspension, arrests cells in the G_1-phase and may, after several hours, trigger initial apoptosis.[15]

1.2.3 Cell-cell adhesion

Cell-cell contacts provide mechanical integrity of tissues and are cytoplasmic associated to the cytoskeleton. Due to their function, four categories are distinguished: anchoring junctions (1), composed of cadherines, are either actin associated (adherens junctions) or, as desmosomes, linked to intermediate filaments, with the exception of ECM binding hemidesmosomes: like focal complexes described above, they are integrin associated. Occluding or tight junctions (2), made up by claudins, limit intercellular cleft diffusion of solutes/ions and provide polarization in epithelial cells (defining apico-basal polarity) through limitation of intramembraneous diffusion. Channel forming-(gap) junctions (3), composed of connexin monomers, which establish a chemical continuum between cells. Signal-relying junctions (4) allow signal transduction across plasma membranes at cell-cell contacts, i.e. chemical or immunological synapses. Cell-cell adhesions are expressed cell-type specific: number and specifity determine the effectiveness of the barrier

formation or trans-epithelial resistance TER. Impedance spectroscopy applied in this study allows to determine the TER or density of cell-cell contacts, which will be discussed in *chapters* 4 and 6.

A short introduction to the two main cell-cell adhesions analysed in this study is given: adherens and tight junctions (*figure* 1.10). Adhesive junctions (*zonula adherens*) are formed, like desmosomes (macula adherens), from homophilic, Ca^{2+} dependent cadherin interactions.[16] From the 180 members of the cadherin superfamily, especially e-cadherin forms the belt-like apical structures with β-catenin and plakoglobin acting on the cytoplasmic side as anchor and α-catenin as linker to actin fibres. Adherens junctions are the first cell-cell contacts built up when filopodia of two cells meet and responsible by Wnt, as mentioned above, for contact inhibition. Members of the Wnt-signaling and special cadherines as *flamingo* are also necessary for a third epithelial polarization mode besides apico-basal and anterior-posterior, the so called planar cell polarity, necessary in cooperative hairy epithelia movement like the inner ear or the respiratory tract.

Tight junctions (TJ, *zonula occludens*) provide selectivity of active uptake mechanism on the apical side of columnar-epithelia as they inhibit passive, paracellular
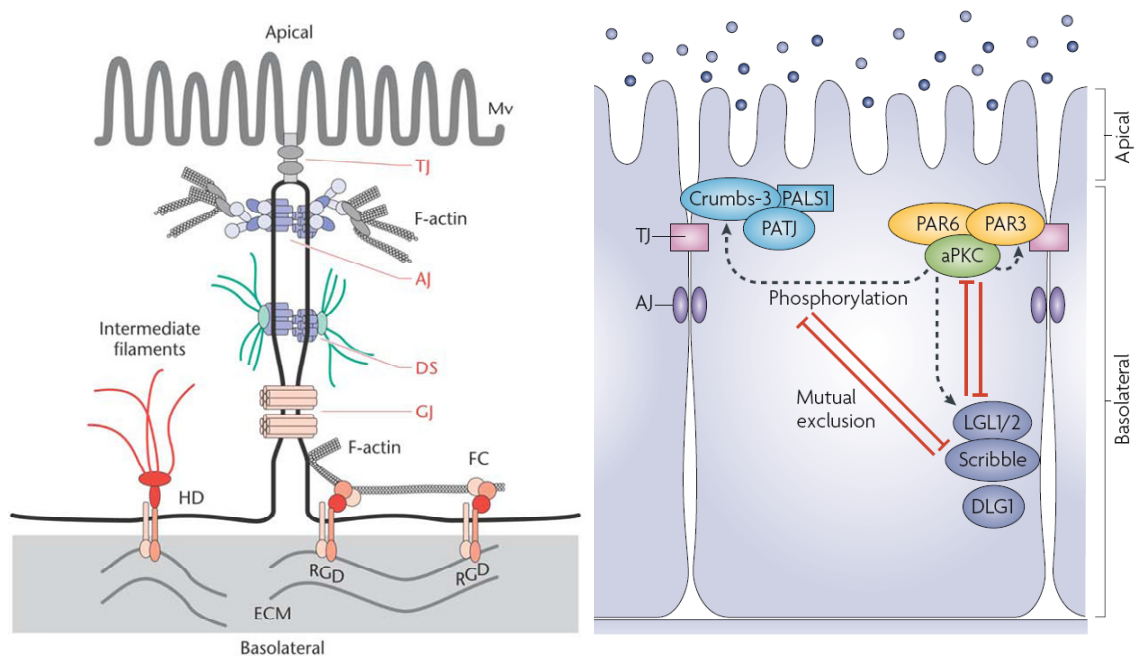
Figure 1.10 Arrangement of cell cell-adhesions in epithelial cells (left)[16]: Tight junctions (TJ) adherens junctions (AJ), desmosomes (DS), gap junctions (GJ), hemidesmosomes (HD), focal contacts (FC) and apical membrane protrusions, microvilli (Mv) are shown. Arrangement of three membrane associated complexes necessary for polarization (right)[17]: the general Par3-Par6-aPKC complex is small GTPase (CDC 42/RAC1) regulated, the two complexes crumbs and scribble are set up by scaffold forming, PDZ-domain containing proteins crumbs/PALS1 (apical) and scribble/discs-large1 (lateral).

diffusion between cells (belt-like seal) for larger solutes. Due to discontinuity of strand contacts, pores of a diameter below 1 nm are formed, each with specific (bidirectional) selectivity for ions and therefore expressed tissue specific. Integral membrane proteins form a branched, intracellular network on the bilayer and strands between cells consist of occludin or claudin: two extracellular and four transmembrane domains are found in both families, and both are linked via i.e. ZO-1 (also found in gap and adherens junctions), ZO-2/cingulin or ZO-3 adaptor proteins to actin fibres. Regulatory units like small rho GTPases RAC1 and CDC42, as well as three membrane associated proteins Par 3 and Par 6 (from partitioning defective mutants) and atypical protein kinase C (aPKC) are involved in general polarity and de-novo TJ formation. Furthermore, in epithelial cells, adherens junctions strengthen TJ, control their leakiness and are prerequisite: the two membrane-associated protein complexes crumbs (apical) and scribble (lateral) are thereby involved. Further intracellular regulation involves second messengers like Ca^{2+} and cAMP, which increase TJ-leakiness; extracellular regulatory signals may be hormones or cytokines, but also mechanical stimuli.

1.2.4 Whole cell motility and migration regulation

Whole cell motility relies, as intracellular motility, on the abundance of cytoskeletal proteins expressed cell-specific and force exertion is based on four processes: polymerization and depolymerization of both actin (1) and microtubules (2) , movement of kinesin/dynein motors on microtubules (3) or actin-myosin contractions (4). Highest velocities for cell motility found in nature exceed mm/s (calcium sensitive, spasmin-based contractile fibres in ciliates), but mammalian cells usually present intermediate speed around 1 to 0.01 µm/s.

In this study, quartz crystal microbalance or impedance spectroscopy based biosensors detecting epithelial cell adhesion, cell-cell and cell-substrate dynamics are presented. For sub- or nonconfluent cells, locomotion occurs via protrusion formation and cell substrate attachment at a leading edge and retraction at a trailing edge. This cell crawling occurs cyclic and in all cells to a different degree or time point (i.e. keratinocytes, fibroblasts, leucocytes, epithelial cells). It is endorsed by three kinds of actin-polymerization driven plasma membrane extensions (see *figure* 1.11): filopodia or
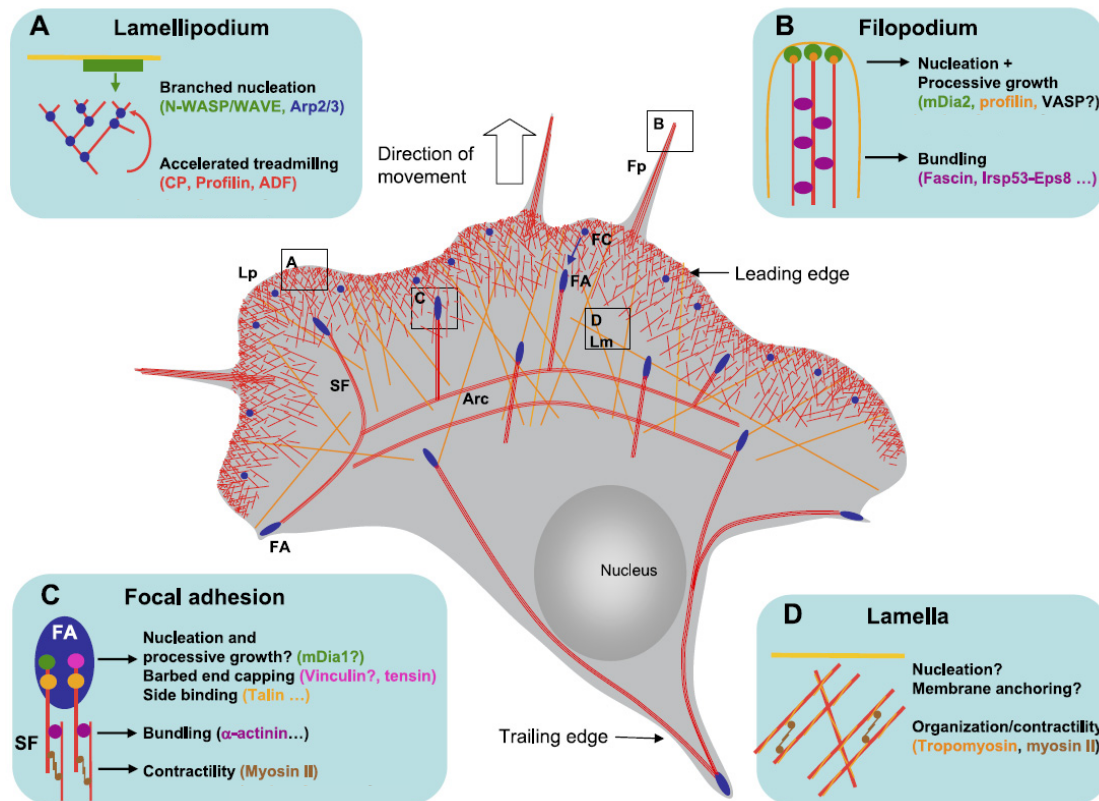
Figure 1.11 Main plasma membrane extensions and cytoskeletal architecture of a migrating cell: A: Lamellipodia (Lp) with branched actin filaments and accessory proteins, anchored at nascent focal adhesions (FA) B: Filopodia(Fp)-actin fibers (assembled with FC for environment-sensing[18]) nucelate and grow via formins and are tightly bundled by i.e. fascin and the Eps8 complex. C: Focal adhesions (assembled via RhoA signaling), see *figure* 1.9. D: Lamella (Lm) with slow actin turnover of focal complex (FC) anchored ventral, dorsal and transverse arcs of actin stress fibers (SF), tropomyosin and myosin II. Some are anchored via fibrillar adhesions.[19]

mikrospikes (a) containing long bundles of actin filaments (microvilli of epithelial cells represent actin-myosin I containing, stable filopodia); lamellipodia (b) with a two dimensional, sheet-like, branched mesh of actin fibers and pseudopodia/lamella (c). The latter are three-dimensional projections filled with actin gels and ventral (both end associated with focal contacts), dorsal (one end associated with focal contacts) or transverse arcs (no focal contact association) of stress fibers as well as microtubules. Membrane ruffles often occur at the leading edge: they represent lamellipodia that fail to be anchored and are dorsally swept back.

In the following, protrusion formation at the leading edge of a lamellipodium and filopodia formation are introduced on a molecular basis (see *figures* 1.12 and 1.13): the constant pool of free ATP-actin maintained by profilin in the cell periphery is used for
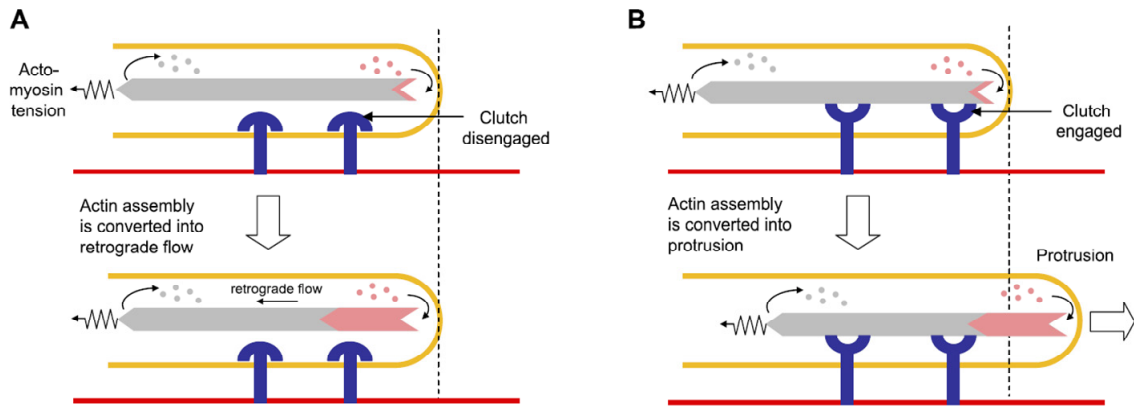
Figure 1.12 Conversion of force is either leading to retrograde flow (A) when clutch is disengaged or to protrusions (B) by substrate anchored, polymerizing actin networks.[19]

barbed-end directed synthesis lateral to existing fibers: minus ends are attached to the side of old fibres, which in turn activates WASp/Scar to guide Arp2/3 nucleated, branched actin growth. This pushes the membrane forward and is Arp2/3 controlled
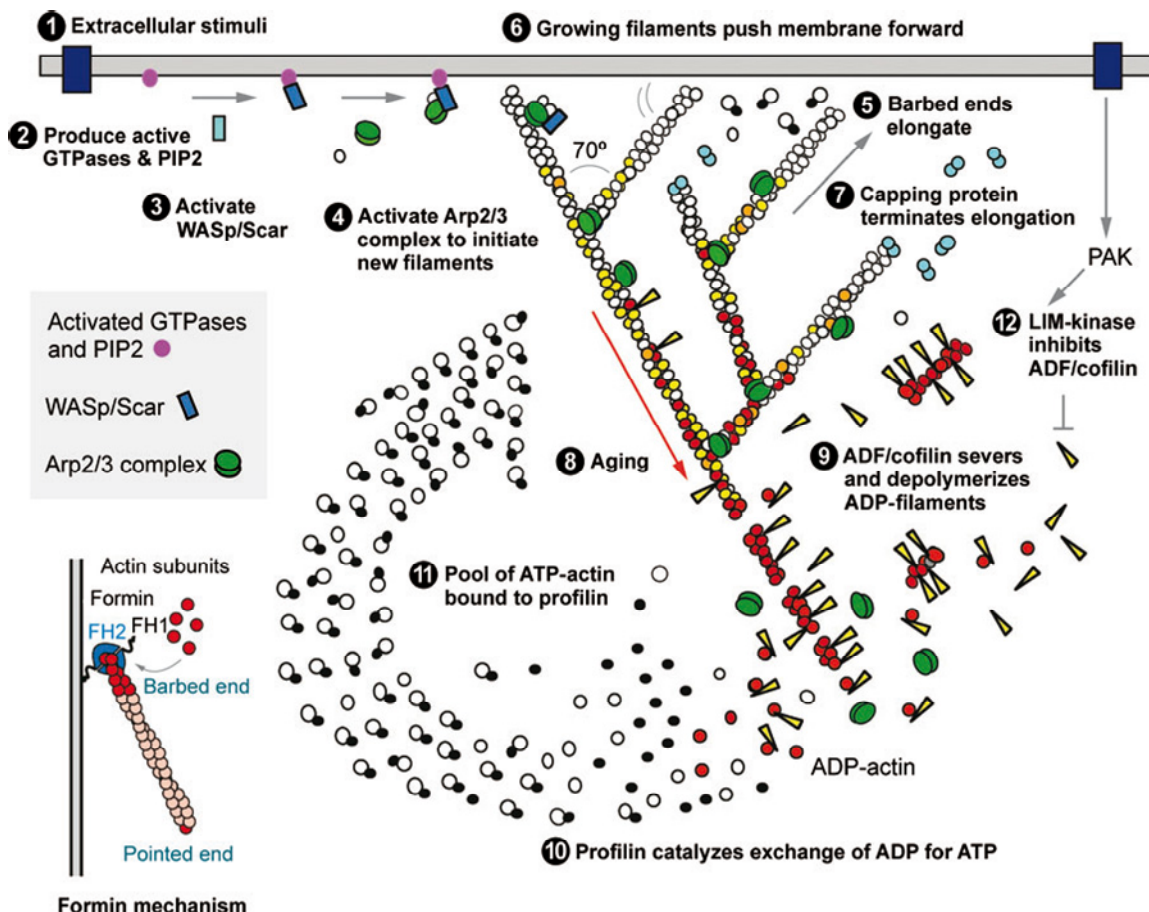
Figure 1.13 Sequential (1-12) growth of actin filaments by Arp2/3 (branched, top) or by formins (bundles, bottom) at the leading edged of motile cells. First is lamellipodia, the latter filopodia-associated. Details in the text.[20] Recently, cortactin contributions are being analyzed.[21, 22]

Figure 1.14 Adhesion disassembly at the trailing edge: NMIIA mediates contraction. Proteolysis occurs through a calpain-dependent cleavage of adhesion components. Microtubule targeting induces relaxation and disassembly via +TIPs: APC, (adenomatous polyposis coli, also present in the leading lamellum), DIAPH1, (diaphanous 1),EB1 (end binding protein 1).[6]
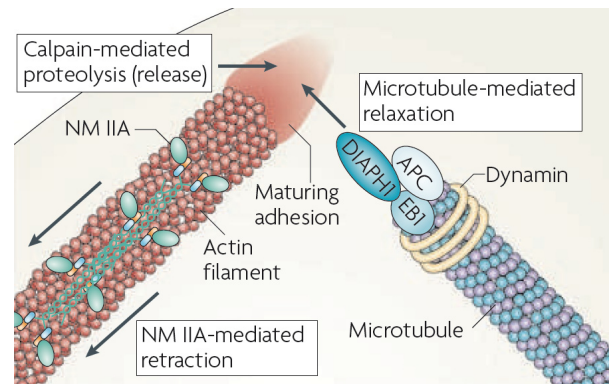
(*figure* 1.13). Furthermore, a cascade of Rho family GTPase (discussed below) is activated by chemical/physical external stimuli. In filopodia and, to a small extent, in lamellipodia of slow moving cells, de-novo synthesis of actin fibres occurs through the actions of the formins mDia1 and 2,[23] which remain attached to the barbed ends upon elongation. Slow moving cells also invest the main part of actin assembly/treadmiling as well as actomyosin contractions in retrograde flow without net walk due to a loose assembly to peripheral nascent focal complexes, while fast moving cell present strong focal complex anchorage (closed molecular clutches, *figure* 1.12) leading to protrusion formation over stationary actin filaments. The growing filaments push the membrane forward with pN forces until a maximum of 1 μm is reached due to the bending stability of fibres, whereupon the heterodimeric capping protein terminates growth. Thereupon, either ADP-rich regions are severed by ADP/cofilin (*figure* 1.13) or stabilized by cross-linking through filamin as well as bundled by NMII contractions and α-actinin (*figure* 1.11). Longer and thinner fibres in the lamella are stabilized by tropomyosin and ADF/cofilin-inhibition (by LIM-kinase) and are anchored in fibrillar adhesions including tensin-capping and $\alpha_5\beta_1$ integrin-connection to fibronectin. Hereby, microtubules are stabilized to maintain cell shape polarity by Rho-GTPases, i.e. to initialized retraction at the trailing edge of cells (see *figure* 1.14): +TIPs mediated relaxation of stress fibers, NMII contractions[24] and calpain-triggered proteolysis of adhesion contacts drive the retraction when tension forces of overcome attractive forces.

Motility-mediated fingerprinting of cells proven in this work is possible, since integrin density and therefore adhesiveness dictate the cell-specific rates of movement. Regulation of migration occurs, on a short time scale, by accessory proteins influencing polymerisation activity. On an intermediate time scale, release of cytoskeletal components and integrins stored in cytoplasmic vesicles is of relevance as well as

upstream effector kinases/phosphatases activated by small-GTPases. On a big time scale, motility activation is achieved by physical or chemical external factors like hormones (chemotaxis) and cytokines such as by TGF-ß, which activate intracellular signaling cascades. The pathway relying on the Ras-superfamiliy of GTPases is thereby of uppermost relevance, i.e. for transcription factors/gene expression activation or for the regulation of migration rates as well as cell shape and cell polarity through the three membrane associated, small GTPases rhoA, RAC1 and CDC42:[25, 26] *figure* 1.15 assembles an overview of their localization and effectors in migration, while *figure* 1.16 assembles an overview of their hierarchical activation and cellular effects.

CDC42 is localized at the leading edge via the scribble–βPIX (PAK‑interacting exchange‑factor‑β) complex after external stimulation, where GEFs (guanine nucleotide exchange factors) are enriched. Activated CDC42 induces spatial activation of aPKC, which in turn initiates RAC1 activation through the T‑cell‑lymphoma invasion and metastasis‑1 factor (TIAM1), and thus actin polymerization and microtubule stabilization. aPKC also mediates a decrease in integrin turn‑over at the front and inactivates GSK3β, whereby association of the adenomatous polyposis coli factor (APC) with microtubules occurs. APC and DLG1 regulate the repositioning of the centrosome,

Figure 1.15 Localization of small GTPases rhoA, RAC1 and CDCD42 in migrating epithelial cells. Effector proteins of CDC42 and RAC1 control front polarization and migration, while rhoA and its effectors regulate the rear polarization and motility. General polarity complex consistent of the proteins PAR3/PAR6 and aPCK has a master regulation function in the front signal transduction cascade, while ROCK is of central relevance at the rear. Note that PATJ and DLG are part of scrumble and crumbs-complexes.[17]

Rear	Front	
RhoA	PAR3	CDC42
ROCK	aPKC	RAC1
Myosin	TIAM1	βPIX
	DLG	PAK
	Scribble	APC
	PATJ	
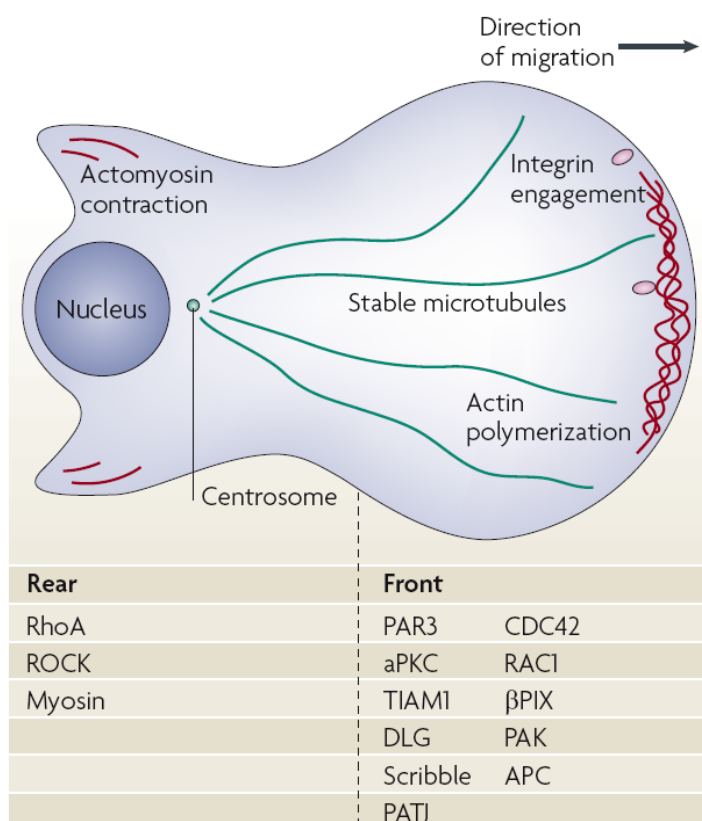
the Golgi and the nucleus towards the direction of migration. Glycogen synthase kinase‑3β (GSK3β) also inhibits p190 A, a Rho-GAP (GTPase activating protein) and therefore spatial suppression or the rhoA activity at the cell front is explained.

By contrast, rhoA activates rho kinase (ROCK) mainly to the trailing rear. In the lamellum, ROCK induces cofilin-inhibition through LIM-kinase activation[27] and inhibits the phosphatase MLC, which usually reverts NMII light chain phosphorylation Both effects together assure more stress fibers and an increased myosin contractility, which is necessary for mature focal contacts. At the trailing edge, dissociation of the PAR complex through ROCK occurs. In summary, the aPKC/PAR6/PAR3 complex holds a master regulator role for the balancing of small rho GTPases in polarization and
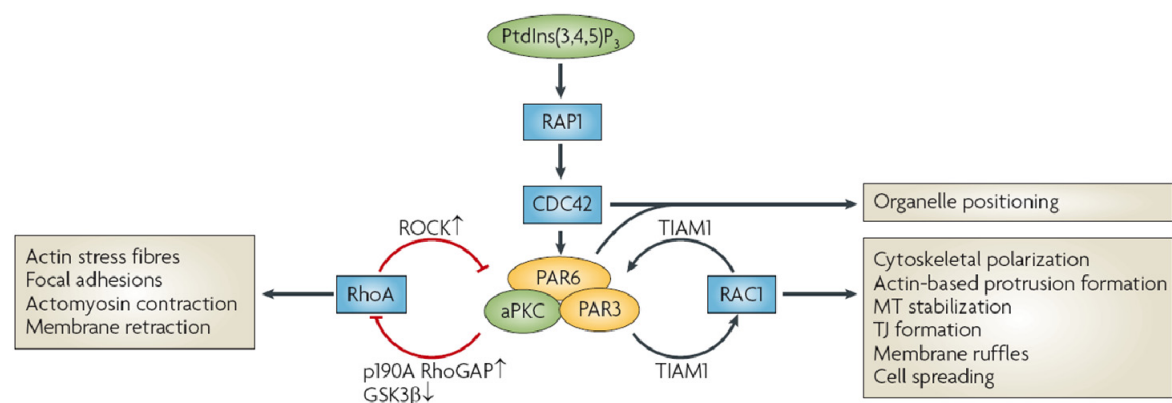
migration (*figure* 1.16).

Figure 1.16 Major contributions of the PIP$_3$ dependent CDC42 activation to the Rho GTPase cross talk. Activation of RAC1 may also occur upstream of the PAR‑complex. ROCK mediates dissociation of the PAR3/PAR6/aPKC complex. Phosphatidylinositol‑3,4,5‑trisphosphate (PI(3,4,5)P3), Ras‑like protein (RAP1).[17]

1.3 REFERENCES AND NOTES

1. Alberts, B., Johnson, A., Lewis, J., Raff, M., Roberts, K., Walter,P. (Eds.), Molecular biology of the cell, 5th Ed. *Garland science, Taylor & Francis New York* **2008**.

2. Hofmann, W. A., Cell and Molecular Biology of Nuclear Actin. *International Review of Cell and Molecular Biology, Vol 273* **2009,** 273, 219-263.

3. Uribe, R.; Jay, D., A review of actin binding proteins: new perspectives. *Molecular Biology Reports* **2009**, 36, (1), 121-125.

4. Etienne-Manneville, S., Actin and microtubules in cell motility: Which one is in control? *Traffic* **2004,** 5, (7), 470-477.

5. Herrmann, H.; Aebi, U., Intermediate filaments and their associates: multi-talented structural elements specifying cytoarchitecture and cytodynamics. *Current Opinion in Cell Biology* **2000,** 12, (1), 79-90.

6. Vicente-Manzanares, M.; Ma, X. F.; Adelstein, R. S.; Horwitz, A. R., Non-muscle myosin II takes centre stage in cell adhesion and migration. *Nature Reviews Molecular Cell Biology* **2009,** 10, (11), 778-790.

7. Pollard, T. D., Earnshaw, W.C.(Eds.), Cell biology, 2nd Ed. *Saunders Elsevier, Philadelphia* **2008**.

8. Page-McCaw, A.; Ewald, A. J.; Werb, Z., Matrix metalloproteinases and the regulation of tissue remodelling. *Nature Reviews Molecular Cell Biology* **2007,** 8, (3), 221-233.

9. Yilmaz, M.; Christofori, G., EMT, the cytoskeleton, and cancer cell invasion. *Cancer and Metastasis Reviews* **2009,** 28, (1-2), 15-33.

10. Linder, S., The matrix corroded: podosomes and invadopodia in extracellular matrix degradation. *Trends in Cell Biology* **2007,** 17, (3), 107-117.

11. Egeblad, M.; Werb, Z., New functions for the matrix metalloproteinases in cancer progression. *Nature Reviews Cancer* **2002,** 2, (3), 161-174.

12. Simpson, K. J.; Selfors, L. M.; Bui, J.; Reynolds, A.; Leake, D.; Khvorova, A.; Brugge, J. S., Identification of genes that regulate epithelial cell migration using an siRNA screening approach. *Nature Cell Biology* **2008,** 10, (9), 1027-1038.

13. van der Flier, A.; Sonnenberg, A., Function and interactions of integrins. *Cell and Tissue Research* **2001,** 305, (3), 285-298.

14. Wegener, J., Cell surface interactions. *Wiley Encyclopedia of biomedical engineering, John Wiley & Sons, Inc.* **2006**.

15. Hood, J. D.; Cheresh, D. A., Role of integrins in cell invasion and migration. *Nature Reviews Cancer* **2002,** 2, (2), 91-+.

16. Wegener, J., Cell junctions. *Nature Encyclopedia of life sciences, Nature publishing group* **2004**.

17. Iden, S.; Collard, J. G., Crosstalk between small GTPases and polarity proteins in cell polarization. *Nature Reviews Molecular Cell Biology* **2008,** 9, (11), 846-859.

18. Geiger, B.; Spatz, J. P.; Bershadsky, A. D., Environmental sensing through focal adhesions. *Nature Reviews Molecular Cell Biology* **2009,** 10, (1), 21-33.

19. Le Clainche, C.; Carlier, M. F., Regulation of actin assembly associated with protrusion and adhesion in cell migration. *Physiological Reviews* **2008,** 88, (2), 489-513.

20. Pollard, T. D., Regulation of actin filament assembly by Arp2/3 complex and formins. *Annual Review of Biophysics and Biomolecular Structure* **2007,** 36, 451-477.

21. Cosen-Binker, L. I.; Kapus, A., Cortactin: The gray eminence of the cytoskeleton. *Physiology* **2006,** 21, 352-361.

22. Lapetina, S.; Mader, C. C.; Machida, K.; Mayer, B. J.; Koleske, A. J., Arg interacts with cortactin to promote adhesion-dependent cell edge protrusion. *Journal of Cell Biology* **2009,** 185, (3), 503-519.

23. Goode, B. L.; Eck, M. J., Mechanism and function of formins in the control of actin assembly. *Annual Review of Biochemistry* **2007,** 76, 593-627.

24. Even-Ram, S.; Doyle, A. D.; Conti, M. A.; Matsumoto, K.; Adelstein, R. S.; Yamada, K. M., Myosin IIA regulates cell motility and actomyosin microtubule crosstalk. *Nature Cell Biology* **2007,** 9, (3), 299-U104.

25. Etienne-Manneville, S.; Hall, A., Rho GTPases in cell biology. *Nature* **2002,** 420, (6916), 629-635.

26. Vega, F. M.; Ridley, A. J., Rho GTPases in cancer cell biology. *Febs Letters* **2008,** 582, (14), 2093-2101.

27. Maekawa, M.; Ishizaki, T.; Boku, S.; Watanabe, N.; Fujita, A.; Iwamatsu, A.; Obinata, T.; Ohashi, K.; Mizuno, K.; Narumiya, S., Signaling from rho to the actin cytoskeleton through protein kinases ROCK and LIM-kinase. *Science* **1999,** 285, (5429), 895-898.

2

Thesis objectives and general concepts
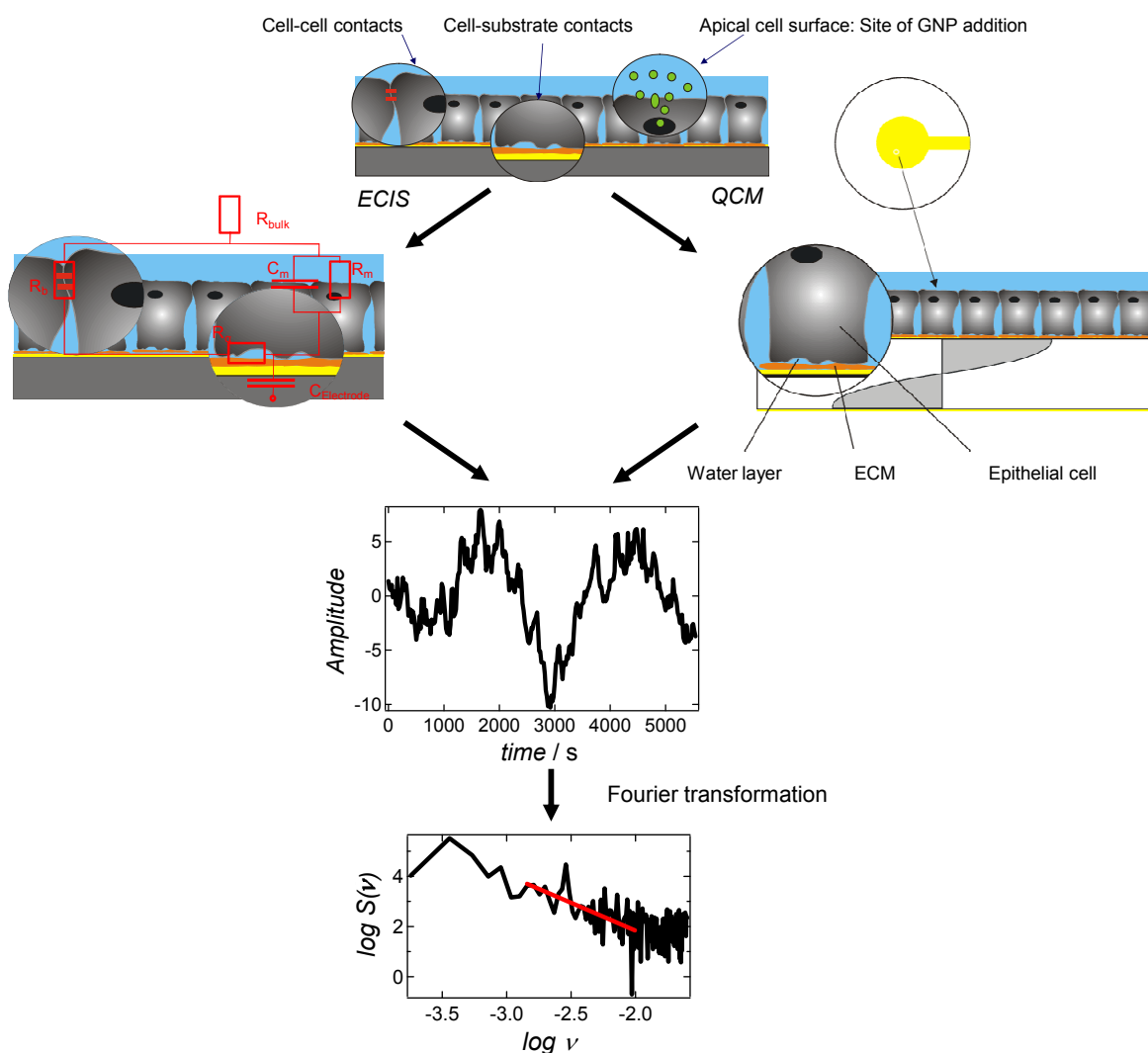
2.1 DEVELOPMENTAL OBJECTIVES

The central aim of this thesis is to develop and validate whole cell biosensors assessing migration dynamics of epithelial monolayers. Electrical cell-substrate impedance sensing (ECIS) and the Quartz crystal microbalance (QCM) are applied as acoustic and impedimetric tools to address cell motility and nanocytotoxicity in a non-invasive and real time manner.

In the ECIS setup (left part of the *scheme* at the top), cells are grown on planar gold-film electrodes that are deposited on the surface of a cell culture vessel. An impedance increase of these electrodes occurs when animal cells adhere and spread on the surface until a confluent cell monolayer is formed. The measured impedance of an epithelial sheet is not constant, but changes with modulations of shape or cell-cell junctions due to altered current pathways around the cells bodies. Besides the detection of complex cellular impedance and transepithelial resistance TER, one scope of the present work is to apply a special mode of ECIS measurements which records the real part of the complex impedance of the cell-covered electrodes at one fixed AC frequency with very high time resolution. The observed fluctuation of the signal mirrors the fluctuations of the three-dimensional shape of the cells on the electrode surface. These fluctuations in cell shape have been termed *micromotion*.

The well-established QCM-technique (see right part of the *scheme* at the top) usually measures the shift in resonance frequency and damping of an oscillating quartz crystal when adsorption, desorption or changes in material properties close to the quartz surface occur. Our goal is to prove that this device is also capable of detecting subtle fluctuations of the cell shape as an indicator for their micromotion. Therefore, this new F-QCM approach analyzes the fluctuations of the resonance frequency and dissipation and reports on the dynamics of the cell body and the cellular micromechanics.

New tools introduced in this study also include quantification methods of biological noise created by adherent cells: fluctuations of both biosensor readouts not only display the general activity of living systems, but also allow us to identify signatures of long-memory correlations in motility as well as fractal, self-similarity and collective motion. Therefore, variance determination, power density estimation and detrended fluctuation analysis are performed.

2.2 GENERAL APPLICATION CONCEPTS

The source of vertical cell migration in epithelial monolayers is the dynamics of biopolymer assembly and disassembly of the cytoskeleton and accessory proteins as well as their orchestration by GTPases (refer to basics presented in *chapter* 1). In the present *in-vitro* biosensor study, we aimed for a detection of dynamics arising from

epithelial cells locomotion. Epithelial cell motility provokes cell shape and height changes without exhibiting net directionality in confluent monolayers, therefore termed vertical micromotility.

The general motility machinery is essential for the activity of malignant, invading cells. Epithelial tumor cells are the prevalent origin of malignancies due to direct carcinogen exposure. Therefore, one target of this work is to study cancer cell migration and thus determine the metastatic potential based on the detection of the vertical cell motility in confluent cell monolayers. In this respect, we make use of this technology to measure, quantify and compare the motility of several different cancer cell lines and correlate these biosensor based results with the outcome of classical Boyden chamber experiments (*chapter* 3).

One further purpose of central relevance for this thesis is to identify and quantify the contributions of cytoskeletal biopolymers to the biological shape fluctuations (*chapter* 4). The impact of small molecule inhibitors/toxins, which target actin or microtubules, on the dynamics of the cytoskeleton, is quantified by detecting changes in the noise pattern. Additionally, chemotherapeutics resveratrol and cis-platin were applied to prove sensitivity of micromotility to the invasive properties of human head and neck tumor cells. For support, cytoskeletal rearrangements and nuclear integrity are visualized by fluorescence microscopy.

A second application concept involves the usage of cell motility as a sensitive measure for the toxicity of nanoparticles. As we face a growing field of nanotechnology, there is an urgent need to determine nanocytotoxicity, since many technical and medical applications are based on controlled exposure to the nanoscale particles. Screening platforms based on high-throughput *in-vitro* biosensors need to be developed to achieve a detailed knowledge of toxicity and biodegradation as a function of the nanoparticles' physical and chemical properties before the *in vivo* implementation. In this study, a central scope is to show that the micromotility of animal cells as monitored by ECIS and F-QCM is highly suitable to quantify *in vitro* cytotoxicity of semiconductor quantum dots and gold nanoparticles (*chapter* 5). Four of the chemical or physical aspects of nanoparticles of actual interest in life sciences are followed: shape, functionalization, intracellular stability and charge. Determination of uptake efficiency and intracellular effects will be realized by scanning for ROS generation, mitochondrial

permeability transitions (MPT) and apoptosis induction. The method is validated by conventional cytotoxicity testing (*chapter* 6).

3

Dynamics of human cancer cell lines monitored by electrical and acoustic noise analysis
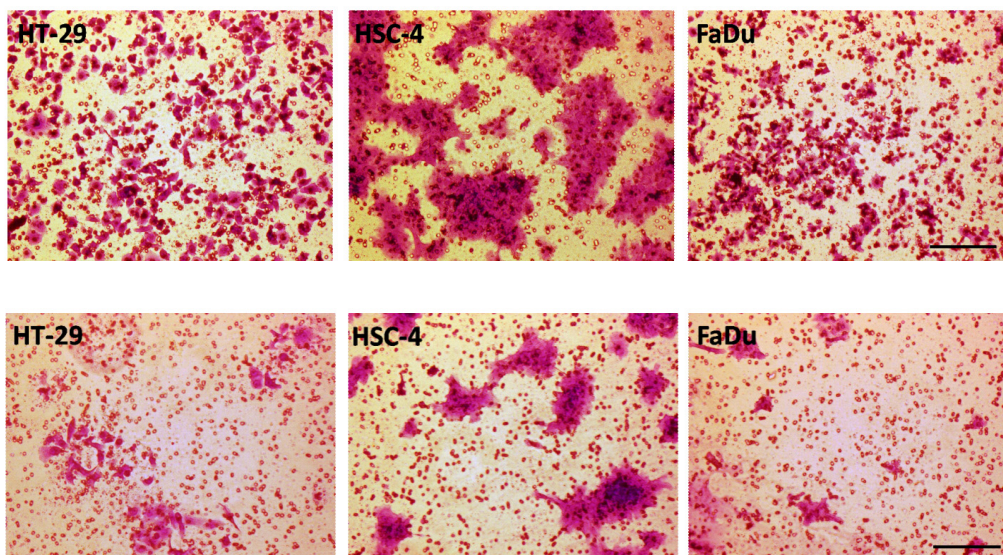
ABSTRACT

Early determination of the metastatic potential of cancer cells is a crucial step for successful oncological treatment. Besides the remarkable progress in molecular genomics- or proteomics-based diagnostics, there is a great demand for *in-vitro* biosensor devices that allow rapid and selective detection of the invasive properties of tumor cells. Here, the classical cancer cell motility *in-vitro* assays for migration and invasion relying on Boyden-chambers are compared to a real-time biosensor that analyzes the dynamic properties of adherent cells electroacoustically with a time resolution in the order of seconds. The sensor relies on the well-established quartz crystal microbalance technique (QCM) that measures the shift in resonance frequency and damping of an oscillating quartz crystal when adsorption, desorption or changes in material properties close to the quartz surface occur. In addition to the monitoring of attachment and spreading of anchorage-dependent cells, this device is capable of detecting the rather subtle fluctuations of the cell bodies as an

indicator for their micromotility. QCM-based micromotility readings of several cancer cell lines are compared with the well-known electrical cell-substrate impedance sensing (ECIS).

3.1 INTRODUCTION

Over the last half century, cancer and non-transferable cardiovascular diseases have replaced bacterial or viral infections as major cause of death. Although, for instance in the US, cancer (22.8 %) and heart diseases (26.6%) are still the leading causes of natural death, the number of cancer victims for the four most common cancers (prostate, breast, lung, colorectal) have been declining since the early 1990s.[1] This positive trend is primarily due to a huge progress in diagnostics but also in the availability of customized therapies. Breakthrough progress, however, is expected from new *in-vitro* assays that sensitively detect the metastatic potential of tumor cells derived from a minimal amount of biopsy material.

Almost 90% of all tumors originate from epithelial tissues, since these are often directly exposed to carcinogenic substances. These cells may then spread from the site of primary transformation to other organs or non-adjacent sites via a cascade of events including invasion trough the basement membrane, migration to the next blood vessel, intravasation, extravasation and eventually secondary tumor formation.[2] The metastatic potential of tumor cells is thought to be mirrored in their ability to invade and to migrate - or in more general terms: in their motility. To quantify the invasive properties of cells *in-vitro*, the Boyden-chamber invasion assay is most commonly applied. It determines the amount of cells per time that migrate through a porous polycarbonate membrane with pores of a defined size (in the micrometer range), coated with a layer of extra-cellular matrix (ECM). Various modifications of this original assay have been developed over the past decades. For instance, migration of cells through the pores of the membrane is quantified without any extracellular matrix coating on the surface of the membrane,[3] with a monolayer of endothelial cells (extravasation assay)[4] that the cells have to pass through or with an attractive or repellent gradient across the membrane (chemo- or haptotaxis assay).[5] Besides the Boyden chamber-based approaches, other assays have been

used extensively in experimental oncology, i.e. sprouting assays,[6] phagokinetic tracking,[7] wound-healing assay[8] and the cell scatter assay.[3] Positive correlation between the metastatic potential as studied *in-vivo* and these *in-vitro* assay has been demonstrated many times.[9] A major drawback of these classical methods is the time and labor consuming as well as material intense data collection, often close to significance due to the limited number of possible experiments.

Modern alternatives to these well-established classical *in-vitro* assays should be non-invasive in order to monitor the cell behavior in real time instead of providing just endpoint readout. With a reasonable time resolution even subtle characteristics of the cellular dynamics should become available, providing the potential of new bioanalytical insights and correlations. Recently, the quartz crystal microbalance (QCM) has gained interest as a label free, non-invasive biosensor to study biomedical applications and to follow adherent eukaryotic cells, also in cancer research.[10] A variety of different application modes have been described like, for instance, comparing the kinetics of cell attachment and spreading for different cell lines and seeding densities,[11] analyzing muscle-cell contraction or integrin-mediated adhesion of ovarian cells,[12, 13] monitoring the cell response upon exposure to various chemotherapeutics or growth-factors[14-17] or measuring the impact of nanoparticles on the viability of cultured epithelial cells.[18] Here, we focus on a rather new QCM approach to study cell motility which is based on analyzing the fluctuations of the resonance frequency of a cell-covered quartz resonator. These fluctuations of the resonance frequency report on the dynamics of the cell body and the cellular micromechanics. Biological noise created by adherent cells displays not only the general activity of living systems, but also allows to identify signatures of long-memory correlations in motility as well as fractal, self-similarity and collective motion.

This new mode of QCM recording expands the existing applications that mainly address shifts of the resonance frequency with time rather than measuring the noise which can be observed even in a totally equilibrated cell layer due to the metabolically driven cell shape changes. In a sense, QCM-based noise analysis of the resonance frequency is similar to the measurement of the so-called micromotion by an impedimetric whole cell biosensor referred to as electric cell-substrate impedance

sensing or short ECIS.[19-22] Recently, we have already reported on the general feasibility of noise analysis as a powerful tool to measure cell motility in a technical paper.[23] Here, we present a quartz-crystal-biosensor application for the study of cancer cell migration and thus determination of the metastatic potential based on the detection of the vertical cell motility in confluent cell monolayers. In this respect, we make use of this technology to measure, quantify and compare the motility of several different cancer cell lines and correlate the QCM-based results with the outcome of classical Boyden chamber and ECIS experiments.

3.2 EXPERIMENTAL SECTION

3.2.1 Cell culture conditions

All human cancer cell lines used in this study originate either from colon, breast or pharynx. FaDu cells,[24] a squamous carcinoma cell line derived from the hypopharynx, is cultured in Dulbecco`s modified Eagles medium with 4.5 g/l glucose and 2 mM L-glutamine (PAA laboratories GmbH, Cölbe, Germany), non essential amino acids NEA (100 µg/ml), sodium pyruvate (1mM) and 10 mM HEPES buffer. The colon carcinoma cell line HT-29 [25] is cultured in DMEM low glucose (1.0 g/l), 1 mM Na-pyruvate and L-glutamine, respectively (PAN, Aidenbach). The second colon carcinoma line, HCT 116,[26] is grown in DMEM high glucose (4.5 g/l) with 2 mM L-glutamine (PAA, Cölbe) supplemented with 20 mM HEPES–buffer (PAA, Cölbe), 1 mM NEA (PAA, Cölbe) and 1 mM Na-pyruvate (PAA, Cölbe). A third colon carcinoma cell line, HCT-8,[27] is cultured in growth medium RPMI 1640 (PAA, Cölbe) with 1 mM NEA (PAA, Cölbe) and 1 mM Na-pyruvate (PAA, Cölbe). The breast cancer cell line BT-474 [28] is grown in DMEM low glucose (1.0 g/l) supplemented with 1 mM Na-pyruvate and L-Glutamine (PAN, Aidenbach). The oral squamous epithelial carcinoma line HSC-4 [29] requires DMEM high glucose (4.5 g/l) with 2 mM L-glutamine (PAA, Cölbe),1 mM Hepes–buffer (PAA, Cölbe), 1 mM NEA (PAA, Cölbe) as well as 1 mM Na-pyruvate (PAA, Cölbe). Passage number is typically kept between 10 and 25 to ensure that the neoplastic phenotype did not change during the experiments.

3.2.2 Boyden chamber migration and invasion assays

To compare the metastatic potentials for all cell lines of this study that are capable of forming confluent monolayers (HSC-4, HT-29 and FaDu), Boyden chamber based migration and invasion assays were performed. Therefore, a 24-well Boyden chamber assay with inserts containing free or ECM-coated filter membranes was performed following the manufacturer's protocols (colorimetric ECMatrix cell invasion assay, ECM 550, and colorimetric Chemotaxis cell migration assay, ECM 508, both from Chemicon, Temecula, CA, USA). Prior to seeding the cells under test upon the filter membrane, they had been pre-incubated in serum free-medium for 24 h. 2.1×10^5 cells suspended in 300 µl of their respective medium were then loaded into

the upper compartment of the invasion/migration-setup. Cells were incubated either for 72 h on ECM-coated (invasion) or for 15 h on non-coated (migration) 8 µm-pore-sized polycarbonate membranes. Medium containing 10 % (v/v) serum was filled into the lower chambers as a chemo-attractant source. Cells that had invaded through the matrix-covered or the uncoated pores of the membrane commonly adhere to the lower membrane surface of the filters and were subsequently quantified (after removal of non-invaded ones with cotton swabs from the upper surface) by using the cell stain solution from the Chemicon-kit. The numbers of migrated or invaded cells were determined by counting six fields of view at 40fold magnification per well with a phase-contrast microscope (Axiovert 200, Zeiss, Germany) before averaging. Experiments were repeated three times.

3.2.3 QCM resonator preparation and phase contrast microscopy

100 nm thick circular gold electrodes (0.2 cm^2) were thermally evaporated on both sides of 5 MHz AT-cut quartzes. 5 nm of chromium was used to ensure adhesion of gold. Optical microscopy is possible with semi-transparent electrodes by evaporating only 12-50 nm gold on a 3 nm chromium underlayer. Before use, the resonators are cleaned in an ultrasonic bath for 15 min at 70°C. Afterwards, the crystals are dried under a stream of nitrogen and treated for 45 seconds in argon plasma for sterilization and hydrophilisation to promote cell adhesion. Regeneration of sensors after the D-QCM experiments was accomplished by immersing them in a 70/30% ethanol-water-mixture followed by a detergent washing step to remove the remaining cells from the surface before the cleaned resonators were rinsed three times in deionized water.

Special Teflon-chambers - used to form a culture vessel with the resonator as the bottom - are assembled aseptically and are then filled with 1.5 ml of culture medium.[23] Sealing of the chamber is ensured by two o-rings clamping either side of the quartz. Finally the chambers are sealed with a screw cap to prevent fluid evaporation. The measurement chambers are placed inside an ordinary cell culture incubator with 37 °C and 5% CO_2-atmosphere (MMM Medcenter Einrichtungen, Gräfelfing, Germany) and connected to the QCM-oscillator circuit. After 2 hours of equilibration, freshly passaged cells are directly transferred onto the resonator.
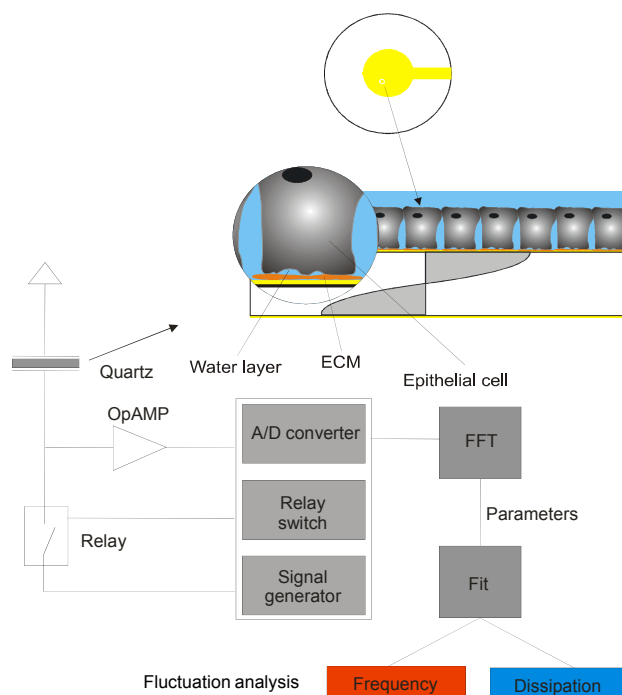
Figure 3.1 Schematic representation of the experimental D-QCM setup. The thickness shear mode resonator is driven by a signal generator and periodically disconnected. An operational amplifier feeds the signal into an A/D-card used to follow and store the free oscillation decay. The decay curves are subject to non-linear fitting which provides the resonance frequency and the decay constant (as a measure for energy dissipation) of the oscillation.

The cells were inoculated at a density of 6-7$\times$10^5 cells/ml in aliquots up to 500 µl in HEPES buffered medium. As the resonator surface is approximately 1 cm^2 and all cell types that are considered in this study are similar in size (mean area of the spread cell is 150-250 µm^2). We adopted an experimental seeding density of 6-7x10^5 cells per cm² to ensure fast and reproducible formation of a confluent monolayer accompanied by moderate medium consumption.

For studying the cells microscopically, cell inoculation was performed under the same conditions but on quartz resonators with thinner electrodes. Cells could be monitored using an inverse phase contrast microscope (Olympus CKX 41, Hamburg, Germany). For each cell line, experiments are done in triplicate. Cell-free resonators either immersed in culture medium or deionized water were used as controls to monitor noise of resonance parameters in the absence of cell adhesion or motility. Further control experiments comprise frequency fluctuations of resonators in contact to glycerol/water mixtures (60 % / 40 %) as this solution imposes a similar acoustic load upon the resonator as living cells, however, with thermal/viscous noise

as the only source for frequency variations.[11] Ultimately, all cellular activities were irreversibly stopped by chemical fixation using 0.5 % glutardialdehyde (Sigma-Aldrich, Germany) to ensure that the observed frequency fluctuations originate from biological activity rather than changes in the load situation.

3.2.4 QCM setup and data acquisition

For QCM-based fluctuation analysis, data acquisition with reasonable time resolution is required, which was achieved with a self-made D-QCM setup (*figure* 3.1*, based on Reiss et al.*[30]). Using this device, the quartz resonator is excited to perform mechanical oscillations near its fundamental resonance of 5 MHz by an 80 MHz signal generator (Agilent 33250A, National Instruments). The excitation source is disconnected from the quartz periodically, after a stationary oscillation is established. The free decay is read out by an A/D-converter (NI 5911, National Instruments), while a self-written software fits the parameters of a damped sine wave transfer function ($U=U_0e^{-t\delta}\sin(2\pi ft+\varphi)$) to the experimental data. The continuous fitting provides the resonance frequency f and decay constant of the oscillation δ as fit parameters. δ is directly proportional to energy dissipation D:

$$D=\frac{\delta}{\pi f_o}=\frac{R}{2\pi f_0 L}=\frac{2\Gamma}{f_0} \tag{1}$$

In equation (1) R denotes the motional resistance of the oscillation and Γ the half-band-half-width (HBH-width). R, δ, and Γ have in common that they are related indicators for the energy dissipation of the quartz oscillation.

Resonance frequency f_0 and dissipation indicator δ are measured for each time point. While energy dissipation is low for rigid masses on the quartz surface due to direct coupling to the quartz oscillation without acoustic losses, viscoelastic bodies like cells exhibit a significant dissipation.

3.2.5 ECIS setup and data acquisition

To record micromotion of the various cell lines by impedimetric monitoring we used a self-made ECIS system consisting of a lock-in amplifier (SR830, SRS Inc., Sunnyvale, CA) with an internal oscillator, a multiplexer with analogue switches for automatic, consecutive addressing of individual wells on the electrode array, and a PC for

experiment control and data storage. The ECIS electrode arrays (type 8W1E) purchased from Applied Biophysics (Troy, USA) consists of eight separate wells, each holding one gold microelectrode of 250 µm diameter and a counter electrode that is roughly 1000fold larger in surface area. In our ECIS setup, a 1 V AC signal is applied to the system through a 1 MΩ series resistor. The in- and out-of-phase voltages across the electrodes are recorded at 4 kHz using a sampling rate of 1 Hz. The in-phase voltage, which is directly proportional to the real part of the complex impedance, was used for further analysis as it provides the most sensitive readout. The sensing voltage applied to the cells is in the order of a few mV and can be considered as being non-invasive.

3.2.6 F-QCM and ECIS noise analysis

The raw data obtained from either D-QCM (Δf and $\Delta \delta$) or ECIS ($\Delta U_{in-phase}$) was processed and analyzed as follows (termed F-QCM): time course data is divided into data blocks of 500 points (with an overlap of 50 % between single blocks for F-QCM). After subtracting a linear trend to remove long term drifts from the analysis, these raw datasets are subjected to Fourier Transformation in order to gain power density spectra (PSD). The slope *m* of the PSD was determined by linear least square fits in a low frequency regime (0.03 to 0.01 Hz for ECIS[23] or from 0.5 to 5 mHz for F-QCM, see *figure* 3.2). For time resolved presentations of the slopes m_{QCM}^{PSD} or m_{ECIS}^{PSD}, the numerical values were smoothed by adjacent averaging over four successive data points. The smoothed slopes are plotted as a function of time assuming quasi-stationary within the given time interval. For the specific noise levels after full cell monolayers were established, slope values from the confluent stages were pooled for each cell line and mean values derived from three experiments are presented. The same procedure was carried out for variance analysis of Δf and $\Delta \delta$ fluctuations as well as $\Delta U_{in-phase}$. The variance was normalized to σ^2 of resonators` electrodes immersed in full culture medium as obtained from the same type of measurement ($\tilde{\sigma}_{QCM}^2$ or $\tilde{\sigma}_{ECIS}^2$) and are hence dimensionless.

Finally, detrended fluctuation analysis (DFA)[31] was applied to fluctuation data to identify cell-specific long-term correlations in the recorded noise and to validate power spectral data to ensure that fractality is correctly determined. In brief, the DFA comprises the following steps. First, the data sequence of length *n* is divided in *n/l* non-
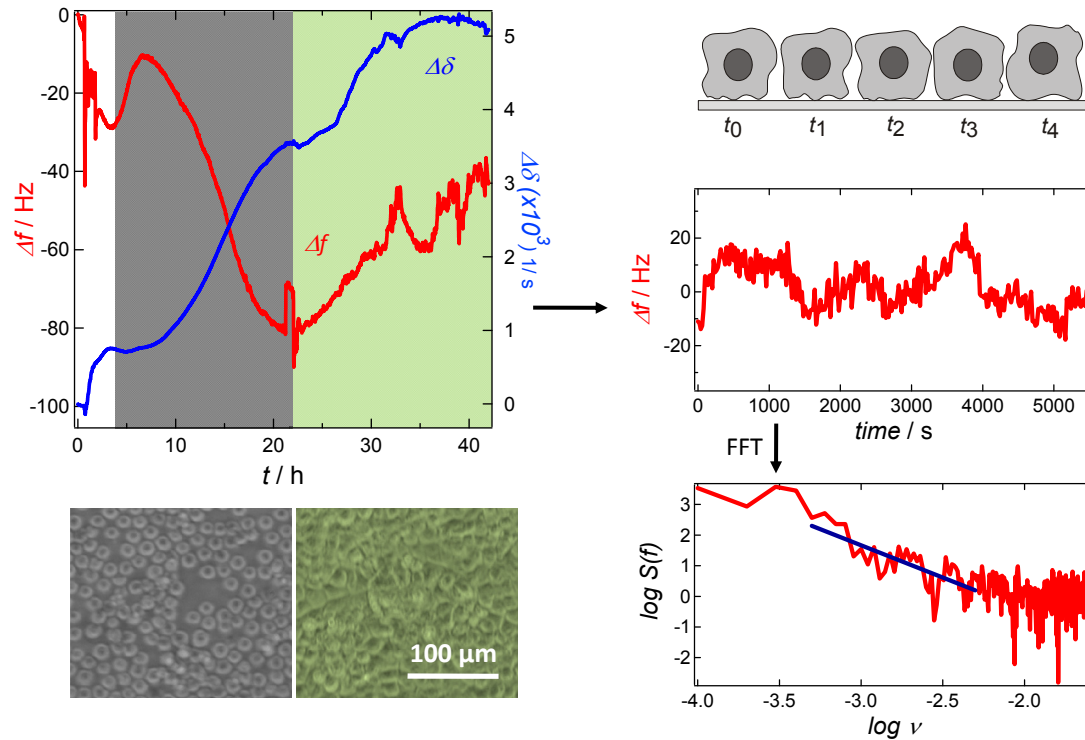
Figure 3.2 Typical time course of Δf and $\Delta \delta$ as recorded in a D-QCM experiment after addition of 6-7×10^5 HT-29 cancer cells; the grey background denotes the time regime of attachment and spreading, whereas the green background highlights the cell monolayer in its confluent state. The labels Δf and $\Delta \delta$ denote the maximal shifts in frequency and dissipation. Fluctuations in frequency/dissipation can be extracted from fixed time intervals. Subsequent FFT analysis provides the PSD (power-spectral density). Slopes of the PSD curves in the frequency regime from 0.0005 to 0.005 Hz are used as one quantitative parameter to describe cell motility as are variance and DFA-analysis.

overlapping boxes. Within each box the local linear trend is removed from the original data and the variance about the detrended walk, which is defined as the difference between original data and the trend is averaged for each box of length *l*, denoted $F_d^2(l)$.

Generally, $F_d^2(l) \propto l^\alpha$ holds, with α denoting the so called DFA exponent. While for uncorrelated noise α=0.5 is valid, long-range power-law correlation memory is characterized by $\alpha \neq 0.5 \ (\alpha > 1)$. Note that $m = 2\alpha - 1$ holds, assuming that the power spectral density follows an inverse power law $PSD \propto f^m$ with *m* < 0.

3.3 RESULTS

The intrinsic properties of cancer cells to grow out of boundaries implicates that not all cancer cell lines form defined confluent monolayers *in-vitro*. In this study two different types of human cancer cell lines were subject to QCM analysis. While the cell lines HT-29, FaDu, and HSC-4 form confluent monolayers on the resonator surface, cell lines HCT 116, BT-474, and HCT-8 do not show defect-free monolayers. In fact, HCT-8 and BT-474 cells even form multilayers. This implies that characteristic quantities such as the maximal frequency decrease make only sense for the confluent cell lines. We include the non-confluent cell lines in our study to give a reasonable and fair judgement to which extend their metastatic potential is assessed in a quantitative manner by frequency and dissipation readings. However, since lateral migration and proliferation cannot be excluded in the case of HCT 116, BT-474, and HCT-8, noise analysis will inevitably be perturbed by these different modes of motility.

Figure 3.2 shows a typical D-QCM time course after seeding of 6-7$\times 10^5$ / cm² synchronized HT-29 colon cancer cells. HT-29 cells are known to form confluent monolayers. After an initial frequency drop (dark grey area), which correspond to the process of spreading after initial attachment the cells become confluent and express their morphological polarity (green area, 20-40 hours after seeding). During this phase the monolayer displays increased frequency fluctuations (*figure* 3.2, inset). Time series data taken from this phase are further processed by stochastic analysis such as power spectral density estimation, variance analysis, and DFA as outlined above. Cell motility monitoring by F-QCM was correlated with optical microscopy (*figure* 3.2, bottom).

3.3.1 D-QCM-characterization of human cancer cells capable of forming confluent monolayers

Figure 3.3 shows the frequency and dissipation response of the cells lines HT-29, FaDu, and HSC-4 upon seeding on the quartz resonator and the corresponding light micrographs. In order to focus our analysis on the micromechanical fluctuations of cells in a tissue-like environment, we seeded a sufficiently high number of cells into the QCM measurement chambers so that a confluent monolayer is immediately
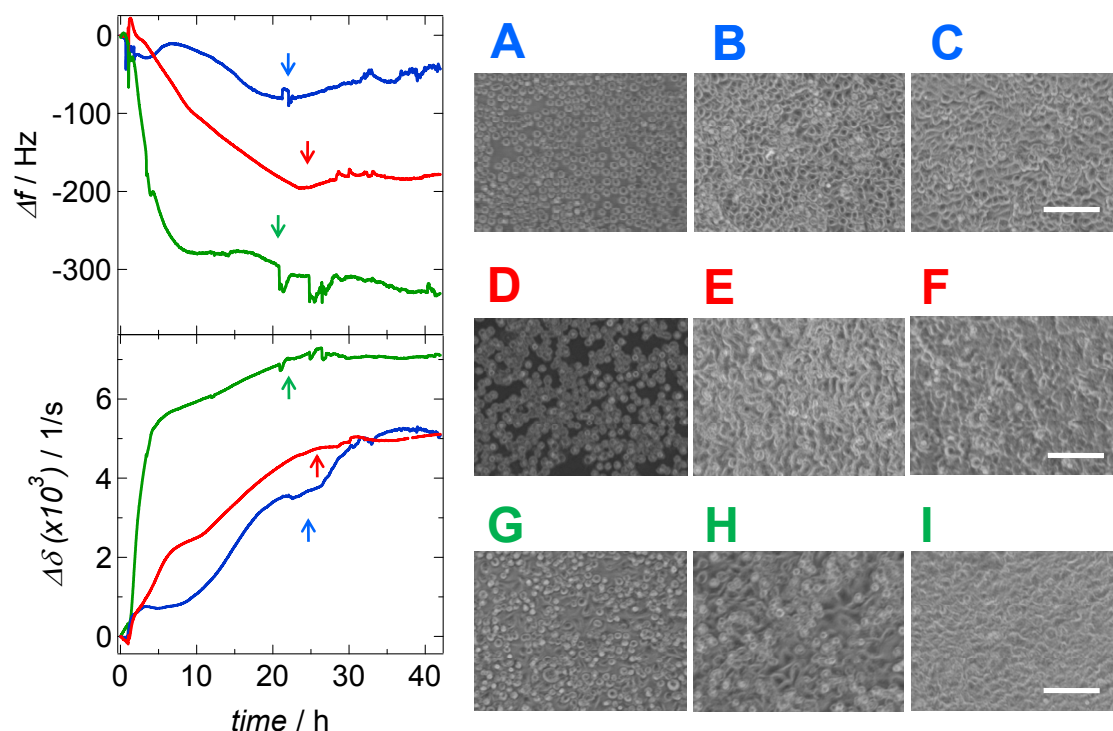
Figure 3.3 Characteristic time courses of Δf and $\Delta \delta$ obtained from D-QCM experiments after addition of 6-7×10^5 cells that are capable of forming a confluent cell layer: colon carcinoma cell line HT-29 (●), hypopharyngial squamous cancer line FaDu (●) and oral squamous epithelial carcinoma line HSC 4 (●). The highest acoustic load was produced by the HSC-4 cell line. Corresponding optical light micrographs are labeled in the same color code shown on the right: *A-C* for HT-29 after 1 h, 16 h, 24 h; *D-F* for FaDu after 2 h, 24 h, 48 h; *G-I* for HSC-4 after 2 h, 4 h, 24 h, scale bar is 100 µm.

formed from the seeded cells. The arrows depict the time when confluency is reached. No multilayers are observed in the duration of the experiment, but a stationary state is found (see *figure* 3.3 A-I).

The mean values of Δf and $\Delta \delta$ obtained from this regime are summarized in *table* 3.1. HSC-4 and FaDu show a generally stronger impact on the acoustic response of the resonator particularly on the frequency, while HT-29 cells mainly affect the dissipation. This reflects the difference in individual cell-substrate distance and natural variations of the micromechanical properties. Notably, FaDu cells often show a characteristic kink in the time course of Δf and $\Delta \delta$, usually between 6-8.5 h.

Remarkably, confluency of cells is accompanied by substantially increased frequency and dissipation fluctuations. This is most likely due to the continuous formation and decomposition of cell-substrate contacts of the cells in the monolayer as well as fluctuations in the cells` height and viscoelasticity.
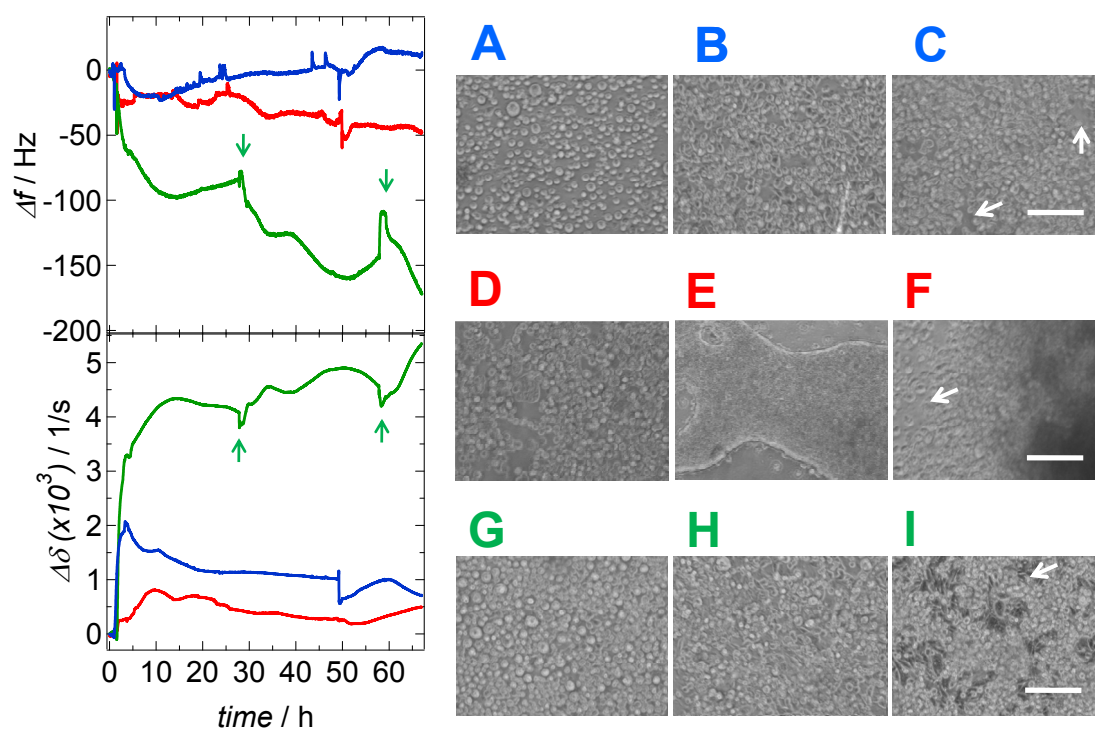
Figure 3.4 Characteristic time courses of Δf and $\Delta \delta$ obtained from D-QCM experiments after addition of 6-7×10^5 cells that are incapable of forming a confluent cell layer: colon cancer lines HCT 116 (●), breast cancer line BT-474 (●) and colon cancer cell line HCT-8 (●). The highest acoustic load was produced by the HCT-8 cell line. Corresponding optical light micrographs are labeled in the same color code shown on the right: *A-C* for HCT 116 after 1 h, 48 h, 72 h; *D-F* for BT-474 after 1 h, 3 h, 48 h, *G-I* for HCT 8 after 1 h, 24 h, 82 h, scale bar is 100 μm.

3.3.2 Characterization of human cancer cell lines incapable of forming defined cell monolayers

In *figure* 3.4, the frequency and dissipation shifts of the cell lines HCT-116, BT-474, and HCT-8 are shown. HCT 116 cells shows the smallest frequency decrease of all cell lines analysed in this study (*figure* 3.4, in blue). The resonance frequency reaches its minimum of merely -25 Hz after 10 hours, while dissipation is maximal (+2120 s^{-1}) already after 2-3 h. Interestingly, after approximately 3-5 h dissipation and frequency both decrease. Since the optical micrographs (*figure* 3.4 A-C) show cells on the gold electrode after 1 h, the damping maximum after 2-3 h, suggests attachment of the dissipative cell bodies to the resonator surface at that time without giving rise to a detectable mass increase. These finding are typical for a weak attachment of cells to the resonator supported also by the rather rounded morphology of the cells. Both values slowly return to their starting values within 48 hours, whereas microscopic

inspection does not reveal any change in surface coverage. HCT 116 are incapable of forming monolayers and arrows indicate non-covered areas.

The BT-474 cell line (*figure* 3.4, red line) has a duplication time of 60-70 h and is known to form multilayers in culture. Both frequency shift (-20 Hz) and damping ($\sim$ -800 s^{-1}) are small compared to other cell lines. The micrographs in *figure* 3.4 D-F reveal that the cells aggregate and form clusters or islands on the quartz without any preference for the gold coated area. After 60 h, frequency and damping show the usual opposite changes with time, i.e. while the frequency decreases, dissipation increases. Beyond the data shown in *figure* 3.4 the resonance frequency decreases to -90 Hz and dissipation increases to a rather small value of + 80 s^{-1}. We observed that single cells loosen their cell-cell contacts and spread out to cover a significant larger fraction of the surface (see arrows in micrograph *F* of *figure* 3.4). Although this slow process lasts up to 5 days, no significant further changes in viscoelastic parameters are observed, neither is the electrode fully covered with cells.

The frequency shift for the ileum-caceum cell line HCT-8 (*figure* 3.4, green line) reaches a first plateau value at -100 Hz after 10-15 h, although after 1-2 h cells are already spreading on the surface as can be seen from the micrographs (*figure* 3.4 G). After 24 h, an incomplete monolayer has formed, but with each medium exchange (arrows in *figure* 3.4) cells start to change the oscillation parameters *Δf* and *Δδ*. Micrographs (*figure* 3.4 H-I) indicate that the cells form multilayers, probably due to the well-known loss of contact inhibition, a hallmark of cancerous mutations.

Table 3.1 Mean values of maximal frequency shift -*Δf* and damping parameter *Δδ* accompanied by the time *t* needed to reach steady state upon loading the quartz plate with 6-7×10^5 cancer cells. [a] Cell-lines not capable of forming a confluent monolayer. [b] Cell-lines capable of forming a confluent monolayer

Cell line	-*Δf* ± SD / Hz	*Δδ* ± SD / s^{-1}	*t* / min
BT-474[a]	85 ± 105	690 ± 80	5000-6000
HCT-8[a]	460 ± 20	8400 ± 170	7500-7900
HCT116[a]	25 ± 15	1320 ± 210	2000-2500
HSC-4[b]	200 ± 100	5550 ± 160	1800-2300
HT-29[b]	110 ± 70	6410 ± 610	1500-2000
FaDu[b]	205 ± 35	5080 ±110	1000-1800

3.3.3 Noise analysis of confluent cancer cells

Prior to noise analysis of the various cancer cell lines grown onto quartz resonators, we confirmed that we are able to distinguish biologically induced fluctuations from other sources of noise by a series of control experiments. In order to rule out that the noise level in the presence of adherent cells is due to an increase in dissipative acoustic load imposed by the cell bodies, i.e. damping of the shear wave, we investigated the impact of a viscous glycerol/water (g/w) mixture on the response of the shear oscillation and the noise in $\Delta f(t)$ as well as $\Delta\delta(t)$. *Figure* 3.5 A and B display a complex experiment, in which our quartz resonator was sequentially exposed to (1) deionized water, (2) a 60/40 v/v g/w mixture , (3) culture medium followed by (4) a suspension of or (5) a confluent layer of HT-29 cells. The experiment was finalized by (6) chemical fixation of the adherent cells after 50 h with 0.5 % glutardialdehyde (GDA). The glycerol-water mixture provides the same viscous damping of the shear oscillation as measured for epithelial cells such as MDCK II.[11] Resonance frequency and dissipation of pure water was set to zero. As clearly visible, upon g/w loading, Δf and $\Delta\delta$ reach new steady state values at -1000 Hz (*figure* 3.5A upper panel) and +6700 s^{-1}, respectively (*figure* 3.5A lower panel). Fluctuation analysis only of the frequency time course shows a slight decrease in the $m_{\mathrm{QCM}}^{\mathrm{PSD}}(\Delta f)$ slope of the spectral density from -0.5 (water) to -0.7 (g/w) accompanied by a slight increase (1 to 4) in normalized variance $\tilde{\sigma}_{\mathrm{QCM}}^{2}$ both for frequency and damping. Accordingly, detrended fluctuation analysis (DFA) of frequency yields a slight increase in the α-factor from 1.22 to 1.34. Replacing the g/w mixture with HEPES-medium (phase 3) leads to recovery of Δf and $\Delta\delta$, however, as compared to pure water, to lower Δf and higher $\Delta\delta$ values, which we attribute to protein adsorption on the gold electrode as detailed previously.[11] Power spectral density estimation provides a decrease from $m_{\mathrm{QCM}}^{\mathrm{PSD}}(\Delta f) = -0.7$ (glycerol/water) to -0.45 (medium), while the values for $\tilde{\sigma}_{\mathrm{QCM}}^{2}$ and α_{DFA} recover to the parameters obtained for pure water. Upon addition of HT-29 cells, we can distinguish between the subconfluent (phase 4) and confluent regime (phase 5). Attachment and spreading of the cells result in frequency shifts of -40 Hz with respect to pure medium. Noise analysis of the frequency data from phase 4 provides a decrease of $m_{\mathrm{QCM}}^{\mathrm{PSD}}$ from -0.6 for the cell-free resonator to -1.27 for the cell-covered sensor, while $\tilde{\sigma}_{\mathrm{QCM}}^{2}$ increases from 1 to 20 and α_{DFA} increases accordingly
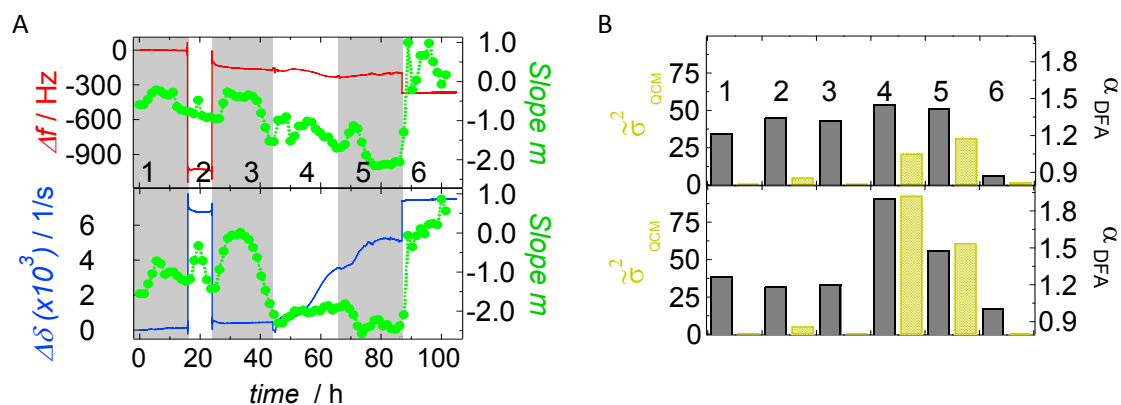
Figure 3.5 Noise analysis of 5 MHz quartz resonator as a function of various acoustic loadings. 500 points from the original time series were used for each data point. A) Δf (red), $\Delta \delta$ (blue) and the corresponding slopes $m_{QCM}^{PSD}(\Delta f, \Delta \delta)$ from the PSD (green) after addition of (1) deionized water, (2) a 60/40 v/v glycerol-water mixture, (3) culture medium followed by (4,5) addition of HT-29 cells. The experiment was finalized by (6) chemical fixation of the adherent cells after 50 h with 0.5% glutardialdehyde (GDA). B) Variance analysis ($\tilde{\sigma}_{QCM}^2$, yellow bar) and DFA (α_{QCM}^{DFA}, grey bar; size of data was 2000 points) obtained from the same regions shown in a).

from 1.32 to 1.46. Employing fluctuations in the dissipation signal results in a similar trend with even more pronounced changes. Note, as we compute sliding averages of m_{QCM}^{PSD}, boundaries between the individual phases are no longer clear cut. When a confluent monolayer is established on the surface (phase 5), maximum shifts for all noise parameters are found with respect to cell-free resonators: increase in variance from 20 to 30 for frequency (or even beyond 50 for dissipation), m_{QCM}^{PSD} of -2 and α_{DFA} values of >1.5. Here, the variance of the damping parameter shows an opposite trend due to strong runaway values in the subconfluent stage. GDA-fixation of the cells increases the shift in Δf by additional -200 Hz, while $\Delta \delta$ increases by +2250 s^{-1}. Upon fixation, cell motility has ceased off, as expected and indicated by the readings of all fluctuation parameters (PSD slope, $\tilde{\sigma}_{QCM}^2$, α_{DFA}). Although the noise of the damping parameter provides larger slopes of the power density spectra, we restrict further analysis to frequency fluctuations due to higher robustness.

Figure 3.6 summarizes the frequency response and fluctuation analysis (PSD slope) of confluent cell lines HT-29, FaDu, and HSC-4. We found that the colon carcinoma line HT-29 shows the least impact on Δf while the strongest change in the PSD slope occurs upon confluency. Oppositely, FaDu cells display a substantially larger change in acoustic load accompanied by the smallest fluctuation amplitude
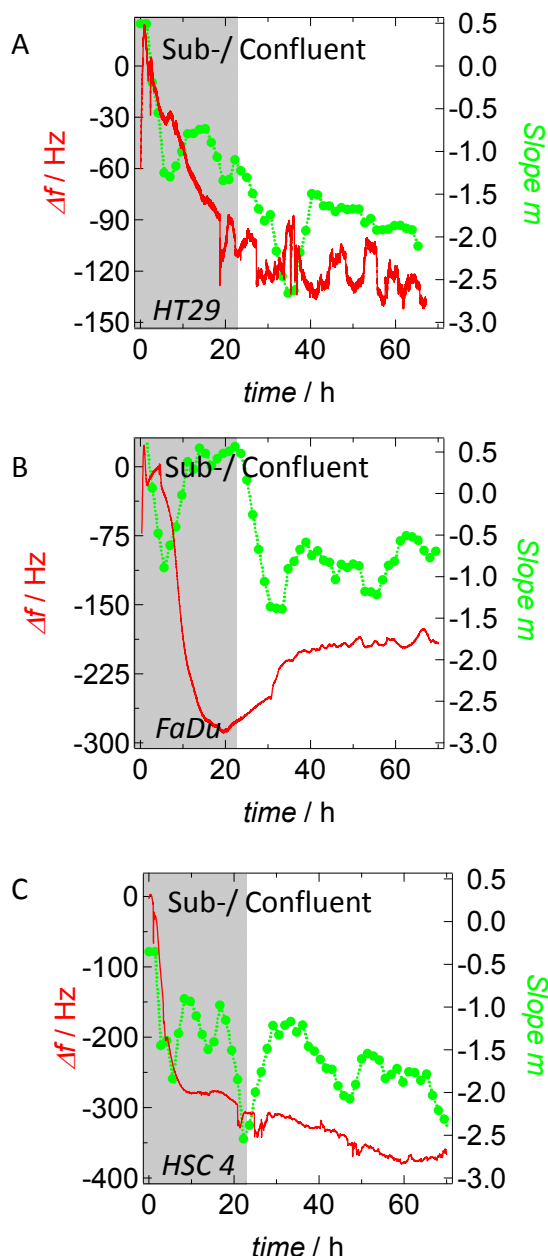
Figure 3.6 Characteristic time courses of Δf and slope m of the PSD-function (m_{QCM}^{PSD}) for three human cancer cell lines (6-7×10^5 cell inoculum) before/after a confluent monolayer is established: A) HT-29 B) FaDu C) HSC-4.

and slope of the PSD. We attribute this to the stronger adhesion to the electrode and less motility. This is not causal, however. For instance, the oral squamous carcinoma line HSC-4 shows large fluctuation amplitudes and PSD slopes as well as considerable changes in resonance frequency and dissipation. Hence, strong adhesion does not necessarily imply slow dynamics. After 30 h of culture, pronounced frequency fluctuations can be found and optical micrographs indicate a fully established cell monolayer. Noteworthy, fluctuation analysis provides two parameter, amplitude (variance) and frequency behaviour (PSD slope) that display two inherently different properties of the biological noise. For example, FaDu cells display an almost tenfold increase in fluctuation amplitude, while the slope of the PSD, the long-time correlation, is altered negligibly. In summary, the order of noise intensities and correlation length as extracted from the raw data by power spectral density estimation and variance analysis in decreasing order is: HT-29 > HSC-4 >> FaDu. This sequence might correlate with decreasing cell-substrate dynamics within the three cell lines or a decrease of the micromechanical dynamics.

To distinguish between the viscoelastic fluctuations recorded by QCM and the fluctuation in the shape of the cells recorded via the established ECIS device (*figure 3.7*), m_{ECIS}^{PSD} and $\tilde{\sigma}_{ECIS}^2$ of all three confluent cancer cell lines were measured and analyzed

over a period of 120 hours. In *figure* 3.7 the time when the cells reached confluency is set to zero, only micromotion data resulting from confluent cell layers are considered. After 60 h, fixation with 0.5 % GDA is carried out and the recorded noise ceases off immediately. Micromotion as measured by ECIS shows largest negative PSD slopes and variance for HSC-4, while F-QCM noise analysis reveals largest slopes and variance for HT-29. FaDu cells display only intermediate $\tilde{\sigma}^2_{ECIS}$ and m^{PSD}_{ECIS} in ECIS, while F-QCM noise analysis yields smallest variance and smallest PSD slopes. Generally, we found: HSC-4 > FaDu >> HT-29 for ECIS micromotion (PSD-slopes). However, F-QCM noise analysis especially by variance analysis discerns the individual motilities of the various cell lines more sensitively than ECIS-based micromotion recordings. In order to correlate the motility indicators as recorded by ECIS and F-QCM with a classical and well-established cytological assay, we performed migration and invasion assays based on the Boyden-Chamber.

Noise analysis of non-confluent cancer cells turned out to be more prone to large errors due to the fact that the biological noise is altered not only by vertical motility but also lateral migration and cell density fluctuation on the electrodes. Formation of multilayers renders the analysis cumbersome and unpredictable. Hence, we refrain from presenting a comprehensive fluctuation analysis as done for confluent cells. *Figure* 3.8 shows frequency fluctuations of HCT 116 cells displaying large peaks due to considerable rearrangements of the cell layer and the corresponding runaways in
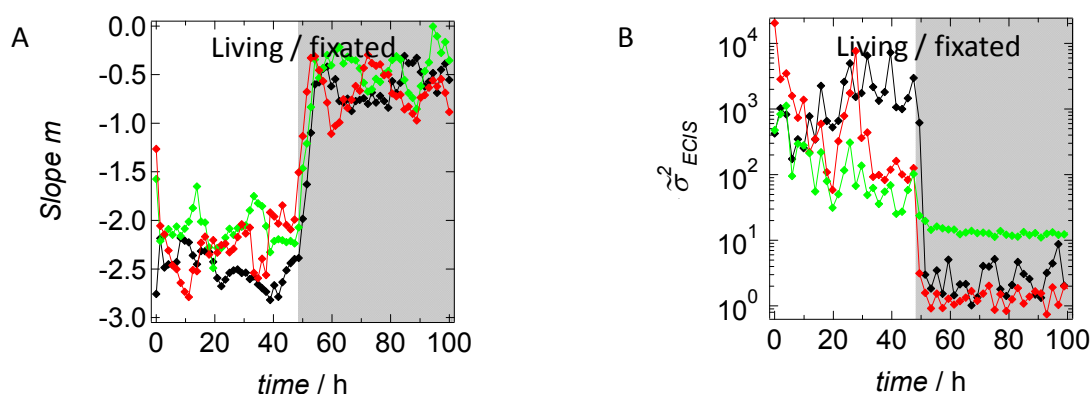
Figure 3.7 ECIS-micromotion (A) and variance recordings (B) for the three human cancer cell lines HT-29, FaDu and HSC-4. The time when a confluent cell monolayer is formed is set to zero; after 60 h, fixation with 0.5 % GDA is carried out. Discrimination of cell lines in this assay is only related to shape fluctuations and not to viscoelastic changes as it might take place in F-QCM measurements.
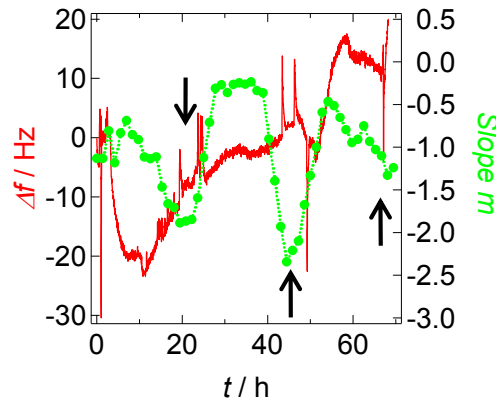
Figure 3.8 Frequency variations observed for non-confluent HCT 116 cells in quartz resonator. Frequently, spikes (arrows) are observed probably due to major rearrangements in the incomplete cell layer preventing a serious noise analysis.

the PSD-slope. These peaks impede with a serious noise analysis and would overemphasize variance values. Similar events avert noise analysis of the BT-474 or HCT-8 cell line .

3.3.4 Boyden chamber migration and invasion assays

The migratory behaviour and the metastatic potential of those cancer cell lines with the capability to grow to confluent layers (HT-29, HSC-4, and FaDu) were measured using the Boyden-chamber assay: here, the amount of cells per time migrating through an either uncoated or ECM-coated polycarbonate membrane is determined.

Table 3.2 Mean *F-QCM-* and *ECIS*-FFT slopes ($m_{\text{QCM}}^{\text{PSD}}$ and $m_{\text{ECIS}}^{\text{PSD}}$) from least-square linear fits in PSD, normalized variances ($\tilde{\sigma}_{\text{QCM}}^{2}$ or $\tilde{\sigma}_{\text{ECIS}}^{2}$) and DFA coefficients ($\alpha_{\text{QCM}}^{\text{DFA}}$ or $\alpha_{\text{ECIS}}^{\text{DFA}}$) as well as mean cell numbers extracted from Boyden chamber migration and invasion assays for the three cancer cell lines HT-29, HSC-4 and FaDu. PSD slopes $m_{\text{QCM}}^{\text{PSD}}$ and $\tilde{\sigma}_{\text{QCM}}^{2}$ were computed from frequency noise.*M* for migration in cell number/field of view (FOV). *I* for Invasion [cell number/ FOV].

Cell line	$m_{\text{QCM}}^{\text{PSD}}$	$m_{\text{ECIS}}^{\text{PSD}}$	$\tilde{\sigma}_{\text{QCM}}^{2}$	$\tilde{\sigma}_{\text{ECIS}}^{2}$	$\alpha_{\text{QCM}}^{\text{DFA}}$	$\alpha_{\text{ECIS}}^{\text{DFA}}$	*M*	*I*
HT-29	-1.8 ± 0.4	-2.1 ± 0.1	33.1 ± 6.2	167 ± 39	1.40 ± 0.04	1.51 ± 0.06	400 ± 160	30 ± 8
HSC-4	-1.5 ± 0.5	-2.5 ± 0.1	24.8 ± 7.6	1793 ± 4	1.37 ± 0.02	1.67 ± 0.02	204 ± 24	29 ± 8
FaDu	-0.6 ± 0.5	-2.2 ± 0.1	9.6 ± 5.2	1002 ± 29	1.22 ± 0.16	1.50 ± 0.05	118 ± 30	12 ± 2

At the end of the assay the cells are stained and counted. In *figure* 3.9A and B, optical micrographs from migration and invasion assays after staining of the cells are shown; *figure* 3.9C shows the results of counting six areas of a defined 0.015 cm^2 field of view (FOV) per chamber after averaging and includes variance frequency and dissipation levels for each cell line. The data comprises the mean and the standard deviation of three individual experiments. HT-29 colon cancer cells show the highest
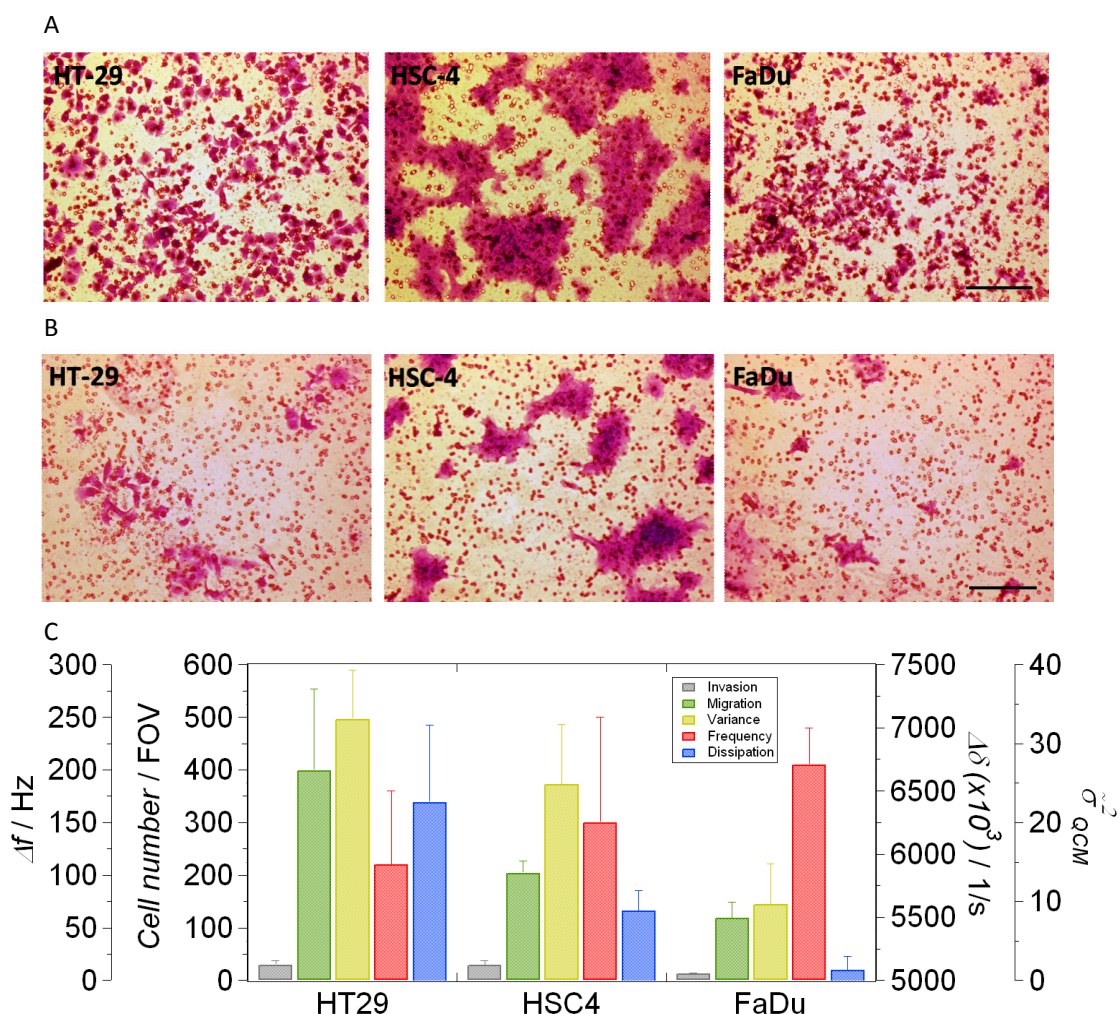
Figure 3.9 Migratory and invasive behavior of the cancer cell lines HT-29, FaDu and HSC-4. Invasion and migration recordings were performed using Chemicon assays based on the well-established Boyden chamber. The migration or invasion of cells is determined by counting stained cells attached to the lower side of the porous polycarbonate filter after 15 h (migration) or 72 h (invasion). a) Migration assay: microscopic field of view in which the number of migrated cells is determined, scale bar is 50 μm. b) Invasion assay: microscopic field of view in which the number of invaded cells is determined, scale bar is 50 μm. c) Counted cells per field of view for migration (geen) and invasion (grey) assay, error bars represent standard deviations (*n* = 3) vs. F-QCM parameters variance (σ^2, yellow), frequency (red, in Hz) and dissipation (blue, in s^{-1}). Seeding density was adjusted to 210 000 cells in 300 μl serum free medium.

migration and invasion activity, followed by the HSC-4 cell line; the latter one is forming islands after migrating through the pores and exhibits a flattened morphology occupying almost twice the area as in its confluent stage. FaDu cells show little migratory and almost no invasive behaviour. *Table* 3.2 summarizes the results from migration, invasion, ECIS-micromotion and F-QCM viscoelastic fluctuations.

3.4 DISCUSSION

The central aim of this study was to quantify the motility of human cancer cells by applying noise analysis algorithms to the fluctuations of the resonance frequencies of cell-covered shear wave resonators. It was the ultimate rationale behind this approach to correlate the cells' motility with their metastatic potential as it can be determined by classical Boyden Chamber assays. For systems like adherent cells, the D-QCM readout provides in principle two parameters, the resonance frequency and the energy dissipation of the oscillation. Both of them were recorded and studied. However, it turned out that the frequency-based noise is more robust and more suitable as the basis of a fluctuation or noise analysis. The fluctuating F-QCM signal must be considered as a wholistic cell parameter that does not reflect one particular cell property or structure but mirrors the motility of the cell as a whole.

Similar approaches that rely on the fluctuating pattern of the resonance frequency have been performed for actively contracting cells in the past. With a low noise and fast acquiring network analyzer setup, Pax *et al.* were the first to analyze QCM-fluctuations induced by actively contracting cardiomyocytes. The authors found periodic fluctuations in both Δf and $\Delta \Gamma$ time courses due to the contractile activity of the cells with a frequency of 1.5 Hz.[32] In this present study, however, fluctuations of non-contractive cancer cells were recorded with smaller long-time correlation and significantly smaller fluctuation amplitudes compared to cardiomyocytes. As we have shown before,[23] metabolically driven, cell fluctuations can be recorded by F-QCM approaches in a similar manner as it has been shown by impedimetric analysis of cell shape changes referred to as ECIS micromotion.

Here, the question was addressed whether noise analysis of (i) micromechanical fluctuations monitored by acoustic shear wave resonators and (ii) cell shape fluctuations as measured by AC impedance analysis are correlated with the metastatic potential of various human cancer cells.

Previously, impedance spectroscopy (referred to as electric cell-substrate impedance sensing or short ECIS) has been used to discriminate between cancer cells that show an individually different metastatic potential.[33] Four breast cancer lines with increasing invasiveness showed different stationary impedance magnitudes and

phase shifts accompanied by alterations in membrane capacitances. With respect to noise analysis, *Lovelady et al.*[34] used power spectral density (PSD) analysis and detrended fluctuation analysis (DFA) of the noise found in ECIS-recordings with the goal to distinguish benign from malign human ovarian surface epithelial cells. The results, however, were neither unique nor unambigous. In a follow-up publication,[35] cells with a higher noise level (human umbilical vein endothelial cells, HUVECs) served as sensors for cytochalasin B cytotoxicity tests based on noise analysis. While micromotion of adherent cells measured by ECIS is a measure of cell-shape dynamics, our approach of F-QCM noise analysis reflects fluctuations of the cells' acoustical impedance which is governed by their overall micromechanics.

We found that epithelial cancer cells, which do not form a confluent monolayer, such as HCT 116, BT-474 and HCT-8 show either the smallest mass and dissipation shifts (cluster forming BT-474, HCT 116 incapable of monolayer-formation) or the highest ones (multilayer-forming HCT-8) upon adhesion, in contrast to those cell lines (HT-29, HSC-4 and FaDu) that grow to confluent monolayers. The time needed to reach steady state frequency shifts is longer for the former than for the latter: it takes up to 5 days for cell lines that do not grow to confluence to reach a steady state value of Δf and $\Delta \delta$, whereas the confluent monolayers are established within approximately 20-40 h after seeding. Current literature supports these findings, as both BT-474 and HCT 116 are known not to grow to confluence or to form continuous monolayers; invasiveness, however, is gradually distributed along subconfluent cell lines. HCT-8 cells are known to display a high metastatic potential, whereas HCT 116 posses merely moderate invasiveness and the BT-474 line is essentially non-invasive.[26, 36-39] As the lateral sensitivity of the quartz resonator is not equal across the sensor surface but peaks in the center and falls off to the periphery of the electrodes. Hence, we did not include those cells in a motility-analysis, that do not grow to confluence. For non-confluent cell layers the fluctuation pattern is dependent on the cell density on the surface and – even harder to estimate or approximate – their lateral distribution on the surface in particular as these cells tend to cluster. In conclusion, lateral migration and proliferation add to the acoustic noise level in an unpredictable and erratic manner. Therefore we restricted our comparison to cell lines capable of confluent monolayer-formation.

In control experiments using highly viscous fluids and fixated cells, we could unequivocally show that fluctuations originating from living cells exceed all other sources of noise. Power spectral density generally reveals a power law dependence $\propto f^m$ with $m \in$ [-0.6, -2.5] depending on the cell type. The value for m is indicative of long-memory stochastic processes and probably goes beyond a simple opening and closing of molecular bonds confirmed by DFA. The biological and physical origin of the fluctuations is most likely a complex interplay of changes in the cell-substrate contact and subtle shape/cell height variations. The QCM is an interface sensitive sensor that is capable of picking up small changes in the distance between the viscoelastic bodies and the resonator's surface. Height changes of adherent cells in the nanometer regime can also be measured due to the high sensitivity of the quartz resonator. Following the argument of Lucklum and coworkers who relate changes in resonance frequency and dissipation to the viscoelastic properties of the attached material a rough estimation is possible.[40] Assuming a storage modulus of adherent cells at 5 MHz of G' = 10^5 Pa and a loss modulus of G'' = 10^6 Pa·s a change in cell height from 4 μm to 4.1 μm translates in a shift of the resonance frequency of 2 Hz, which can be readily detected with our setup. In turn, changes in G' at constant cell heigth in the order of few kPa produce changes in f of about 1-3 Hz. Hence, it is difficult to determine whether shape fluctuations or viscoelastic changes dominate the frequency noise.

Power spectral density analysis of resistance noise as a measure for micromotion as recorded by ECIS displays slopes that are generally larger ($m \in$ [-2.1, -3.0]) compared to those found in F-QCM fluctuations (see *table* 3.2). Hence, we assume that even though both methods are sensitive to cell shape changes, slightly different information is retrieved by F-QCM noise analysis. Recalling that the shear wave produced by the quartz resonator decays exponentially in a viscous fluid it is straightforward to propose that the F-QCM is more sensitive towards changes in the cell-substrate contact regime compared to changes occuring in regions of the cell body that are more distant to the surface. Undoubtedly, metabolically driven motions of the cells can be monitored in a non-invasive fashion by both ECIS and F-QCM noise analysis but the question is whether the fluctuations correlate with classical tests of invasiveness and migration behavior.

The cell motility measured by noise analysis of the resonance frequency (PSD slope, variance, DFA) was found to decrease in the following order: HT-29 > HSC-4 > FaDu. Fluctuation analysis of the resonance frequency was compared to ECIS micromotion and classical migration and invasion tests using a Boyden chamber. In general, we can confirm the trend observed in the classical Boyden chamber assay with F-QCM-based noise analysis. We found that variance analysis of the resonance frequency provides the most sensitive measure for the metastatic potential while the PSD slopes undergo only slight changes (and present overlapping standard deviations). For instance, HT-29 and HSC-4 cells are characterized by the highest migration and invasion potential as confirmed by F-QCM-based variance analysis (*figure* 3.9C). Various publications on, for instance, efficiency of matrix-metalloprotease activity, draw a similar picture: the three human cancer cell lines studied here are considered as being gradually invasive. HT-29 are often used as a model system in experimental invasion studies, while FaDu and HSC-4 are reported to be slightly and moderately invasive, respectively.[41-44]

3.5 CONCLUSIONS

A novel sensor approach based on resonance frequency fluctuations of F-QCM measurements is introduced to assay cell motility of human cancer cells. The method allows label-free and non-invasive monitoring of the cell body dynamics. Frequency fluctuations reproduce the metastatic potential that was determined by conventional assays based on the well-established Boyden chamber approach. Long-memory stochastic processes were found to govern the response of the adherent cells displayed in both F-QCM and ECIS micromotion measurements.

3.6 REFERENCES AND NOTES

1.   Ries L.A.G., M. D., Krapcho M, Stinchcomb DG, Howlader N, Horner MJ, Mariotto A, Miller BA, Feuer EJ, Altekruse SF, Lewis DR, Clegg L, Eisner MP, Reichman M, Edwards BK (eds). , SEER Cancer Statistics Review. 1975-2005, National Cancer Institute. Bethesda, MD, http://seer.cancer.gov/csr/1975_2005/, based on November 2007 SEER data submission, posted to the SEER web site, **2008**.

2.   Mundy, G. R., Metastasis to bone: Causes, consequences and therapeutic opportunities. *Nature Reviews Cancer* **2002,** 2, (8), 584-593.

3.   Chen, H.-C., Boyden Chamber Assay. *In Cell Migration Developmental Methods and Protocols Guan, Jun-Lin* **2005**.

4.   Kramer, R. H.; Nicolson, G. L., Interactions of Tumor-Cells with Vascular Endothelial Cell Monolayers - Model for Metastatic Invasion. *Proceedings of the National Academy of Sciences of the United States of America* **1979,** 76, (11), 5704-5708.

5.   Sieg, D. J.; Hauck, C. R.; Schlaepfer, D. D., Required role of focal adhesion kinase (FAK) for integrin-stimulated cell migration. *Journal of Cell Science* **1999,** 112, (16), 2677-2691.

6.   Folkman, J., Clinical-Applications of Angiogenesis Research. *Journal of Acquired Immune Deficiency Syndromes and Human Retrovirology* **1993,** 6, (6), 686-686.

7.   Albrechtbuehler, G., Daughter 3T3 Cells - Are They Mirror Images of Each Other. *Journal of Cell Biology* **1977,** 72, (3), 595-603.

8.   Todaro, G. J.; Lazar, G. K.; Green, H., Initiation of Cell Division in a Contact-Inhibited Mammalian Cell Line. *Journal of Cellular and Comparative Physiology* **1965,** 66, (3P1), 325-&.

9.   Brooks, S. A. S., U., Metastasis research protocols vol II Analysis of cell behavior in vitro and in vivo. **2001**.

10.   Cooper, M. A.; Singleton, V. T., A survey of the 2001 to 2005 quartz crystal microbalance biosensor literature: applications of acoustic physics to the analysis of biomolecular interactions. *Journal of Molecular Recognition* **2007,** 20, (3), 154-184.

11.   Wegener, J.; Janshoff, A.; Galla, H. J., Cell adhesion monitoring using a quartz crystal microbalance: comparative analysis of different mammalian cell lines. *European Biophysics Journal with Biophysics Letters* **1998,** 28, (1), 26-37.

12.   Li, P. C. H.; Wang, W. J.; Parameswaran, M., An acoustic wave sensor incorporated with a microfluidic chip for analyzing muscle cell contraction. *Analyst* **2003,** 128, (3), 225-231.

13.   Li, J.; Thielemann, C.; Reuning, U.; Johannsmann, D., Monitoring of integrin-mediated adhesion of human ovarian cancer cells to model protein surfaces by quartz crystal resonators: evaluation in the impedance analysis mode. *Biosensors & Bioelectronics* **2005,** 20, (7), 1333-1340.

14.   Zhou, T.; Marx, K. A.; Warren, M.; Schulze, H.; Braunhut, S. J., The quartz crystal microbalance as a continuous monitoring tool for the study of endothelial cell surface attachment and growth. *Biotechnology Progress* **2000,** 16, (2), 268-277.

15.   Marx, K. A.; Zhou, T.; Montrone, A.; McIntosh, D.; Braunhut, S. J., A comparative study of the cytoskeleton binding drugs nocodazole and taxol with a mammalian

cell quartz crystal microbalance biosensor: Different dynamic responses and energy dissipation effects. *Analytical Biochemistry* **2007,** 361, (1), 77-92.

16. Marxer, C. M.; Coen, M. C.; Greber, T.; Greber, U. F.; Schlapbach, L., Cell spreading on quartz crystal microbalance elicits positive frequency shifts indicative of viscosity changes. *Analytical and Bioanalytical Chemistry* **2003,** 377, (3), 578-586.

17. Braunhut, S. J.; McIntosh, D.; Vorotnikova, E.; Zhou, T.; Marx, K. A., Detection of apoptosis and drug resistance of human breast cancer cells to taxane treatments using quartz crystal microbalance biosensor technology. *Assay and Drug Development Technologies* **2005,** 3, (1), 77-88.

18. Wei, X. L.; Mo, Z. H.; Li, B.; Wei, J. M., Disruption of HepG2 cell adhesion by gold nanoparticle and Paclitaxel disclosed by in situ QCM measurement. *Colloids and Surfaces B-Biointerfaces* **2007,** 59, (1), 100-104.

19. Giaever, I.; Keese, C. R., Monitoring Fibroblast Behavior in Tissue-Culture with an Applied Electric-Field. *Proceedings of the National Academy of Sciences of the United States of America-Biological Sciences* **1984,** 81, (12), 3761-3764.

20. Asphahani, F.; Zhang, M., Cellular impedance biosensors for drug screening and toxin detection. *Analyst* **2007,** 132, (9), 835-841.

21. Hug, T. S., Biophysical methods for monitoring cell-substrate interactions in drug discovery. *Assay and Drug Development Technologies* **2003,** 1, (3), 479-488.

22. Luong, J. H. T., An emerging impedance sensor based on cell-protein interactions: Applications in cell biology and analytical biochemistry. *Analytical Letters* **2003,** 36, (15), 3147-3164.

23. Sapper, A.; Wegener, J.; Janshoff, A., Cell motility probed by noise analysis of thickness shear mode resonators. *Analytical Chemistry* **2006,** 78, (14), 5184-5191.

24. Rangan, S. R. S., New Human Cell Line (Fadu) from a Hypopharyngeal Carcinoma. *Cancer* **1972,** 29, (1), 117-&.

25. Fogh, J. a. T. G., New human tumor cell lines. *In: J. Fogh (ed.)Human Tumor Cells "in Vitro," pp. 115-141. New York: Plenum Press* **1975**.

26. Brattain, M. G.; Fine, W. D.; Khaled, F. M.; Thompson, J.; Brattain, D. E., Heterogeneity of Malignant-Cells from a Human Colonic-Carcinoma. *Cancer Research* **1981,** 41, (5), 1751-1756.

27. Tompkins, W. A.; Watrach, A. M.; Schmale, J. D.; Schultz, R. M.; Harris, J. A., Cultural and Antigenic Properties of Newly Established Cell Strains Derived from Adenocarcinomas of Human Colon and Rectum. *Journal of the National Cancer Institute* **1974,** 52, (4), 1101-1110.

28. Lasfargues, E. Y.; Coutinho, W. G.; Redfield, E. S., Isolation of 2 Human Tumor Epithelial-Cell Lines from Solid Breast Carcinomas. *Journal of the National Cancer Institute* **1978,** 61, (4), 967-978.

29. Momose, F.; Araida, T.; Negishi, A.; Ichijo, H.; Shioda, S.; Sasaki, S., Variant Sublines with Different Metastatic Potentials Selected in Nude-Mice from Human Oral Squamous-Cell Carcinomas. *Journal of Oral Pathology & Medicine* **1989,** 18, (7), 391-395.

30. Reiss, B.; Janshoff, A.; Steinem, C.; Seebach, J.; Wegener, J., Adhesion kinetics of functionalized vesicles and mammalian cells: A comparative study. *Langmuir* **2003,** 19, (5), 1816-1823.

31. Lovelady, D. C.; Friedman, J.; Patel, S.; Rabson, D. A.; Lo, C. M., Detecting effects of low levels of cytochalasin B in 3T3 fibroblast cultures by analysis of electrical noise obtained from cellular micromotion. *Biosensors & Bioelectronics* **2009,** 24, (7), 2250-2254.

32. Pax, M.; Rieger, J.; Eibl, R. H.; Thielemann, C.; Johannsmann, D., Measurements of fast fluctuations of viscoelastic properties with the quartz crystal microbalance. *Analyst* **2005,** 130, (11), 1474-1477.

33. Han, A.; Yang, L.; Frazier, A. B., Quantification of the heterogeneity in breast cancer cell lines using whole-cell impedance spectroscopy. *Clinical Cancer Research* **2007,** 13, (1), 139-143.

34. Lovelady, D. C.; Richmond, T. C.; Maggi, A. N.; Lo, C. M.; Rabson, D. A., Distinguishing cancerous from noncancerous cells through analysis of electrical noise. *Physical Review E* **2007,** 76, (4), -.

35. Opp, D.; Wafula, B.; Lim, J.; Huang, E.; Lo, J. C.; Lo, C. M., Use of electric cell-substrate impedance sensing to assess in vitro cytotoxicity. *Biosensors & Bioelectronics* **2009,** 24, (8), 2625-2629.

36. Vermeulen, S. J.; Bruyneel, E. A.; Bracke, M. E.; Debruyne, G. K.; Vennekens, K. M.; Vleminckx, K. L.; Berx, G. J.; Vanroy, F. M.; Mareel, M. M., Transition from the Noninvasive to the Invasive Phenotype and Loss of Alpha-Catenin in Human Colon-Cancer Cells. *Cancer Research* **1995,** 55, (20), 4722-4728.

37. Vermeulen, S. J.; Chen, T. R.; Speleman, F.; Nollet, F.; Van Roy, F. M.; Mareel, M. M., Did the four human cancer cell lines DLD-1, HCT-15, HCT-8, and HRT-18 originate from one and the same patient? *Cancer Genetics and Cytogenetics* **1998,** 107, (1), 76-79.

38. Van Hoorde, L.; Pocard, M.; Maryns, I.; Poupon, M. F.; Mareel, M., Induction of invasion in vivo of alpha-catenin-positive HCT-8 human colon-cancer cells. *International Journal of Cancer* **2000,** 88, (5), 751-758.

39. Goicoechea, S. M.; Bednarski, B.; Garcia-Mata, R.; Prentice-Dunn, H.; Kim, H. J.; Otey, C. A., Palladin contributes to invasive motility in human breast cancer cells. *Oncogene* **2009,** 28, (4), 587-598.

40. Lucklum, R.; Behling, C.; Cernosek, R. W.; Martin, S. J., Determination of complex shear modulus with thickness shear mode resonators. *Journal of Physics D-Applied Physics* **1997,** 30, (3), 346-356.

41. Khatib, A. M.; Siegfried, G.; Prat, A.; Luis, J.; Chretien, M.; Metrakos, P.; Seidah, N. G., Inhibition of proprotein convertases is associated with loss of growth and tumorigenicity of HT-29 human colon carcinoma cells - Importance of insulin-like growth factor-1 (IGF-1) receptor processing in IGF-1-mediated functions. *Journal of Biological Chemistry* **2001,** 276, (33), 30686-30693.

42. Khan, M. H.; Yasuda, M.; Higashino, F.; Haque, S.; Kohgo, T.; Nakamura, M.; Shindoh, M., nm23-h1 suppresses invasion of oral squamous cell carcinoma-derived cell lines without modifying matrix metalloproteinase-2 and matrix metalloproteinase-9 expression. *American Journal of Pathology* **2001,** 158, (5), 1785-1791.

43. Hoteiya, T.; Hayashi, E.; Satomura, K.; Kamata, N.; Nagayama, M., Expression of E-cadherin in oral cancer cell lines and its relationship to invasiveness in SCID mice in vivo. *Journal of Oral Pathology & Medicine* **1999,** 28, (3), 107-111.

44.   De Angelis, T.; Noe, A.; Chatterjee, M.; Mulholland, J., Stromelysin-1 activation correlates with invasiveness in squamous cell carcinoma. *Journal of Investigative Dermatology* **2002,** 118, (5), 759-766.

4

Dissecting vertical motility of epithelial cells by small molecule inhibitors

Cancer cells (*FaDu*) on QCM

Incubation time:
72 h
24 h

A↓ (*Cyt.-D*)
M↓ (*Noco.*) 10 µm
A↑ (*Phall.*)
M↑ (*Tax.*)

Micromotion / %

A↓ A↑ M↑ M↓
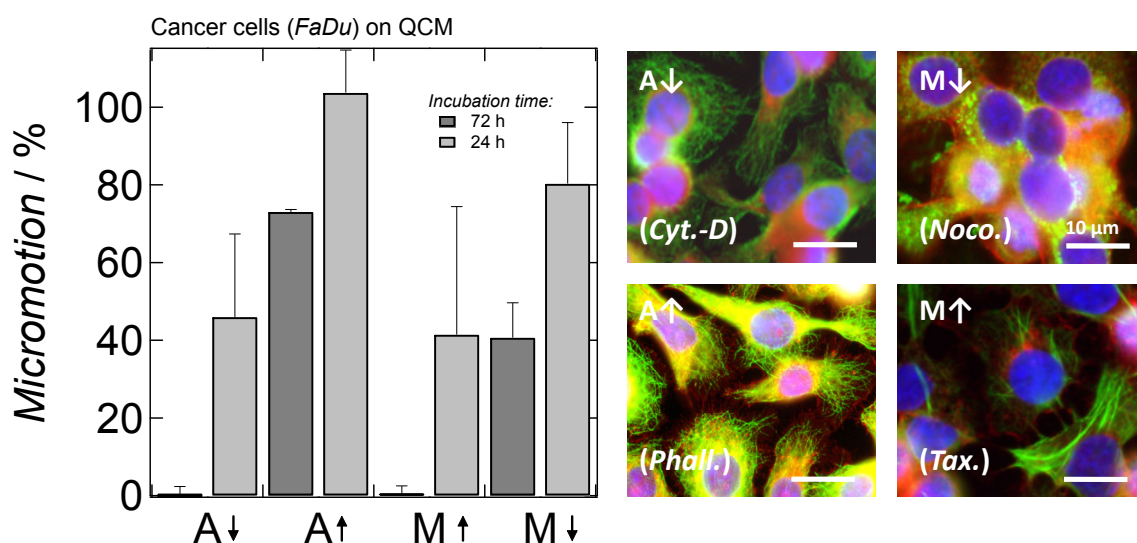
ABSTRACT

Cellular motility is a process of uppermost importance for homeostasis and therefore involved in numerous biological phenomena including wound healing, immune system functions and embryogenesis. Cell migration also accompanies pathologies like cancer formation and metastasis, with epithelial cells being the prevalent origin of malignancies. We studied dynamics of epithelial MDCKII and FaDu monolayers cultured on gold electrodes of an acoustic resonator (quartz crystal microbalance, QCM) or an impedance sensor (electrical cell-substrate impedance sensing, ECIS). Epithelial cell motility provokes cell shape and height changes without exhibiting net directionality in confluent monolayers, therefore termed vertical motility. The impact of small molecule inhibitors on the dynamics of the cytoskeleton, such as cytochalasin D, phalloidin and blebbistatin as well as taxol, nocodazol and colchicin were quantified by detecting changes in the noise pattern. Additionally, chemotherapeutics resveratrol and cis-platin were applied to prove sensitivity of micromotility to the invasive properties of FaDu

human head and neck tumor cells. Cytoskeletal rearrangements and nuclear integrity were visualized by fluorescence microscopy and correlated to QCM, ECIS and MTS.

4.1 INTRODUCTION

An essential activity of malignant, invading cells is migration.[1] Epithelial tumor cells, the prevalent origin of malignancies due to direct carcinogen exposure, translocate dependent on modulated cell motility, remodeling of cell-cell- as well as cell-matrix adhesion and reorganization of the extracellular matrix.[2] The source of the net vertical cell migration in epithelial monolayers is the dynamics of biopolymer assembly and disassembly of the cytoskeleton and accessory proteins[3, 4] in the cytosol as well as in membrane proximity.[5] Dynamics are primarily governed by the actin networks[6] with fibers and bundles building protrusions and retraction[7] as well as by microtubules, which partially control actin-activity[8] and present a dynamic instability for fast network reorganization;[9] intermediate filaments contribute only to the static, mechanical stabilization of the cell.[10, 11] Additionally, regulatory Rho-GTPases orchestrate cellular migration, with RAC1 controlling extensions and new anchorage sites, CDC42 supervising cell polarity and rhoA mediating cell adhesion through integrins and motility via actin-NMII contractions.[12] This dynamic cellular migration assembly is not restricted to cancer neoplasia, but also found similar in normal cells.[13] In the present *in-vitro* biosensor study, dynamics arising from epithelial cells locomotion are detected and dissected via small molecule inhibitors. Processes contributing to biological fluctuations are thereby quantified and the utility of quartz crystal microbalances (QCM) and electrical cell-substrate impedance sensors (ECIS) as real-time, non-invasive, high-throughput biosensors is confirmed. We compared the motility of two cell lines, the human squamous pharyngial Fadu cancer cells,[14] involved in development of head and neck cancer, and the canine kidney MDCKII cell line, considered representative of the general cellular motility machinery.

Both QCM and ECIS applications as biosensors for adherent cells were established within the last two to three decades.[15-17] Single cells or whole monolayers are thereby cultured on gold-electrodes integrated in culture vessels. While ECIS measurements provide spectral information of the complex resistance *IZI*, QCM displays changes in mass and energy dissipation represented by *f* and *δ*. as cells adhere and

spread on the electrode surface.[18, 19] A broad range of biological and medical applications of QCM and ECIS exist,[20] often involving modulators of cellular micromechanics such as adhesion under nocodazol influence (Q),[21] viscoelasticity modulated by a battery of drugs including actin polymerizing, phalloidin resembling jasplakinolide (Q),[22] cellular attachment upon cytochalasin-D treatment (Q),[23] toxicity of cis-platin or other metal compounds (E)[24] as well as its chemotherapeutic, apoptotic effect on cancer cells (E)[25, 26] and energy dissipation of various adherent cells upon taxol-treatment (Q)[27] including detected resistance of breast cancers to paclitaxel or combined therapies (Q)[28, 29] (Q for QCM, E for ECIS/electrochemical biosensors). However, the focus is generally on static rather than dynamic features of cellular integrity produced by adherent living cells.

In the present study, we analyzed epithelial monolayers, which, upon reaching a quasi-stationary state at confluence, show residual fluctuations in f, δ or $|Z|$ due to metabolically driven cell shape or height changes correlated with vertical locomotion. Micromotility monitoring is achieved by analyzing either real part impedance, frequency or dissipation fluctuations by PSD-estimation or variance analysis, as presented before.[30, 31] Thereby, we quantify fluctuation amplitudes or long-term correlations of the biological noise.

Besides noise analysis, we followed shifts of basic parameters f, δ or $|Z|$. Additionally, barrier function (via trans-epithelial resistance TER) upon small molecule treatment was assessed as a function of time and dose. Recently, we proved both techniques to be sensitive enough to follow the invasive behavior of cancer cells[32] or the toxicity of nanoparticles [33].

The biological origin of micromotility however, remains unclear. Here, we seek a deeper understanding of the various contributions to the fluctuations generated by adhesive cells by using small molecule inhibitors. We adopted equitoxic IC$_{50}$ concentrations of small molecule inhibitors or activators of actin fiber dynamics and the Rho controlled motor protein myosin II (cytochalasin-D, phalloidin,[34] blebbistatin[35-37]) as well as microtubule and tubulin monomer reagents (taxol, nocodazol, colchicin)[38] and two distinct transcription influencing chemotherapeutics, resveratrol[39, 40] and cis-platin,[41] which both may induce extrinsic or intrinsic apoptosis. *Figure* 4.1 gives an

Taxol: Tubulin monomer binding and reduction of microtubules-depolymerization

Phalloidin: Actin-filament stabilization

Blebbistatin: Actin-myosin II complexes inhibited

Resveratrol: Antioxidans or apoptosis induction

cis-Platin: DNA-binding and apoptosis induction

Colchicin: Binding of free tubulin monomeres

Nocodazol: Increase of microtubules-depolymerization

Cytochalasin-D: Shortening of actin-filaments

Figure 4.1 Structure of the small molecule inhibitors applied in the present work (exemplary threefold-staining of MDCKII cells in the center): compounds that manipulate actin filaments (red) are cytochalasin-D, phalloidin and blebbistatin; agents interfering with microtubules (green) are taxol, nocodazol and colchicin. Chemotherapeutics resveratrol and cis-platin are two known inductors of apoptosis; nucleus is labelled in blue.

overview of the specific cellular effects of each inhibitor. Finally, cell-cytoskeleton disruption and nuclear integrity was captured by fluorescence microscopy, thus cell specific toxin sensitivity of fluctuations could be correlated to cell morphology.

4.2 Experimental section

4.2.1 Cell culture and biosensor preparation

MDCK II cells are maintained in Earle's minimum essential medium supplemented with 4 mM glutamine, 100 g/mL of both penicillin and streptomycin (purchased by Biochrom, Berlin, Germany), 10% (v/v) fetal calf serum (PAA Laboratories GmbH, Coelbe, Germany);[42] FaDu cells,[14] a squamous carcinoma cell line derived from the hypopharynx, is cultured in Dulbecco's modified Eagles medium with 4.5 g/l glucose and 2 mM L-glutamine (PAA laboratories GmbH, Cölbe, Germany), non essential amino acids NEA (100 µg/ml), sodium pyruvate (1mM) and 10 mM HEPES buffer. Both cell lines are stored in incubators (HERA cell 150, Heraeus, Germany) with a 5% CO_2 atmosphere. Cells are subcultured weekly after reaching confluence by washing with PBS, followed by trypsinization and centrifugation at 110×g. Counting is carried out using a Neubauer chamber, and viability is determined using trypan blue exclusion. Passage number is typically kept between 20 and 40 to ensure that the neoplastic phenotype did not change during the experiments.

For the biosensor setups, cells are seeded either directly onto the QCM quartz or in the 8-well ECIS electrode arrays: for quartz biosensor preparation, after routine cleaning procedure, special designed teflon-cells are assembled and, as the ECIS electrodes, transferred to a culture incubator with 37 °C and 5% CO_2 atmosphere (MMM Medcenter Einrichtungen GmbH, Gräfelfing, Germany).[43] Cells are inoculated at a density of 6-7×10^5 cells/ml and handled as described before.[32] Fixation of cells is carried out using 0.5 % glutardialdehyde (GDA) (Sigma-Aldrich, Germany) solution and exchange of medium with toxins is carried out upon reaching confluence, i.e. 15 - 24 h after seeding.

4.2.2 D-QCM based viscoelastic monitoring, ECIS-based impedance studies and noise analysis

With a self made D-QCM-biosensor approach,[32] time series of viscoelastic parameters (frequency and dissipation) were recorded under influence of various toxins; additionally, noise analysis (termed F-QCM) based on viscoelastic fluctuations was monitored. Therefore, confluent cell layers were subjected to noise analysis of

frequency and dissipation fluctuations.[32] In brief, short time FFT and variance analysis of linearly detrended time blocks were carried out. For power density spectra (PSD) analysis of the viscoelastic fluctuation data, the slope *m* was determined in the low frequency regime as described previously[44] and assigned to cells` viability. Time series were smoothed with adjacent averaging over four consecutive points. Mean values of the 0-24 h interval (*n* = 12 ± S.D.) and the interval form 24 h to the end of experiment (usually 24-72h) are presented after normalization to the values for untreated cells for both viscoelastic and fluctuation parameters; for the latter, mean normalization factors of -1.5 for MDCKII and -0.9 for FaDu cells were used. Standardization of viscoelastic parameters and noise levels to gain percentage values was applied in reference to fixated cells (mean standardization numerical value of -0.3 for both cell lines, comparable to the values found with medium immersed electrodes).[32] The noise amplitude was captured by variance analysis handled correspondingly (mean normalization factor of 15 for MDCKII and 5 for FaDu cells, mean standardization zero level of 0.027 for both cell lines).

For AC-impedance analysis, a homemade ECIS system was employed, as introduced before.[33] In the ECIS setup, a 1 V AC signal is applied to the system through a 1 MΩ series resistor, and the in-phase- and out-of-phase voltages across the electrodes are recorded at 4 kHz at a sampling rate of 1 Hz (based on Gaiever *et al.*). [45] Complex impedance *IZI* (normalized to its starting value) as well as micromotion (fluctuations of the impedance real part determining in-phase voltages at non-invasive 1 µA amplitudes) as function of time were recorded and smoothened as the F-QCM data. Besides impedance spectroscopy at one fixed frequency, we also monitored changes in the barrier function of the adherent epithelial cell layer: trans-epithelial electrical resistance (TER) measure $\Delta R_{b,\ norm}$ was extracted from frequency-resolved impedance readings (10-10^5 Hz) and subjected to equivalent circuit modeling as detailed by Giaever *et al.*[46] Micromotion and $\Delta R_{b,\ norm}$ readings were carried out on one and the same cell layer. Noise analysis based on micromotion data, which is a time series of resistance fluctuations, was also achieved by PSD-estimation and variance analysis. Here, the linear fit of the low frequency part of the power density spectra provided slopes up to - 2.7 for living cells. Normalization of IZI, TER and fluctuation parameters (micromotion PSD-slope and variance) to levels found for untreated cells before toxin addition and

standardization to the signal gained from empty electrode was employed, comparable to the F-QCM data analysis (mean PSD-slope normalization factor of 15 for MDCKII and 5 for FaDu, mean standardization PSD zero level of -0.28 for both cell lines; mean variance normalization factor of 2×10^{-10} for MDCKII or 0.08×10^{-10} for FaDu cells; mean standardization variance zero level of 0.04 for both cell lines).

4.2.3 Cytotoxicity assay

The MTS cytotoxicity test has been applied according to the manufacturers' protocol (Promega*, Mannheim, Germany). Briefly, epithelial cells are grown to a predetermined optimal number of 12 000/well in a 96-well plate and subsequently incubated with toxins solutions for 24 h. Thereafter, washing is carried out with full medium before adding 20 µl MTS agent to 100 µl medium-containing wells. Control experiments were carried out using cell-free wells or Triton-X-100 permeabilized cells (1 %v/v). Cells are incubated for 45 min and absorbance is determined using at 490 nm. The color change is a direct measure of the cell's metabolic activity due to the reduction of MTS educts to formazan by the action of mitochondrial dehydrogenases. Experiments are repeated three times and data pooled for determination of IC_{50} concentrations for biosensor experiments. DMSO solvent controls for MDCKII yielded IC_{50} values of 6.6% (v/v) for MDCKII and 6.8% (v/v) for FaDu cells. Toxin dilutions were kept reasonably below this regime.

4.2.4 Immuno- / Fluorescence-microscopy

Immunostaining, fluorescence and bright field phase contrast microscopy are applied to visualize changes in the integrity of the cell cytoskeleton as well as overall morphology alterations. Therefore, cells are grown to confluence on petri-dishes and afterwards incubated with corresponding IC_{50} concentrations of toxins. For actin and microtubules staining, washing with PBS and fixation/permeabilization is carried out by immersing the cells into a -20 °C cold acetone/methanol mixture (1:1 vol %) for 10 min. Afterward, the cells are washed three times with PBS, nonspecific binding sites saturated with FCS, and incubation in staining solutions carried out according to the manufacturer's recommendation: Alexa Fluor 546 phalloidin (invitrogen, Paisley, UK) is used for f-Actin staining, Alexa Fluor-488-conjugated IgG1 anti-β-tubulin (BD Bioscience, Heidelberg, Germany) from mouse for labeling microtubules, 4',6 diamidino-2-phenyindole (DAPI,

Sigma-Aldrich, Seelze) for nucleus/DNA labeling and monoclonal anti-ZO-1 or anti-occluding rabbit antibody (Zymed Gmbh, Munich) followed by polyclonal Alexa Flour-conjugated goat-anti rabbit IgG1 antibody (BD Bioscience, Heidelberg, Germany) for staining tight junctions proteins. Staining is carried out for 10 min (DAPI) or 30 min (Alexa) at room temperature, and cells are washed subsequently. Untreated cells served as controls (for the same incubation duration) and were stained correspondingly. Examination occurs under an upright Olympus fluorescence microscope (Olympus BX51, 10, 40 or 100 × water immersion (0.8 or 1.0 NA), Germany), equipped with a color camera (DP71).

4.3 RESULTS

4.3.1 Determination of IC$_{50}$ values of small molecule inhibitors

Aim of this study was to elucidate the origins of biological noise detected by two recently introduced cell motility biosensors based on fluctuation analysis: dynamics of cellular locomotion as detected by the quartz crystal microbalance, equipped with dissipation monitoring (D-QCM) was compared to the micromotility as recorded by the electrical-cell substrate impedance sensing (ECIS). Therefore, cytoskeletal toxins and chemotherapeutics were applied to two different cell model systems, a mammalian kidney cell line (MDCKII) and a human squamous cancer cell line (FaDu). Thereby, the toxins` impact on two measures of biological noise was evaluated: influence on noise amplitudes as assessed by variance analysis as well as long-time correlations described by PSD-estimation.

As a first approach to determine the typical working regimes of the toxins under investigation, MTS tests were conducted on all eight agents, subdivided into three categories: first, actin affine reagents such as cytochalasin D, phalloidin and blebbistatin, second, microtubuli altering substances like taxol, nocodazol or colchicin and third chemotherapeutics such as resveratrol and cis-platin. The chemical structure and the function of each toxin is given in *figure* 4.1.

Differences between the two cell lines as the molar amount of cytoskeletal components, the metastatic potential and therefore cytoskeletal dynamics or even membrane permeability issues caused IC$_{50}$ values within a wide concentration regime. *Figure* 4.2 illustrates exemplary results of the MTS test. Actin reagents cause cell death of MDCKII cells at lower concentrations than corresponding toxins added to FaDu cells.
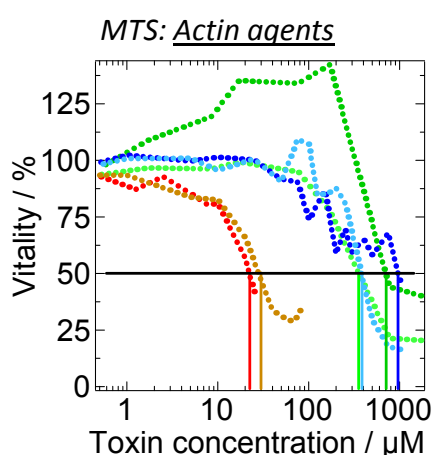
Figure 4.2 MTS-toxicity test for mitochondrial activity, exemplary for actin agent category. Toxicity for both cell lines, FaDu (F) and MDCKII (M), is depicted: M-*Cyt-D.* (●), M-*Blebb.* (●), M-*Phall.* (●), F-*Cyt-D.* (●), F-*Blebb.* (●), F-*Phall.* (●); IC$_{50}$line included for better orientation. IC$_{50}$ values are assembled in *Tab.1*. Mean of experiments done in triplicate with each *n* = 6 is shown. Drugs sorted by increasing toxicity: Cyt-D < Blebb. < Phall.. MDCKII cells are more sensitive to the action of toxins Note the stimulatory effect of F-*Blebb.* at concentrations ≤ 110 μM.

Furthermore, phalloidin is less toxic than cytochalasin D. Notably, an increase of the metabolism of FaDu cells under influence of blebbistatin can be detected, possibly due to an synthesis overshoot as a response to its ATPase inhibiting activity. Equitoxic IC_{50} regimes for all chemicals applied in this study are summarized in *table* 4.1.

Table 4.1*:* Average *IC_{50}* values of all chemotherapeutics and toxins acting on actin, microtubules or inducing apoptosis for the mammalian kidney model system MDCKII and the human squamous carcinoma cell line FaDu derived from the hypopharynx. Means of three experiments with each *n* = 6 and SD of ± 15 % are given.

Toxin	IC_{50}MDCK II/µM	IC_{50}FaDu/µM
Cytochalasin-D	22	30
Phalloidin	400	970
Blebbistatin	425	730
Colchicin	150	745
Nocodazol	130	50
Taxol	30	145
cis-platin	20	30
Resveratrol	250	50

4.3.2 Monolayer morphology of epithelial MDCKII and FaDu cells

Morphology of FaDu and MDCKII cell monolayers 24 hours after seeding to confluence is shown in *figure* 4.3: Occludin (1) and ZO-1 (2) fluorescence is not cell-border located, as usual for tight junctions proteins. We believe that occludin is ER-correlated and ZO-1 to be in membrane proximity. The corresponding phase contrast image (3) underlines incomplete tight-junction formation of the cancer cell line by variable intercellular spacing, whereas ZO-1 fluorescence micrograph (4) for the canine kidney MDCKII line confirms a uniform monolayer with continuous ZO-1 boundaries.
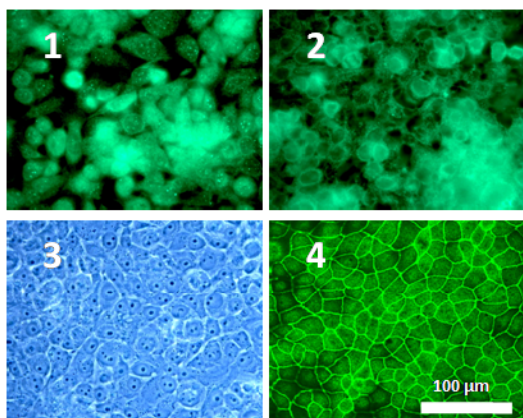
Figure 4.3 Monolayer morphology for FaDu and MDCKII cell lines: Occludin (1) and ZO-1 (2) fluorescence micrographs as well as phase contrast image (3) for FaDu cells 24 h after inoculums. ZO-1 fluorescence micrograph (4) of the canine kidney MDCKII line. MDCKII cells form monolayers which allow a continuous ZO-1 staining, while tight junctions integrity of the FaDu cell line is reduced due to cancerous mutations.

4.3.3 Influence of toxins and chemotherapeutics on cellular impedance, cell-cell contact density and cell-substrate dynamics

The cellular response to toxins and chemotherapeutics is monitored by ECIS and D-QCM providing a large variety of different parameters related to dynamic morphological changes. The oscillating quartz resonator is capable of detecting subtle changes in viscoelasticity, shape and height[32] due to an evanescent acoustic shear wave penetrating through the basal membrane of cells. The impedance based setup captures the overall cellular impedance correlated to adhesion and spreading behavior of cells, thereby detecting i.e. membrane capacitance and resistance (not shown) as well as cell shape changes related to cell-cell- or cell-substrate dynamics.[33,43, 44]

Figure 4.4 exemplary presents an ECIS-measurement of MDCKII (A) and FaDu cells (B) exposed to colchicin. Complex impedance IZI_{norm}, transepithelial resistance measure $\Delta R_{b,\ norm}$ as well as the two fluctuation analysis parameter m_{ECIS}^{PSD} from PSD-estimations and $\tilde{\sigma}_{ECIS}^2$ from variance analysis of the impedance real part noise are shown. Untreated cell controls are displayed in green and empty electrodes in black. Addition of colchicin in concentrations below, at exactly or above IC_{50} concentrations were labeled in blue, orange or red. The time scale of the experiment can be divided into five intervals: subconfluent stage (a), confluence (b), time of adding the toxins (c), 0-24 h interval (d), interval from 24 h to the end of the experiment, lasting usually 48 h. The grey-shaded area denotes the time until addition of the toxin, flanked by the addition time interval (c). This period of time was excluded from noise evaluation due to thermal perturbation of the system. Note that IZI_{norm}, $\Delta R_{b,\ norm}$, m_{ECIS}^{PSD} and $\tilde{\sigma}_{ECIS}^2$, were normalized to mean values of (b) and standardized to starting values of (a).

The ECIS-biosensor clearly discerns the two cell types (*figure* 4.4). MDCKII cells show a 1.5 times higher cellular impedance than FaDu cells, although they both form epithelial monolayers. The incomplete cell-junction integrity of FaDu cells and therefore strongly reduced $\Delta R_{b,norm}$ values directly influence the IZI_{norm}-values. Although seeded to confluence, FaDu cells, which have almost twice the duplication time of MDCKII cells, may also need longer times for polarization than MDCKII cells.
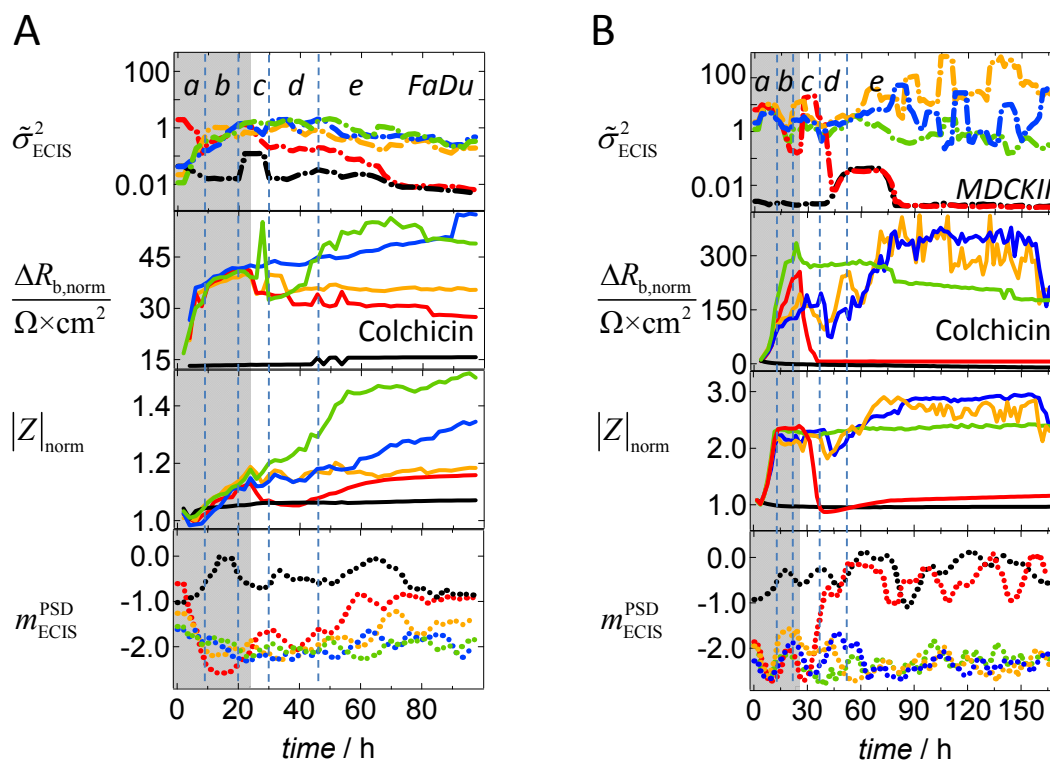
Figure 4.4 Electrical cell-substrate impedance sensing (ECIS)-measurements, exemplary shown for free microtubules monomer binding colchicin and both cell lines (regime before addition is marke in grey). In descending order: variance analysis $\tilde{\sigma}^2_{ECIS}$ (normalized to values for confluency), TER measure $\Delta R_{b,norm}$ (normalized to electrode area), cellular impedance $|Z|_{norm}$ (normalized to starting value, recorded at 4 kHz) and low-frequency regime slope from PSD-estimation m^{PSD}_{ECIS}. Noise parameters $\tilde{\sigma}^2_{ECIS}$ and m^{PSD}_{ECIS} are based on real part fluctuations of $|Z|_{norm}$. Five consecutive time regimes are distinguished: seeding/spreading and polarization (a), confluency (b), toxin addition (c), 0-24h interval, >24h interval until the end of experiment (e). A) 6×10^5 FaDu cells inoculum with subtoxic 500 µM (●), 750 µM or IC$_{50}$ conc.(●), 1000 µM (●) colchicin addition. B) 6×10^5 MDCKII cells inoculums with subtoxic 50 µM (●), 150 µM or IC$_{50}$ conc.(●), 500 µM (●) colchicin addition. Controls for both cell lines are: untreated cell monolayer (●), electrode immersed in full culture medium without cells (●). Note that FaDu cells show increasing cellular impedance also after (microscopically determined) confluency, correlated with increasing TER.

Addition of colchicin in a concentration above the IC$_{50}$ reduces all four parameters $|Z|_{norm}$, $\Delta R_{b, norm}$, m^{PSD}_{ECIS} and $\tilde{\sigma}^2_{ECIS}$, nearly to the level of a bare untreated electrode. It turned out that for FaDu cells, $|Z|_{norm}$ and m^{PSD}_{ECIS} responds more sensitive to changes in colchicin concentration than $\Delta R_{b, norm}$ and $\tilde{\sigma}^2_{ECIS}$. Generally, MDCK II cells are less sensitive to colchicin concentrations below the IC$_{50}$. Remarkably, although the MTS test reveals a reduced cell viability upon addition of colchicin below IC$_{50}$, cellular micromotility is increased for MDCKII cells. Reorganization of the actin-network overcoming the lack of microtubules may be one reason for the increase of micromotion (*figure* 4.8 B).

4.3.4 Biological activity of cells cultured on thickness shear mode resonators.

Exemplary, the response of the F-QCM to addition of cytochalasin D to FaDu and MDCKII cells is shown in *figure* 4.5. The F-QCM monitors fluctuations of Δf and $\Delta \delta$ as a function of external stimuli and hence delivers information about cellular dynamics complementary to ECIS micromotion. The experimental time scale is subdivided corresponding to the ECIS experiments. In contrast to complex impedance, *both* parameters frequency and dissipation time shifts Δf and $\Delta \delta$ are subjected to fluctuation analysis yielding m_{QCM}^{PSD} and $\tilde{\sigma}_{QCM}^{2}$ of both f and δ. As opposed to ECIS, no information on cell-cell contacts were gathered and only IC$_{50}$ concentrations considered.

For frequency and dissipation time courses, values upon addition of chemotherapeutics and toxins were arbitrary set to zero. Untreated MDCKII cells produce Δf shifts of $-(150 \pm 100)$ Hz and $\Delta \delta$ shifts of (5550 ± 455) s^{-1}, whereas FaDu cells show Δf shifts of $-(205 \pm 35)$ Hz and $\Delta \delta$ shifts of (5080 ± 110) s^{-1}. Besides viscoelastic parameters such as the complex shear modulus derived from Δf and $\Delta \delta$, F-QCM fluctuation analysis of the PSD in the frequency range of 0.5 to 5 mHz [32] from confluent cells yields mean slopes of -1.5 (MDCKII) and -0.9 (FaDu).

Upon the addition of cytochalasin D, frequency Δf and dissipation $\Delta \delta$ shifts show an antidromic trend for both cell lines, however not reaching starting values by the end of the experiments, what would indicate complete loss of attached mass and energy dissipation reduced to cell-free level. Untreated cells with medium in contact to the resonator monitored over the same time interval essentially revealed unchanged viscoelasticity of the epithelial cell layer as well as constant fluctuation parameters (data not shown). Interestingly, the toxin evokes either reduced fluctuation amplitudes for both MDCKII and FaDu cells, as represented by a reduction of $\tilde{\sigma}_{QCM}^{2}$ of both f and δ levels after addition of toxin (22 µM for MDCKII and 30 µM for FaDu cells) or it reduces the long-time correlations described by m_{QCM}^{PSD} of f and δ. Both effects occur clearly in the first 24 hour interval of the experiments. Note, that during a first phase of 10 hours after toxin addition, a slight mass increase is detectable in both cell models.
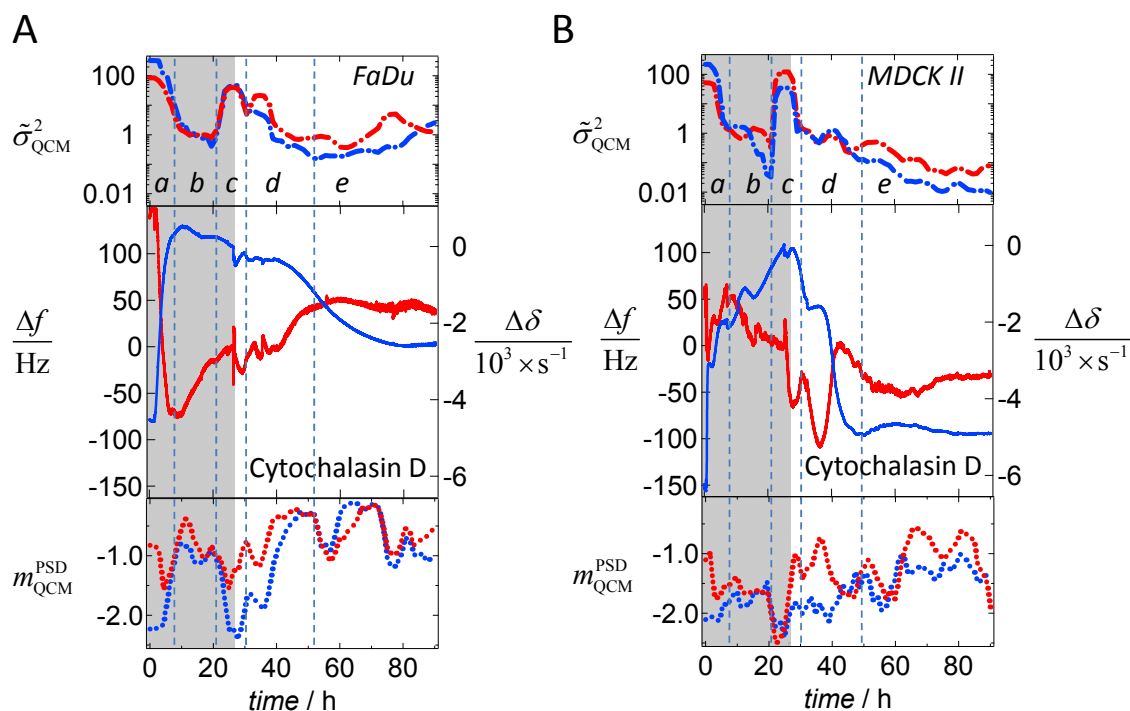
Figure 4.5 Quartz crystal microbalance with dissipation monitoring (D-QCM)-measurement, exemplary shown for cytochalasin-D acting on MDCK II and FaDu cells (regime before addition is marked in grey). In descending order: variance analysis $\tilde{\sigma}^2_{QCM}$ (normalized to values for confluency), frequency and dissipation shifts Δf and $\Delta \delta$ (● and ●, normalized to toxin addition = 0) and low-frequency regime slope from PSD-estimation m^{PSD}_{QCM}. Noise analysis parameters $\tilde{\sigma}^2_{QCM}$ and m^{PSD}_{QCM} (F-QCM) are obtained from fluctuations of Δf and $\Delta \delta$. Five different time regimes a-e are distinguished. A) 6×10^5 FaDu cells inoculum with 30 µM (IC_{50} conc). cytochalasin-D addition. B) 6×10^5 MDCKII cells inoculums with 22 µM (IC_{50} conc.) cytochalasin-D addition. Cell specific action of cytochalasin-D is detected: m^{PSD}_{QCM} of FaDu cells is considerably affected by cytochalasin-D, whereas $\tilde{\sigma}^2_{QCM}$ is significantly diminished in the case of MDCKII cells.

4.3.5 Correlation of sensor output and perturbed cellular integrity:

4.3.5.1 Resonance frequency, dissipation and overall impedance.

Figure 4.6A and B highlight the impact of cytoskeletal disruption by actin manipulating toxins, microtubule influencing drugs as well as transcription inhibiting chemotherapeutics on the sensor output. Viscoelastic and impedimetric parameters Δf, $\Delta \delta$, ΔIZI_{norm} and $\Delta R_{b,norm}$, representing the cell-cell contact density, were monitored. D-QCM results (*figure* 4.6 A) are directly comparable to ECIS results (*figure* 4.6 B) by standardization to percentage values. Generally, we found that the D- QCM parameters are less sensitive to cell specific toxin actions than the ECIS parameters.

4.3.5.1.1 Actin-agents

The actin stabilizing substance phalloidin causes a prominent effect on D-QCM parameters: as compared to the ECIS parameters: for FaDu cells, Δf and $\Delta \delta$ are reduced
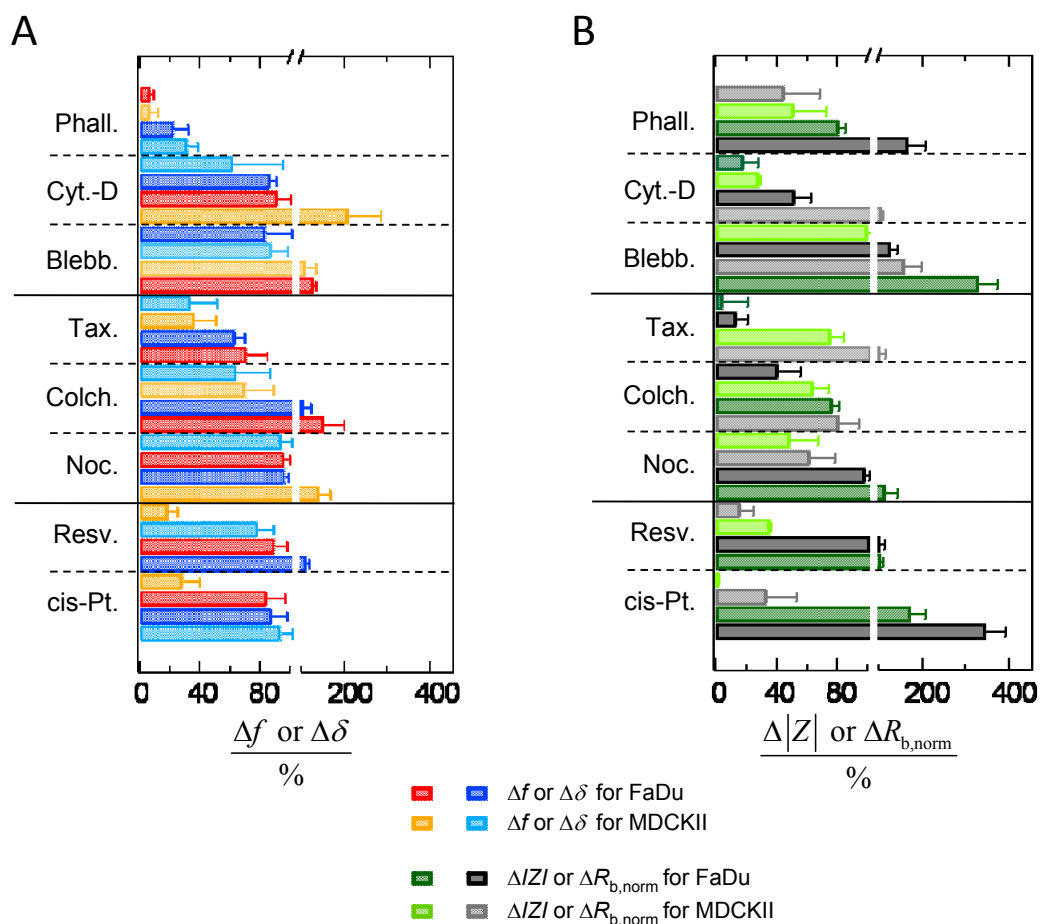
Figure 4.6 Comparison of D-QCM and ECIS sensor response to equitoxic, IC_{50}-concentrations: influence of all three small molecule inhibitor categories (actin, microtubules and nucleus agents) on the direct readout parameters of D-QCM (Δf and $\Delta\delta$) and ECIS ($\Delta R_{b,norm}$ and $\Delta|Z|_{norm}$). Standardized to confluency values (time regime b = 100%) and empty electrodes signal (starting values of time regime a, 0%): Δf is mass-sensitive, $\Delta\delta$ adresses dissipation on the resonator surface, $\Delta R_{b,norm}$ is a measure for cell-cell contact density and $|Z|_{norm}$ for the overall cellular insulating behaviour. Values are sorted by increasing order. Note splitted axis` scale change

below 40 %, while $\Delta|Z|_{norm}$ is only slightly reduced (to 80 %) and $\Delta R_{b,norm}$ even increases up to 160 %. MDCKII cells show a comparable decrease in QCM parameters, whereas both ECIS parameters are reduced to 40-45%. Addition of destabilizing cytochalasin to FaDu monolayers produces a more pronounced decrease in $\Delta|Z|_{norm}$ (a reduction to 20-%) as opposed to unchanged Δf and $\Delta\delta$ parameters, while MDCKII cells present a strong frequency (and therefore mass) increase of 200 % and a dissipation decrease to 60%. As for FaDu cells, $\Delta|Z|_{norm}$ of MDCKII cells under cytochalasin D influence is reduced roughly to 20% , but $\Delta R_{b,\ norm}$ is not affected. Blebbistatin produces a significant increase in transcellular resistance of FaDu and MDCKII cell layers (note the changed scaling after

axis split) and a strong increase in cellular impedance for FaDu cells, while all D-QCM parameters are not affected.

4.3.5.1.2 Microtubuli-agents

Small molecules affecting microtubules show generally a stronger sensor response upon stabilization than destabilization. Taxol, know to stabilize microtubules, strongly reduces ΔIZI_{norm} and $\Delta R_{b,norm}$ of FaDu cells (below10 %), while the QCM parameter $\Delta\delta$ and Δf are only reduced by 20%. Interestingly, MDCKII cells respond to the addition of taxol with a strong decrease in $\Delta\delta$ and a corresponding decrease in Δf to 40%, while ECIS parameters ΔIZI_{norm} (-20%) and $\Delta R_{b,norm}$ (+5%) are less affected. Colchicin, which binds free tubulin monomeres, does not impact $\Delta\delta$ of FaDu cells and increases Δf to 130% , but produces a pronounced change in $\Delta R_{b,norm}$ to 40% and a slight ΔIZI_{norm} decrease to 80%*.* ECIS data obtained from MDCKII monolayers exposed to colchicin shows a moderate reduction of both parameters by 20-30% and corresponding decreases of $\Delta\delta$ and Δf.

FaDu cells treated with nocodazol, which increases microtubuli-depolymerization, however, display virtually no QCM and no ECIS response, while addition of nocodazol to MDCKII monolayers reduces $\Delta R_{b,norm}$ and ΔIZI_{norm} by 40-60%. and causes an Δf increase by 20%, leaving $\Delta\delta$ unchanged.

This indicates that, for non-cancerous cells, viscoelasticity is strongly manipulated by taxol, whereas nocodazol influences the complex impedance. Surprisingly, by impedimetric data, FaDu cells show an exact inverted trend to MDCKII cells, with nocodazol having almost no influence on ΔIZI_{norm} and $\Delta R_{b, norm}$, colchicin being intermediate and taxol almost abolishes any signal to zero level.

4.3.5.1.3 Apoptosis-inductors

As far as the effect of chemotherapeutics is concerned, the ECIS is more sensitive than the D-QCM. While only MDCKII cells Δf indicate a significant mass decrease for both substances, both ΔIZI_{norm} and $\Delta R_{b, norm}$ are strongly decreased for MDCKII cells in the ECIS setup. Additionally, a strong impedance and transcellular resistance increasing effect upon cis-platin administration to FaDu cells is detected with the ECIS setup, indicating the cancer cells` sensitivity for the DNA-intercalating substance.

4.3.5.2 Shape and viscoelastic fluctuations measured by ECIS and F-QCM.

4.3.5.2.1 Actin-agents

In *figure* 4.7A, the effect of cytochalasin D, phalloidin and blebbistatin on the noise parameters m^{PSD} and $\tilde{\sigma}^2$ of *f, δ* and *IZI*_{norm} is shown. All values are given as percentage shifts after standardization. *Figure* 4.7B and C correlate noise parameters to cell specific effects on the cytoskeltal architecture by fluorescence microscopy. Micrographs depict phalloidin-stained actin in red, anti-β-tubulin-labeled microtubules in green and the overlay including DAPI-stained, blue nuclei for facilitation of intracellular localization.

The actin-destabilizing and -shortening effect of Cytochalasin D on actin fibers is clearly detectable for the 24-72 h interval for both the F-QCM and the ECIS noise parameters, while after 24 hours the effect is more pronounced in $m_{\mathrm{QCM}}^{\mathrm{PSD}}$ of *f* and $\tilde{\sigma}_{\mathrm{ECIS}}^2$. Microscopically, a clearly disrupted actin cytoskeleton is visible lacking stress fibers and a cortical ring for MDCKII cells, while both cell lines show actin aggregates/plaques in nuclear vicinity as a consequence of actin depolymerization.

Actin-stabilizing effects of phalloidin are clearly visible for both cell types for the 24 h interval in the case of $m_{\mathrm{QCM}}^{\mathrm{PSD}}$, whereas $\tilde{\sigma}_{\mathrm{QCM}}^2$ reveals a strong decrease to values below 20 % only on FaDu cells. $\tilde{\sigma}_{\mathrm{QCM}}^2$ of MDCKII cells even increase by 200 % as compared to controls. F-QCM results obtained for the 24-72 h interval show FaDu cells with $m_{\mathrm{QCM}}^{\mathrm{PSD}}$ between 60-90% and small $\tilde{\sigma}_{\mathrm{QCM}}^2$ (below 5%) in contrast to MDCKII cells with $m_{\mathrm{QCM}}^{\mathrm{PSD}}$ of 50% and lower, whereas $\tilde{\sigma}_{\mathrm{QCM}}^2$ .are still elevated (>>100%). Micromotion analysis of ECIS data ($m_{\mathrm{ECIS}}^{\mathrm{PSD}}$ and $\tilde{\sigma}_{\mathrm{ECIS}}^2$) turned out to be more responsive to phalloidin than F-QCM data within the first 24 h. $\tilde{\sigma}_{\mathrm{ECIS}}^2$ is, upon phalloidin addition to both cell types, reduced to 10-60% of the noise level produced by vital FaDu or MDCKII cells. For the 24-72 h interval, all four ECIS parameters of both cell types drop below 25 %. Depending on the cell type, fluorescence micrographs display long, stiff actin fibers and a large amount of substrate contacts (FaDu *and* MDCKII cells, see fibers and dots marked by arrows) and a fibroid, longitudinal shape (MDCKII cells) or no shape changes (FaDu cells), possibly explaining the small $m_{\mathrm{QCM}}^{\mathrm{PSD}}$ decrease found for the latter cell type. Blebbistatin, which blocks actin-myosin II ATPase in the actin-unbound state, does strongly increase $\tilde{\sigma}_{\mathrm{QCM}}^2$ of MDCKII and especially FaDu cells in both time intervals (0-24 h, 24-72 h) and for both entities
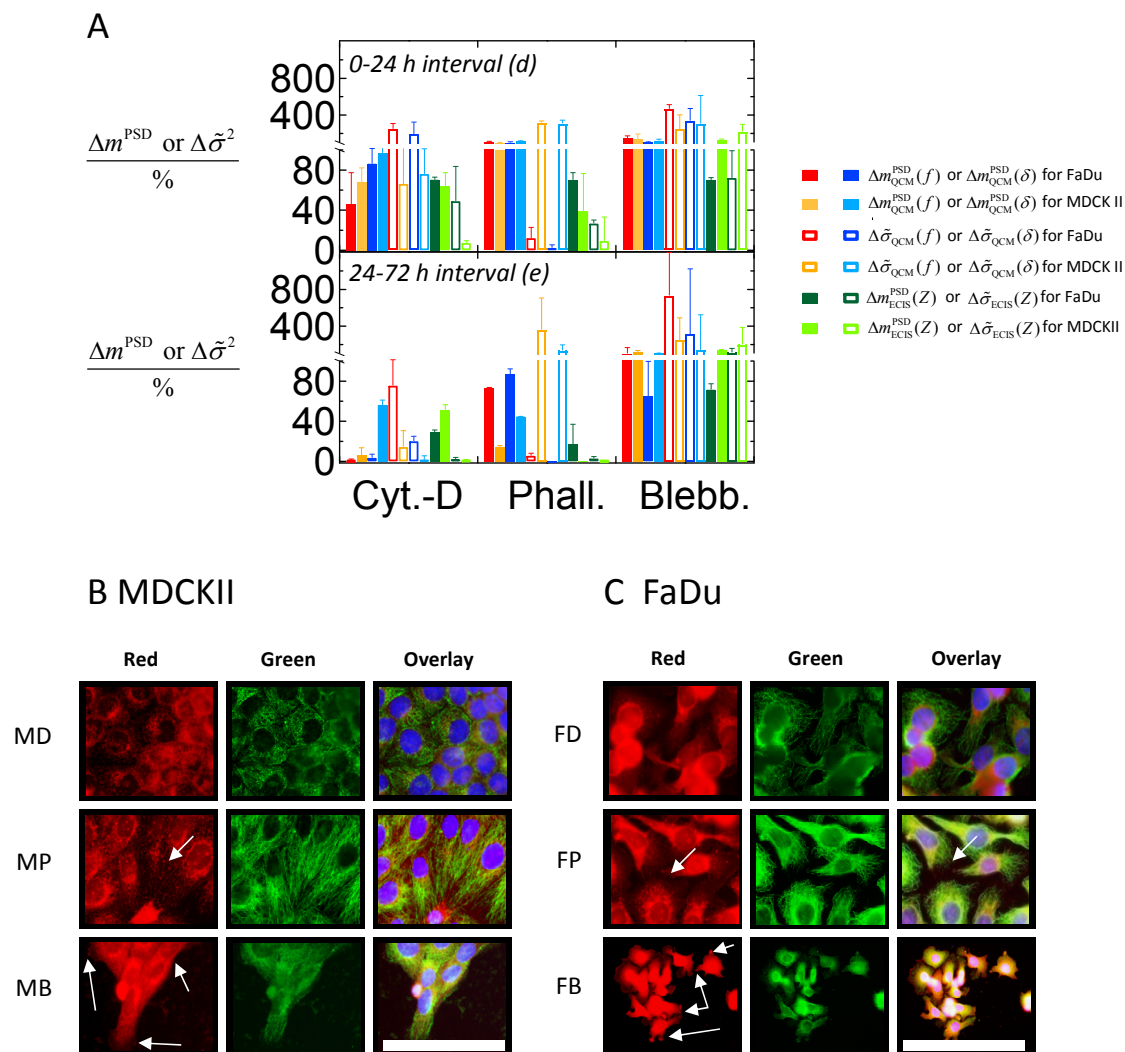
Figure 4.7 A) Cellular motility altered by small molecule inhibitors: Influence of actin manipulating agents Cyt.-D (D), Phall. (P), and Blebb. (B) at equitoxic IC_{50} concentrations on motility. Fluctuations in frequency Δf, dissipation $\Delta \delta$ and cellular impedance shifts $\Delta |Z|_{norm}$ .are shown. Biological noise is analysed in terms of variance $\tilde{\sigma}^2_{QCM/ECIS}$ and PSD-estimation $m^{PSD}_{QCM/ECIS}$ over the first 24 h interval or from 24 h until the end of the experiment, usually 72 hours. Standardization to percentage data through confluency values (time regime b, 100%) and empty electrodes signal (starting values of time regime a, 0%); $\tilde{\sigma}^2_{QCM/ECIS}$ describes the noise amplitude, $m^{PSD}_{QCM/ECIS}$ the long time correlations in the cellular fluctuations. Fluorescence micrographs visualize cell specific small molecule effects on cytoskeletal integrity of MDCKII (B) or FaDu (C) cells by Alexa Fluor 546 phalloidin f-Actin staining (red), Alexa Fluor-488-conjugated IgG1 anti-β-tubulin labeling (green) or DAPI-dye for visualization of nucleus localization in overlays. For arrow highlights, refer to text. Scale equals 100 μm (250 μm in the FB category).

f and *δ*. Corresponding to the MTS-results of blebbistatin treated FaDu cells (see *figure*

4.2) indicating increased metabolism, we find a rise of $\tilde{\sigma}^2_{QCM}$ up to 800 % for the 24-72 h

interval for *f*. m^{PSD}_{QCM} of MDCKII and FaDu cells is, however, not influenced by blebbistatin,

with the exception of an m^{PSD}_{QCM} decrease in the 24-72 h interval for *δ* to 60% for FaDu cells.

Impedance noise parameters $m_{\text{ECIS}}^{\text{PSD}}$ and $\tilde{\sigma}_{\text{ECIS}}^2$ are diminished by 30 % for FaDu cells within the first 24 hours, while MDCKII cells show a small increase of $m_{\text{ECIS}}^{\text{PSD}}$ (+25%) and a large increase of $\tilde{\sigma}_{\text{ECIS}}^2$ (+120%). For the 24-72h interval, all ECIS noise parameters are not modified as corresponding to the first 24 h interval, besides a recovery of $\tilde{\sigma}_{\text{ECIS}}^2$ to the level of untreated FaDu cells. Micrographs indicate a possible origin of the $\tilde{\sigma}_{\text{QCM}}^2$ increase in F-QCM: while the actin cytoskeleton appears dense, longer cell bodies and filopodia-like extensions arise (see arrows in MB and FB of *figure* 4.7B and C) and therefore alter monolayer architecture.

4.3.5.2.2 Microtubuli-agents

In *figure* 4.8, the specific dynamic contributions of microtubules to the biological noise are shown. For this purpose, the microtubules-stabilizing taxol, the destabilizing agent nocodazol and the monomer binding colchicin are applied.

Taxol reduces overall noise in a cell dependent manner. MDCKII cells display a large reduction of $m_{\text{QCM}}^{\text{PSD}}$ and $\tilde{\sigma}_{\text{QCM}}^2$ during the 0-24 h time interval (decrease to 7-27 %) and noise parameters derived from ECIS micromotion for MDCKII cells (0-24 h) also follow this trend. All noise parameters derived from FaDu cells are less affected by taxol (maximum reduction to 65%) aside from $m_{\text{QCM}}^{\text{PSD}}$ of f reaching 41 % of the level of fully vital FaDu cells. After the 24-72 h interval, six of eight F-QCM noise parameters of both cell lines are reduced below 25 % of the vital cells (besides $\tilde{\sigma}_{\text{QCM}}^2$ of f for MDCKII and FaDu cells). ECIS noise level of both cell types in the 24-72 h interval are between 40-60% apart from $\tilde{\sigma}_{\text{ECIS}}^2$ of MDCKII cells, which is completely reduced to zero level. Micrographs underline the stronger taxol effect on MDCKII cells for the 0-24 h interval: efficiency is more pronounced, as cells show multiple asters and microtubule organizing centers (see arrow in green channel) and apoptosis is observed more frequently for MDCKII than for FaDu (arrows in overlays). FaDu cells show strong aggregation of microtubules into bundles (arrow in green channel), whereas the actin skeleton of both cell lines remains fairly unaffected.

Addition of nocodazol to FaDu cells results in a significant reduction of $m_{\text{QCM}}^{\text{PSD}}$ and $\tilde{\sigma}_{\text{QCM}}^2$ for the 0-24 h interval, whereas F-QCM parameters of MDCKII cells show a small

A

$$\frac{\Delta m^{\mathrm{PSD}} \text{ or } \Delta \tilde{\sigma}^2}{\%}$$

0-24 h interval (d)

$$\frac{\Delta m^{\mathrm{PSD}} \text{ or } \Delta \tilde{\sigma}^2}{\%}$$

24-72 h interval (e)

Tax.   Noc.   Colch.

Legend:
- $\Delta m_{\mathrm{QCM}}^{\mathrm{PSD}}(f)$ or $\Delta m_{\mathrm{QCM}}^{\mathrm{PSD}}(\delta)$ for FaDu
- $\Delta m_{\mathrm{QCM}}^{\mathrm{PSD}}(f)$ or $\Delta m_{\mathrm{QCM}}^{\mathrm{PSD}}(\delta)$ for MDCK II
- $\Delta \tilde{\sigma}_{\mathrm{QCM}}(f)$ or $\Delta \tilde{\sigma}_{\mathrm{QCM}}(\delta)$ for FaDu
- $\Delta \tilde{\sigma}_{\mathrm{QCM}}(f)$ or $\Delta \tilde{\sigma}_{\mathrm{QCM}}(\delta)$ for MDCK II
- $\Delta m_{\mathrm{ECIS}}^{\mathrm{PSD}}(Z)$ or $\Delta \tilde{\sigma}_{\mathrm{ECIS}}(Z)$ for FaDu
- $\Delta m_{\mathrm{ECIS}}^{\mathrm{PSD}}(Z)$ or $\Delta \tilde{\sigma}_{\mathrm{ECIS}}(Z)$ for MDCKII

B MDCKII

Red   Green   Overlay

MT

MN

MC

C FaDu

Red   Green   Overlay

FT

FN

FC
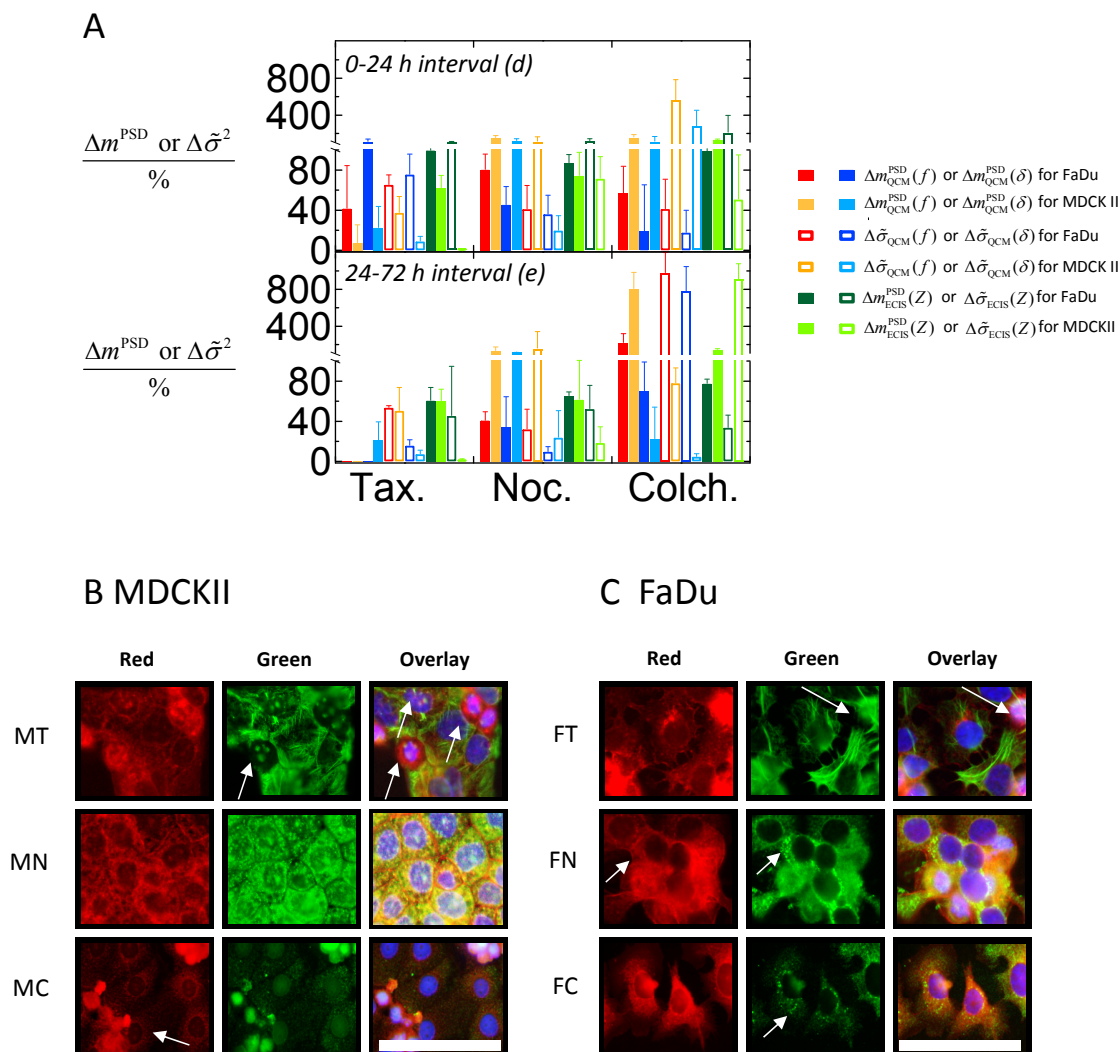
Figure 4.8 A) Alteration of cellular motility by addition of small molecule inhibitors that are directed to microtubuli organization: Tax. (T), Noc. (N), and Colch. (C) at equitoxic IC$_{50}$ concentrations. Fluorescence micrographs display cell specific small molecule effects on cytoskeletal integrity of MDCKII (B) or FaDu (C) cells labelled in the same manner as in *figure* 4.7. Scale: bottom image size equals 100 μm.

increase upon addition of nocodazol by 11 to 50 % (with the exception of an $\tilde{\sigma}_{\mathrm{QCM}}^2$ (δ) decrease of 80%). The 24-72h interval retains these F-QCM parameter regimes for both cell lines with a trend to lower values. Generally, as far as F-QCM parameters are concerned, only FaDu cells show a significant decrease. For ECIS, addition of nocodazol to either MDCKII cells or FaDu cells results, within the first 24 h, in a significant reduction of $m_{\mathrm{ECIS}}^{\mathrm{PSD}}$ and $\tilde{\sigma}_{\mathrm{ECIS}}^2$ by 13-29% with the exception of $\tilde{\sigma}_{\mathrm{ECIS}}^2$ of FaDu cells increasing by 15%. For the 24-72h time interval upon nocodazol treatment, ECIS micromotion data of both cell types is slightly reduced as compared to the 0-24h interval and comparable to the micromotion found for taxol treatment after 72 h. Micrographs reveal a strong

degradation of microtubules for both cell lines. Monolayer architecture of MDCKII cells is not affected, whereas the actin network of FaDu cells shows slight reorganization upon microtubule degradation (arrows in red and green channel of micrographs from nocodazol treated FaDu cells (FN)).

Colchicin addition to FaDu cells significantly reduces all F-QCM parameter to 20-60 % of the level found for untreated FaDu cells within the first 24h. MDCKII cells show a small increase of m_{QCM}^{PSD} (10-50%) and a large increase of $\tilde{\sigma}_{QCM}^{2}$ (200-400%) in the 0-24 h interval. Colchicin addition to both cell lines only reduces $\tilde{\sigma}_{ECIS}^{2}$ of MDCKII cells to 51 % after 24 h, whereas it does not affect m_{ECIS}^{PSD} of FaDu cells or even increases other impedance noise categories (m_{ECIS}^{PSD} of MDCKII, $\tilde{\sigma}_{ECIS}^{2}$ of FaDu cells). We find a prominent increase up to values above 800% for MDCKII and FaDu cells m_{QCM}^{PSD} (*f*) and for FaDu cells $\tilde{\sigma}_{QCM}^{2}$ (*f* and *δ*) for the prolonged measurement (24-72h), as far as F-QCM is concerned. A comparable increase with values beyond 800 % is also detected for impedance micromotion of MDCKII cells for the 24-72 h interval. When compared to micrographs, we find a strong reorganization of the MDCKII actin-cytoskeleton (red channel arrow) upon microtubules degradation, which is more pronounced for MDCKII than for FaDu cells.

4.3.5.2.3 Apoptosis-inductors

Figure 4.9 shows the impact of resveratrol and cis-platin, the first drug being an antioxidant inducing apoptosis at elevated concentrations, while the latter is known to cause apoptosis by DNA-intercalation. Here, for the sake of clarification, 10-40 fold magnifications with an overlay of green and red on the one hand and blue channel on the other are shown to present representative degree of apoptosis.

Cis-platin affects the PSD slope m_{QCM}^{PSD} of FaDu cells, particularly after long incubation (24-72h), whereas F-QCM parameters of MDCKII cells are less affected by 24 h cis-platin incubation. After 24 h, $\tilde{\sigma}_{QCM}^{2}$ of FaDu cells remain unaffected, whereas three of four ECIS noise parameters (m_{ECIS}^{PSD} and $\tilde{\sigma}_{ECIS}^{2}$ of FaDu cells, $\tilde{\sigma}_{ECIS}^{2}$ of MDCK II cells) mark an initial decrease. Both cis-platin and resveratrol cause reduced micromotion as monitored by ECIS for both decrease for the 0-24h interval and stay constant afterwards (24-72h). Noise parameters originating from F-QCM measurements show decreased dynamics for
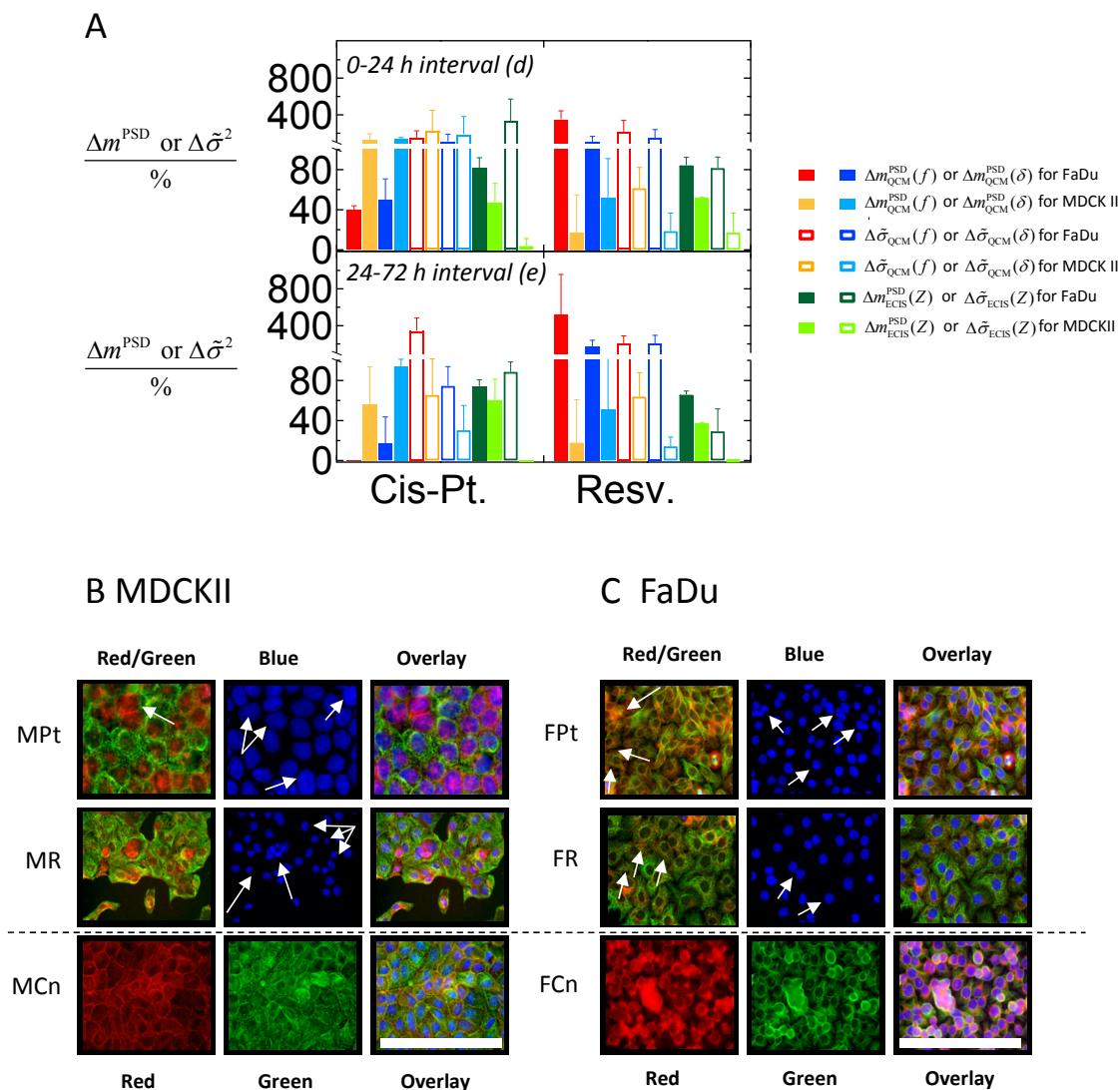
Figure 4.9. A) Changes in cellular viability due to exposure of FaDu and MDCK II to small molecule inhibitors that induce apoptosis. Cis-platin (Pt) and resv. (R) were added at equitoxic IC$_{50}$ concentrations, evaluated corresponding to results presented in figure 7. Fluorescence micrographs show the cell specific small molecule effects on cytoskeletal integrity of MDCKII (B) or FaDu (C) cells by an overlay of Alexa Fluor 546 phalloidin f-Actin staining (red) and Alexa Fluor-488-conjugated IgG1 anti-β-tubulin labeling (green), DAPI-dye for visualization of nuclear integrity as well as localization in overlays. Untreated MDKII and FaDu cell controls (Cn) are depicted in the bottom row. Scale equals 250 μm (100 μm in the MPt category).

MDCKII cells but enhanced motility and long-term correlation for FaDu cells upon exposure to resveratrol. 0-24 h as well as 24-72 h intervals and for both cell lines with the exception of $\tilde{\sigma}^2_{\mathrm{ECIS}}$ of FaDu cells treated with cis-platin after 24 h. Micrographs of MDCKII cells under influence of cis-platin show numerous-apoptotic nuclei (arrows in blue channel), whereas a slight degradation of actin and, to a lesser extent, microtubuli occurs. Resveratrol shows similar actions on MDCKII cells, probably due to apoptotic proteolysis (arrows in green/red channel). Apoptotic nuclei are, however, more

prominent for FaDu cells treated with cis-platin and less frequent in micrographs of resveratrol-treated FaDu cells. Both chemotherapeutics, however, induce a smaller amount of apoptotic cells (for both FaDu and MDCKII cells) than taxol. The bottom row of *figures* 4.9 B and C show the morphology of untreated cells for all three staining categories. *Table* 4.2 summarizes all fluctuation parameters determined within the 24 hours interval.

***Table* 4.2:** Mean PSD-slopes and variances of F-QCM ($m_{QCM_f}^{PSD}$, $m_{QCM_\delta}^{PSD}$, $\tilde{\sigma}^2_{QCM_f}$ $\tilde{\sigma}^2_{QCM_\delta}$) and ECIS (m_{ECIS}^{PSD} and $\tilde{\sigma}^2_{ECIS}$) noise analysis for all chemotherapeutics and toxins acting on actin, microtubules or inducing apoptosis applied to the mammalian kidney model system MDCKII and the human squamous carcinoma cell line FaDu derived from the hypopharynx. Only the first 24 h interval is used for analysis, mean over *n* = 12 is given, normalized with ± S.D or standardized as %.

Agents	Toxins and cells	$m_{QCM_{f/\delta}}^{PSD}$	%	m_{ECIS}^{PSD}	%	$\tilde{\sigma}^2_{QCM_{f/\delta}}$	%	$\tilde{\sigma}^2_{ECIS}$	%
Actin	FP	1.05 ± 0.15	+4	0.73 ± 0.06	-30	0.14 ± 0.11	-88	0.27 ± 0.04	-73
		1.01 ± 0.13	+1			0.05 ± 0.03	-98		
	MP	1.00 ± 0.05	+0.2	0.59 ± 0.20	-61	2.52 ± 0.11	+216	0.09 ± 0.20	-91
		1.15 ± 0.11	+15			2.45 ± 0.38	+207		
	FD	0.65 ± 0.43	-54	0.71 ± 0.04	-30	2.54 ± 1.36	+149	0.49 ± 0.35	-51
		0.92 ± 0.63	-14			1.90 ± 1.24	+92		
	MD	0.79 ± 0.19	-32	0.72 ± 0.11	-36	0.82 ± 0.68	-33	0.07 ± 0.02	-93
		0.98 ± 0.12	-3			0.79 ± 0.43	-24		
	FB	1.69 ± 0.31	+50	0.73 ± 0.03	-29	5.52 ± 2.77	+367	0.72 ± 0.31	-28
		1.07 ± 0.03	+6			3.74 ± 1.57	+238		
	MB	1.54 ± 0.74	+40	1.22 ± 0.13	+25	2.40 ± 1.54	+144	2.20 ± 0.79	+120
		1.26 ± 0.24	+19			2.98 ± 3.00	+204		
MT	FN	0.27 ± 0.19	-80	0.91 ± 0.05	-13	0.43 ± 0.23	-59	1.15 ± 0.28	+15
		0.55 ±0.24	-45			0.38 ±-0.19	-64		
	MN	1.68 ± 0.39	+50	0.83 ± 0.22	-26	1.11 ± 0.51	+11	0.61 ± 0.57	-29
		1.25 ± 0.34	+18			0.22 ± 0.15	-80		
	FC	0.72 ± 0.17	-43	0.98 ± 0.03	-1	0.43 ± 0.29	-59	2.05 ±1.83	+108
		0.48 ± 0.30	-81			0.19 ± 0.22	-82		
	MC	1.60 ± 2.01	+56	1.21 ± 0.12	+25	5.49 ± 8.01	+462	0.51 ± 0.4	-49
		1.07 ± 0.37	+11			2.74 ±1.69	+179		
	FT	0.63 ± 0.28	-59	0.99 ± 0.04	-1	0.66 ± 0.10	-35	1.08 ± 0.06	+7
		1.07 ± 0.19	+10			0.75 ± 0.84	-25		
	MT	0.34 ± 0.12	-93	0.78 ± 0.07	-38	0.39 ± 0.16	-63	0.02 ± 0.01	-100
		0.50 ± 0.14	-78			0.11 ± 0.05	-92		
Apoptosis	FR	3.87 ± 0.81	+248	0.85 ± 0.08	-16	2.10 ± 1.23	+112	0.84 ± 0.09	-18
		1.02 ± 0.39	+4			1.43 ± 0.91	+45		
	MR	0.10 ± 0.88	-83	0.66 ± 0.19	-48	0.63 ± 0.20	-38	0.18 ± 0.20	-83
		0.69 ± 0.25	-48			0.21 ± 0.18	-81		
	FcPt	0.19 ± 0.18	-60	0.88 ± 0.07	-18	1.48 ± 0.74	+49	2.93 ± 1.98	+233
		0.28 ± 0.02	-51			0.75 ± 0.77	+8		
	McPt	1.19 ± 0.41	+29	0.59 ± 0.15	-53	2.17 ± 2.24	+121	0.07 ± 0.08	-96
		1.25 ± 0.08	+39			1.84 ± 1.88	+87		

4.4 DISCUSSION

Molecular genomics have opened a wide array of applications in the field of cytoskeletal dynamics or cell motility and inhibition of precise contributions of individual proteins became possible: i.e. generation of genetic null-mutants, overexpression of participating proteins or constitutive activation of mutant/fragment complexes. As these applications, however, require invasive microinjection/transfection procedures, the chemical biology approach of specific, cell-permeable small molecule inhibitors was favored in our study.

In the present study, we investigated the impact of a variety of small molecule inhibitors of the main intracellular locomotive machinery of actin fibers and microtubules and a direct upstream component, the motor protein myosin II on the noise created by two epithelial cell lines. The aim was to follow and quantify vertical motility by two established biosensors, QCM and ECIS. We applied noise analysis to fluctuations detected in frequency, dissipation and impedance time courses. Additionally, as both non-cancerous (MDCKII) and malign cells (FaDu) were applied, we tested resveratrol as inhibitor of Rho-GTPases and apoptosis inductor as well as cis-platin as direct apoptosis activator. Therefore, comparison of controlled cell death triggered by chemotherapeutics with cytoskeleton targeting substances was possible. Since primarily mechanical properties of the cytosolic biopolymer gel are manipulated by addition of small molecule inhibitors, we first discuss the influence of drugs on the static viscoelastic and impedimetric parameters, before we analyze changes in cytoskeletal dynamics.

Phalloidin, an actin stabilizing and polymerization promoting substance with poor membrane-permeability,[47-49] reduces both the detected mass (frequency increase, but standardized Δf reduction) as well as the energy dissipation, indicative of softening of the cells. A similar effect was found for jasplakinolide. As micrographs do not reveal cellular desorption and show slightly augmented front lamellipodia size for FaDu cells, we believe that a decrease in intercellular spacing explains the increase in TER for FaDu cells. Generally, as elasticity was described to be uninfluenced by phalloidin,[50] reduced viscosity due to loss of cytosolic G-actin as a result of F-actin polymer stabilization might account for the decrease in dissipation. Since both mass and, to lesser extent, impedance decrease, we furthermore assume an increased cell-substrate distances to accompany the observed cell shape elongation, which would also explain the reduction

in $\Delta\delta$ and Δf. Cytochalasin-D treatment also results in a decrease of energy loss, but a mass increase for MDCKII cells. An increase in frequency shift might be explained by a decrease of the cell-substrate distance. This would, however, result in an increase in impedance, which was not observed. It is conceivable that an impedance increase is masked by a loss of cells or cell components due to the toxic nature of cytochalasin D. A similar change of Δf and $\Delta\delta$ was described for A549 cells by Marxer *et al.*, for MDCKII cells by Wegener *et al.* and for 3T3/NRK fibroblasts by Rotsch *et al.*[22, 23, 50] In contrast, micrographs of FaDu cells show a slight shape contraction upon administration of cytochalasin D, which is captured by a decreasing impedance, but does not affect QCM parameters. Cell mechanics under blebbistatin triggered, myosin II-ATPase activity repression,[35] exhibits a slight decrease in cell rigidity combined with decreasing actin cytoskeleton stiffness as measured by microrheology, AFM and optical tweezers.[51-53] We found decreased QCM dissipation levels indicative of cell softening in good agreement with previous studies. Especially for FaDu cells, prolonged cell extensions are found, (possible due to the larger intercellular space) accompanied by a slight increase in mass and a significant impedance increase. Therefore, myosin II inhibition is assumed to be responsible, as missing myosin involvement in actin-severing of filopodia may lead to their growth.[7]

Microtubules do aggregate, are stabilized and prolonged under taxol treatment and form asters and fibers/bundles in fluorescence micrographs, whereas actin remains unaffected, as originally described.[54] Minor desorption of FaDu and MDCKII cells was monitored at IC_{50} concentrations, probably contributing to reduced mass and dissipation levels of D-QCM, which were also found by Marx *et al.*[27] Though elasticity and viscosity were often described to be only slightly changed,[22, 50, 55] we do not confirm this trend for IC_{50} concentrations of taxol, as dissipation decreases significantly, especially for MDCKII cells. We find, however, an increased amount of apoptotic cells in both cell lines coinciding with an impedance breakdown, especially for FaDu cells. Recently, this was also observed for impedance and TER by Arndt *et al.*[56] for cycloheximid-triggered apoptosis. Nocodazol and colchicin, a synthetic benzimidazol and a plant alkaloid, both destabilize microtubules by binding the dimeric subunit and elicit a secondary, regulatory effect on overall migration.[34, 57, 58] We found colchicin to reduce mass and dissipation for MDCKII cells and slightly increase them for FaDu cells, whereas a decrease

of IZI_{norm} was found. The latter may be attributed to tubulin aggregates and reorganized peripheral actin skeleton as well as, especially for FaDu cells, to a reduced cell spreading. Micropipette aspiration experiments revealed parallels between neutrophils and FaDu cells under colchicin treatment: an increase of actin polymerization, an augment in cell rigidity and viscosity elevated by 50% have been described before.[59] Elasticity was, however, not found to be altered on colchicin treated fibroblasts.,[50] Nocodazol provokes a reduction of MDCKII impedance values by 40-60 % and a mass increase in our study. This can be explained by increased cell spreading or induction of peripheral actin-polymerization, which is controversially discussed in QCM and AFM literature.[21, 27, 60]

For MDCKII cells treated with resveratrol and cis-platin, at least one universal characteristic of apoptosis, i.e. loss of cell volume and/or cell shrinkage[61] can be monitored with QCM and ECIS. For FaDu cells, an antioxidant, viability promoting effect of resveratrol [62] may obscure cell shrinkage, as impedance stays unaffected. In the first 24 hour interval only few apoptotic cells are found in micrographs: ECIS values for resveratrol concentrations above IC_{50} even slightly increased complex impedance. Cis-platin produced a strong increase in cellular impedance and TER of FaDu cells for the first 20 hours, before entering an opposing trend for the following 48 hours. Such two-phase-effects were also found in literature for low-dose treatment.[25] Time needed for transport into the nucleus and Intercalation into the DNA may account for this time shift.[63]

Taking a closer look at the biological fluctuations recorded with our combined biosensors approach, the following general observations can be made. The origins of the noise are mainly accounted to microtubuli-depolymerization and actin-based polymerization. We believe that the first is accounted to the dynamic instability of the microtubuli, while the latter may either be directly correlated to polymer stability or to indirect regulatory effects (exhibited by microtubules and Rho GTPases). Overall, noise parameters display higher sensitivity than static viscoelastic and impedimetric parameters or the MTS-tests, as values frequently undercut 50%. While the actin-stabilizing phalloidin shows almost no noise decrease (though it reduces viscosity significantly), cytochalasin-D efficiently reduces detected noise as a result of actin-depolymerization. Stabilizing microtubules by taxol also reduces noise levels found, whereas we find an increase of fluctuations with blebbistatin or colchicin.

Preponderance of studies ascribes this effect to deregulated actin-severing and 50% reduced retrograde flow in lamellipodia and filopodia.[7, 9] Nocodazol and colchicin interfere with cell polarization through peripheral CDC42 GTPase activation[64] and control actin-dynamics through microtubuli polymerization feedback loops. This induces Rac-(more efficiently by colchicin) [65, 66] or rhoA [67] GTPase activation and therefore either lamellipodia protrusions or integrin adhesion/actomyosin contractions. Therefore, while blebbistatin inhibits the actomyosin contractions directly through the motor protein, colchicin takes influence in all three GTPase signaling pathways. This more complex effect of colchicin is also displayed in an increased noise level as compared to blebbistatin and nocodazol and produces the highest fluctuation amplitude and long term correlations found in this study. It has to be mentioned that taxol does not influence lamellipodia and filopodia formation and only slightly reduces RAC1-GTPase activity in comparison to colchicin, excluding a similar explanation for that toxin.[34, 68] As far as cancer drugs are concerned, cis-platin induced apoptosis strongly reduces long term correlations in biological noise of cancer cells by F-QCM parameters but only slightly ECIS shape fluctuations. Instead, ECIS is more sensitive to the resveratrol effects of apoptosis, whereby the Rho GTPase influencing ability may enhance QCM parameters of FaDu cells. Furthermore, we found that ECIS reacts less sensitive to microtubule agents than to actin manipulating substances, as cell shape and cell-cell adhesion detected with impedance spectroscopy are determined mainly by the peripheral actin network. F-QCM derived parameters are, however, sensitive to changes of both cytoskeletal polymers since F-QCM is susceptible to faint changes in viscoelasticity that is affected by microtubules as well as F-actin. Although it is an open question in literature whether lateral migration and cell crawling rely more on cortical actin, actin, NMII dynamics or microtubules treadmiling[9, 68-72] our results imply actin polymerization and microtubule depolymerization to be of equal relevance for vertical, epithelia cell motility.

Regional metastasis formation in head and neck squamous cell carcinoma may decreases the patient`s survival to merely 50 %.[73, 74] Therefore, besides directed disruption of cytoskeleton dynamics or force generation, our aim was to detect cancer cell specific migration modes with our setup. The comparison of MDCKII cells to the cancer line FaDu on MTS basis revealed generally higher IC_{50} values for all drugs except

for nocodazol and resveratrol administration. The latter may be possible due to cancerous mutations responsible for drug resistance. We found however, that nocodazol (as all microtubuli agents) elicited neither influence on the viscoelasticity of FaDu cells nor on ΔIZI_{norm} and $\Delta R_{b,\ norm}$, whereas it clearly reduced all fluctuation parameters. Resveratrol, colchicin and blebbistatin even increased viscoelastic fluctuations of FaDu cells and reduced impedimetric fluctuations. Resveratrol, known to act on all three stages (initiation, promotion, progression)[40] of tumor growth, showed, however, no effect on FaDu cells` viscoelasticity or impedance. Cis-platin reduced mainly long time correlations of these cancer cells` viscoelastic fluctuations. Intriguingly, though literature describes more microtubuli-binding cancer drugs[34], not only the small molecule inhibitor taxol, but also cytochalasin-D was more efficient in reducing FaDu micromotion than equitoxic concentration of cis-platin or resveratrol. Our findings are in agreement with literature, as taxol was found to be 100 times more potent than cis-platin.[75] Cytochalasin D, which strongly reduced micromotion, was also found to inhibit cancer cell migration in wound scratch assays.[76]

Recently introduced small molecule inhibitors act also against regulating/assessing proteins or signal transduction besides of the force generating machinery, i.e. monastrol, wiskostatin, PBP10, proapoptotic or antiangiogenic drugs.[34, 77-84] In future studies, these second or third generation chemotherapeutics and cytoskeleton agents should be applied to further validate the sensitivity of ECIS/F-QCM noise analysis.

4.5 CONCLUSION

In the present study on cell migration, we were able to identify actin-polymerization as well as microtubule depolymerization to be the main contributors of viscoelastic or impedimetric fluctuations as detected by quartz crystal microbalances (F-QCM) or electrical cell substrate impedance sensors (ECIS). Besides direct targeting of cytoskeletal biopolymers, interference with motor protein myosin II could be detected as well as indirect activation of Rho GTPase by colchicin. Cis-platin, taxol and cytochalasin-D proved to be sufficient powerful to reduce micromotility of human head and neck tumour cell line FaDu, whereas resveratrol did not affect biological noise produced by cancerous cells. In general, as impedance spectroscopy relies on current flowing underneath or in between adherent cells, it is more sensitive to actin dynamics powering cell shape fluctuations. In surplus, the oscillating, acoustic quartz biosensor is able to detect *in vivo* microtubule-based stochastic instabilities occurring in the cytosol by the penetrating standing wave.

4.6 REFERENCES AND NOTES

1. Woodhouse, E. C.; Chuaqui, R. F.; Liotta, L. A., General mechanisms of metastasis. *Cancer* **1997,** 80, (8), 1529-1537.

2. Mareel, M.; Leroy, A., Clinical, cellular, and molecular aspects of cancer invasion. *Physiological Reviews* **2003,** 83, (2), 337-376.

3. Pollard, T. D., Regulation of actin filament assembly by Arp2/3 complex and formins. *Annual Review of Biophysics and Biomolecular Structure* **2007,** 36, 451-477.

4. Le Clainche, C.; Carlier, M. F., Regulation of actin assembly associated with protrusion and adhesion in cell migration. *Physiological Reviews* **2008,** 88, (2), 489-513.

5. Bray, Cell movements. **2000**.

6. Ponti, A.; Machacek, M.; Gupton, S. L.; Waterman-Storer, C. M.; Danuser, G., Two distinct actin networks drive the protrusion of migrating cells. *Science* **2004,** 305, (5691), 1782-1786.

7. Medeiros, N. A.; Burnette, D. T.; Forscher, P., Myosin II functions in actin-bundle turnover in neuronal growth cones. *Nature Cell Biology* **2006,** 8, (3), 215-226.

8. Etienne-Manneville, S., Actin and microtubules in cell motility: Which one is in control? *Traffic* **2004,** 5, (7), 470-477.

9. Burnette, D. T.; Schaefer, A. W.; Ji, L.; Danuser, G.; Forscher, P., Filopodial actin bundles are not necessary for microtubule advance into the peripheral domain of Aplysia neuronal growth cones. *Nature Cell Biology* **2007,** 9, (12), 1360-U39.

10. Herrmann, H.; Aebi, U., Intermediate filaments and their associates: multi-talented structural elements specifying cytoarchitecture and cytodynamics. *Current Opinion in Cell Biology* **2000,** 12, (1), 79-90.

11. Ridley, Cell motility. **2004**.

12. Etienne-Manneville, S.; Hall, A., Rho GTPases in cell biology. *Nature* **2002,** 420, (6916), 629-635.

13. Schulz, W. A., Molecular biology of human cancers. **2007**.

14. Rangan, S. R. S., New Human Cell Line (Fadu) from a Hypopharyngeal Carcinoma. *Cancer* **1972,** 29, (1), 117-&.

15. Giaever, I.; Keese, C. R., Monitoring Fibroblast Behavior in Tissue-Culture with an Applied Electric-Field. *Proceedings of the National Academy of Sciences of the United States of America-Biological Sciences* **1984,** 81, (12), 3761-3764.

16. Gryte, D. M.; Ward, M. D.; Hu, W. S., Real-Time Measurement of Anchorage-Dependent Cell-Adhesion Using a Quartz Crystal Microbalance. *Biotechnology Progress* **1993,** 9, (1), 105-108.

17. Redepenning, J.; Schlesinger, T. K.; Mechalke, E. J.; Puleo, D. A.; Bizios, R., Osteoblast Attachment Monitored with a Quartz-Crystal Microbalance. *Analytical Chemistry* **1993,** 65, (23), 3378-3381.

18. Wegener, J.; Janshoff, A.; Steinem, C., The quartz crystal microbalance as a novel means to study cell-substrate interactions in situ. *Cell Biochemistry and Biophysics* **2001,** 34, (1), 121-151.

19. Luong, J. H. T., An emerging impedance sensor based on cell-protein interactions: Applications in cell biology and analytical biochemistry. *Analytical Letters* **2003,** 36, (15), 3147-3164.

20.   Cooper, M. A.; Singleton, V. T., A survey of the 2001 to 2005 quartz crystal microbalance biosensor literature: applications of acoustic physics to the analysis of biomolecular interactions. *Journal of Molecular Recognition* **2007,** 20, (3), 154-184.

21.   Marx, K. A.; Zhou, T. A.; Montrone, A.; Schulze, H.; Braunhut, S. J., A quartz crystal microbalance cell biosensor: detection of microtubule alterations in living cells at nM nocodazole concentrations. *Biosensors & Bioelectronics* **2001,** 16, (9-12), 773-782.

22.   Marxer, C. G.; Coen, M. C.; Bissig, H.; Greber, U. F.; Schlapbach, L., Simultaneous measurement of the maximum oscillation amplitude and the transient decay time constant of the QCM reveals stiffness changes of the adlayer. *Analytical and Bioanalytical Chemistry* **2003,** 377, (3), 570-577.

23.   Wegener, J.; Seebach, J.; Janshoff, A.; Galla, H. J., Analysis of the composite response of shear wave resonators to the attachment of mammalian cells. *Biophysical Journal* **2000,** 78, (6), 2821-2833.

24.   Ceriotti, L.; Ponti, J.; Broggi, F.; Kob, A.; Drechsler, S.; Thedinga, E.; Colpo, P.; Sabbioni, E.; Ehret, R.; Rossi, F., Real-time assessment of cytotoxicity by impedance measurement on a 96-well plate. *Sensors and Actuators B-Chemical* **2007,** 123, (2), 769-778.

25.   Liu, Q. J.; Yu, J. J.; Xiao, L.; Tang, J. C. O.; Zhang, Y.; Wang, P.; Yang, M., Impedance studies of bio-behavior and chemosensitivity of cancer cells by micro-electrode arrays. *Biosensors & Bioelectronics* **2009,** 24, (5), 1305-1310.

26.   Woolley, D. E.; Tetlow, L. C.; Adlam, D. J.; Gearey, D.; Eden, R. D.; Ward, T. H.; Allen, T. D., Electrochemical monitoring of anticancer compounds on the human ovarian carcinoma cell line A2780 and its adriamycin- and cis-platin-resistant variants. *Experimental Cell Research* **2002,** 273, (1), 65-72.

27.   Marx, K. A.; Zhou, T.; Montrone, A.; McIntosh, D.; Braunhut, S. J., A comparative study of the cytoskeleton binding drugs nocodazole and taxol with a mammalian cell quartz crystal microbalance biosensor: Different dynamic responses and energy dissipation effects. *Analytical Biochemistry* **2007,** 361, (1), 77-92.

28.   Wei, X. L.; Mo, Z. H.; Li, B.; Wei, J. M., Disruption of HepG2 cell adhesion by gold nanoparticle and Paclitaxel disclosed by in situ QCM measurement. *Colloids and Surfaces B-Biointerfaces* **2007,** 59, (1), 100-104.

29.   Braunhut, S. J.; McIntosh, D.; Vorotnikova, E.; Zhou, T.; Marx, K. A., Detection of apoptosis and drug resistance of human breast cancer cells to taxane treatments using quartz crystal microbalance biosensor technology. *Assay and Drug Development Technologies* **2005,** 3, (1), 77-88.

30.   Lovelady, D. C.; Friedman, J.; Patel, S.; Rabson, D. A.; Lo, C. M., Detecting effects of low levels of cytochalasin B in 3T3 fibroblast cultures by analysis of electrical noise obtained from cellular micromotion. *Biosensors & Bioelectronics* **2009,** 24, (7), 2250-2254.

31.   Opp, D.; Wafula, B.; Lim, J.; Huang, E.; Lo, J. C.; Lo, C. M., Use of electric cell-substrate impedance sensing to assess in vitro cytotoxicity. *Biosensors & Bioelectronics* **2009,** 24, (8), 2625-2629.

32.   Tarantola, M., Dynamics of human cancer cell lines monitored by electrical and acoustic noise analysis. **2009**.

33.   Tarantola, M.; Schneider, D.; Sunnick, E.; Adam, H.; Pierrat, S.; Rosman, C.; Breus, V.; Sonnichsen, C.; Basche, T.; Wegener, J.; Janshoff, A., Cytotoxicity of Metal and Semiconductor Nanoparticles Indicated by Cellular Micromotility. *Acs Nano* **2009,** 3, (1), 213-222.

34.   Fenteany, G.; Zhu, S. T., Small-molecule inhibitors of actin dynamics and cell motility. *Current Topics in Medicinal Chemistry* **2003,** 3, (6), 593-616.

35.   Kovacs, M.; Toth, J.; Hetenyi, C.; Malnasi-Csizmadia, A.; Sellers, J. R., Mechanism of blebbistatin inhibition of myosin II. *Journal of Biological Chemistry* **2004,** 279, (34), 35557-35563.

36.   Limouze, J.; Straight, A. F.; Mitchison, T.; Sellers, J. E., Specificity of blebbistatin, an inhibitor of myosin II. *Journal of Muscle Research and Cell Motility* **2004,** 25, (4-5), 337-341.

37.   Straight, A. F.; Cheung, A.; Limouze, J.; Chen, I.; Westwood, N. J.; Sellers, J. R.; Mitchison, T. J., Dissecting temporal and spatial control of cytokinesis with a myosin II inhibitor. *Science* **2003,** 299, (5613), 1743-1747.

38.   Peterson, J. R.; Mitchison, T. J., Small molecules, big impact: A history of chemical inhibitors and the cytoskeleton. *Chemistry & Biology* **2002,** 9, (12), 1275-1285.

39.   Aggarwal, B. B.; Bhardwaj, A.; Aggarwal, R. S.; Seeram, N. P.; Shishodia, S.; Takada, Y., Role of resveratrol in prevention and therapy of cancer: Preclinical and clinical studies. *Anticancer Research* **2004,** 24, (5A), 2783-2840.

40.   Jang, M. S.; Cai, E. N.; Udeani, G. O.; Slowing, K. V.; Thomas, C. F.; Beecher, C. W. W.; Fong, H. H. S.; Farnsworth, N. R.; Kinghorn, A. D.; Mehta, R. G.; Moon, R. C.; Pezzuto, J. M., Cancer chemopreventive activity of resveratrol, a natural product derived from grapes. *Science* **1997,** 275, (5297), 218-220.

41.   Kelland, L., The resurgence of platinum-based cancer chemotherapy. *Nature Reviews Cancer* **2007,** 7, (8), 573-584.

42.   Wegener, J.; Janshoff, A.; Galla, H. J., Cell adhesion monitoring using a quartz crystal microbalance: comparative analysis of different mammalian cell lines. *European Biophysics Journal with Biophysics Letters* **1998,** 28, (1), 26-37.

43.   Sapper, A.; Wegener, J.; Janshoff, A., Cell motility probed by noise analysis of thickness shear mode resonators. *Analytical Chemistry* **2006,** 78, (14), 5184-5191.

44.   Tarantola, M., Shape-dependent toxicity of gold-nanoparticles investigated by impedance and acoustic biosensors. **2010**.

45.   Giaever, I.; Keese, C. R., Use of Electric-Fields to Monitor the Dynamic Aspect of Cell Behavior in Tissue-Culture. *Ieee Transactions on Biomedical Engineering* **1986,** 33, (2), 242-247.

46.   Giaever, I.; Keese, C. R., Micromotion of Mammalian-Cells Measured Electrically. *Proceedings of the National Academy of Sciences of the United States of America* **1991,** 88, (17), 7896-7900.

47.   Wieland, T.; Wieland, O., Chemistry and Toxicology of the Toxins of Amanita-Phalloides. *Pharmacological Reviews* **1959,** 11, (1), 87-107.

48.   Lengsfel.Am; Low, I.; Wieland, T.; Dancker, P.; Hasselba.W, Interaction of Phalloidin with Actin. *Proceedings of the National Academy of Sciences of the United States of America* **1974,** 71, (7), 2803-2807.

49.   Cooper, J. A., Effects of Cytochalasin and Phalloidin on Actin. *Journal of Cell Biology* **1987,** 105, (4), 1473-1478.

50. Rotsch, C.; Radmacher, M., Drug-induced changes of cytoskeletal structure and mechanics in fibroblasts: An atomic force microscopy study. *Biophysical Journal* **2000,** 78, (1), 520-535.

51. Gabriele, S.; Benoliel, A. M.; Bongrand, P.; Theodoly, O., Microfluidic Investigation Reveals Distinct Roles for Actin Cytoskeleton and Myosin II Activity in Capillary Leukocyte Trafficking. *Biophysical Journal* **2009,** 96, (10), 4308-4318.

52. Martens, J. C.; Radmacher, M., Softening of the actin cytoskeleton by inhibition of myosin II. *Pflugers Archiv-European Journal of Physiology* **2008,** 456, (1), 95-100.

53. Balland, M.; Richert, A.; Gallet, F., The dissipative contribution of myosin II in the cytoskeleton dynamics of myoblasts. *European Biophysics Journal with Biophysics Letters* **2005,** 34, (3), 255-261.

54. Schiff, P. B.; Fant, J.; Horwitz, S. B., Promotion of Microtubule Assembly Invitro by Taxol. *Nature* **1979,** 277, (5698), 665-667.

55. Wang, N., Mechanical interactions among cytoskeletal filaments. *Hypertension* **1998,** 32, (1), 162-165.

56. Arndt, S.; Seebach, J.; Psathaki, K.; Galla, H. J.; Wegener, J., Bioelectrical impedance assay to monitor changes in cell shape during apoptosis. *Biosensors & Bioelectronics* **2004,** 19, (6), 583-594.

57. Shelansk.Ml; Taylor, E. W., Isolation of a Protein Subunit from Microtubules. *Journal of Cell Biology* **1967,** 34, (2), 549-&.

58. Hoebeke, J.; Vannijen, G.; Debrabander, M., Interaction of Oncodazole (R 17934), New Anti-Tumoral Drug, with Rat-Brain Tubulin. *Biochemical and Biophysical Research Communications* **1976,** 69, (2), 319-324.

59. Tsai, M. A.; Waugh, R. E.; Keng, P. C., Passive mechanical behavior of human neutrophils: Effects of colchicine and paclitaxel. *Biophysical Journal* **1998,** 74, (6), 3282-3291.

60. Pesen, D.; Hoh, J. H., Micromechanical architecture of the endothelial cell cortex. *Biophysical Journal* **2005,** 88, (1), 670-679.

61. Bortner, C. D.; Cidlowski, J. A., The role of apoptotic volume decrease and ionic homeostasis in the activation and repression of apoptosis. *Pflugers Archiv-European Journal of Physiology* **2004,** 448, (3), 313-318.

62. Goswami, S. K.; Das, D. K., Resveratrol and chemoprevention. *Cancer Letters* **2009,** 284, (1), 1-6.

63. Siddik, Z. H., Cis-platin: mode of cytotoxic action and molecular basis of resistance. *Oncogene* **2003,** 22, (47), 7265-7279.

64. Nalbant, P.; Hodgson, L.; Kraynov, V.; Toutchkine, A.; Hahn, K. M., Activation of endogenous Cdc42 visualized in living cells. *Science* **2004,** 305, (5690), 1615-1619.

65. Waterman-Storer, C. M.; Worthylake, R. A.; Liu, B. P.; Burridge, K.; Salmon, E. D., Microtubule growth activates Rac1 to promote lamellipodial profusion in fibroblasts. *Nature Cell Biology* **1999,** 1, (1), 45-50.

66. Best, A.; Ahmed, S.; Kozma, R.; Lim, L., The Ras-related GTPase Rac1 binds tubulin. *Journal of Biological Chemistry* **1996,** 271, (7), 3756-3762.

67. Ren, X. D.; Kiosses, W. B.; Schwartz, M. A., Regulation of the small GTP-binding protein Rho by cell adhesion and the cytoskeleton. *Embo Journal* **1999,** 18, (3), 578-585.

68. Bijman, M. N. A.; van Berkel, M. P. A.; Amerongen, G. P. V.; Bouen, E., Interference with actin dynamics is superior to disturbance of microtubule function in the inhibition of human ovarian cancer cell motility. *Biochemical Pharmacology* **2008,** 76, (6), 707-716.

69. Wittmann, T.; Waterman-Storer, C. M., Cell motility: can Rho GTPases and microtubules point the way? *Journal of Cell Science* **2001,** 114, (21), 3795-3803.

70. Ridley, A. J.; Schwartz, M. A.; Burridge, K.; Firtel, R. A.; Ginsberg, M. H.; Borisy, G.; Parsons, J. T.; Horwitz, A. R., Cell migration: Integrating signals from front to back. *Science* **2003,** 302, (5651), 1704-1709.

71. Vicente-Manzanares, M.; Koach, M. A.; Whitmore, L.; Lamers, M. L.; Horwitz, A. F., Segregation and activation of myosin IIB creates a rear in migrating cells. *Journal of Cell Biology* **2008,** 183, (3), 543-554.

72. Irimia, D.; Toner, M., Spontaneous migration of cancer cells under conditions of mechanical confinement. *Integrative Biology* **2009,** 1, (8-9), 506-512.

73. Myers, J. N.; Greenberg, J. S.; Mo, V.; Roberts, D., Extracapsular spread - A significant predictor of treatment failure in patients with squamous cell carcinoma of the tongue. *Cancer* **2001,** 92, (12), 3030-3036.

74. Rosenthal, E. L.; Matrisian, L. M., Matrix metalloproteases in head and neck cancer. *Head and Neck-Journal for the Sciences and Specialties of the Head and Neck* **2006,** 28, (7), 639-648.

75. Fuller, T. L.; Canada, R. G., Enhancement of cis-platin cytotoxicity by terbium in cis-platin-resistant MDA/CH human breast cancer cells. *Cancer Chemotherapy and Pharmacology* **1999,** 44, (3), 249-252.

76. Hayot, C.; Debeir, O.; Van Ham, P.; Van Damme, M.; Kiss, R.; Decaestecker, C., Characterization of the activities of actin-affecting drugs on tumor cell migration. *Toxicology and Applied Pharmacology* **2006,** 211, (1), 30-40.

77. Mayer, T. U.; Kapoor, T. M.; Haggarty, S. J.; King, R. W.; Schreiber, S. L.; Mitchison, T. J., Small molecule inhibitor of mitotic spindle bipolarity identified in a phenotype-based screen. *Science* **1999,** 286, (5441), 971-974.

78. Usui, T., Actin- and microtubule-targeting bioprobes: Their binding sites and inhibitory mechanisms. *Bioscience Biotechnology and Biochemistry* **2007,** 71, (2), 300-308.

79. Wakeling, A. E., Inhibitors of growth factor signalling. *Endocrine-Related Cancer* **2005,** 12, S183-S187.

80. Marel, A. K.; Lizard, G.; Izard, J. C.; Latruffe, N.; Delmas, D., Inhibitory effects of trans-resveratrol analogs molecules on the proliferation and the cell cycle progression of human colon tumoral cells. *Molecular Nutrition & Food Research* **2008,** 52, (5), 538-548.

81. Singh, N.; Nigam, M.; Ranjan, V.; Sharma, R.; Balapure, A. K.; Rath, S. K., Caspase Mediated Enhanced Apoptotic Action of Cyclophosphamide- and Resveratrol-Treated MCF-7 Cells. *Journal of Pharmacological Sciences* **2009,** 109, (4), 473-485.

82. Wesierska-Gadek, J.; Kramer, M. P.; Maurer, M., Resveratrol modulates roscovitine-mediated cell cycle arrest of human MCF-7 breast cancer cells. *Food and Chemical Toxicology* **2008,** 46, (4), 1327-1333.

83. Eccles, S. A., Targeting key steps in metastatic tumour progression. *Current Opinion in Genetics & Development* **2005,** 15, (1), 77-86.

84. Ashkenazi, A., Directing cancer cells to self-destruct with pro-apoptotic receptor agonists. *Nature Reviews Drug Discovery* **2008,** 7, (12), 1001-1012.

Cytotoxicity of metal and semiconductor nanoparticles indicated by cellular micromotility
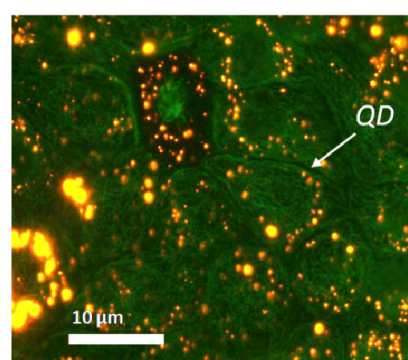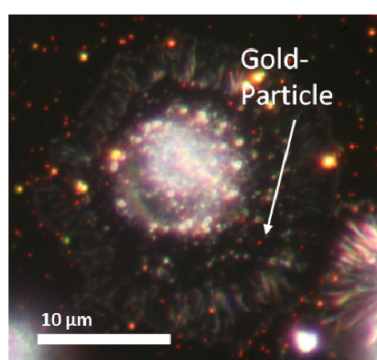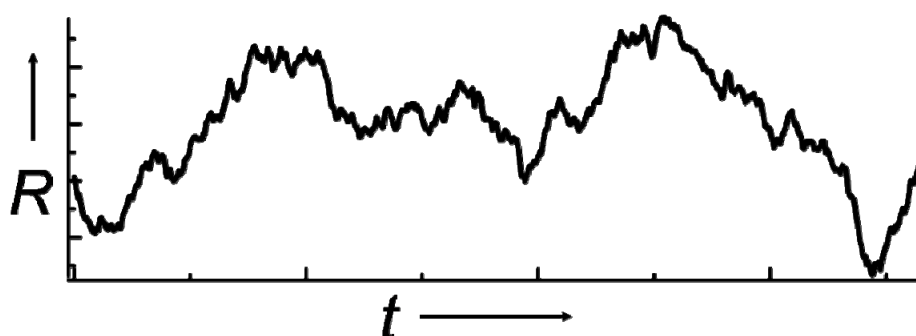
ABSTRACT

In the growing field of nanotechnology, there is an urgent need to sensitively determine the toxicity of nanoparticles, since many technical and medical applications are based on controlled exposure to particles, i.e. as contrast agents or for drug delivery. Before the in vivo implementation, in vitro cell experiments are required to achieve a detailed knowledge of toxicity and biodegradation as a function of the nanoparticles' physical and chemical properties. In this study, we show that the micromotility of animal cells as monitored by electrical cell-substrate impedance analysis (ECIS) is highly suitable to quantify in vitro cytotoxicity of semiconductor quantum dots and gold nanorods. The method is validated by conventional cytotoxicity testing and accompanied by fluorescence and dark-field microscopy to visualize changes in the cytoskeleton integrity and to determine the location of the particles within the cell.

5.1 INTRODUCTION

In the last years, nanoscale objects with dimensions in the range of 1 to 100 nm became ubiquitous and these nanomaterials are released from a variety of sources such as common industrial or consumer products. As a consequence, the environment is exposed to particles of variable origin cast in the atmosphere, water, and soil. Human exposure to nanomaterials occurs most likely during manufacturing processes, but inhalation of nanomaterials released to the atmosphere and ingestion of water or food may also be possible. [1] Dermal exposure from various sources such as sunscreen might also be likely.[2] These circumstances call for effective and reliable screening assays capable of reporting the response of cells to the exposure to nanoscale particles (NPs). Conventional cytotoxicity assays address the cellular metabolic activity like the 3-(4,5-dimethylthiazol-2-yl)-2,5 diphenyl tetrazolium bromide test (MTT), the integrity of the cellular plasma membranes (e.g. lactate-dehydrogenase (LDH) release assay) or the activity of intracellular housekeeping enzymes (Calcein acetoxymethyl ester). These tests are time consuming, invasive and crude as far as the amount of information is concerned. Moreover, many colorimetric or fluorescence-based approaches to quantify cytotoxicity are impaired by the presence of the nanoparticles in the test tube and their peculiar optical properties (e.g. autofluorescence, fluorescence quenching, light scattering). Hence, alternative label-free and – for the purpose of dynamic toxicity screening – non-invasive methods are required to meet the growing demand of vast and versatile cytotoxicity assays[3] that permit a quick assessment of the impact of nanomaterials on various cell types.

In this study, label-free and non-invasive AC impedance measurements have been used to quantify the impact of nanoparticles on the viability of adherent cells. The general approach to monitor adherent cells by impedance measurements is referred to as electric cell-substrate impedance sensing (ECIS) and it has been first described by Giaever and Keese.[4] In the ECIS setup, the cells are grown on planar gold-film electrodes that are deposited on the surface of a cell culture vessel. The impedance of these electrodes increases when animal cells adhere and spread on the surface of these electrodes until a confluent cell monolayer is formed (cp. *figure* 5.1). In confluent cell layers, the measured impedance is not a constant value but changes whenever the

shape, height or viscoelasticity of the cells or the cell-cell junctions change as the dimensions of the current pathways around the cells bodies are altered (see *figure* 5.1). As cell shape and the cell-cell junctions determine the impedance readout, ECIS has found broad range of applications in biomedical research from simple measurements of cell adhesion to studies addressing the invasion of metastatic cancer cells *in vitro*. It has also been successfully applied to monitor cytotoxicity of various chemical or biological challenges. [5-8] In all studies, ECIS results were reported to be in closest agreement with classical cytotoxicity approaches as mentioned above, but provide time-resolved information without the need to label the cells.

One special mode of ECIS measurements records the complex impedance of the cell-covered electrodes at one fixed AC frequency with very high time resolution (< 1 sec). The observed fluctuation of the signal mirrors the fluctuations of the 3-dimensional shape of the cells on the electrode surface. These fluctuations in cell shape have been termed *micromotion*. Micromotion is completely and irreversibly suppressed when the cells are exposed to formalin [9] which is well-known to cross-link all cellular proteins. By comparing the degree of micromotion as a function of temperature or glucose-supply, Lo *et al.* were able to correlate micromotion to the metabolic activity of the cells and their overall viability.[10] Recently, ECIS-based micromotion measurements were evaluated as a possible indicator to distinguish cancerous from non-cancerous cell lines due to their different motility.[11]

The present work reports on repeated micromotion measurements on epithelial MDCK (type II) cells, which are continuously exposed to increasing amounts of colloidal semiconductor quantum dots (QD) and gold nanorods. MDCK cells are an established and well-characterized model system for barrier forming epithelial cell lines. Micromotion results were validated by a conventional MTS cytotoxicity assays and supported by microscopic studies addressing cytoskeletal integrity after NP exposure. Two kinds of particles have been studied: gold nanorods with a mean size of size of 17 by 39 nanometers and CdSe/CdS/ZnCdS/ZnS multishell QDs with a diameter of 5-6 nanometers. Rod-shaped gold nanoparticles show extremely high polarizability at the plasmon frequency and are thus useful as contrast agents in biomedical imaging and as photothermal transducers for localized hyperthermia therapies. In the latter, the idea is to bind them specifically to designated target cells by appropriate surface modification

and subsequently to heat them using their strong light absorption in the near-infrared.[12] Semiconductor QDs are well suited for fluorescent labelling and single particle tracking. In fact, due to their photostability QD are already frequently used as biomarkers *in vitro* and *in vivo*. [13, 14]
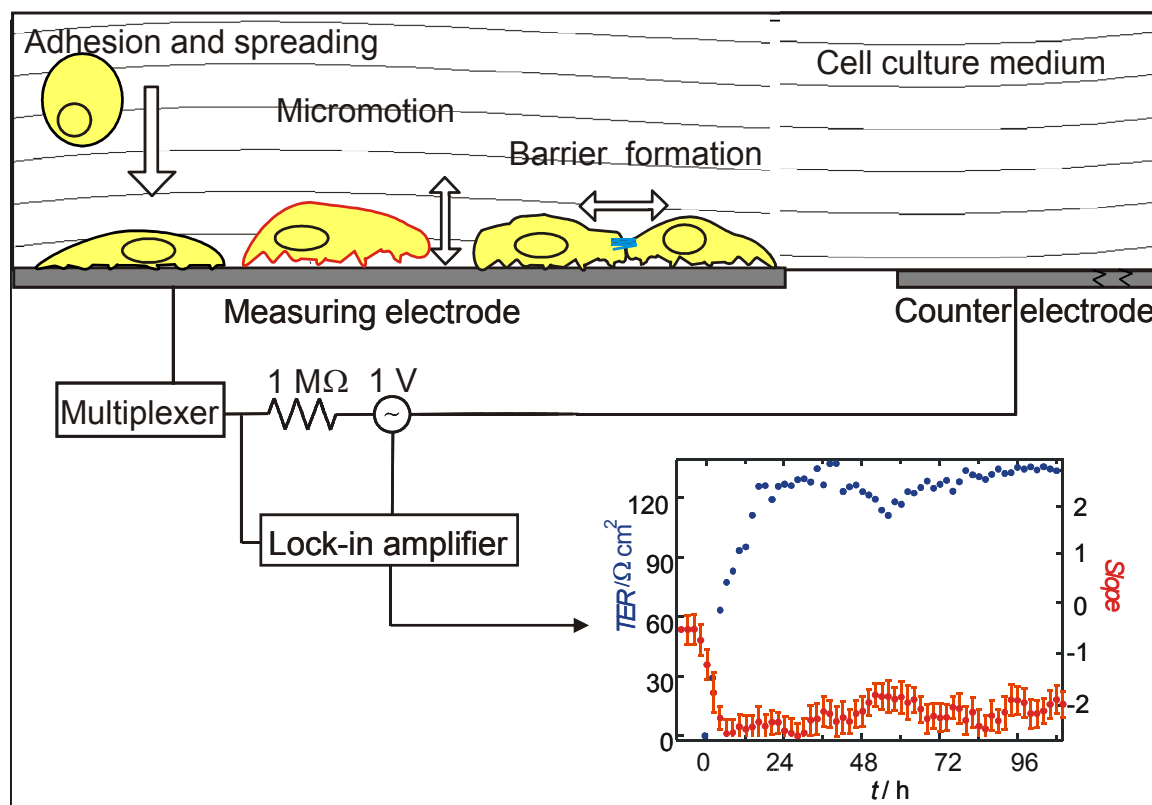
Figure 5.1 Experimental setup (based on [9]): The graph shows both the transepithelial restistance TER recorded between 10 and 10^4 Hz (●) and the slope (●) of the Fourier analysis of micromotion recorded at 4 kHz as a function of time. Cell seeding was at 0 h.

5.2 EXPERIMENTAL SECTION

5.2.1 ECIS-based micromotion experiments and noise analysis

A home-made ECIS-system was employed, consisting of a lock-in amplifier (SR830, SRS, Inc., Sunnyvale, CA) with an internal oscillator, a multiplexer with analogue switches for automatic, consecutive addressing of individual wells on the electrode array and a PC for experiment control and data storage. The ECIS electrode arrays (type 8W1E) purchased from Applied Biophysics (Troy, USA) consists of eight separate wells, each holding one gold micro-electrode of 250 µm diameter and a large (7×46 mm^2) counter electrode. In our ECIS setup, a 1 V AC signal is applied to the system through a 1 MΩ series resistor and the in- and out-of-phase voltages across the electrodes are recorded at 4 kHz at a sampling rate of 1 Hz. For micromotion recordings, the in-phase voltage which is directly proportional to the real part of the complex impedance was used for further analysis as it provides the most sensitive readout. The applied constant current of 1 µA amplitude is non-invasive to the cell layer.

Besides micromotion recordings at one fixed frequency, we also monitored changes in the barrier function of the adherent MDCK cell layer when exposed to the NPs. Barrier function can be most easily expressed by means of the so-called transepithelial electrical resistance (TER) which is a direct measure for the ionic permeability of the cell-cell junctions. TER values were extracted from frequency resolved impedance readings (10-10^4 Hz) and subsequent equivalent circuit modelling according to the procedures described by Wegener *et al.*.[15] In contrast to the most commonly applied approach to determine TER values, there is no need to grow the cells on permeable filter substrates for the measurement. Micromotion and TER readings can be performed on one and the same cell layer with just different ECIS measurement modes.

As suggested by Giaever and co-workers, micromotion data, which is essentially a time series of resistance fluctuations, was subject to Fourier transformation after subtracting a linear trend (*figure* 5.2 A).[32] A linear fit of the low frequency part of the power density spectra provided slopes from -2,1 to -2,7 s^{-2} for living cells (*figure* 5.2 B). Time courses of the slope representing micromotion activity, and the TER are recorded

as a function of particle type and concentration, exemplary depicted for $1.38 \cdot 10^{11}$ p./ml gold rods and $7.5 \cdot 10^{13}$ p./ml QDs (*figure* 5.2 C and D).

5.2.2 Cell culture conditions and measurement procedures

MDCKII cells are maintained in Earle's minimum essential medium supplemented with 4 mM glutamine, 100 µg/mL of both penicillin and streptomycin (purchased by Biochrom, Berlin, Germany), 10% (v/v) fetal calf serum (PAA Laboratories GmbH, Cölbe, Germany) and stored in incubators (HERA cell 150, Heraeus, Germany) with a 5 % CO_2 atmosphere. Cells are subcultured weekly after reaching confluence by washing with PBS, followed by trypsinization and centrifugation at 110 g. Counting is carried out using a Neubauer-chamber and viability is determined using trypan blue exclusion. For the measurements, cells are seeded in the 8-well electrode arrays, that had been pre-incubated with HEPES buffered full medium for 2 hours, and are then transferred to an incubator (CO_2Cell, MMM, Germany) set to 37°C and 5% CO_2. The electrode array is connected to the homemade ECIS setup to allow for continuous ECIS recordings. Seeding density was adjusted to $6 \cdot 10^5$ cells per well to reach confluence in seven of the eight wells, the remaining well served as a cell-free reference filled with an equal amount of medium only. Exchange of medium with medium containing nanoparticles or pure Cd^{2+} and cetryl-triammonium-bromide (CTAB) detergent solution is carried out 15-24 hours after seeding.

5.2.3 Nanoparticle preparation

Gold nanorods are prepared using the seed growth method as reported by Nikoobakht et al. and Jana *et al.*.[33, 34] Briefly, seeds are prepared by reducing 10ml of an aqueous solution containing 0.25 mM gold tetrachloride (HAuCl4) in 0.1 M Hexadecyl-trimethyl-ammonium-bromide (CTAB, Sigma) adding 0.6 ml of 0.01 M sodium borohydride (NaBH4). 15 µl of this seeds solution is added to 10 ml of a growth solution consisting of 0.5 mM HAuCl4 and 0.08 mM silver nitrate in 0.1 M CTAB mixed with 70 µl of 0.0788 M ascorbic acid. A strong color change indicates the formation of the gold nanorods after about 20 min, resulting in a stable suspension of CTAB-coated nanorods. In a further step, for stabilisation in various solvents and biofunctionalization, either carboxyl- or amino-terminated PEG-thiol (Iris Biotech) is covalently grafted on the nanorods surface

as described in detail by Pierrat *et al.*.[35] Gold particles are freshly prepared, centrifuged two times and resuspended in HEPES-buffered complete medium to gain stock-solutions of $6.6 \cdot 10^{11}$ p./ml; concentrations from twice the stock to $4.6 \cdot 10^9$ have been used. CdSe/CdS/ZnCdS/ZnS multishell QDs with good quantum yield are prepared as described previously.[36] A mercaptopropionic acid (MPA) coating, needed to change the surface polarity from hydrophobic to hydrophilic, is added as the outermost layer. The aqueous stock solutions of $6 \cdot 10^{14}$ or $6 \cdot 10^{15}$ p./ml at basic pH of 10.8 have been diluted in HEPES-buffered complete medium to the desired concentrations ranging from $6 \cdot 10^{11}$ - $3 \cdot 10^{14}$ p./ml and pH 7.4. In control experiments, $Cd(Ac)_2$ solution and pure CTAB detergent dissolved in culture medium are applied in the concentration range from 0.16 to 31.25 µM for $Cd(Ac)_2$ and 0.625 to 31.25 µM for CTAB.

5.2.4 Cytotoxicity assay, immunochemistry, dark-field and fluorescence microscopy

The MTS-cytotoxicity test has been applied according to the manufacturers` protocol. In brief, cells are grown to a predetermined optimal number of 12000/well in a 96 well-plate and were subsequently incubated with eight different concentrations of nanoparticles or toxins for 24h or 48 h. Washing is carried out three times with PBS[++] and full medium before adding the MTS-agent to remove the NPs or air bubbles that might disturb the photometric assay. Control experiments were carried out using cell-free wells but also fully vital cells that were not exposed to the NPs. The cells are incubated with the tetrazolium educt for 45 minutes. Absorbance is determined subsequently using a 96-well-plate photometer at a wavelength of 490 nm. The colour change is a direct measure of the cell's metabolic activity due to the reduction of MTS-educts to formazan by mitochondrial dehydrogenases. Experiments are performed three times.

Immunostaining and fluorescence microscopy is applied to monitor alterations in the cell cytoskeleton upon nanoparticle exposure. Therefore, MDCKII cells grown to confluence on petridishes are incubated with nanoparticles or pure Cd^{2+} and CTAB-detergent solution for time intervals and cell numbers similar to the ECIS measurements. After washing with PBS, fixation is carried out by immersing the cells into a -20°C cold aceton/methanol mixture (1:1 vol %) for 10 min. Afterward, the cells are washed three times with PBS, unspecific binding sites blocked with FCS, and incubation in staining

solutions carried out according to the manufacturer's recommendation: alexa Fluor 488 phalloidin (invitrogen, Paisley, UK) is used for F-actin staining, Alexa Fluor-conjugated IgG$_1$ anti β-tubulin (BD bioscience, Heidelberg, Germany) from mouse for labelling microtubules, 4'-6-Diamidino-2-phenyindole (DAPI, Sigma-Aldrich, Seelze) for nucleus and DNA labelling, and polyclonal IgG$_1$ mouse antibody (Zymed Gmbh, Munich) followed by Alexa Flour-conjugated goat-anti-mouse IgG$_1$ antibody (BD bioscience, Heidelberg, Germany) is used for staining tight junctions (ZO1-staining). Staining is carried out for 30 min at room temperature, and cells are then washed and examined under an upright Olympus fluorescence microscope (Olympus BX51, 40× water immersion, Germany), equipped with a colour camera (3 MP) and a dark-field condensor. Distribution of gold nanorods is visualized by dark-field microscopy, while semiconductor QDs are located with the fluorescence microscope.

5.3 RESULTS

5.3.1 Micromotion as an indicator for nanoparticle cytotoxicity

Our aim was to elucidate whether the fluctuations in the real part of the impedance caused by the metabolically driven shape fluctuations of confluent cells adhered to the surface of a gold micro-electrode (*figure* 5.2 A/B) can serve as an indicator for dose-dependent cytotoxicity of nanoparticles.

Micromotion (*figure* 5.2 A) raw data was Fourier transformed (*figure* 5.2 B) to produce power density spectra. The slope *m* from the low frequency regime (*figure* 5.2 B) serves as a quantitative measure to what extent the adherent cells are vital.[10] As a first reference and control, 4% (v/v) paraformaldehyde-fixated cells showing no residual motility were employed.

Figure 5.2 C or D shows the degree of micromotion – quantified by the slope of the power spectrum- as a function of time when confluent MDCK II cells are exposed to gold nanorods coated with detergent Cetryl-triammonium-bromide (CTAB) to stabilize the particles in solution (*figure* 5.2 C) or QDs (*figure* 5.2 D) (addition time marked with arrows). Besides the slope of the power density *m*, we also plotted the time course of the transepithelial resistance (*TER*), which is a measure for the tightness of cell-cell junctions,[15] and only meaningful when a confluent, fully formed monolayer has established. It coincides with full micromotion that is typically characterized by a slope of the power density of *m* ≈ -2.5 (*figure* 5.1 *inset*). Nanoparticles were only added after equilibrium values for *TER* and *m* had been reached*.* Time courses of the power density slopes *m* show a continuous increase (from -2.5 to -1) upon the addition of both types of nanoparticles to the established cell monolayer, starting after 2 hours of incubation, which is indicative of a reduction of cell motility with exposure time (*figure* 5.2 C/D); the standard deviation of the slope is around ± - 0.2. However, the time courses of the transepithelial resistance *TER* do not show a significant change during particle exposure for the QDs concentrations ($7.5 \cdot 10^{13}$ p./ml) (*figure* 5.2 C) used here and one third of reduction (from 150 to 100 Ωcm^2) for gold nanoparticle concentrations of $1.38 \cdot 10^{11}$ p./ml, (*figure* 5.2 D). Hence conclude that micromotion is a better suited indicator for the onset of cytotoxicity than TER-monitoring. Apparently, MDCK cells
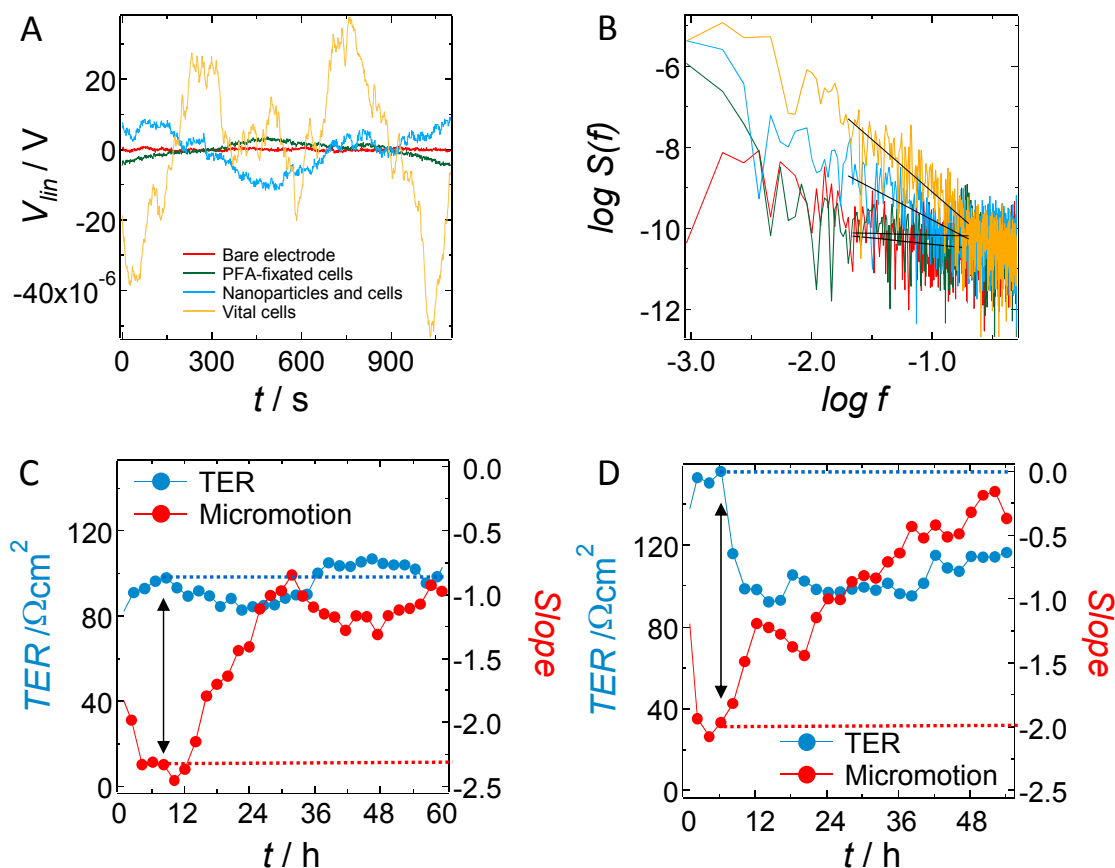
Figure 5.2 A) In-phase voltage fluctuations (micromotion raw data) under various load situations. The highest fluctuation amplitude is found for living untreated cells (■), while cells exposed to nanoparticles exhibit significantly lower micromotion (■). Fixated cells (■) and cell-free gold electrodes (■) display merely digital noise. B) Power spectral densities under the corresponding load situations: Empty electrodes (■) and fixated cells (■) show a slope close to zero, while motility (■) of vital cells provides an average slope of -2.6. Addition of CTAB coated gold nanorods results in a reduction of motility (■) expressed by a slope of approximately -1. C) Transepithelial resistance (TER) (●) and micromotion slope (●) after addition of $7.5 \cdot 10^{13}$ p./ml QDs as a function of time. D) Time course of TER (●) and micromotion slope (●) after addition of $1.38 \cdot 10^{11}$ p./ml CTAB-gold nanorods. Time upon reaching confluency is set to zero.

show a significant alteration of their metabolically driven motility before their predominant physiological function to serve as an interfacial tissue is compromised.

Typical time courses of normalized micromotion values are depicted in *figure* 5.3 for four kinds of nanoparticles (QD, gold nanorods either coated with CTAB, PEG-NH$_2$, or PEG-COOH) and the two components that may be released from the individually particles - CTAB and Cd^{2+} - for control purposes. Exemplary, four different concentrations are shown but for the sake of clarity only the highest concentration was subjected to an empirical sigmoid fit. Results for the two controls, either untreated cells or cell-free electrodes, are included in the diagrams. For standardization, the slope $m(t)$

is corrected by the mean values of the cell-free-electrode control $\langle N \rangle$ and related to the slope originated from untreated cells $\langle M \rangle - \langle N \rangle$ for each well (*eq. (1)*):

$$W(t) = \frac{m(t) - \langle N \rangle}{\langle M \rangle - \langle N \rangle} \times 100 \tag{1}$$

The standard deviation of *m* (not shown) is about 10 % in all experiments. All *W(t)* datasets were smoothed with adjacent averaging over 4 consecutive values and the experiments were conducted more than two times with a standard deviation of 10%, indicating good reproducibility.

QDs and CTAB coated gold rods (*fig.* 5.3 A/B) at particle concentration of $3 \cdot 10^{14}$ QDs (p./ml) and $1.38 \cdot 10^{11}$ CTAB-rods (p./ml) reduce cell motility of the confluent MDCK II monolayer drastically, while low concentrations of $4 \cdot 10^{12}$ (QDs) or $4.6 \cdot 10^{9}$ (CTAB rods) p./ml show no influence on cell motility. A substantial recovery of micromotion at medium particle concentrations, i.e. $2.4 \cdot 10^{14}$ for the semiconductor ones or $1.02 \cdot 10^{11}$ for the metallic ones, was found, which can be attributed to adaptation of the epithelial kidney cell lines, although this recovery effect was short termed in the case of QDs (6-8h as compared to full recovery for gold particles). We found that, at intermediate concentrations, cells recover twice as fast from particle treatment as from addition of pure CTAB solution. Addition of $CdAc_2$, however, did not result in viability recovery within the observation time scale (*fig.* 5.3C/D). At the same time, microscopic images (phase contrast) showed no evidence for cell detachment on the measuring electrode so that we can exclude that the observed recovery is caused by cell proliferation and replacement of dead cells. Importantly, substitution of the CTAB layer surrounding the gold nanorods by amino terminated polyethylenglycol leads to full cytocompatibility over the monitored 48 h interval up to a particle concentration of $1.32 \cdot 10^{12}$ p./ml (*fig.*5.3, E, shown for $4.6 \cdot 10^{11}$ p./ml). The untreated cell population and those treated with NH_2-PEG-nanoparticles are virtually indistinguishable confirming the expected 'stealth' character of the PEG coating.[16] However, using carboxy-terminated PEG as a coating for gold nanorods resulted in a decrease in micromotion almost down to 50 % within the first 24 h of incubation followed by a slow recovery to nearly 60 %. The results contradict observations by Goodman *et al.* [17]; in their study, quaternary ammonium groups on monolayer-coated gold clusters showed a considerable toxicity, while

nanoparticles functionalized with negatively charged side chains revealed no toxicity. *Figure* 5.3 F stresses one of the advantages of impedance measurements over classical,
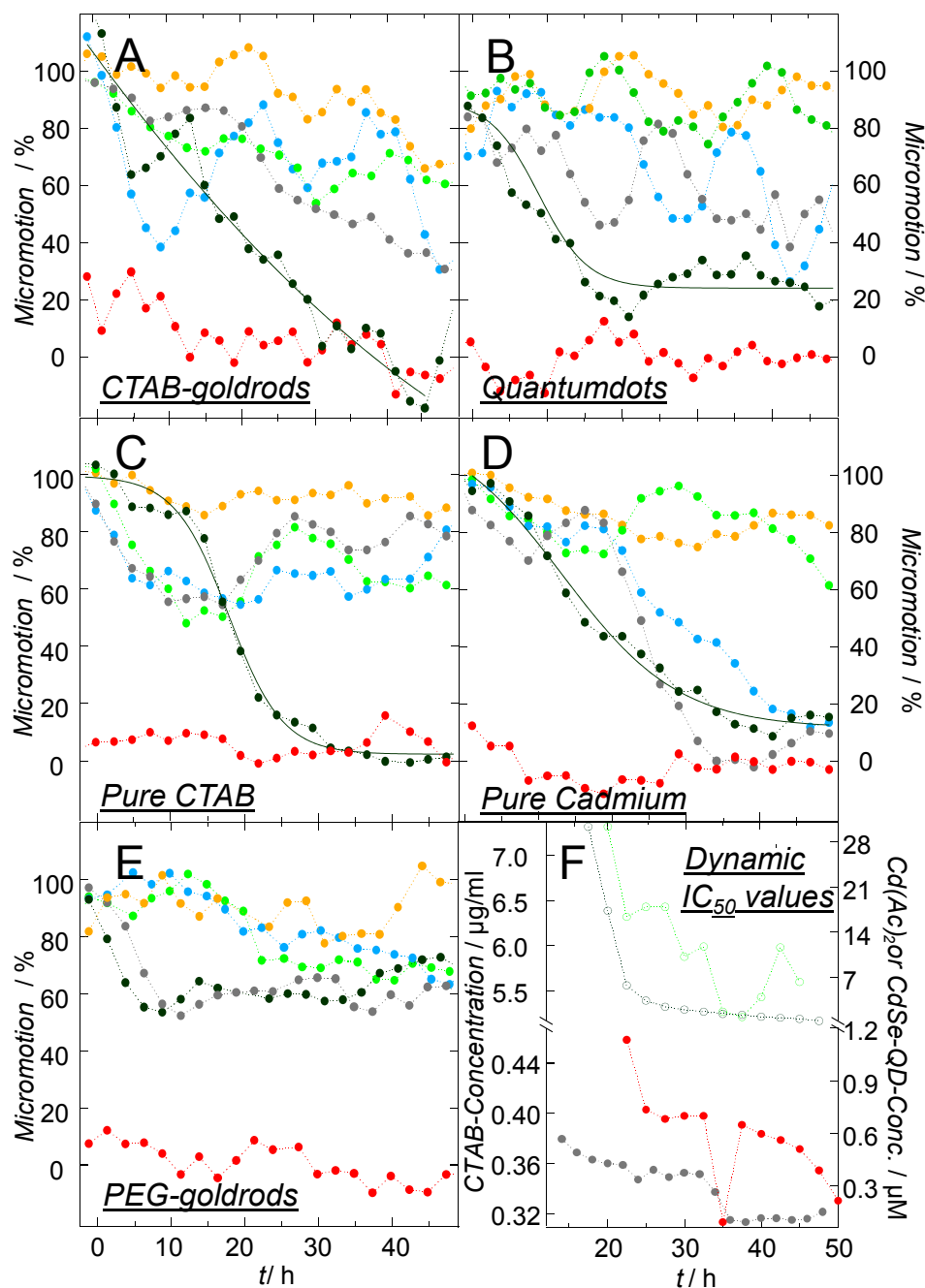
Figure 5.3 Micromotion of living cells (•) and bare electrode signal (•) as a function of nanoparticle exposure: A) CTAB gold nanorods (in p./ml): $1.38 \cdot 10^{11}$(•), $1.02 \cdot 10^{11}$(•), $6.6 \cdot 10^{10}$(•), $4.6 \cdot 10^{9}$(•). B) QDs (in p./ml): $3 \cdot 10^{14}$(•), $2.4 \cdot 10^{14}$(•), $1.5 \cdot 10^{14}$(•), $4 \cdot 10^{12}$(•). C) Pure CTAB (in µM): 31.25(•), 6.25(•), 3.125(•), 0.625(•). D) Pure cadmium ($CdAc_2$ in µM): 31.25(•), 6.25(•), 3.125(•), 0.156 (•). E) PEGylated gold nanorods (in p./ml): $1.38 \cdot 10^{11}$ (•), $4.6 \cdot 10^{11}$(•): COOH-terminated rods. $1.38 \cdot 10^{11}$(•), $4.6 \cdot 10^{11}$ (•): NH_2-terminated PEG rods. F) Dynamic IC_{50}-values determined from micromotion: CTAB concentration on nanorods (•), free CTAB (in µg/ml) (○), QDs (•), and $CdAc_2$ (○) (in µM).

end-point cytotoxicity tests. ECIS allows monitoring of the dynamic IC_{50} value, i.e., the individual IC_{50} values after different exposure times. For this purpose, the particle concentration at half-maximum micromotion was determined for increasing exposure times. For comparison, concentrations of QD particles and $CdAc_2$ are given in μM, CTAB concentration surrounding the CTAB gold particles as well as the pure CTAB in solution in μg/ml.

In general, the dynamic IC_{50} decreases with increasing time – as one would expect. However, for QDs, scaled in μM, we found a biphasic decrease of the dynamic IC_{50} with a plateau phase around 20 h exposure times with an IC_{50} of 350 nM. This behaviour is indicative of a fast toxic effect at concentrations higher than 350 nM, equivalent to $2 \cdot 10^{14}$ p./ml. after addition, followed by a slower process with significant lower IC_{50} below 100 nM. We attribute this biphasic behaviour to a quick response of cells to the uptake of QD and a delayed answer to washing out of toxic cadmium ions from the QD-particles. The delay can be explained by the diffusion barrier provided by the multishell arrangement, as reported by Kirchner *et al.*.[18] Cadmium ions from solution display a faster response of the micromotion assay as expected due to its immediate availability.

As far as the toxicity of CTAB coated gold nanorods expressed in IC_{50} value is concerned, we refer to it in *figure* 5.4 and *table* 5.1. In *figure* 5.3F for dynamic IC_{50} values instead, we show that pure CTAB added from solution affects micromotion to a smaller extent than the same concentration of CTAB found on the coated particles.

We determined the amount of CTAB attached to the gold particles by thermal gravimetric analysis (TGA, 24 μg CTAB/ mg gold indicating a bilayer of CTAB surrounding a single rod) to find out to what extend toxicity is influenced by the uptake and presence of particles as compared to pure CTAB. We found a 20 fold lower dynamic IC_{50} values for CTAB coated particle as neat CTAB solution. From this we conclude that either the particles itself are toxic or the amount of membrane-active CTAB within the cells is higher if the particles were used as carriers.[19] The latter finding is supported by our observation that CTAB coated particles show the tendency to form clusters once taken up by the cell (data not shown).

5.3.2 Comparison of micromotion with conventional MTS-assay

The non-invasive micromotion assay is validated by the established MTS test. For this purpose, the time courses of resistance fluctuations are recorded for various concentrations of different particles and free cadmium acetate and pure CTAB. We compared the viability measured through micromotion under identical conditions (exposure time and particle concentration) with the viability readings provided by the MTS test (*fig.* 5.4). Experiments were carried out in triplicate. Cell viability determined by MTS and micromotion are determined after 24 h of exposure of the cell to the particles. We found good agreement between both assays, although with bigger fluctuations in the ECIS assay, as far as the general trend is concerned, however, the micromotion assay shows a significant higher sensitivity than the MTS test since it responds already at lower particle concentration. IC_{50} values for both assays are compiled in *table 1* for the 24h and 48h exposure time. The micromotion assay reports approximately 20-fold lower IC_{50} values for the two chemicals (CTAB and $CdAc_2$) and 2-4 fold lower values for the nanoparticles after 24h intervals compared to MTS tests. After 48 h, the IC_{50} values are closer together although the highly toxic QDs produce a 200-fold lower IC_{50} in the micromotion assay as compared to the MTS-test. The discrepancy in sensitivity between the micromotion assay and the MTS test is even more pronounced if confluent cells were used for the MTS test instead of subconfluent cells.[20] Confluent cells in the MTS test result in 20 % higher IC_{50} values (data not shown) as compared to subconfluent ones (*table* 5.1).

Regarding the analytical performance of impedance-based measurement of cellular micromotility, it should be noted that this assay can be applied to all adherent

Table 5.1: *IC_{50}* values after 24 h and 48 h determined by micromotion and MTS.

Nanoparticle or toxin	IC_{50} Micromotion$_{24h}$	IC_{50} MTS$_{24h}$	IC_{50} Micromotion$_{48h}$	IC_{50} MTS$_{48h}$
Pure CTAB (µM)	6.4	111.2	5.5	16.5
Pure Cd(Ac)$_2$ (µM)	4.3	73.9	0.3	nontoxic up to 0.3
CTAB-rods (p./ml)	$1.20 \cdot 10^{11}$	nontoxic up to $2.30 \cdot 10^{11}$	$8.5 \cdot 10^{10}$	$8.75 \cdot 10^{10}$
Multishell QDs (p./ml)	$2 \cdot 10^{14}$	nontoxic up to $4 \cdot 10^{14}$	$1 \cdot 10^{14}$	$190 \cdot 10^{14}$
COOH-PEG rods (p./ml)	-	-	nontoxic up to $1.32 \cdot 10^{12}$ in 2.2 days	-
NH$_2$-PEG rods (p./ml)	-	-	nontoxic up to $1.32 \cdot 10^{12}$ in 2.5 days	-
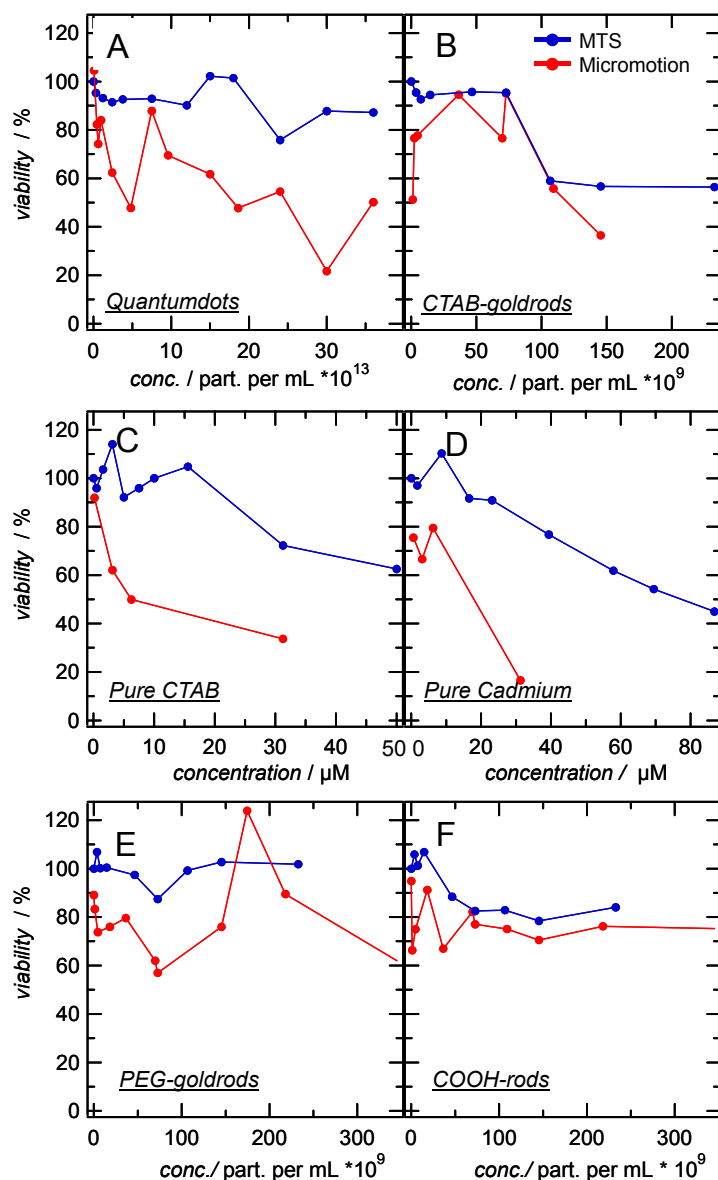
Figure 5.4 Comparison of cell viability determined by micromotion (●) and by the conventional MTS-test (●). Graphs depict viability as a function of concentrations: A) NH$_2$-PEG gold rods B) COOH-PEG gold nanorods C) CTAB gold nanorods D) Pure CTAB E) Multishell Quantum dots F) Pure CdAc$_2$.

cells that show measurable fluctuations in their cell shape. Micromotion should be clearly distinguished from measurements on cellular migration which involves lateral movement of the cell body into an open space on the culture substrate. In micromotion experiments as performed here we used confluent cell layers such that the readout reports more on shape fluctuations rather than cell movement. Micromotion readings have been reported for several different adherent cell types before. It was shown that the recorded impedance fluctuation are metabolically driven and mediated by the cytoskeleton. In a very recent paper,[21] Lovelady *et al.* could show that micromotion readings on 3T3 fibroblasts report on cellular changes for levels of toxin exposure that have previously not been considered as being harmful. Moreover, different cell types show a very individual pattern in the time course of impedance fluctuations, for instance, with respect to long-range and short-range fluctuations. However, this latter point is also a weak spot of the assay that it shares with other cytotoxicity assays. Measurements with different cell types, with individual levels of micromotion under control conditions, suffer from the problem of

correct normalization for this individual noise signature. Simple use of relative fluctuation changes might be an oversimplified way to deal with this problem. In most studies, however, a direct comparison of micromotion levels is not very relevant. Also, ECIS-based micromotion readings are clearly a holistic approach to read cytotoxicity. For instance, we can not distinguish between *apoptosis* and *necrosis* as the cause for cell death from ECIS readings today as other assays based on molecular recognition might. But these have shown to be less sensitive[22].

5.3.3 Localization of nanoparticles and visualization of the cytoskeleton by optical microscopy

Both the MTS and micromotion assay are quantitative but functional tests. Cytotoxicity of nanoparticles depends heavily on the uptake of the particles into the cell, i.e. the concentration of particles in the cytosol or any intracellular compartment. Thus, we addressed the question whether the different particles enter the cells to different degrees and where they are located inside the cell. While gold nanorods are visualized within the cells by dark field microscopy making use of their plasmonic resonance, QDs are readily imaged by fluorescence microscopy. Since micromotion relies on an intact cytoskeleton we also stained the actin and microtubule network using different particle concentrations and exposure times. In *figure* 5.5, fluorescence micrographs of actin stained with alexa-labeled phalloidin (1, 2, 5 and 6) as well as alexa-labeled IgG$_1$ specific for β-tubulin (3, 4, 7 and 8) are compared for different incubation times and particle concentrations. The immunofluorescence of the control upon reaching confluency (0h, *fig.* 5.1 and 3) and after 48 h (*fig.* 5.2 and 4) without particles shows typical intracellular actin filaments and microtubules: f-actin fibres, a cortical ring, tubules and β-tubulin monomeres in vesicles. After 48 h cells occupy a smaller area and bundles of actin as well as small internal aggregates can be found, while microtubules are too dense to distinguish single tubules anymore. *Figure* 5.5, 5-8 shows a cell monolayer after addition of $1.38 \cdot 10^{11}$ gold nanoparticles (5 and 7 coated with CTAB, 6 and 8 with NH$_2$-PEG) and after a 48 h incubation time. Cells exposed to CTAB rods show gaps between adjacent cells in the actin staining (corresponding to reduced TER recordings), where the cortical

Controls

Gold nanorods
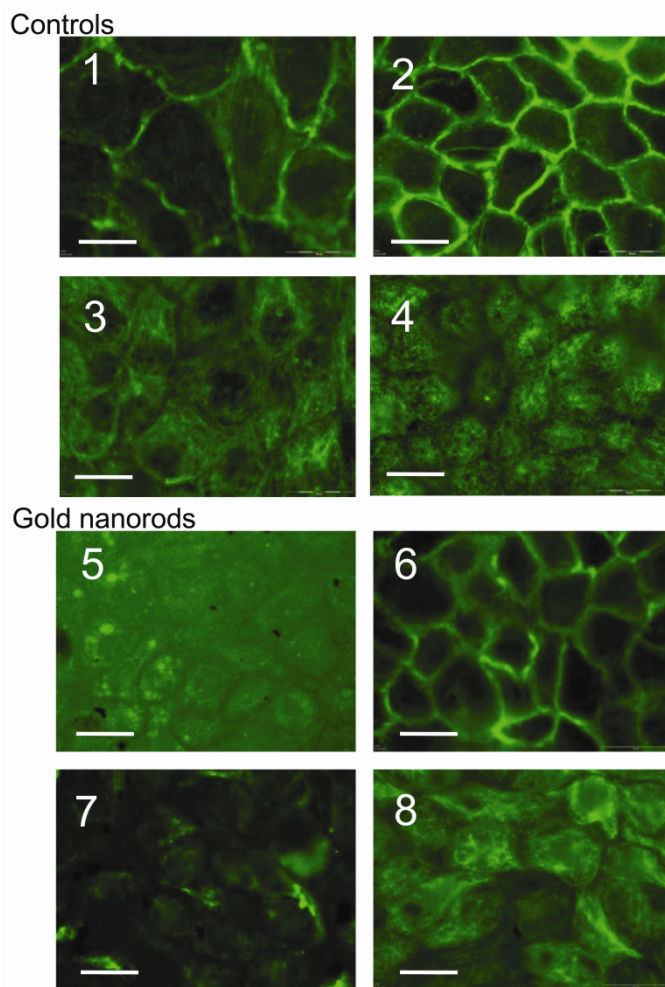
Figure 5.5 Fluorescence light microscopic images after staining of actin (first and third row) or microtubules (second and fourth row); 1-4: Controls after 24 hours upon attaining confluency (t=0) (1 and 3) and 48 h after reaching confluency (2 and 4) without nanoparticles. 5-8: Micrographs after 48 hours of incubation with $1.38 \cdot 10^{11}$ p./ml gold nanorods (5 and 7: CTAB; 6 and 8 NH$_2$-PEG). Scale bar is 20 µm.

ring used to be, while unusual aggregates of actin occur in the cytosol (*fig.* 5.5, 5). β-tubulin is redistributed in monomers to the cell periphery and cells are generally diminished in size (*fig.* 5.5, 7). In contrast, PEGylated particles do not show any visible changes in the cells' cytoskeleton (*fig.* 5.5, 6 and 8).

We also managed to localize the gold nanoparticles in or outside the cells by means of dark-field microscopy. In order to improve the precision of particle localization we co-stained both the nucleus by DAPI and the tight junctions by ZO-1 staining (*figure* 5.6, 1-4). The particles are easily identified by the orange to red colour originating from localized plasmon resonance. Notably, up to 20% of the solution consists of spherical gold particles that appear green in the scattered light. Generally, we found that the particles - regardless of their coating – preferably arrange around the nucleus without entering it, which has also been reported previously.[23]

While CTAB coated gold nanorods accumulate in the cytosol already at low particle concentrations, we found substantially less particles with PEG coatings within the cells. At low particle concentration ($4.6 \cdot 10^{10}$ p./ml), individual CTAB coated nanorods and many aggregates are distinguishable without affecting cell-cell boundaries (*fig.*5.6, image 1). By moving the focal plane, we made sure that the particles are indeed in the

Gold nanorods: Dark-field, ZO-1 and DAPI-staining
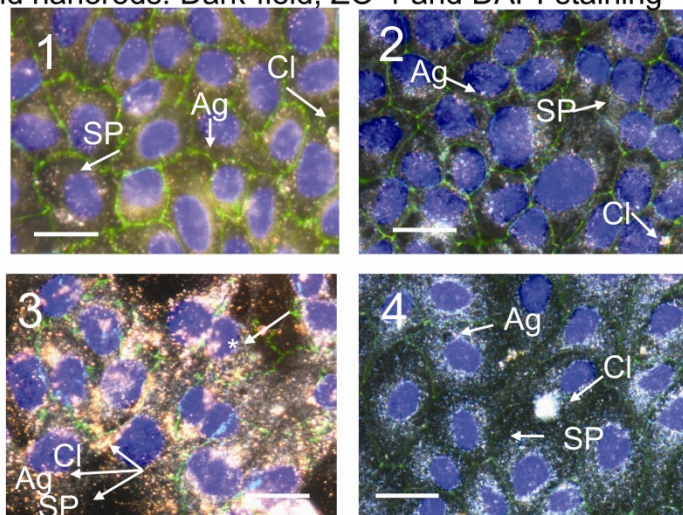
Quantum dots
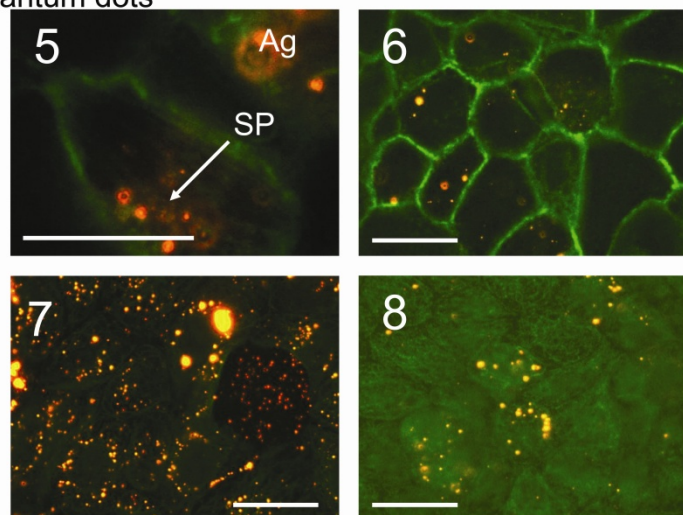
Figure 5.6 1-4: Overlay of dark-field images and fluorescence images with ZO-1 and nucleus staining after 48 h incubation with (1) $4.6 \cdot 10^{10}$ or (3) $6.6 \cdot 10^{11}$ CTAB rods as well as (2) COOH-PEG gold nanorods and (4) NH_2-PEG gold nanorods ($1.32 \cdot 10^{12}$ p./ml); arrows pointing at single particles (SP), aggregates of 2-20 particles (Ag), or clusters (20 and more particles). Additionally (under 3), discontinuous ZO-1 staining (*) is highlighted; 5-8: Fluorescence image of MDCK cells after 24 hours of incubation with Multishell quantum dots at two concentrations: $3.75 \cdot 10^{14}$ (5 and 7) and $1.9 \cdot 10^{14}$ p./ml (6 and 8). Arrow in 1 is pointing at single particles aligned with actin fibres. Scale bar is 20 µm.

cytosol and not above or beneath the cells. At higher particle concentrations ($6.6 \cdot 10^{11}$ p./ml, *fig.* 5.6, image 3), CTAB rods tend to form larger aggregates and the cell-cell- boundaries are destroyed. Moreover, detachment of cells has occurred.

Figure 5.6, images 2 and 4, show the results of cells exposed to PEG coated gold particles (with NH_2 or COOH groups; $1.32 \cdot 10^{12}$p./ml); it can be seen, that nuclei are unaffected and ZO-1 staining is continuous. Comparing image 1 (CTAB) with image 2 (COOH-PEG), roughly the same amount of gold nanorods are found in the cytosol, although the first ones are aggregated and the latter not. However, for PEGylated particles (COOH) a 10 fold higher concentration was necessary to achieve the same particle density in the cells. Although our findings confirm the nontoxic nature of PEGylated particles, which enter the cells less efficiently but do not alter their internal structure (cytoskeleton, nucleus, cell-cell boundaries), particle uptake is reduced by roughly a factor of 10 compared to CTAB coated particles.

In *figure* 5.6, 5-8*,* the impact of two different QDs concentrations, $3.75 \cdot 10^{14}$ and $1.9 \cdot 10^{14}$ p./ml on the confluent MDCK II cells is shown. At higher particle concentration, particle-aggregates within the cells as well as cell-desorption from the surface occurs (*fig.*5.6 image 5 and 7), while at lower concentration (*fig.* 5.6, image 6 and 8), which has been used for the micromotion assay, no effect on the cell layer integrity is found. Cadmium ions are known to depolymerise F-actin and affect the cadherin-catenin complex [24] and our images suggest that this is exactly what happens if the cells are exposed to QD supporting the hypothesis that indeed cadmium ions are released from the multishell QDs. The cell's cortical actin ring is less pronounced than in controls and nanoparticles seem to arrange along fibres. Notably, QD, like gold particles, do not enter the nucleus.

5.4 DISCUSSION

Although nowadays the call for in vivo characterisation of nanotoxicity is strong [25], cell culture models are important for physiological and toxicological preclinical research; therefore, an approach comparing various assays on common model cell lines and standardized particles is desirable: for the latter case, gold particles seem to be an appropriate candidate, since in many studies on different cells lines they are referred to be only slightly toxic, usually decreasing vitality from 10 to 20 percent. A comprehensive overview of cytotoxicity generated by carbon-, gold- and semiconductor nanoparticles is given by Lewinski *et al.*.[23] To date, however, impedance spectroscopy has only sparsely been applied to assess particle toxicity and only once recently to address nanoparticles toxicity in focus.[26] Male *et al.* herein found an IC_{50} toxicity for semiconductor nanoparticles without multishell arrangement, by montoring IZI as a function of time, to lay around 154 nM, indicating that our IC_{50} value of 300 nM found is due to an enhanced diffusion barrier by the multishell arrangement. Ceriotti *et al.* [27] report on cobalt-based metallic nanoparticles, which showed toxicity at concentrations larger than 300 µM after 24 h, which is 500 times higher than the toxic dose QDs and 400 times higher than the dose of gold particles used in our study. Krol and co-workers investigated the toxicity of gold nanoparticles with four- layer PAH coating by means of impedance spectroscopy. The authors found strong toxicity of particles after 17 h.[28] The concentration regime at which the particles showed toxicity was in the range of 2000 µg/ml, considerably lower than the concentration regime in which CTAB coated rods are cytotoxic. Another widely used approach is to monitor cell motility and/or toxicity of nanoparticles via optical microscopy: Parak *et al.* [29] found quantum dots with CdSe/ZnS/SiO$_2$ composition of 8 and 16 nm diameter to be non toxic to the two epithelial cell lines MDA-MB 231 and MCF-10. The particles were placed at high density on the substrate and internalized to a great degree resulting in perinuclear arrangement. Thereby, cell motility could be observed via migratory pathways comparable to the phagokinetic tracking assay. By means of DIC-microscopy, Kirchner *et al.* [18] determined the toxic concentration for MPA coated QDs with multishell structure to be 0.65 µM. This is in good accordance with our ECIS-micromotion assay, which provided values in the range of 0.3 µM, while the MTS test reported a concentration of 2 µM. The examples clearly support our

conclusion that the sensitivity of micromotion to the exposure of nanoparticles is higher than that of conventional cytotoxicity assays.

Impedance spectroscopy is a versatile tool to quantify cell viability. Apart from micromotion, which measures the motility of already adherent cells, cell-cell contact and adhesion of cells can be investigated by AC impedance analysis. For instance, Zimmerhackl *et al.* measured the TER of MDCK cells to determine the cytotoxic concentration of cadmium ions applied from the basolateral side.[24] The authors found an IC$_{50}$ larger than 12.5 µM, which is a factor of three higher than the value we determined by our micromotion assay. For comparison, Ceriotti *et al.* [27] found an inhibition concentration of 34 µM after 24h exposure to cadmium ions by measuring the impedance upon adhesion of fibroblasts. However, combination with classical cytotoxicity assays and advanced optical single particle microscopy is necessary to elucidate the fate of the nanoparticles, as done by Shukla *et al.*.[30] Due to the fact that not all cells display a measurable TER and the influence of nanoparticles on tight junctions varies between particles or cells, micromotion is a more appropriate and universal approach to determine toxicity rather than monitoring of the TER.

Particle toxicity is a function of size, shape, and most importantly surface functionalization.[31] The surface coating of particles influences their uptake and fate once they entered the cell. In the present work, we found by recording the micromotion of confluent epithelial cells that PEGylation increases the biocompatibility substantially. Dark field microscopy in conjunction with immunofluorescence of cytoskeleton filaments shows that CTAB coated particles enter cells with high efficiency, while PEGylation suppresses the particle uptake of cells significantly. However, even at particle concentrations, which lead to accumulation of PEGylated gold nanorods within the cytosol, cytotoxicity measured by micromotion is negligible.

5.5 CONCLUSIONS

Micromotion measured by impedance analysis provides a non-invasive and versatile tool to assess the toxicity of nanoparticles with high sensitivity. Compared to conventional cytotoxicity test, micromotion detects minute changes in cell viability already at very low particle concentrations without the need for colorimetric or fluorescent labels and in real-time. The latter provides dynamic IC_{50} values, which increase our insight into mechanisms of particle-cell interaction. Dark field microscopy of gold nanorods is the ideal counterpart to micromotion since it allows visualizing the location of particle also in a non-invasive manner. We found that even when QDs are capped and stabilized against Cd^{2+} diffusion with an external ZnS shell in a sixfold monolayer arrangement, they are highly toxic, while PEGylated nanorods are esentially harmless to adherent epithelial cells.

5.6 REFERENCES AND NOTES

1. Harrison, R. Nanoparticles in the Atmosphere. In: Nanotechnology - *Consequences for Human Health and the Environment*; Hester, R. E., Harrison, R.M., Eds.; RCS Publishing: Cambridge, **2007**; pp 35-48.

2. Long, T. C.; Saleh, N.; Tilton, R. D.; Lowry, G. V.; Veronesi, B., Titanium Dioxide (P25) Produces Reactive Oxygen Species in Immortalized Brain Microglia (BV2): Implications for Nanoparticle Neurotoxicity. *Environ. Sci. Technol.* **2006,** *40*, 4346-4352.

3. Hodgson, E., LeBlanc, G.A., Meyer, S.A., Smart, R.C. Introduction to Biochemical and Molecular Methods in Toxicology. In: *A Textbook of Modern Toxicology*; Hodgson, E., Ed.; John Wiley & Sons, Inc., Hoboken, **2004**; pp 13-22

4. Giaever, I.; Keese, C. R., Monitoring Fibroblast Behaviour in Tissue-Culture with an Applied Electric-Field. *Proc. Natl. Acad. Sci.* **1984,** *81*, 3761-3764.

5. Xiao, C.; Lachance, B.; Sunahara, G.; Luong, J. H. T., An In-Depth Analysis of Electric Cell-Substrate Impedance Sensing to Study the Attachment and Spreading of Mammalian Cells. *Anal. Chem.* **2002,** *74*, 1333-1339.

6. Ceriotti, L.; Ponti, J.; Colpo, P.; Sabbioni, E.; Rossi, F., Assessment of Cytotoxicity by Impedance Spectroscopy. *Biosens. Bioelectron.* **2007,** *22*, 3057-3063.

7. Wegener,J. Keese, C.R., Giaever, I. Electric Cell–Substrate Impedance Sensing (ECIS) as a Noninvasive Means to Monitor the Kinetics of Cell Spreading to Artificial Surfaces. *Exp. Cell Res.* **2000**,*259,* 158–166.

8. McCoy, M. H.; Wang, E., Use of Electric Cell-Substrate Impedance Sensing as a Tool for Quantifying Cytopathic Effect in Influenza A Virus Infected MDCK Cells in Real-Time. *J. Virol. Methods* **2005,** *130*, 157-161.

9. Giaever, I.; Keese, C. R., Micromotion of Mammalian-Cells Measured Electrically. *Proc. Natl. Acad. Sci.* **1991,** *88*, 7896-7900.

10. Lo, C. M.; Keese, C. R.; Giaever, I., Monitoring Motion of Confluent Cells in Tissue-Culture. *Exp. Cell Res.* **1993,** *204*, 102-109.

11. Lovelady, D. C.; Richmond, T. C.; Maggi, A. N.; Lo, C. M.; Rabson, D. A., Distinguishing Cancerous from Noncancerous Cells Through Analysis of Electrical Noise. *Phys. Rev. E* **2007,** *76*, (4),1-10

12. Huff, T. B.; Tong, L.; Zhao, Y.; Hansen, M. N.; Cheng, J. X.; Wei, A., Hyperthermic Effects of Gold Nanorods on Tumor Cells. *Nanomed.* **2007,** *2*, 125-132.

13. Vashist, S. K. T., R.; Bajpai, R.P.; Mohan, B.; Raiteri, R., Review of Quantum Dot Technologies for Cancer Detection and Treatment. *Nanotech Online* **2006,** *2*, 1-14.

14. Michalet, X.; Pinaud, F. F.; Bentolila, L. A.; Tsay, J. M.; Doose, S.; Li, J. J.; Sundaresan, G.; Wu, A. M.; Gambhir, S. S.; Weiss, S., Quantum Dots for Live Cells, In Vivo Imaging, and Diagnostics. *Science* **2005,** *307*, 538-544.

15. Wegener, J.; Sieber, M.; Galla, H. J., Impedance Analysis of Epithelial and Endothelial Cell Monolayers Cultured on Gold Surfaces. *J. Biochem. Biophys. Methods* **1996,** *32*, 151-170.

16. Hillaireau, H., Couvreur, P. Polymeric Nanoparticles as Drug Carrier. In *Polymers in Drug Delivery;* Uchegbu, I.F., Schatzlein, A.G., Eds.; Taylor and Francis: New York, **2006**; pp 101-110.

17.   Goodman, C. M.; McCusker, C. D.; Yilmaz, T.; Rotello, V. M., Toxicity of Gold Nanoparticles Functionalized with Cationic and Anionic Side Chains. *Bioconjugate Chem.* **2004,** *15*, 897-900.

18.   Kirchner, C.; Liedl, T.; Kudera, S.; Pellegrino, T.; Javier, A. M.; Gaub, H. E.; Stolzle, S.; Fertig, N.; Parak, W. J., Cytotoxicity of Colloidal CdSe and CdSe/ZnS Nanoparticles. *Nano Lett.* **2005,** *5*, 331-338.

19.   Wei, X. L.; Mo, Z. H.; Li, B.; Wei, J. M., Disruption of HepG2 Cell Adhesion by Gold Nanoparticle and Paclitaxel Disclosed by In Situ QCM Measurement. *Colloids Surf., B* **2007,** *59*, 100-104.

20.   Pan, Y.; Neuss, S.; Leifert, A.; Fischler, M.; Wen, F.; Simon, U.; Schmid, G.; Brandau, W.; Jahnen-Dechent, W., Size-Dependent Cytotoxicity of Gold Nanoparticles. *Small* **2007,** *3*, 1941-1949.

21.   Lovelady, D.C.; Friedman, J.; Patel, S.;Rabson, D.A.; Lo, C. M., Detecting Effects of Low Levels of Cytochalasin B in 3T3 Fibroblast Cultures by Analysis of Electrical Noise Obtained From Cellular Micromotion. *Biosens. Bioelectron.* **2008,** doi:10.1016/j.bios.2008.09.033

22.   Arndt, S.; Seebach, J.; Psathaki, K.; Galla, H.J.; Wegener, J., Bioelectrical Impedance Assay to Monitor Changes in Cell Shape During Apoptosis. *Biosens. Bioelectron.* **2004,** *19*, 583–594.

23.   Lewinski, N.; Colvin, V.; Drezek, R., Cytotoxicity of Nanoparticles. *Small* **2008,** *4*, 26-49.

24.   Zimmerhackl, L. B.; Momm, F.; Wiegele, G.; Brandis, M., Cadmium is More Toxic to LLC-PK1 Cells Than to MDCK Cells Acting on the Cadherin-Catenin Complex. *Am. J. Physiol-renal.* **1998,** *44*, F143-F153.

25.   Fischer, H. C.; Chan, W. C., Nanotoxicity: the Growing Need for In Vivo Study. *Curr. Opin. Biotechnol.* **2007,** *18*, 565-571.

26.   Male, K. B.; Lachance, B.; Hrapovic, S.; Sunahara, G.; Luong, J. H. T., Assessment of Cytotoxicity of Quantumdots and Gold Nanoparticles using Cell-Based Impedance Spectroscopy. *Anal. Chem.* **2008,** *80*, 5487-5493.

27.   Ceriotti, L.; Ponti, J.; Broggi, F.; Kob, A.; Drechsler, S.; Thedinga, E.; Colpo, P.; Sabbioni, E.; Ehret, R.; Rossi, F., Real-Time Assessment of Cytotoxicity by Impedance Measurement on a 96-Well Plate. *Sens. Actuators, B* **2007,** *123*, 769-778.

28.   Chanana, M.; Gliozzi, A.; Diaspro, A.; Chodnevskaja, I.; Huewel, S.; Moskalenko, V.; Ulrichs, K.; Galla, H. J.; Krol, S., Interaction of Polyelectrolytes and Their Composites with Living Cells. *Nano Lett.* **2005,** *5*, 2605-2612.

29.   Parak, W. J.; Boudreau, R.; Le Gros, M.; Gerion, D.; Zanchet, D.; Micheel, C. M.; Williams, S. C. ; Alivisatos, A. P.; Larabell, C., Cell Motility and Metastatic Potential Studies Based on Quantum Dot Imaging of Phagokinetic Tracks. *Adv. Mater.* **2002,** *14*, 882-885.

30.   Shukla, R.; Bansal, V.; Chaudhary, M.; Basu, A.; Bhonde, R. R.; Sastry, M., Biocompatibility of Gold Nanoparticles and Their Endocytotic Fate Inside the Cellular Compartment: A Microscopic Overview. *Langmuir* **2005,** *21*, 10644-10654.

31.   Hoshino, A.; Fujioka, K.; Oku, T.; Suga, M.; Sasaki, Y. F.; Ohta, T.; Yasuhara, M.; Suzuki, K.; Yamamoto, K., Physicochemical Properties and Cellular Toxicity of Nanocrystal Quantum Dots Depend on Their Surface Modification. *Nano Lett.* **2004,** *4*, 2163-2169.

32. Sapper, A.; Wegener, J.; Janshoff, A., Cell Motility Probed by Noise Analysis of Thickness Shear Mode Resonators. *Anal. Chem.* **2006,** *78*, 5184-5191.

33. Nikoobakht, B.; El-Sayed, M. A., Preparation and Growth Mechanism of Gold Nanorods (NRs) Using Seed-Mediated Growth Method. *Chem. Mater.* **2003,** *15*, 1957-1962.

34. Jana, N. R.; Gearheart, L.; Murphy, C. J., Seed-Mediated Growth Approach for Shape-Controlled Synthesis of Spheroidal and Rod-Like Gold Nanoparticles Using a Surfactant Template. *Adv. Mater.* **2001,** *13*, 1389-1393.

35. Pierrat, S.; Zins, I.; Breivogel, A.; Sönnichsen, C., Self-Assembly of Small Gold Colloids with Functionalized Gold Nanorods. *Nano Lett.* **2007,** *7*, 259-263.

36. Xie, R. G.; Kolb, U.; Li, J. X.; Basché, T.; Mews, A., Synthesis and Characterization of Highly Luminescent CdSe-Core CdS/Zn0.5Cd0.5S/ZnS Multishell Nanocrystal. *J. Am. Chem. Soc.* **2005,** *127*, 7480-7488.

6

Shape-dependent toxicity of gold-nanoparticles
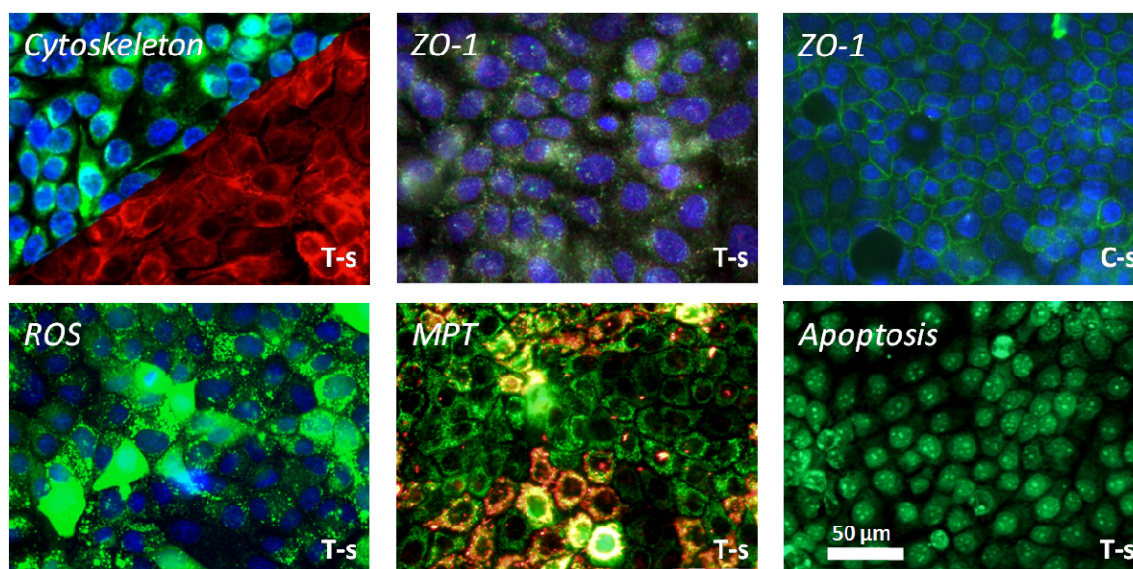
ABSTRACT

Nanoparticles are present in everyday life and therefore create a demand for test paradigms to control cytotoxicity upon exposure. In this study, we present a comprehensive interfacial analysis monitoring viscoelastic changes by a quartz-crystal microbalance equipped with dissipation monitoring (D-QCM) and impedance spectroscopy via electrical cell-substrate impedance sensing (ECIS) that enables us to record both adhesion/desorption processes and cell-cell contacts degradation upon nanoparticles application. Additionally, we follow cell-substrate dynamics via micromotility and viscoelastic fluctuations as a measure for nanotoxicity. We scrutinized the impact of gold-nanoparticles with various surface functionalizations and two distinct shapes, spheres with a diameter of 42.9 ± 4.0 nm and rods with a size of 37.8 ± 6.5 nm × 17.2 ± 2.9 nm as a function of concentration. Conventional cytotoxicity testing as well as fluorescence, dark-field, and atomic force microscopic imaging complement this double-biosensor approach and allow monitoring of intracellular particles, assessment of cytoskeletal integrity and imaging of reactive oxygen species (ROS)-, mitochondrial permeability transition (MPT) and apoptosis-onset.

6.1 INTRODUCTION

Although the concept of nanoparticle technology was already pioneered in the sixties, chemical industry discovered the benefits of this growing field only in the early ninenties.[1] Nowadays, ubiquitous applications can be found, whether it is on big scale, i.e. in the automobile industry for friction coatings, for consumer applications or in novel medical research, ranging from targeted gene delivery systems to imaging agents or synergistic/photothermal cancer therapy.[2, 3] However, predictions for the manifold increase in production of nanoparticles (60000 tons by 2020)[4] run in parallel to the urge for strategic research on the risks upon environmental as well as human exposure, both for accidental or controlled delivery. As a consequence, high-throughput, dynamic toxicity-testing protocols will be of great interest to support the design of safe engineering methods.[5]

Gold nanoparticles (GNPs) attract high interest in biomedical research due to their supposed inertness, high electron density and versatile surface chemistry. Chemical and physical properties of the 1-100 nm sized objects thereby relate, among other factors, to their composition and stability, solubility, size, shape, functionalization and uptake efficiency/specifity. In current literature on gold nanoparticle toxicity, interaction with serum containing or serum-free media has attracted great interest concerning the aspect of increased biocompatibility and uptake due to serum protein adsorption on the GNP surface. On the opposite, on the basis of solubility and aggregation behavior, the question arose, how biological media influence stability and particle aggregate`s size and shape.[6-8] However, few publications are dedicated to the toxicity of various GNPs shapes[9, 10] and sizes.[11, 12] Concerning functional groups of surface ligands, among many other, citrate[9]- as well as triphenylphosphin[8]- and cetyl-trimethyl-ammonium bromide(CTAB)-capping[13] have been analyzed. Despite recent efforts to elucidate the fate of GNPs in mammalian cells, most studies lack unambiguous quantification data from non-invasive techniques.[14-17]

Hence, in the work presented, two label-free and non-invasive, real-time assessing biosensor approaches involving AC impedance and quartz-crystal microbalance measurements are utilized. Four of the aspects of GNPs of actual interest in life sciences mentioned above are followed: shape, functionalization, uptake and intracellular effects

as, in this case, by inflammation precursor ROS generation, mitochondrial permeability transition (MPT) and apoptosis induction.

Impedance spectroscopy based on electric-cell substrate impedance sensing (ECIS) was introduced more than two decades ago,[18] attracting great interest as a non-invasive biosensor to follow adhesion and spreading of mammalian cells. Motility monitoring of confluent cells with the ECIS setup was described first in 1986.[19] Real part impedance fluctuations are analyzed by fourier transformation or variance analysis and serve as a measure for the vitality of cultured cells.[20] Besides, biotechnologists recently gained interest in a biosensor concept based on oscillating piezoelectric substrates referred to as the quartz crystal microbalance.[21] Frequency and dissipation shifts of resonators exposed to biomolecules or cells were recorded simultaneously, leading to numerous biophysical and medical applications due to the unprecedented sensitivity.[22] In the case of cells, usually the adhesion and spreading behavior is followed. Fluctuations of these basic parameters were first described for a network analyzing QCM setup by Pax *et al.*[23] to analyze cardiomyocite contractions and by Cans *et al.*[24] following exocytosis and vesicle retrieval. Recently, we proved this technique to be sensitive enough to follow electrically non-active cells and fingerprint their cell-substrate dynamics.[25, 26]

In the work presented herein, the toxicity correlated concentration dependency of the fluctuations in frequency and dissipation of a home-made D-QCM setup is proven and compared to the ECIS micromotility analysis as a label-free monitoring tool to study nanoparticle-cell interaction, as done previously;[27] additionally, since for external GNP exposition pathways, cells with barrier function are of interest, MDCKII epithelial cells` barrier function is assessed: trans-epithelial resistance (TER) upon nanoparticle exposure is recorded as a time or concentration function. Validation of the nanotoxicity detected by the double-biosensors approach is carried out via classical, established MTS assay. Finally, cell-cytoskeleton disruption, generation of ROS as inflammation indicator, mitochondrial permeability transition (MPT) as indicator of apoptosom activation and the cell death pathway are analyzed by live cell fluorescence microscopy and cell-cell contacts integrity captured by immunochemistry and AFM-imaging.

6.2 EXPERIMENTAL SECTION

6.2.1 Cell culture conditions, measurement procedures and nanoparticle preparation

MDCKII cells are maintained in Earle's minimum essential medium supplemented with 4 mM glutamine, 100 g/mL of both penicillin and streptomycin (purchased by Biochrom, Berlin, Germany), 10% (v/v) fetal calf serum (PAA Laboratories GmbH, Coelbe, Germany) and stored in incubators (HERA cell 150, Heraeus, Germany) with a 5% CO2 atmosphere. Cells are subcultured weekly after reaching confluence by washing with PBS, followed by trypsinization and centrifugation at 110×*g*. Counting is carried out using a Neubauer chamber, and viability is determined using trypan blue exclusion. For the ECIS-biosensor setup, 6×10^5 cells are seeded in the 8-well electrode arrays and are treated as described before.[27] For quartz biosensor preparation, after routine cleaning procedure, special designed teflon-cells are assembled and, as the ECIS electrodes, transferred to a culture incubator with 37 °C and 5% CO_2- atmosphere (MMM Medcenter Einrichtungen GmbH, Gräfelfing, Germany). Cells are inoculated at a density of $6\text{-}7 \times 10^5$ cells/ml and handled as described before.[26] Terminal fixation of cells is carried out via 0.5 % glutardialdehyde (GDA) (Sigma-Aldrich, Germany) solution and exchange of medium with medium containing nanoparticles is carried out upon confluence, i.e. 15 - 24 h after seeding.

For gold-nanorod preparation, the seed growth method adopting CTAB-stabilizing agent is applied, as reported by Nikoobakht *et al.* and Jana *et al.*.[27] A strong color change indicates the formation of the gold nanorods after about 20 min, resulting in a stable suspension of CTAB-coated nanorods. Substitution by carboxy- or amino-terminated PEG for biocompatibility and improved solubility is described in detail by Pierrat *et al.*.[28] Spherical particles are purchased from British BioCell (British BioCell International, Cardiff, UK) and treated to gain comparable surface chemistry to rod-shaped particles. Before use, gold particles are centrifuged two times in deionized water and resuspended in HEPES buffered complete medium; stock solution concentrations are determined using Lambert-Beer`s law as detailed by Rosman *et al.*.[29]

6.2.2 D-QCM based viscoelastic monitoring, ECIS-based impedance studies and noise analysis

Noise analysis based on viscoelastic fluctuations was monitored with a self-made D-QCM setup (*figure* 6.1*, right path)*[30]: confluent cell layers were subjected to noise analysis of

frequency and dissipation fluctuations as described elsewhere.[13] In brief, short time FFT and variance analysis of linearly detrended time blocks were carried out. For power density spectra (PSD) analysis of the viscoelastic fluctuation data (referred to as F-QCM), the slope *m* was determined in the low frequency regime (*figure* 6.1, lower part) as described previously[14] and assigned to cells` viability.
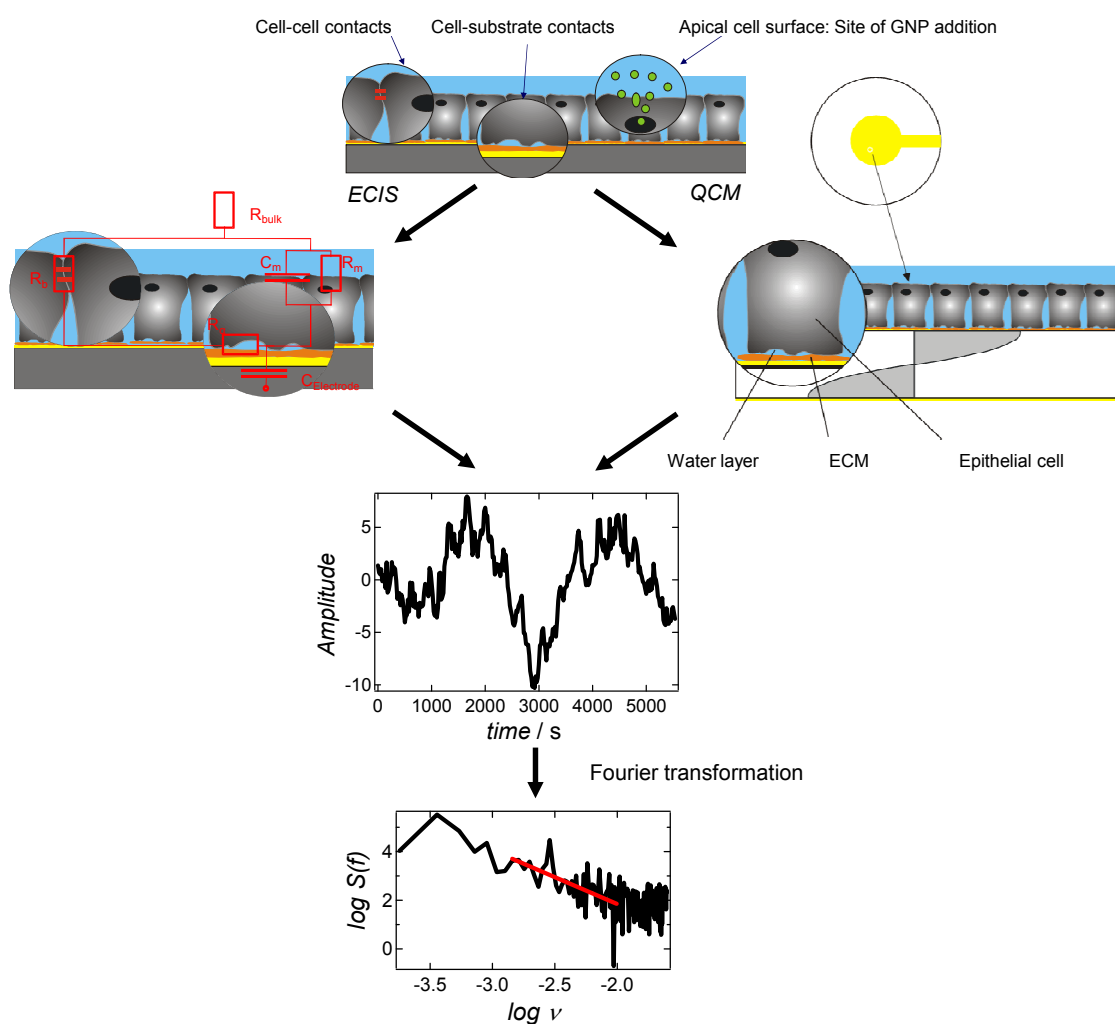

Figure 6.1 Schematic of the experimental setups: Cells are cultured directly on the biosensors (quartz or electrode) and present cell-cell and cell-substrate contacts: GNPs are added to the apical site. *QCM* (taken from ref [26]): Cell monolayers of 500-600 $\times10^3$ cells are cultured directly on evaporated gold electrodes ($\varnothing$ = 0,2 cm^2) on quartz disks. Parameters f and δ as a function of time follow adsorption and spreading; fluctuations subjected to FFT analysis of time courses yield PSD (power-spectral density)-diagrams. Linear slopes in the low-frequency regime serve as measure for vertical motility. Same datasets are subjected to variance analysis. *ECIS* (taken from ref [27]): R_b, is fitted via the equivalent circuit shown and is a measure for the TER; it is recorded between 10 and 10^4 Hz. Micromotion is mainly determined by R_α, the resistance between cells and the ECM/electrode surface; the slope of the Fourier analysis of the impedance real-part fluctuations (i.e. in-phase voltages), the 'micromotion', is recorded at 4 kHz as a function of time.

For AC-impedance analysis, a homemade ECIS system was employed, as introduced before[27]; in our ECIS setup, a 1 V AC signal is applied to the system through a 1 MΩ series resistor, and the in- and out-of phase voltages across the electrodes are recorded at 4 kHz at a sampling rate of 1 Hz (*figure* 6.1, *left path,* based on Gaiever *et al.*[19]). For micromotion recordings, fluctuations of the in-phase voltages at non-invasive 1 μA amplitude were employed. Besides micromotion recordings at one fixed frequency, we also monitored changes in the barrier function of the adherent MDCKII cell layer: trans-epithelial electrical resistance (TER) was extracted from frequency-resolved impedance readings (10-10^4 Hz) and subjected to equivalent circuit modeling as detailed by Wegener *et al.*.[31] Micromotion and TER readings were carried out on one and the same cell layer. Noise analysis based on micromotion data, which is a time series of resistance fluctuations, was achieved by Fourier transformation after subtracting a linear trend (*figure* 6.1, lower part), as described recently.[12] A linear fit of the low frequency part of the power density spectra provided slopes up to - 2.7 for living cells. Time courses of the slope and the TER are recorded as a function of particle type and concentration.

6.2.3 Dark-field- and transmission electron microscopy

For the experiment, confluent cells were incubated with a fixed concentration of 14.8 μg/ml of gold, corresponding to 10^4 gold nanorods or 2×10^3 gold nanospheres per cell.[29] After 20 h incubation, cells were trypsinized, fixated and embedded in an epoxy resin for preparation of cell sections for dark-field (DF) and transmission-electron-microscopy (TEM). For fixation, cells were incubated for 1 hour with 3 mL of 2.5 % glutaraldehyde in cacodylate buffer (0.1 M sodium cacodylate and 0.1M sucrose at pH 7.4), washed three times with cacodylate buffer, incubated for 1 h with 1 mL of 2 % osmium tetroxide (OsO_4) in cacodylate buffer, and finally washed two times with deionizedwater. For embedding, these cells were exposed to 2 wt % agar, which was dehydrated using an increasing ethanol concentration (30 %, 50 %, 70 %, 80 %, 96 %, absolute), and transferred into araldite epoxy resin with the help of propylene oxide. The resin was polymerized by heating to 65°C for three days. Cells in resin were cut in 1 μm or 50 nm thick sections using a Reichert Ultracut S ultramicrotome. Thin sections of 1 μm thickness were placed on freshly cleaned microscope slides for optical dark-field

microscopy and ultra-thin sections of 50 nm thickness were transferred to copper grids for TEM. Contrast enhancement of biological tissue for TEM was achieved by incubation of the sample in a solution of 2 % uranyl acetate in 50 % ethanol for 2 min[32] and a lead salt solution prepared according to a modification of Sato´s method for 2 min.[33] Before investigation in the TEM, samples were rinsed thoroughly with deionized water and dried in air.

6.2.4 Cytotoxicity assay, immuno-/fluorescence-microscopy

The MTS cytotoxicity test has been applied according to the manufacturers' protocol (Promega, Mannheim, Germany).[14] Briefly, cells are grown to a predetermined optimal number of 12 000/well in a 96-well plate and subsequently incubated with eight different concentrations of nanoparticles for 24 or 48 h. Washing is carried out three times with PBS and full medium before adding the MTS agent. Control experiments were carried out using cell-free wells and fully vital cells. The cells are incubated with the tetrazolium educt for 45 min and absorbance is determined using a 96-well plate photometer at a wavelength of 490 nm. The color change is a direct measure of the cell's metabolic activity due to the reduction of MTS educts to formazan by the action of mitochondrial dehydrogenases. Experiments are done in triplicate.

Immunostaining and fluorescence microscopy are applied to monitor alterations in the cell cytoskeleton and cell-cell contacts upon nanoparticle exposure. Therefore, MDCKII cells are grown to confluence on petri-dishes and afterwards incubated with nanoparticles for 24 h. For actin and microtubules staining, washing with PBS and fixation is carried out by immersing the cells into a -20 °C cold acetone/methanol mixture (1:1 vol %) for 10 min. Afterward, the cells are washed three times with PBS, nonspecific binding sites saturated with FCS, and incubation in staining solutions carried out according to the manufacturer's recommendation: Alexa Fluor-546 phalloidin (invitrogen, Paisley, UK) is used for f-Actin staining, Alexa Fluor-488 conjugated IgG1 anti-β-tubulin (BD Bioscience, Heidelberg, Germany) from mouse for labeling microtubules, 4',6 diamidino-2-phenyindole (DAPI, Sigma-Aldrich, Seelze) for nucleus/DNA labeling, and polyclonal IgG1 mouse antibody (Zymed Gmbh, Munich) followed by Alexa Flour-conjugated goat-antimouse IgG1 antibody (BD Bioscience,

Heidelberg, Germany) are used for staining tight junctions (ZO-1 staining). Staining is carried out for 30 min at room temperature, and cells are washed subsequently.

Oxidative stress was proven by life cell staining of cells after 24 h exposure to GNPs: 5-(and-6)-chloromethyl-2'7'-dichlorodihydrofluorescein-diacetate acetyl ester (CM-H2DCFDA) (Molecular Probes, Invitrogen) was added to GNP-treated cells and the following controls carried out: besides autofluorescence of untreated samples and GNP treated, but unstained cells, positive controls (inflammation induced by 0.03 v/v% H_2O_2 treatment for 30 min before staining) and negative controls (cells treated with anti-oxidant resveratrol (50μM) and 0.03 vol% H_2O_2) are carried out. CM-H2DCFDA appears green when oxidized by ROS; Co-staining with DAPI was applied to illustrate the topology of the cell-monolayer.

YO-PRO-1 and propidium iodide were applied for monitoring apoptosis and necrosis. 1 μl of YO-PRO-1 iodide(491/509 nm, Molecular Probes, Invitrogen), and 1 μl of propidium iodide (P3566, Molecular Probes, Invitrogen) were diluted in 1 ml of culture medium and, after PBS-washing, 400 μl were added to 600×10^3 adherent cells and incubated for 30 min., whereafter washing and observation occurred. Positive controls adopting optimized 10 μM staurosporine for apoptosis induction and negative controls adopting 10 μM caspase 3/7 inhibitor Ac-DEVD-CHO (Sigma Aldrich, Germany) were computed.

For fluorescent mitochondria potential staining, after GNP incubation, 400μL JC-1 stain (Molecuar Probes, Invitrogen) at 1 μg/ml concentration was added to 600×10^3 adherent cells and incubated for 30 min at 37°C. Cells were rinsed, mounted in fresh culture medium and analyzed by fluorescence microscopy. Untreated cells with polarized mitochondria served as negative controls.

Examination occurs under an upright Olympus fluorescence microscope (Olympus BX51, 40 or 100 × water immersion (0.8 or 1.0 NA), Germany), equipped with a color camera (3 MP, DP71) and a dark-field condenser. Distribution of gold nanorods is visualized by dark-field microscopy, where plasmon resonance leads to green (spheres), red (rods) or orange to white (aggregates) appearance.

6.2.5 Atomic force microscopy

Imaging was realized by using atomic force microscopy (AFM) in contact mode applying minimal forces to the cells (pN-regime). Therefore, images were taken in HEPES-buffered medium (Minimal essential medium (MEM), Biochrom, Berlin, Germany) after equilibrating the system for one hour. A NanoWizard® II AFM (JPK Instruments AG, Berlin) setup was combined with an inverse optical microscope (Zeiss Observer D1) was used with commercialy available silicon nitride cantilevers (k_{24h} = 54.1 mN/m and k_{48h} = 29.7 mN/m) (Veeco, MLCT-AUHW). For observing the cells under physiological conditions (37°C) a fluid cell (Biocell™, NanoWizard®, JPK Instrument AG, Berlin) specially designed for this AFM was used. The images were recorded with a scan rate about 0.5 Hz.

6.3 RESULTS

6.3.1 Exposition of GNPs to epithelial cells – Influence of surface chemistry on viability and adhesion

The objective of this study was to elucidate whether shape dependent cytotoxicity of rod- and spherical-shaped gold-nanoparticles exists (r/sGNPs). We employed acoustic resonator setups as well as impedance spectroscopy, accompanied by classical imaging techniques as fluorescence or darkfield and TEM/AFM imaging to draw a comprehensive picture of the impact of GNPs on epithelial cells. We recently showed that metabolically driven micromotion of confluent cells adherent on gold-microelectrodes monitored via ECIS serves as an indicator for dose-dependent nanoparticle toxicity for various nanoparticles: semiconductor quantum-dots[27], synthetic HPMA-nanospheres[34] and multifunctional, spherical magnetic MnO-nanoparticles.[35]
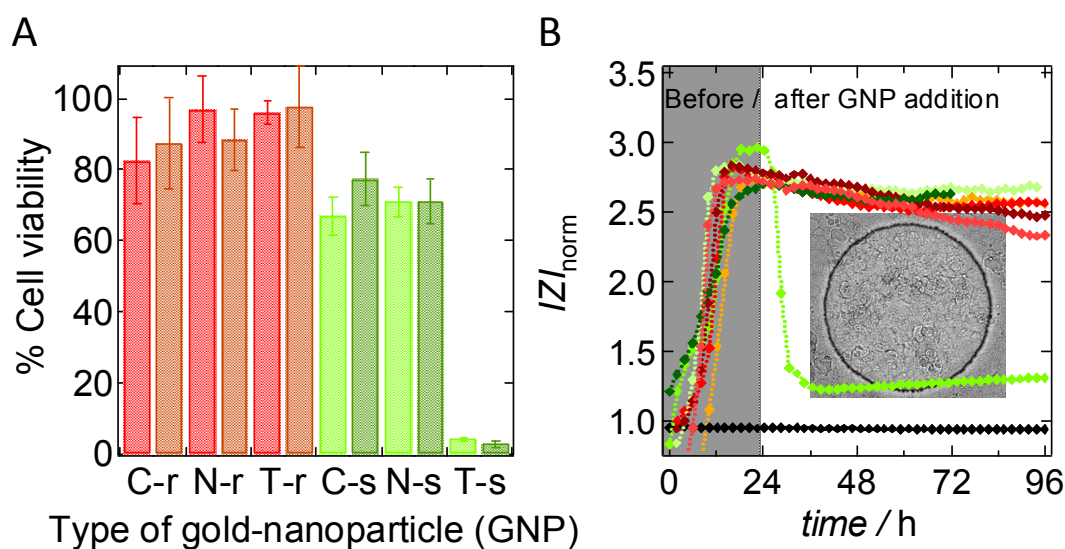

Figure 6.2 A) MTS-test for mitochondrial activity at two concentrations for various functionalizations and two shapes of GNPs: Bright/dark red: 6/9 µg/ml gold rods (r), bright/dark green 6/9 µg/ml gold spheres (s); C denotes COOH-PEG-termination of GNP, N is NH$_2$-PEG termination, T is for CTAB-coated particles. At both concentrations, three toxic levels are found (increasing order): rods<C and N-s< T-s. Error bars represent one standard deviation. B) Time courses of impedance IZI normalized to starting values derived from mean values of micromotion-datasets for exposition of cells to 9 µg/ml GNPs: ◆ untreated cells, ◆ empty electrode, ◆ T-s, ◆ T-r, ◆ N-s, ◆ N-r, ◆ C-s, ◆ C-r. |Z| serves as a measure for adhesion and spreading of cells and is reduced for T-s treated cells; light micrographs indicate cells fixed to electrode (inlet, diameter of 250 µm).

In a first step, the effect of low-dose GNP-treatment of MDCKII cells are shown. *Figure* 6.2A summarizes the cells` viability after 24h GNP-treatment for six different categories as obtained from the classical cytotoxicity test (MTS) for 6 (red/green) and 9 (dark red/green) µg/ml gold concentration: PEGylated rods with carboxy-(C-r) or amino-(N-r) termination, as well as the detergent coated CTAB-rods (T-r) reduced the mitochondrial enzyme activity by 18 percent at most, while the same surface modifications for PEGylated spheres (C-s, N-s) reduced the viability almost twice as much to values between 60 and 75. The spherical CTAB-coated particles (T-s) displayed the highest toxicity in this concentration regime with cell viabilities close to zero. To corroborate this findings with a real-time assay, cell-substrate sensing bioelectrochemical (ECIS, *figure* 6.2B) or bioacoustic (D-QCM, *figure* 6.3) techniques were applied. *Figure* 6.2B depicts the time course of the impedance $|Z|$: while this parameter provided insight in adhesion and insulating behavior of the entire cell monolayer, we were not able to discern between exposition to any rGNPs or PEGylated sGNPs; just the T-s application proved to be distinct, hereby producing a drop in cells` impedance of nearly 60 %. No cells were found to desorb from the gold surface, as comparable to permeabilizing aceton/methanol-treatment (inlet: T-s treated cells on a 250 µm-diameter ECIS electrode) and the monolayer seems to be intact. D-QCM results,

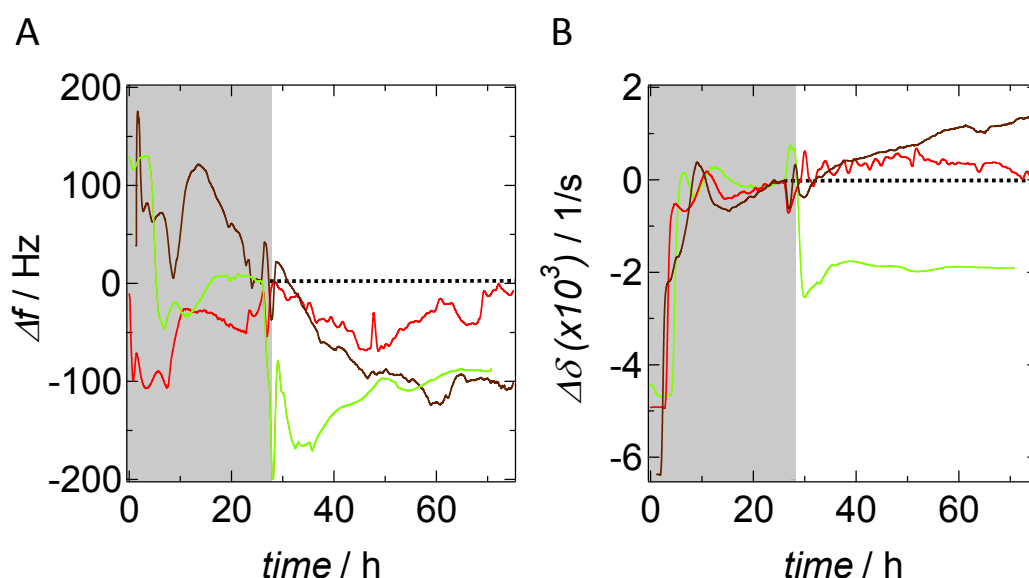**Figure 6.3** D-QCM time courses of Δf (A) and dissipation $\Delta\delta$ (B) for 6-7×10^5 contact-synchronized MDCKII cells treated with three GNP categories (shaded area before addition) distinguishable by classical MTS vitality assay. ◆ T-s, ◆ T-r, ◆ N-r. Dissipation allows to discern three viscoelastic categories and indicates uptake of T-s and T-r as well as proliferation inhibition.

(not shown) indicate that only the T-s category elicits a distinct effect on frequency (Δf) and dissipation ($\Delta\delta$) time shifts, corresponding to increased mass and elasticity.

6.3.2 Cell substrate dynamics as a function of GNPs exposition – Concentration dependent toxicity and particle uptake

Recently, we reported on impedimetric and acoustic toxicity and motility assays based either on ECIS micromotion or viscoelastic fluctuations displayed by shear oscillating quartz resonators. We could unequivocally show that ECIS micromotion is suitable to detect subtle changes in biological activity due to exposure of adherent cells to nanoparticles as well as F-QCM is appropriate to fingerprint specific cell-substrate dynamics correlated to forming and decomposing of focal contacts. Here, we adopted the two inherently different assays to elucidate the dose-uptake relation of GNPs as a function of surface chemistry and particle shape.

Figure 6.4A summarizes ECIS micromotion of MDCKII cells exposed to various GNPs at 9 µg/ml. Generally, greenish lines denote spherical particles, while reddish colored lines represent rod-like particles. Vital untreated cells (orange lines) and those treated with PEGylated rGNPs were virtually indistinguishable while T-r reduced viability by roughly 40 %. Spheres at the same concentration exhibit higher cytotoxicity. Even C-s displayed a reduction in vertical motility to 25%. However, N-s did not affect the cells` micromotion as compared to untreated cells. In summary, at this comparable low concentration (see below), micromotion measured by ECIS is significantly susceptible to sGNP exposure. We also carried out F-QCM-noise analysis in order to monitor viscoelastic fluctuations as a response to particle uptake. *Figure* 6.4B shows frequency fluctuations for all GNP categories at a concentration of 6 µg/ml. It is clearly visible, that all rGNPs reduced the viscoelastic fluctuations to a smaller extent than their spherical counterparts, where the fluctuations are reduced to the level of the medium-filled D-QCM-chamber in the absence of living cells. For N-s, recovery effects were observed setting in after 48 h of incubation (marked by arrow). These results are very similar to the fluctuations recorded with the ECIS-setup (*figure* 6.4A), although slight differences on a subtoxic level could be found: rGNPs presented higher toxicity on the ECIS assay, while N-s have no impact on shape fluctuations recorded with the impedance setup. These differences are summarized in *figure* 6.4C for ECIS and MTS data on a broad

concentration range at classically available time intervals. Reduction of viability was found for spherical and rod-like CTAB-GNPs as well as for C-s, albeit at higher concentrations. In general, micromotion recorded by ECIS is much more sensitive to the impact of particle exposure
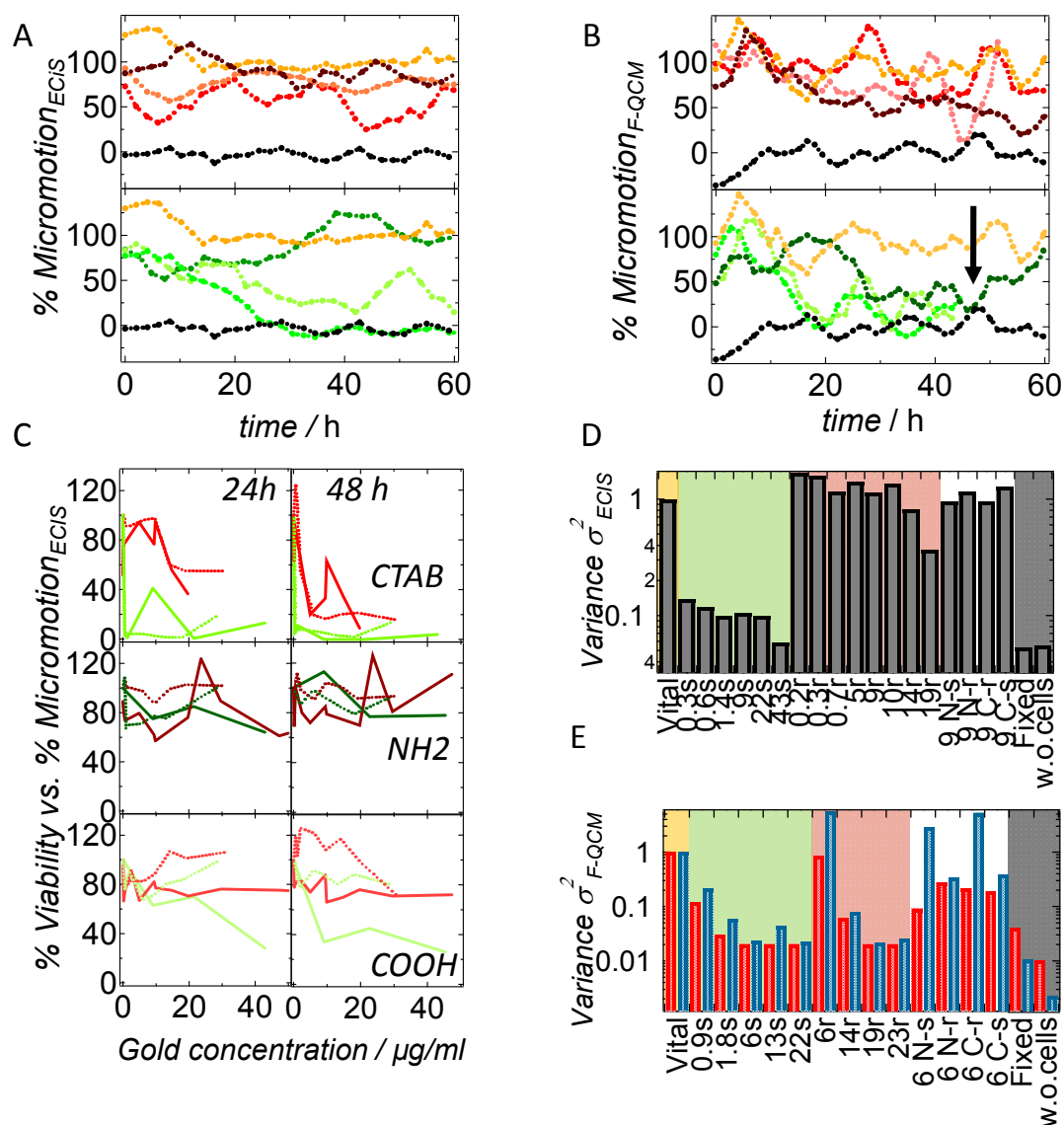

Figure 6.4 A) ECIS-micromotion time courses for GNP treated MDCKII cells (9 µg/ml): NH_2-PEG-rods (●), COOH-PEG-rods (●), CTAB rods (●), NH_2-PEG-spheres (●), COOH-PEG-spherers (●), CTAB-spheres (●) as well as references: untreated cells (●) and noise generated from bare electrodes immersed in culture medium (●). B) F-QCM micromotion for GNP exposed MDCKII cells (same colour code as under A). C) Nanocytotoxicity of GNPs as determined by micromotion compared to MTS as function of concentration. D) and E) Variance analysis of ECIS *IZI* time courses (*D*) or F-QCM Δf and $\Delta \delta$ fluctuations *(E)* after 24 h intervals, as a function of concentration for the CTAB-GNPS (red/green) and for 6 or 9 µg/ml for PEGylated particles (white). Vital (orange) and GDA-fixed cells and cell-free electrodes (black) as reference. Normalized for both setups to the vital cells` variance level.

than the classical photometric MTS assay, while F-QCM evaluated by PSD-analysis are less sensitive. In the case of T-s, toxicity is so strong, that sensitivity discrepancies between the first two assays reduce for the 24h interval. *Table* 6.1 summarizes the results in IC_{50} values for the GNPs found to be toxic.

Table 6.1: IC_{50} values of gold-nanoparticles after 24 h and 48 h exposition to MDCKII cells as determined by MTS, ECIS-micromotion and F-QCM-PSD-fluctuation analysis; values are given in µg/ml. Mean SD ± 0.1 for MTS, ± 0.15 for micromotion $_{ECIS}$ and ± 0.5 for micromotion $_{F-QCM}$

Nanocytotoxicity assay	IC_{50} T-s (24/48 h)	IC_{50} T-r (24/48 h)	IC_{50} C-s (24/48 h)
MTS	0.3 / 0.3	- / 1.8	- / -
Micromotion $_{ECIS}$	0.2 / 0.1	16.3 / 1.1	31.8 / 6.9
Micromotion $_{F-QCM}$	1.5 / 2.3	16.0 / 12.0	- / -

A simplified way to analyze fluctuations in impedance, frequency or dissipation time courses is variance analysis, applied here both to ECIS and D-QCM fluctuations; *figure* 6.4D and E summarizes the 24 hour variance values for the ECIS in-phase voltage fluctuations and F-QCM`s Δf and $\Delta \delta$ shifts for all GNPs: in general, the variance of ECIS in-phase fluctuations, Δf and $\Delta \delta$ decreased with increasing dose of T-s and T-r with variance$_{ECIS}$ being more sensitive to toxic effect than variance$_{F-QCM}$; T-s produce stronger reduction in fluctuation amplitude at almost ten-fold smaller concentrations than T-r. At higher particle concentrations, variance becomes insensitive to increasing the dose in contrast to power density spectra analysis of frequency fluctuations, speaking in favor of a combined analysis. Fixated cells exhibiting no viscoelastic fluctuations present variance values comparable to that one of cell exposed to high concentrations of GNPs, while cells exposed to PEGylated particles present the same variance range as fully vital cells.

Uptake and fate of gold nanoparticles was followed by combined optical dark-field and transmission electron microscopy. While DF was performed on 1 µm thick slices (*figure* 6.5, 1), a thickness of only 50 nm was used for TEM-analysis. Exemplary, *figures* 6.5, 1 and 2 show the uptake of T-s by MDCKII cells. A thorough study of this method to quantify the uptake of GNPs is on the way (Rosman *et al*).[29] The results indicated the following uptake sequence of particles per cell: 3000 T-r > 2300 T-s > 150 N-r > 16 C-r > 5 C-s/N-s. The amount of gold taken up by the cells is, however, shape
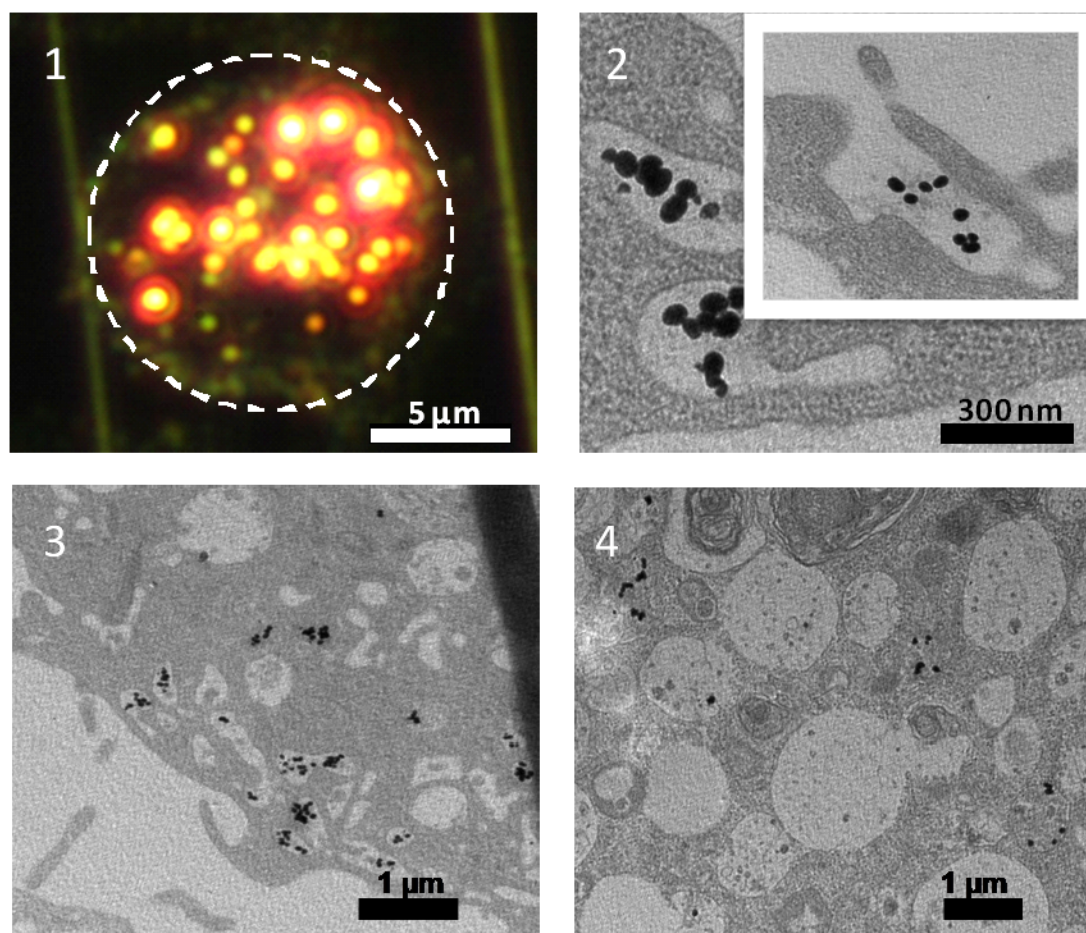
Figure 6.5 A) Dark-field image of 1 µm thick slices after T-s incubation for 20 h, indicating aggregates (yellow and orange) single spherical GNPs (green) within cell boundaries. B) TEM image of T-s treated cells depicting macropinocytosis of singular particles (inlet) and aggregation inside early endosomes. C) TEM-slice of an MDCKII cell undergoing vacuolization upon GNP-uptake/particle aggregation inside multivesicular bodies. D) TEM-image of cells presenting initial T-s escape from multivesicular bodies or late endosomes/lysosomes and severe blebbing as well as vacuolization (incubation time for D-F is 20 h.)

dependent: we found a higher gold amount in the case of the sGNPs as compared to rGNPs. As qualitative TEM analysis is concerned, the inlet in *figure* 6.5, 2 shows a typical unspecific uptake pathway: macropinocytosis.

Moreover, we found that particles aggregate mainly inside early endosomes forming clusters of 48 ± 18 (T-r) or 44 ± 12 (T-s) particles/aggregate, although the *number* of T-s aggregates is 1.3 times higher than for T-r. In *figures* 6.5, 3 and 4, two other cells of the same sample are shown. The cell in *figure* 6.5 3 shows initial vacuolization, which we assume to occur due to CTAB desorbing from aggregating particles. This implies that GNPs serve as carriers for toxic CTAB, as presented previously.[14] Another process is visible in *figure* 6.5, 4 besides the aggregates in late endosomes or lysosomes, initial

endosomal escape and severe vacuolization indicative of cell stress and necrosis can be observed. Aggregation of GNPs in endosomes is also found for CTAB-rods, but they stay locked in lysosomes. Strong vacuolization, however, is not found for any other GNP type besides T-s.

6.3.3 Adverse effects of GNP exposition - Reactive oxygen generation and cytoskeletal integrity

The molecular reason for changes in cell motility and/or viscoelasticity is the cytoskeletal integrity. Hence, we investigated by fluorescence microscopy integrity of actin or microtubule filaments under GNP influence. Additionally, cell stress upon GNP incubation as presented upon production of reactive oxygen species (ROS) was followed. Appendix *figure* 6.S.1 summarizes the corresponding controls. Fluorescence micrographs in *figure* 6.6 A depict the proinflammatory reaction presented upon various GNP exposures; the presence of hydrogen-peroxide ROS species produces green fluorescence and is initially mitochondria-associated. *Figure* 6.6 A 1 showed 6-7×10^5 cells treated 24 h with 6 µg/ml N-r: this non-viability reducing category presents no ROS-signs and therefore equals the control with untreated cells. *Figures* 6.6 A 2 and 3 show a slightly increased ROS level found mainly at single spots, for 6 µg/ml C-s and T-r treatment, whereas only in *figure* 6.6 A 4 (T-s), severe ROS-generation, both at multiple single subcellular (mostly perinuclear) spots as well as on fully fluorescent cells level was found. The ROS-level found for the positive control, after treatment of cells with 0.03 % H$_2$O$_2$-solution for 0.5 h (*figure* 6.S 1), is, however, substantially higher.

Figure 6.6 B shows results of the combined Alexa-546-Phalloidin staining for f-actin, immunofluorescence staining of microtubules with alexa-488-marked mouse-anti-ß tubulin and DAPI-DNA staining of the nucleus. The fluorescence micrographs of are splitted diagonally: the control (*figure* 6.S 1) at 24h after reaching confluence (48 h after seeding) shows a cortical actin ring, long stress fibers and dense crosslinked cytosolic actin; thick bundles of microtubules were found around the nucleus and homogenous distributed in the whole cell. After 24 h of incubation with N-r, as compared to C-r and N-s (data not shown), microscopic images do not differ from this state, as shown in *figure* 6.6 B 1 for the concentration of 2 µg/ml. C-s, however, show a slightly reduced
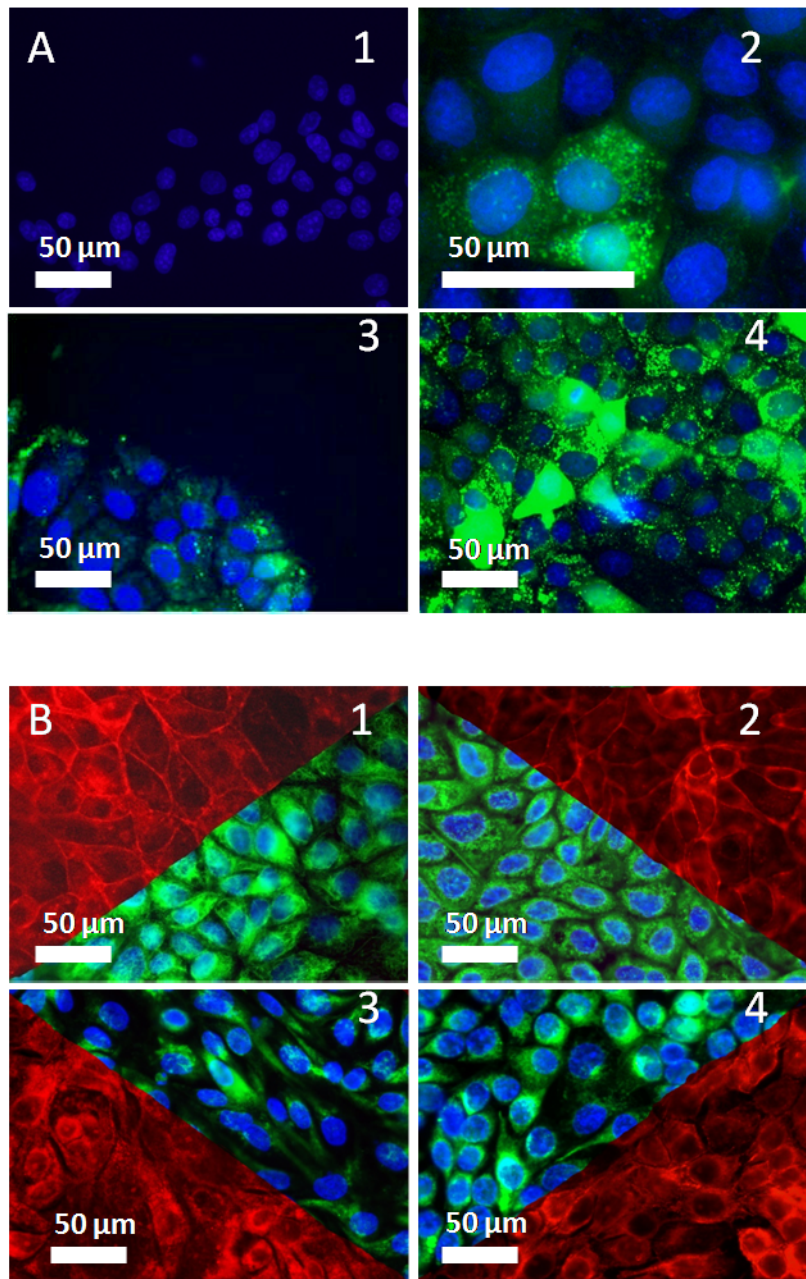
Figure 6.6 Fluorescence light microscopic images after co-staining of actin, microtubules, nucleus and/or reactive oxygen species. A) Typical, qualitative view of proinflammatory ROS generation upon GNP exposition (24 h, 6 µg/ml per GNP category, CM-H2D-CFDA-staining). Clockwise: N-r (1), C-s (2), T-r (3), T-s (4), scale bar is 50 µm.
B) MDCKII cells exposed to low dose GNP treatments (clockwise : 3,5 µg/ml NH_2-PEG rods, 2 µg/ml COOH-PEG-rods, 3 µg/ml CTAB rods, 3 µg/ml CTAB spheres), imaged after 24 h incubation.

microtubule-network integrity at a concentration of 3.4 µg/ml : the usually long fibers are regularly interrupted, but still visible (*figure* 6.6 B 2). In the case of the T-r (*figure* 6.6 B 3), the cortical actin ring is partially interrupted and spacing between the cells is increased, probably due to the missing anchoring; the microtubules degradation is stronger than in the case of C-s, but still single long fibers in the cell extensions were found. In the case of T-s (*figure* 6.6 B 4), applied in a comparable concentration, whole stress fibers are missing and the cortical actin ring has vanished. The degradation of the dense network is accompanied by large intercellular clefts; microtubules are only found

in perinuclear arrangement, indicating complete degradation in the cytoplasm and/or storage of monomers in Golgi-associated vesicles. Therefore, it is safe to assume that the origin of variations (ECIS and QCM) in motility reflects the partially degraded cytoskeleton as a result of GNP exposure (see *chapters* 4 and 5).

6.3.4 Secondary damage of GNP exposition - Mitochondrial permeability transition and apoptosis induction

As we have presented before, oxidative stress especially upon T-s and T-r treatment occurs and therefore may trigger oxidation of a wide array of proteins and lipids. An amplification cascade of ROS damage occurs often upon severe stress, especially when mitochondrial components are oxidized. Mitochondrial permeability transition pores (MPT pores) may open and lead to disturbed electron transport, radical generation and loss of membrane potential. Additionally, solvents below 1,5 kDa, i.e. antioxidants as glutathione, may evade and therefore reduce ROS neutralization efficiency of mitochondria. Ultimately, such an increase of membrane permeability can lead to programmed cell death by cytochrom C efflux and the following apoptosom activation cascade.

The fluorescent dye JC-1 detects MPT and accumulates in mitochondrial intermembranes of viable cells, where it dimerizes to a red fluorescent product. MPT-leakage sets JC-1 free into the cytosol, where the monomer presents green fluorescence. *Figure* 6.S. 2 A-C shows JC-1 staining of polarized mitochondria in untreated cells, whereas *figure* 6.7 presents JC-1 staining for 12 and 24 hours of CTAB-GNP exposition at 6 µg/ml: after 12 hours, T-s damaged the majority of mitochondria (*figure* 6.7 lower row), whereas even after 24 hours only a slight loss of JC-1 dimers in combination with detection of the monomer is found for T-r (*figure* 6.7 upper row). Often, we found damaged and healthy specimen within one cell, as can be seen in T-s treated mitochondria at higher magnification (*figure* 6.7 right image in lower row).

Interruption of electron transport and ATP synthesis either may lead to fast necrosis or gradual apoptosis, thereby implying a possible dose-dependency. We assessed the pathway of cell death by using vybrant apoptosis assay: here, living cells exhibit little to no green fluorescence, apoptotic cells appear green (due to the first dye component YoPro) and propidium iodide labeled, dead cells appear red and eventually
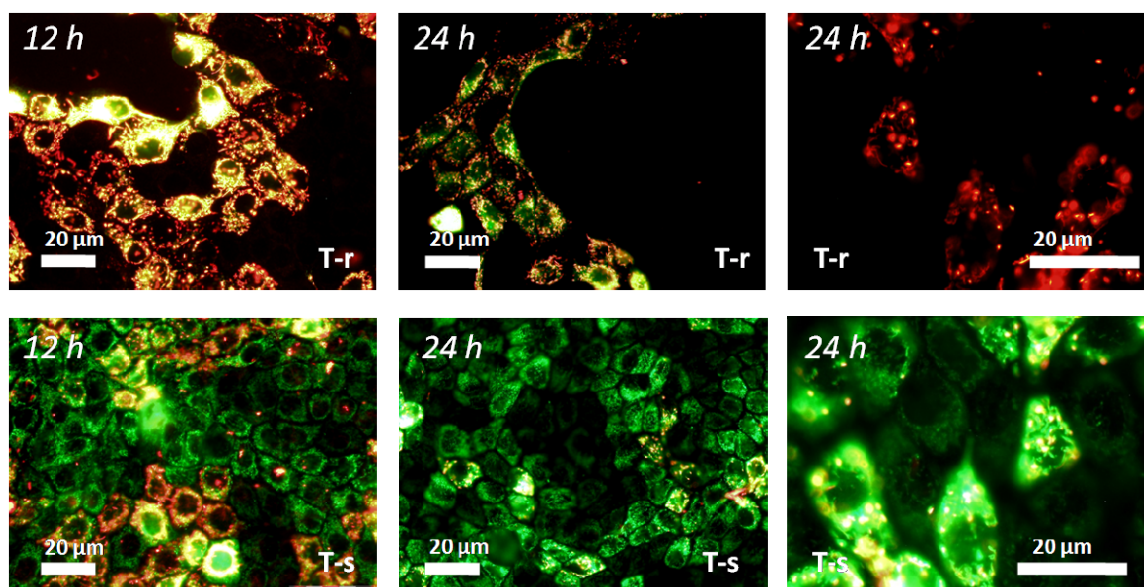
Figure 6.7 Mitochondrial potential staining JC-1 depicting mitochondrial depolarization after incubation with 6 µg/ml T-r (upper row) or T-s (lower row). Red fluorescent dots mark dimerized fluorophor in intact mictochondrial intermembrane, while green staining indicates depolarization and mitochondrial permeability transition (MPT), whereupon green JC-1 monomer is released into the cytopsol. Hours of incubation with GNPs are given. Note that even after 24 hours of progressive MPT, some mitochondria retain polarization (left column zoom in).

green, too (mainly yellow in images due to the overlay of both channels). As the staining itself relies on changes in cell permeability occurring with time, dead cells are either indicative of secondary apoptosis (yellow) or direct necrosis (red). *Figure* 6.S. 2 D-F displays controls for staurosporine (a prototypic apoptosis inductor) induced apoptosis after 12 hours (D, only green fluorescence found) and secondary apoptosis after 24 hours with apoptotic bodies and fluorescence in both channels, red and green. A second set of controls is depicted in *figure* 6.S. 2 G-I, where caspase inhibitor Ac-DEVD-CHO was administered; all three images are taken after 24 hours and only slight to no green fluorescence indicates direct necrosis. Since apoptosis is predominantly caspase-dependent, it is blocked and necrosis not. As for JC-1 staining, in this set of experiments just T-s and T-r were analyzed. *Figure* 6.8 shows exemplary results of CTAB-GNP exposition and cell death pathways. Cells are unaffected at 0.5 µg/ml T-r and mainly underwent apoptosis upon 1.5 and 15 µg/ml T-r treatment, as most cells appear green or yellow (upper row).However, a small amount of cells shows necrosis and secondary apoptosis, probably due to the 24 h time interval. We found a significant higher amount of dead cells under T-s influence at comparable concentrations of 0.5 and 1.5 µg/ml with

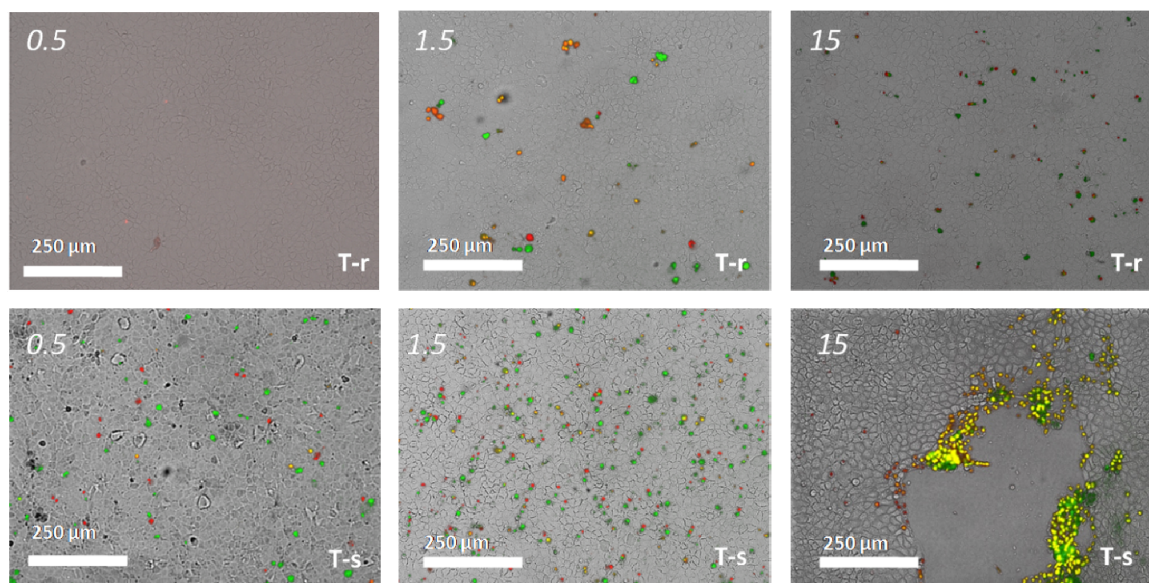**Figure 6.8** Fluorescent vybrant apoptosis assay after 24 hours of T-r or T-s incubation, concentrations given in µg/ml. Green cells are apoptotic, red celss underwent direct necrosis and yellow cell are dead after reaching secondary apoptosis. Both GNPs are inducing concentration dependent cell death with T-s provoking more necrotic cells.

slightly more apoptotic than direct necrotic cells. At 15 µg/ml T-s treatments, cells start to detach and residual cells mainly present secondary apoptosis at detachment sites. As results are only qualitative, quantification via FACS is aimed for in current studies.

6.3.5 GNPs influence on cell-cell contacts – Barrier breakdown and recovery after exposition

So far we investigated the influence of GNP exposure to cells on their adhesion/spreading and cell-substrate dynamics. In this section, we concentrate on cell-cell anchorage-integrity as a function of particle concentration, shape, and functionalization employing TER monitoring and fluorescence microscopy. The orange line in *figure* 6.9 A represents the positive control, i.e. the change in TER $\Delta R_{b,norm}$ of living cells. Since TER is, by definition, only valid for confluent cell layers, light micrographs were recorded to follow the stages until confluence (data not shown). After reaching the stage of confluence (grey), thus 15-24 h after seeding, the addition of T-r (0,6 µg/ml) leads to a decrease in the TER of 30 % as compared to untreated controls, followed by a recovery to the normal level 24-30 hours after addition (red open squares). By applying the same concentration of T-s (green open squares), the reduction of the TER to zero level occurs within 18-20 hours without recovering of the barrier. Increasing T-r
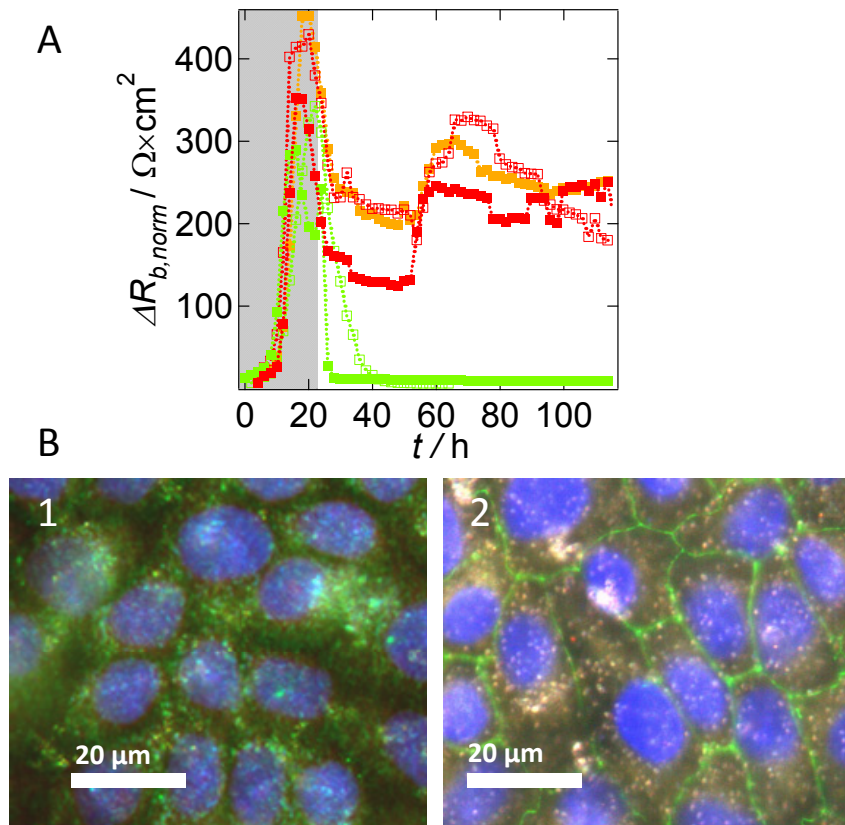
Figure 6.9 A) Time course of $\Delta R_{b,norm}$, a measure for the transepithelial resistance, assessed at two toxic GNP concentrations: 0,6 µg/ml (□) or 9 µg/ml CTAB-spheres (■); 0,6 µg/ml (□) or 9 µg/ml (■)CTAB-rods. Addition of CTAB-GNPs to established MDCKII cell monolayers after 24 hours. As references: untreated cells (■). The dotted line is added to guide the eye. B) Overlay of dark-field images and fluorescence images with ZO-1/e-cadherine staining and nucleus staining after 24 h incubation with T-s (1) or T-r (2). Due to Plasmon resonance, single spherical particles appear green, rod-shaped particles red and aggregates orange to white.

concentrations by a factor of 15 to 9 µg/ml results in a more pronounced decrease of the TER but partial recovery is still not suppressed. T-s added at a concentration of 9 µg/ml lead to an immediate loss of the barrier function within 2-4 hours after exposition (again without recovery). It can be therefore deduced, that TER is extremely sensitive to concentration and shape variations of added nanoparticles. Moreover, the time course of the TER shows recovery of cells if exposed to rod-like particles. To corroborate this recovery recorded with the ECIS setup, immunofluorescence of the cell-junctions was carried out to follow their integrity (*figures* 6.9 B and 6.10 B) using either ZO-1 (tight junctions) or e-Cadherine (adherens junctions) staining.
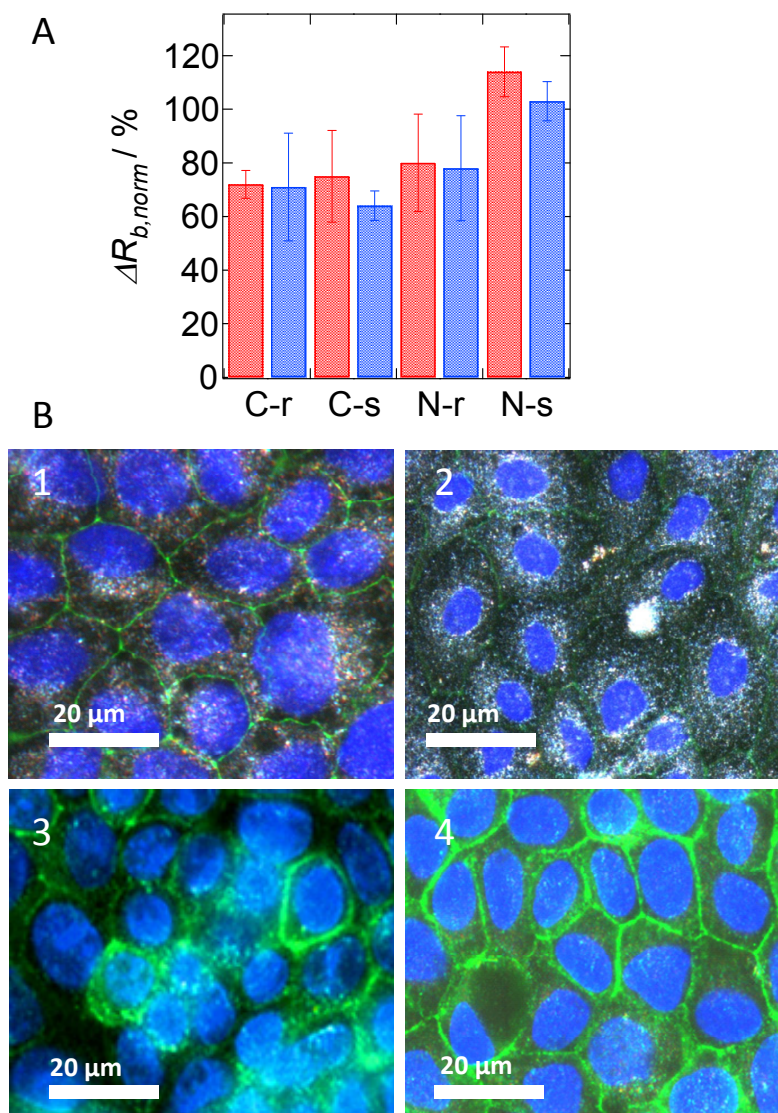
Figure 6.10 A) Percentage $\Delta R_{b,norm}$ for MDCKII cells incubated with biocompatible PEG-GNPs for 24 hours in reference to untreated cells: 9 μg/ml (■) or 21 μg/ml (■) treatment. B) Overlay of dark-field images and fluorescence images with ZO-1/e-cadherine staining and nucleus staining after 24 h incubation with all four PEGylated GNP categories: 1 C-r, 2 N-r, 3 C-s, 4 N-s.

In the case of exposure to gold- nanorods, darkfield and fluorescence microscopy images (bright spots are aggregates, red spots single particles) were merged. Intact tight junctions found for cells exposed to 6 μg/ml T-r (*figure* 6.9 B 2). Addition of 91 μg/ml T-r results in partial cell desorption from the electrodes and ZO-1 staining gets discontinuous (data shown previously[27]). Therefore, although micromotion has decayed to almost zero and actin as well as microtubules staining reveals cytoskeleton degradation, tight junctions seem to be the most resistant structure. Cell-cell contacts are even maintained when first cells desorb due to toxicity of the high GNP-concentration. In *figure* 6.9 B 1, the impact of most toxic T-s on the integrity of a region

of the cell-cell junctions buried more deeply in the intracellular cleft, the adherens junctions, is followed. The combined darkfield/fluorescence approach allows identification of individual gold particles. Cell-cell contacts were entirely destroyed as expected from TER readings. In summary, cell-cell contacts are severely damaged if cells were exposed to T-s in contrast to detergent coated T-r, where TER-recovery was found after 50h from seeding, even at elevated concentrations. In fact, while at exposure to T-r cells rather detach than cell-cell contacts were destroyed, incubation with T-s leads predominately to dissolution of tight junction and cells remain attached to the surface.

Apart from detergent coated particles, also the impact of PEGylated ones on the barrier function of in-vitro cultured epithelial cell monolayers was investigated. *Figure* 6.10 A shows the TER as a function of concentration and shape (9 µg/ml in red and 21 µg/ml in blue) for a 24 h interval. The corresponding darkfield/fluorescence images for localization of GNPs and visualization of cell-cell contacts are shown in *figure* 6.10 B. Impedance spectroscopy indicates comparable effects of carboxylated GNPs and amino-terminated GNPs on $\Delta R_{b,norm}$ for a 24 h interval: a decrease to values between 65 and 85 % of the untreated cells` TER can be found for the three categories C-r, C-s, and N-r at both concentrations, while amino-terminated PEGylated spheres even increase the TER to values slightly above the control (128 percent for 9 µg/ml). Therefore, the PEGylation does not only ensure biocompatibility concerning the cellular motility, but also concerning cell-cell linkage. At higher concentrations of C-s (21 µg/ml), which results in a reduction of cellular micromotility below 50 %, the TER is decreased by 20 %. Fluorescence micrographs support the biocompatible effects of PEGylated particles (see *figure* 6.10 B): both ZO-1 and e-Cadherine staining show continuous lines in cell monolayers, with occasional vesicular localization for C-s in perinuclear regions, whereas in the case of N-s, e-Cadherine is located homogenous at the cellular borders. Additionally, perinuclear arrangement of PEGylated rods appearing red or aggregates appearing white is more evident than in the case of greenish spheres distributed randomly on the cells and in the cytoplasm.
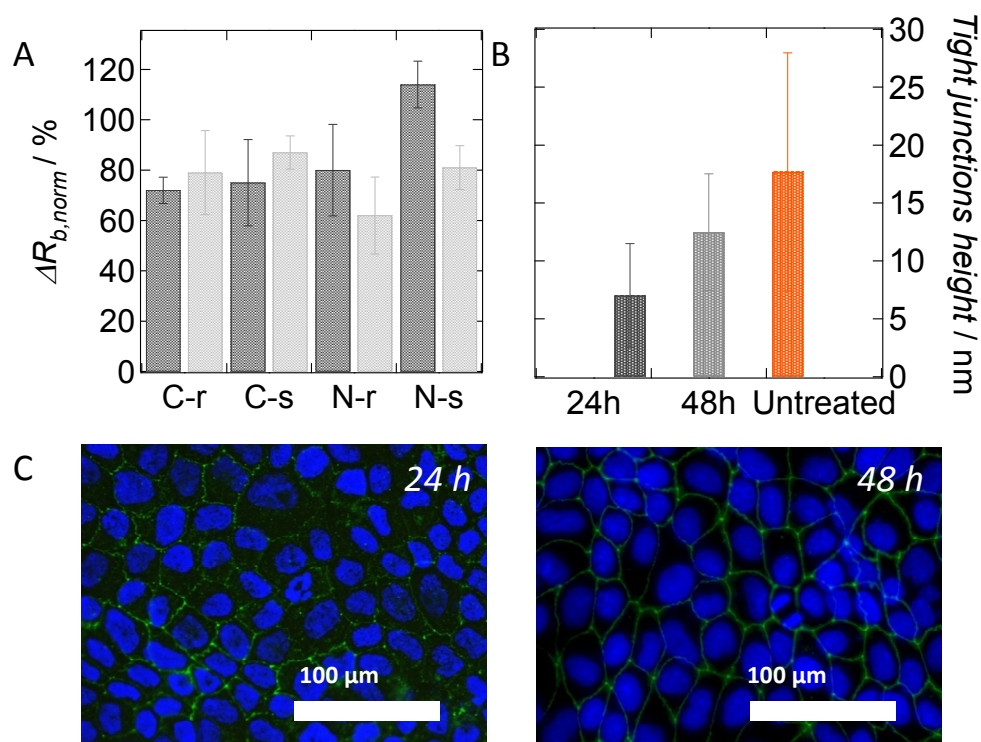
Figure 6.11. TER upon exposure with 9 µg/ml PEGylated rods indicating transient epithelial barrier leakage and/or recovery from GNP treatment. A) TER after 24 h (black) or 48 h (grey) incubation indicating TER reduction for amino-terminated and recovery for carboxylated PEG-nanoparticles. B) Tight junction-height for 4 µg/ml C-r incubation over 24 and 48 hours compared to TJ-height of untreated cells. C) Fluorescence microscopic images with co-staining of DAPI and ZO-1 after 24 h and 48 h incubation with 4 µg/ml C-r.

The recovery of TER after the initial drop is not unique for T-r but was also found for C-s and C-r. *Figure* 6.11 presents results for the impedance spectroscopy for 24 (dark grey) and 48 (light grey) hours of incubation to GNPs (*figure* 6.11 A) compared to time resolved AFM-(B) and fluorescence imaging of C-r (C). Partial recovery of TER, found for both C-r and C-s, is not observed for amino-PEG particles, which reduce the TER after 48 h exposition to epithelial cells by 10-30%. The AFM imaging employed (*figure* 6.S 3) is presented via the morphological deflection image at comparable imaging forces of 200 pN; the 24h treatment reveals intercellular spacing with slight traces of tight junctions at the location of cell-cell contacts, while the images for the 48 h interval and untreated cells present clear elevations at the cell borders. Besides deflection images, time courses of TER for PEGylated GNPs are assembled in *figure* 6.S 3. The cross-sectional analysis of minimum 5 cells per height image reveals junctional heights of 7/12.5/17.7 nm for these three categories (*figure* 6.11 B). Fluorescence imaging adopted, depicted in micrograph of *figure* 6.11 C, clearly presents non-continuous ZO-1

staining for the 24 h interval, while after 48 h tight junctional homogeneity is restored and therefore supports the results found with ECIS and AFM-imaging.

6.4 DISCUSSION

To study the interaction of nanoparticles with mammalian cells is unquestionable an urgent task considering the increasing number and variety of available particles in the world. Classical cytotoxicity tests addressing the vitality of cells after a fixed time are labor intensive, prone to subjective errors and might not be sufficient to capture subtle changes in the biological activity of cells and are definitely unsuited to monitor the recovery from nanoparticle exposure. In the work presented herein, we scrutinized the toxicity of nanoparticles by monitoring non-invasively cell-cell and cell-substrate dynamics over time employing electrical cell substrate sensing (ECIS) and fluctuation mode quartz crystal microbalance (F-QCM) measurements. Previously, we showed that monitoring micromotion of cells by recording resistance fluctuations using ECIS is generally suited to capture nanoparticle toxicity as compared to classical tests such as LDH or MTS. We found that surface functionalization plays a dominant role in toxicity of gold nanoparticles.

The goal was now to elucidate the impact of shape of the particles on uptake efficiency and cell dynamics comprising cell shape fluctuations and changes in the transepithelial resistance. Rod-like gold nanoparticles with an aspect ratio of approximately 40x20 nm^2 or roughly 2 were compared to spherical ones with the identical coating. A prerequisite for a quantitative comparison is exact knowledge of the uptake efficiency. In a previous publication we introduced an approach based on a combination of dark field and transmission electron microscopy to count the number of particle within a cell. In brief, adding the same amount of CTAB coated gold (particle concentration in µg/ml) to MDCKII cells results in roughly the same number of particles within the cells, i.e. ~ 2000-3000 gold nanoparticles were found per cell if a solution of 15 µg/ml is used. Uptake efficiency of spherical CTAB-coated particles was 4-5 times higher than for rod-like particles exhibiting a bilayer of CTAB, as more spherical gold was internalized. As a consequence we can safely state that given the same number density of CTAB coated particles, spherical ones reduce cellular vitality and dynamics to a substantially larger extend.

Mitochondrial activity screening (24 h interval) for small particle concentrations (below 10 µg gold/ml) showed that CTAB-coated spheres reduce metabolic activity to

zero level, whereas 60-80% of the initial activity is maintained after exposure to PEGylated spherical particles. At these low particle concentrations no significant reduction in viability was found for all rod shaped particles regardless of their functionalization. These results indicate a shape *and* surface chemistry dependence of toxicity.

Following the overall impedance of a gold electrode covered with a confluent MDCKII layer as a function of time, a reduced insulating behavior of the adherent cells was found for CTAB-spheres, while all other GNPs showed virtually no influence. Interestingly, often cells remain attached to the surface although displaying no sign of live anymore.

Particle uptake and cell dynamics. The impact of particle uptake of MDCKII cells on shape fluctuations displayed in F-QCM and ECIS micromotion measurements draws a clear picture in good agreement with biochemical assays of cytotoxicity. Both variance analysis as well as power law dependency of the PSD were employed to quantify cell dynamics from resonance frequency fluctuations (F-QCM) and resistance noise (ECIS). Spherical particles coated with CTAB show the strongest decrease in micromotion. Surprisingly, we found a significant decrease in motility if COOH terminated PEGylated spheres were used in contrast to NH_2-terminated PEGylated spheres and the corresponding rod-like particles. This finding was unexpected due to the natural repulsion expected between negatively charged particles and a negatively charged cell surface. COOH-PEG-spheres showed an IC_{50} value of twice the value found for CTAB-rods contradicting current literature, where no surface charge influences are described due to homogenous coverage by serum proteins. Usually, it is found that positively charge particles show the strongest influence. It has to be noted, however, that we found more amino-terminate PEG-particles inside the cells, and therefore pure uptake efficiency is not the reason for the observed toxic effect. [13, 36, 37, 38, 39, 40] In summary, PEGylated particles show considerably less uptake and as a consequence a drastically reduced toxicity as compared to CTAB coated particles. It remains to be speculated whether COOH-terminated PEG-GNPs might in fact be more toxic than CTAB coated ones if related to their intracellular particle concentration. It was, however, not possible to add

so many COOH GNPs to the medium in order to match the intracellular concentration of CTAB coated GNPs.

Moreover, we were able to find a distinct concentration dependency of the frequency fluctuations for CTAB-GNPs. Upon comparison of IC_{50} values for 24 hours, however, F-QCM viscoelastic fluctuation analysis not only lacks the sensitivity of the ECIS micromotion analysis, but is also less sensitive as the MTS-test. For 48 hours however, recovery effects can be detected both with F-QCM and ECIS, but not with the classical assay.

Simple variance analysis turned out to be more sensitive than evaluating the slope of the power density spectra. This means that the long- term memory of cells is less affected by particles than the fluctuation amplitude. Variance analysis of F-QCM data showed a decrease in motility correlated fluctuations *below* the concentration level where CTAB-GNPs started to influence the PSD-slope.

Proposed explanation for particle toxicity. TEM images were qualitatively analyzed to elucidate possible uptake mechanisms. We found that (after 20h) macropinocytosis prevails as the uptake pathway as expected for these rather large particles. Uptake of particle still occurs after 20 hours, thus continuous accumulation of particles takes place. This is also confirmed by both ECIS and F-QCM fluctuation analysis indicating a continuous rise in cell toxicity. Additionally, we found that MDCKII cells display extensive vacuolization upon GNP-aggregation inside early endosomes or multivesicular bodies in the same time interval. Spheres present particle escape from multivesicular bodies or late endosomes/lysosomes correlated with severe blebbing/vacuolization. MTS-tests of CTAB-particles incubated with cells at 4°C (*figure* 6.12) support this assumption, as almost no toxicity was detected due to the lack of ATP for active uptake; no passive diffusion through the membrane barrier seems to occur. Additionally, this proved that specific interactions with the outer leaflet of the cell membrane were not responsible for the strong toxic effects found for CTAB-GNPs, but uptake correlated effects. Since dark field microscopy and TEM indicated that aggregation of particles occurs inside early endosomes and multivesicular bodies, as also described elsewhere, [13] we believe the dissolution of the known BSA-corona [7, 41, 42] and the intracellular release of former surface-bound CTAB to be the main cause for toxicity monitored. We envision that CTAB
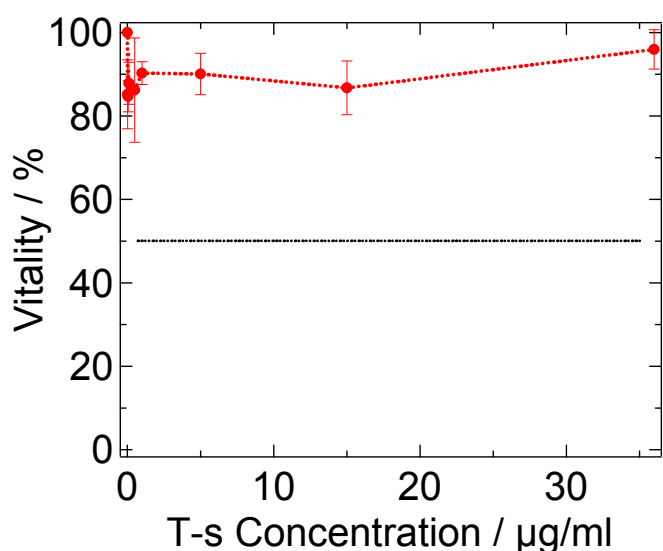
Figure 6.12 MTS-cytotoxicity assay of MDCKII cells exposed to various concentrations of T-s nanoparticles at 4° Celsius. No toxicity is found (in contrast to 37 ° C incubation), indicating that an ATP-dependent, active uptake mechanism for GNPs is occurring. IC_{50} line included to guide the line.

is set free from clustering GNP within the endosomal environment destroying inner membranes and provoking the production of ROS, a MPT at the mitochondria and the onset of predominantly apoptosis at lower concentrations and, with increasing amount of particles, increasing amounts of necrotic cells, whereby secondary apoptotic cells retain substrate adhesion although the cytoskeleton is degraded (see below). Alkilany *et al.*[6] suggest that cell toxicity arises from released, free CTAB in solution. We found, however, that addition of comparable concentrations of pure CTAB to the culture medium does not explain the observed toxic response of the cells. Along the lines, we observed a stronger propensity to form clusters in cells for spheres as opposed to rod-like GNPs, which might explain the increased level of toxicity observed for spherical particles.

Nanogeometry therefore seems to be less relevant in this case.[43, 44] This assumption is further supported by the fact that some groups described already gold-nanoparticles of ≥ 15 nm to be inert like bulk gold [17, 45].

Loss of actin fibers and at higher particle concentration even complete microtubule degradation was found for CTAB coated GNPs. Since CTAB is not only used for seeded growth or as phase-transfer-catalyst in chemistry, but also in biology for complexation of nucleic acids at low salt conditions or protein/polysaccharide aggregation at NaCl-concentration above 0,5 mol/l, the latter effect could account for the degradation detected. Additionally, hydrogen-peroxide found with our ROS assay may amplify the cytoskeletal degradation effect of CTAB.

Nanoparticle impact on cell-cell-contacts. Impedance spectroscopy followed by nonlinear fitting of adequate models, allows to monitor changes in the TER and gives quantitative means of the integrity of cell-cell contacts. TER-based nanotoxicity studies have been sparsely applied before for nano- and microparticles, indicating no or slightly decreased permeability upon exposition.[46-49] While CTAB-spheres leads to a concentration dependent, time-resolved full breakage of the barrier effect, CTAB-rods only temporarily produce a reduced TER, whereupon a concentration dependent recovery of cell-cell sealing is detected. ZO-1- and e-cadherine immunofluorescence staining for 24 hour incubation confirms that initially destroyed cell-cell contacts recover except for those exposed to CTAB-spheres in accordance with impedance spectroscopy. Time dependent recovery effects were also found for PEGylated GNPs. AFM-imaging and time resolved ZO-1 immunofluorescence staining show unequivocally that cell-cell contacts self-repair with time. These are the subtle dynamic aspect of nanotoxicity, which cannot be addressed with conventional cytotoxicity assays and require non-invasive real time methods such as ECIS or F-QCM.

6.5 CONCLUSION

In vitro nanocytotoxicity studies are crucial steps in defining strategic safety mechanisms against the possible risks upon environmental as well as human exposure to nanomaterials. Although long term *in-vivo* effects like, i.e. accumulation, failure to degrade and chronic inflammation are thereby neglected, predictions upon the factors triggering toxicity can be made. Especially time-resolved biosensors with higher sensitivity, faster readout, non-invasiveness are desirable for high-throughput screening systems that are required to respond to the tremendous increase in nanoparticle synthesis. Here, we present a double biosensor-approach employing D-QCM and ECIS to follow cell dynamics as a measure for toxicity. With the help of fluorescence imaging of actin, microtubules, ROS, MPT, cell death and adherens/tight junctions under GNP influence, we obtained a first glimpse of the processes involved in nanotoxicity. Taking together these results, a hierarchical picture of the factors, which govern the toxicity of gold nanoparticle can be drawn. Inherent toxicity of the surface ligand and the chemical stability of the shell-core bond influencing solubility and aggregation behaviour are of uttermost importance. We found that spherical gold nanoparticles are generally more toxic than rod-like shaped and display higher uptake efficiency. We attribute the high toxicity of CTAB coated spherical particles to cluster formation and as a consequence release of CTAB into the cell interior.

6.6 REFERENCES AND NOTES

1.   Oberdorster, G.; Stone, V.; Donaldson, K., Toxicology of nanoparticles: A historical perspective. *Nanotoxicology* **2007,** 1, (1), 2-25.

2.   Kumar, C., Nanomaterials for cancer diagsnosis. *1st Edn., Wiley-VHC, Weinheim* **2007**.

3.   Basu, S.; Harfouche, R.; Soni, S.; Chimote, G.; Mashelkar, R. A.; Sengupta, S., Nanoparticle-mediated targeting of MAPK signaling predisposes tumor to chemotherapy. *Proceedings of the National Academy of Sciences of the United States of America* **2009,** 106, (19), 7957-7961.

4.   Lewinski, N.; Colvin, V.; Drezek, R., Cytotoxicity of nanoparticles. *Small* **2008,** 4, (1), 26-49.

5.   Maynard, A. D.; Aitken, R. J.; Butz, T.; Colvin, V.; Donaldson, K.; Oberdorster, G.; Philbert, M. A.; Ryan, J.; Seaton, A.; Stone, V.; Tinkle, S. S.; Tran, L.; Walker, N. J.; Warheit, D. B., Safe handling of nanotechnology. *Nature* **2006,** 444, (7117), 267-269.

6.   Alkilany, A. M.; Nagaria, P. K.; Hexel, C. R.; Shaw, T. J.; Murphy, C. J.; Wyatt, M. D., Cellular Uptake and Cytotoxicity of Gold Nanorods: Molecular Origin of Cytotoxicity and Surface Effects. *Small* **2009,** 5, (6), 701-708.

7.   Lundqvist, M.; Stigler, J.; Elia, G.; Lynch, I.; Cedervall, T.; Dawson, K. A., Nanoparticle size and surface properties determine the protein corona with possible implications for biological impacts. *Proceedings of the National Academy of Sciences of the United States of America* **2008,** 105, (38), 14265-14270.

8.   Pan, Y.; Neuss, S.; Leifert, A.; Fischler, M.; Wen, F.; Simon, U.; Schmid, G.; Brandau, W.; Jahnen-Dechent, W., Size-dependent cytotoxicity of gold nanoparticles. *Small* **2007,** 3, (11), 1941-1949.

9.   Chithrani, B. D.; Ghazani, A. A.; Chan, W. C. W., Determining the size and shape dependence of gold nanoparticle uptake into mammalian cells. *Nano Letters* **2006,** 6, (4), 662-668.

10. Wang, S. G.; Lu, W. T.; Tovmachenko, O.; Rai, U. S.; Yu, H. T.; Ray, P. C., Challenge in understanding size and shape dependent toxicity of gold nanomaterials in human skin keratinocytes. *Chemical Physics Letters* **2008,** 463, (1-3), 145-149.

11. Yen, H. J.; Hsu, S. H.; Tsai, C. L., Cytotoxicity and Immunological Response of Gold and Silver Nanoparticles of Different Sizes. *Small* **2009,** 5, (13), 1553-1561.

12. Chithrani, B. D.; Chan, W. C. W., Elucidating the mechanism of cellular uptake and removal of protein-coated gold nanoparticles of different sizes and shapes. *Nano Letters* **2007,** 7, (6), 1542-1550.

13. Connor, E. E.; Mwamuka, J.; Gole, A.; Murphy, C. J.; Wyatt, M. D., Gold nanoparticles are taken up by human cells but do not cause acute cytotoxicity. *Small* **2005,** 1, (3), 325-327.

14. Takahashi, H.; Niidome, Y.; Niidome, T.; Kaneko, K.; Kawasaki, H.; Yamada, S., Modification of gold nanorods using phospatidylcholine to reduce cytotoxicity. *Langmuir* **2006,** 22, (1), 2-5.

15. de la Fuente, J. M.; Berry, C. C.; Riehle, M. O.; Curtis, A. S. G., Nanoparticle targeting at cells. *Langmuir* **2006,** 22, (7), 3286-3293.

16. Nativo, P.; Prior, I. A.; Brust, M., Uptake and intracellular fate of surface-modified gold nanoparticles. *Acs Nano* **2008,** 2, (8), 1639-1644.

17. Khan, J. A.; Pillai, B.; Das, T. K.; Singh, Y.; Maiti, S., Molecular effects of uptake of gold nanoparticles in HeLa cells. *Chembiochem* **2007,** 8, (11), 1237-1240.

18. Giaever, I.; Keese, C. R., A Morphological Biosensor for Mammalian-Cells. *Nature* **1993,** 366, (6455), 591-592.

19. Giaever, I.; Keese, C. R., Use of Electric-Fields to Monitor the Dynamic Aspect of Cell Behavior in Tissue-Culture. *Ieee Transactions on Biomedical Engineering* **1986,** 33, (2), 242-247.

20. Lo, C. M.; Keese, C. R.; Giaever, I., Monitoring Motion of Confluent Cells in Tissue-Culture. *Experimental Cell Research* **1993,** 204, (1), 102-109.

21. Wegener, J.; Janshoff, A.; Steinem, C., The quartz crystal microbalance as a novel means to study cell-substrate interactions in situ. *Cell Biochemistry and Biophysics* **2001,** 34, (1), 121-151.

22. Cooper, M. A.; Singleton, V. T., A survey of the 2001 to 2005 quartz crystal microbalance biosensor literature: applications of acoustic physics to the analysis of biomolecular interactions. *Journal of Molecular Recognition* **2007,** 20, (3), 154-184.

23. Pax, M.; Rieger, J.; Eibl, R. H.; Thielemann, C.; Johannsmann, D., Measurements of fast fluctuations of viscoelastic properties with the quartz crystal microbalance. *Analyst* **2005,** 130, (11), 1474-1477.

24. Cans, A. S.; Hook, F.; Shupliakov, O.; Ewing, A. G.; Eriksson, P. S.; Brodin, L.; Orwar, O., Measurement of the dynamics of exocytosis and vesicle retrieval at cell populations using a quartz crystal microbalance. *Analytical Chemistry* **2001,** 73, (24), 5805-5811.

25. Sapper, A.; Wegener, J.; Janshoff, A., Cell motility probed by noise analysis of thickness shear mode resonators. *Analytical Chemistry* **2006,** 78, (14), 5184-5191.

26. Tarantola, M., Non-invasive monitoring of cell dynamics by noise analysis of thickness shear mode resonators. **2009**.

27. Tarantola, M.; Schneider, D.; Sunnick, E.; Adam, H.; Pierrat, S.; Rosman, C.; Breus, V.; Sonnichsen, C.; Basche, T.; Wegener, J.; Janshoff, A., Cytotoxicity of Metal and Semiconductor Nanoparticles Indicated by Cellular Micromotility. *Acs Nano* **2009,** 3, (1), 213-222.

28. Pierrat, S.; Zins, I.; Breivogel, A.; Sonnichsen, C., Self-assembly of small gold colloids with functionalized gold nanorods. *Nano Letters* **2007,** 7, (2), 259-263.

29. Rosman, C., Combined optical and TEM quantification of gold nanoparticle uptake and its effect on micromotility. **2009**.

30. Reiss, B.; Janshoff, A.; Steinem, C.; Seebach, J.; Wegener, J., Adhesion kinetics of functionalized vesicles and mammalian cells: A comparative study. *Langmuir* **2003,** 19, (5), 1816-1823.

31. Wegener, J.; Sieber, M.; Galla, H. J., Impedance analysis of epithelial and endothelial cell monolayers cultured on gold surfaces. *Journal of Biochemical and Biophysical Methods* **1996,** 32, (3), 151-170.

32. Hayat, M. A., Principles and Techniques of Electron Microscopy: Biological Application 4th ed. *Cambridge University Press, Cambridge* **2000**.

33. Hanaichi, T.; Sato, T.; Iwamoto, T.; Malavasiyamashiro, J.; Hoshino, M.; Mizuno, N., A Stable Lead by Modification of Sato Method. *Journal of Electron Microscopy* **1986,** 35, (3), 304-306.

34.   Barz, M.; Tarantola, M.; Fischer, K.; Schmidt, M.; Luxenhofer, R.; Janshoff, A.; Theato, P.; Zentel, R., From Defined Reactive Diblock Copolymers to Functional HPMA-Based Self-Assembled Nanoaggregates. *Biomacromolecules* **2008,** 9, (11), 3114-3118.

35.   Shukoor, I., Pathogen-Mimicking MnO Nanoparticles for Selective Activation of TLR9 Pathway and Imaging of Cancer Cells. *Advanced functional materials* **2009**.

36.   Goodman, C. M.; McCusker, C. D.; Yilmaz, T.; Rotello, V. M., Toxicity of gold nanoparticles functionalized with cationic and anionic side chains. *Bioconjugate Chemistry* **2004,** 15, (4), 897-900.

37.   Hauck, T. S.; Ghazani, A. A.; Chan, W. C. W., Assessing the effect of surface chemistry on gold nanorod uptake, toxicity, and gene expression in mammalian cells. *Small* **2008,** 4, (1), 153-159.

38.   Nan, A. J.; Bai, X.; Son, S. J.; Lee, S. B.; Ghandehari, H., Cellular uptake and cytotoxicity of silica nanotubes. *Nano Letters* **2008,** 8, (8), 2150-2154.

39.   Slowing, I.; Trewyn, B. G.; Lin, V. S. Y., Effect of surface functionalization of MCM-41-type mesoporous silica nanoparticleson the endocytosis by human cancer cells. *Journal of the American Chemical Society* **2006,** 128, (46), 14792-14793.

40.   Kostarelos, K.; Lacerda, L.; Pastorin, G.; Wu, W.; Wieckowski, S.; Luangsivilay, J.; Godefroy, S.; Pantarotto, D.; Briand, J. P.; Muller, S.; Prato, M.; Bianco, A., Cellular uptake of functionalized carbon nanotubes is independent of functional group and cell type. *Nature Nanotechnology* **2007,** 2, (2), 108-113.

41.   Cedervall, T.; Lynch, I.; Foy, M.; Berggad, T.; Donnelly, S. C.; Cagney, G.; Linse, S.; Dawson, K. A., Detailed identification of plasma proteins adsorbed on copolymer nanoparticles. *Angewandte Chemie-International Edition* **2007,** 46, (30), 5754-5756.

42.   Lynch, I.; Cedervall, T.; Lundqvist, M.; Cabaleiro-Lago, C.; Linse, S.; Dawson, K. A., The nanoparticle - protein complex as a biological entity; a complex fluids and surface science challenge for the 21st century. *Advances in Colloid and Interface Science* **2007,** 134-35, 167-174.

43.   Ferrari, M., Beyond drug delivery. *Nature Nanotechnology* **2008,** 3, (3), 131-132.

44.   Jiang, W.; Kim, B. Y. S.; Rutka, J. T.; Chan, W. C. W., Nanoparticle-mediated cellular response is size-dependent. *Nature Nanotechnology* **2008,** 3, (3), 145-150.

45.   Shukla, R.; Bansal, V.; Chaudhary, M.; Basu, A.; Bhonde, R. R.; Sastry, M., Biocompatibility of gold nanoparticles and their endocytotic fate inside the cellular compartment: A microscopic overview. *Langmuir* **2005,** 21, (23), 10644-10654.

46.   Chanana, M.; Gliozzi, A.; Diaspro, A.; Chodnevskaja, I.; Huewel, S.; Moskalenko, V.; Ulrichs, K.; Galla, H. J.; Krol, S., Interaction of polyelectrolytes and their composites with living cells. *Nano Letters* **2005,** 5, (12), 2605-2612.

47.   Grenha, A.; Grainger, C. I.; Dailey, L. A.; Seijo, B.; Martin, G. P.; Remunan-Lopez, C.; Forbes, B., Chitosan nanoparticles are compatible with respiratory epithelial cells in vitro. *European Journal of Pharmaceutical Sciences* **2007,** 31, (2), 73-84.

48.   Moyes, S. M.; Smyth, S. H.; Shipman, A.; Long, S.; Morris, J. F.; Carr, K. E., Parameters influencing intestinal epithelial permeability and microparticle uptake in vitro. *International Journal of Pharmaceutics* **2007,** 337, (1-2), 133-141.

49.   Rothen-Rutishauser, B.; Grass, R. N.; Blank, F.; Limbach, L. K.; Muehlfeld, C.; Brandenberger, C.; Raemy, D. O.; Gehr, P.; Stark, W. J., Direct Combination of Nanoparticle Fabrication and Exposure to Lung Cell Cultures in a Closed Setup as a Method To Simulate Accidental Nanoparticle Exposure of Humans. *Environmental Science & Technology* **2009,** 43, (7), 2634-2640.
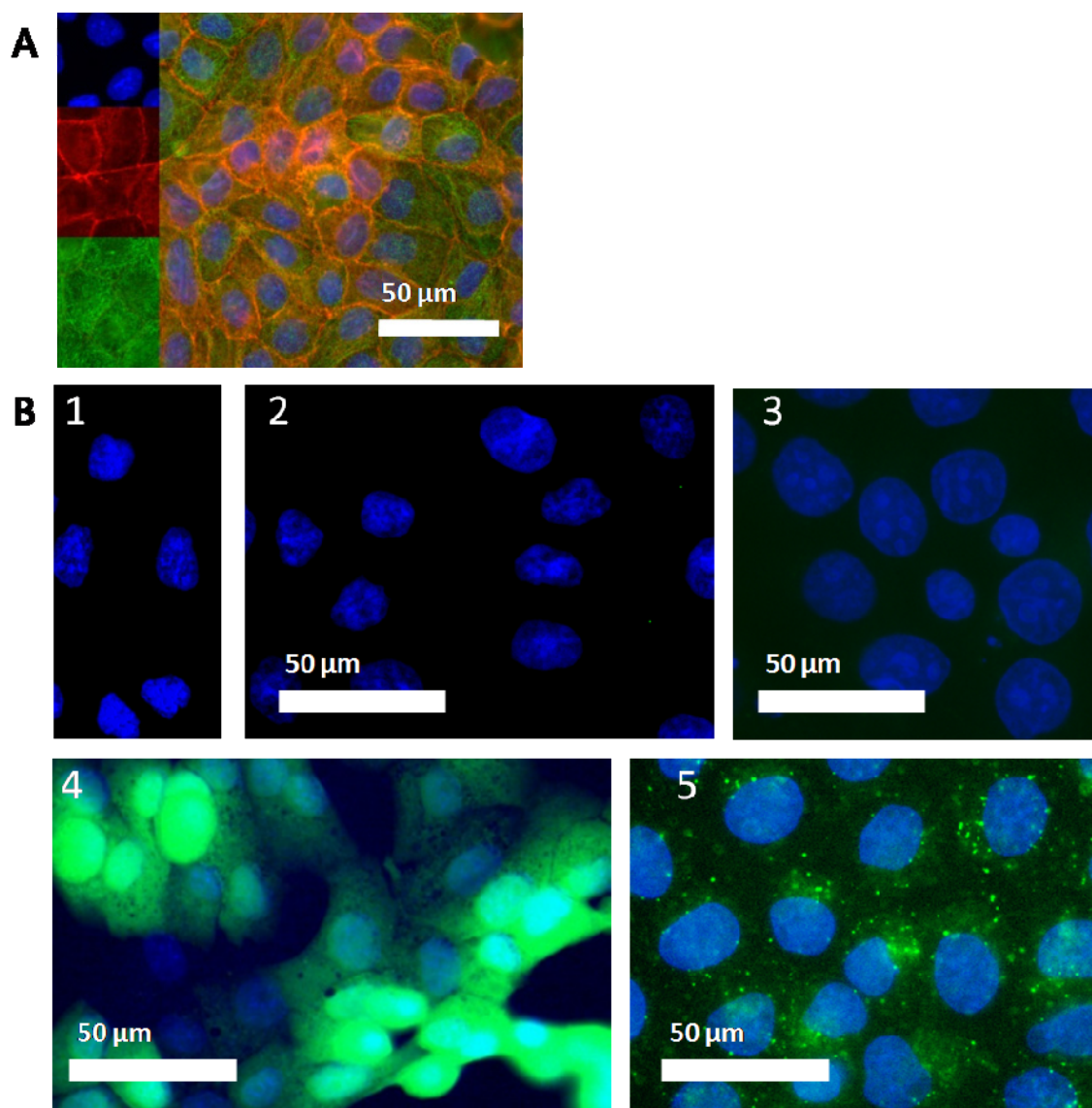
Appendix

Figure 6.S. 1 Fluorescence controls. A) 1:1 v/v % Acteon-/Methanol fixated MDCKII cells without nanoparticle treatment with combined ß-Tubulin, Phalloidin-Actin and DAPI-staining; B) 1. MDCKII cells stained with DAPI and CM-H2DCFDA after 24 h upon attaining confluency. No ROS detectable (comparable exposure times). 2. Green-autofluorescence of GNP-treated MDCKII cells (6 µg/ml T-s) stained with DAPI. No autofluorescence found. 3. MDCKII cells stained with DAPI and CM-H2DCFDA after 24 h exposition to pure CTAB solution comparable to the concentration adsorbed on T-s. (0,144 µg/ml): slight ROS-signal. 4. MDCKII cells stained with DAPI and CM-H2DCFDA, treated with 0.03 vol % H_2O_2 as positive control 5. MDCKII cells stained with DAPI and CM-H2DCFDA, treated with anti-oxidant resveratrol (50µM) and 0.03 vol% H_2O_2 as negative control for ROS-generation.
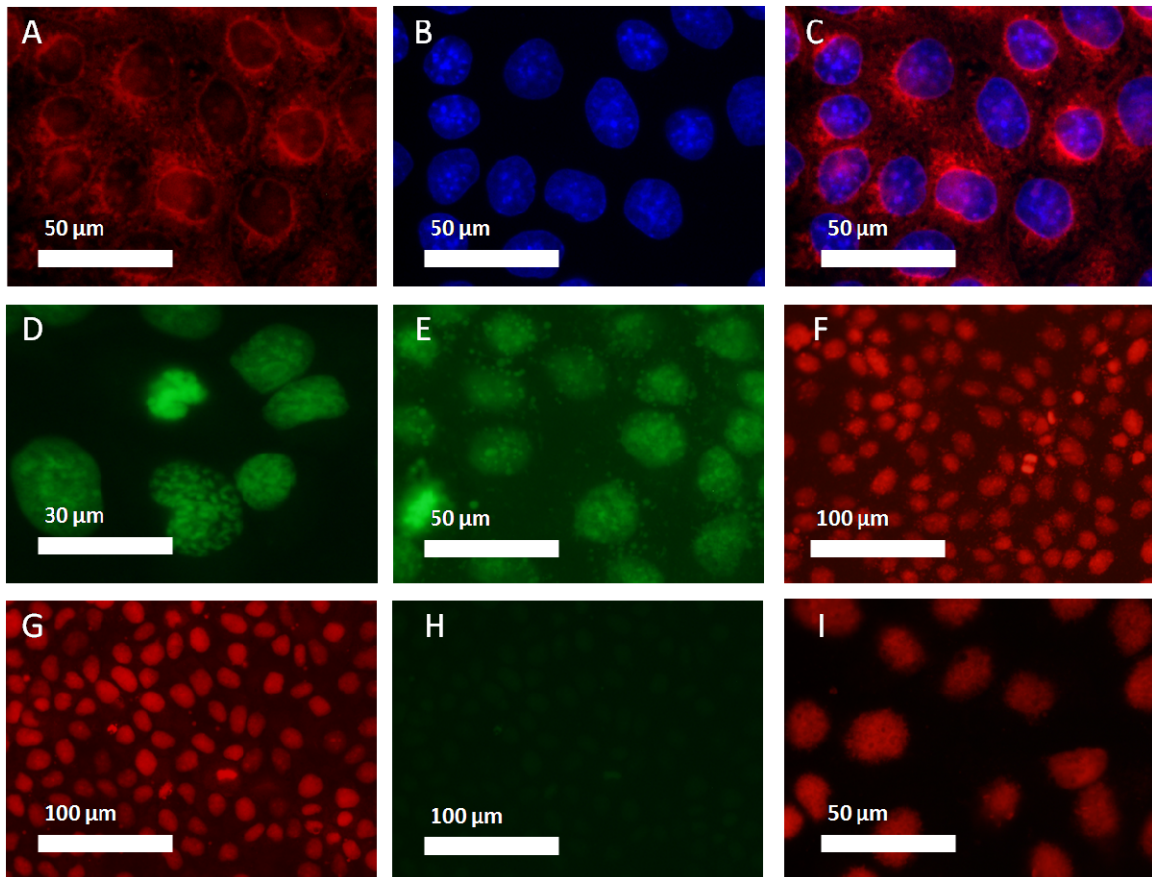
Figure 6.S. 2 JC-1 staining of untreated cells (A-C, with B as overlay of green and blue channel and C as threefold overlay) with intact mitochondrial permeability. D-F showing apoptotic cells after 12 h (D) and 24 h (E,F, secondary apoptosis) staurosporin treatment. G-I depicts necrotic cells after combined staurosporine and caspase inhibitor treatment after 24 h with H being the green channel.
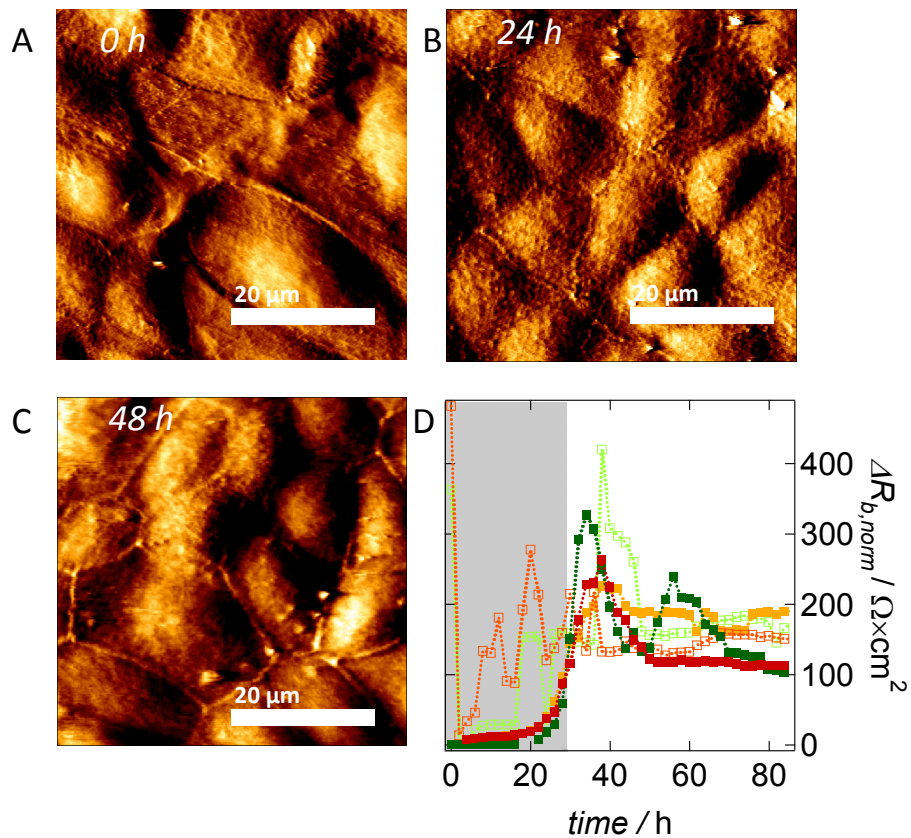
Figure 6.S. 3 A-C) AFM-imaging (deflection images shown for morphological contrast) of confluent MDCKII cells (A), 4 µg/ml C-r treated MDCKII monolayers after 24 h (B) and 48 h (C) incubation showing increased TJ-elevations upon recovery; scale bar is 20 µm. D) Exemplary time courses of TER $\Delta R_{b,norm}$ shown for 9 µg/ml PEGylate particles (green spheres, red rods): C-s and C-r (open squares), N-s and N-r (closed squares) with TER of untreated cells as control (orange). Recovery 60 hours after seeding is only found for carboxylated GNPs.

7

Summary

The central aim of this work was focused on scrutinizing migration dynamics of epithelial monolayers by two novel *in vitro* biosensors: electrical cell-substrate impedance sensing (ECIS) and quartz crystal microbalance (QCM). Both proved to be suitable to address cell motility and nanocytotoxicity.

In the first project, we were able to distinguish cancer cells by their cell body dynamics and the generated electrical or acoustic noise. A real time sensor approach, based on resonance frequency and dissipation fluctuations of D-QCM (F-QCM) measurements was introduced. Cell motility of human cancer cells could be assessed label-free and non-invasive. Furthermore, for cancer cells organized in monolayers, frequency fluctuations reproduced the metastatic potential that was determined by conventional assays based on the well-established Boyden chamber approach. Long-memory stochastic processes were found to govern the response of the adherent cells displayed in both F-QCM and ECIS micromotion measurements, with variance analysis of QCM frequency fluctuations providing the strongest correlation to classical invasion assays.

Furthermore, we were able to identify actin-polymerization as well as microtubule depolymerization to be the main contributors of viscoelastic or impedimetric fluctuations. Besides direct targeting of cytoskeletal biopolymers, interference with motor protein myosin II could be detected as well as presumably the indirect activation of Rho GTPase by colchicin. Cis-platin, taxol and cytochalasin-D proved to be sufficient powerful to reduce micromotility of human head and neck tumor cell line FaDu, whereas the chemotherapeutic resveratrol did not significantly affect biological noise produced by cancerous cells. In general, as impedance spectroscopy relies on current flowing underneath or in between adherent cells, it is more sensitive to actin dynamics powering cell shape fluctuations. In surplus, the oscillating, acoustic quartz biosensor is able to detect *in vivo* microtubule-based stochastic instabilities occurring in the cytosol by the penetrating standing wave. One the one hand, this makes

QCM a more versatile tool than ECIS for the detection of cell substrate fluctuations. On the other hand, the penetration depth of the standing wave is too short to account for the shape fluctuations aligned to apical dynamics of epithelial cells; ECIS does not lack this sensitivity, as TER monitoring showed.

In the second project, we have shown that micromotion measured by impedance analysis provides a non-invasive and versatile tool to assess the toxicity of nanoparticles with high sensitivity. Compared to conventional cytotoxicity test, micromotion detects minute changes in cell viability already at very low particle concentrations without the need for colorimetric or fluorescent labels and in real-time. Especially the provided dynamic IC_{50} values increase insight into mechanisms of particle-cell interaction. Dark field microscopy of gold nanorods was revealed to be the ideal counterpart to micromotion, since it allows visualizing the location of particle also in a non-invasive manner. We found that even when QDs are capped and stabilized against Cd^{2+} diffusion with an external ZnS shell, they are highly toxic.

In vitro nanocytotoxicity studies on the gold nanoparticles were achieved using the double biosensor-approach employing F-QCM and ECIS: with the help of fluorescence imaging of actin, microtubules, ROS, MPT, cell death and adherens/tight junctions under GNP influence, we obtained a first glimpse of the processes involved in nanotoxicity. Taking together these results, a hierarchical picture of the factors, which govern the toxicity of gold nanoparticles can be drawn. Inherent toxicity of the surface ligand and the chemical stability of the shell-core bond influencing solubility and aggregation behavior are of uttermost importance. We found that spherical gold nanoparticles are generally more toxic than rod-like shaped and display higher uptake efficiency. We attribute the high toxicity of CTAB coated spherical particles to cluster formation and as a consequence release of CTAB into the cell interior. Furthermore, dependent on the intracellular CTAB concentration, the ROS signaling may lead to mitochondrial permeability transitions and apoptosis, or, at higher CTAB doses, directly to necrosis.

In summary, the novel real time biosensor approach based on fluctuation analysis of acoustic and impedimetric readouts of QCM and ECIS displays a high cellular specifity and sensitivity for the dynamics of the cellular cytoskeleton and may serve also as a very sensitive measure for cellular viability.

8

Lebenslauf

Marco Tarantola

Geburtsdatum: 30. Oktober 1979

Geburtsort: Wiesbaden, aufgewachsen in Sizilien

Familienstand: ledig

Staatsangehörigkeit: Deutsch und Italienisch

Dissertationsvorhaben

01/2006 – 12/2008	Wissenschaftlicher Mitarbeiter am Institut für Physikalische Chemie der Johannes Gutenberg-Universität Mainz
01/2009 –12/2009	Wissenschaftlicher Mitarbeiter am Institut für Physikalische Chemie der Georg-August-Universität Göttingen

Studium

06/2005	Diplom im Fach Biologie (Note: 1,27)
09/2004 – 05/2005	Diplomarbeit an den Instituten für Biotechnologie und Biophysik der Bayerischen Julius-Maximilians-Universität Würzburg, Arbeitsgruppe Prof. Dr. U. Zimmermann und Prof. Dr. A. Haase
	Thema: *„Untersuchung zum Wasser- und Stofftransport in höheren Pflanzen: Veränderung von Xylemdruck, Volumenfluss und NMR-Parametern während des Eintrocknens und der Rehydrierung von Nicotiana tabacum"*

Stipendien

10/2006 – 08/2007	Kollegiat der „Material science in Mainz Graduate school" (MAINZ)
09/2007 – 12/2008	Stipendiat der Bundesexellenz-Graduiertenschule „ Polymers in advanced technologies"(POLYMAT)

Zivildienst und Schulbildung

09/1999 – 07/2000	Zivildienst in der Verwaltung/Finanzbuchhaltung, Asklepios Paulinen-Klinik, Wiesbaden
07/1990 – 07/1999	Elly-Heuss-Gymnasium, Wiesbaden, Abitur (Note: 1,3)
07/1986 – 07/1990	Friedrich-von-Schiller Grundschule, Wiesbaden

Veröffentlichungen

M. Tarantola, D.Schneider, E.Sunnick, H. Adam, S. Pierrat, C.Rosman, V. Breus, C. Sönnichsen, T. Basche, J. Wegener, A. Janshoff *Cytotoxicity of metal and semiconductor nanoparticles indicated by cellular micromotility.* ACS nano,**2008**, 3 (1), 213-222

M. Tarantola, A. Marel, E. Sunnick, H. Adam, J. Wegener, A. Janhoff *Dynamicsof human cancer cells lines monitored by electrical and acoustic noise analysis.* Integrative Biology,**2009** manuscript accepted

M. Tarantola, A. Pietuch, D. Schneider, E. Sunnick, J. Rother, C. Rosmann, S. Pierrat, C. Soennichsen, Wegener, J., A. Janshoff *Shape-dependent toxicity of gold-nanoparticles investigated by impedance and acoustic biosensors*. RSC Nanoscale, **2010** manuscript in preparation

M.Tarantola, E. Sunnick, Marel, A., Sapper, A., Wegener, J., Janshoff, A. *Dissecting vertical motility of epithelial cells by small molecule inhibitors.* Chemical Research in Toxicology, **2010**, manuscript in preparation

M. Barz, M. Tarantola, K. Fischer, M. Schmidt, R. Luxenhofer, A. Janshoff, P.Theato, R. Zentel *From defined reactive diblock copolymers to functional HPMA-based self-assembled nanoaggregates*. Biomacromlecules, **2008**, 9, 3114-3118

M. Shukoor, F. Natalio, M. Tahir, M. Wiens, M. Tarantola, H. Therese, M. Barz, S. Weber, M. Terekhov, H. Schröder, W. Müller, A. Janshoff, R. Zentel, L. Schreiber, W. Tremel *Pathogen-mimicking MnO nanoparticles for selective activation of the TLR9 pathway and imaging of cancer cells.* Advanced Functional Materials, **2009,** 19, 1-9

A. Janshoff, T. Fine, B. Lörenz, A. Pietuch, M.Tarantola, C. Steinem, J. Wegener *Cell adhesion on ordered pores: consequences for cellular elasticity,* Journal of adhesion science and technology, **2010**, manuscript accepted

C. Rosman, S. Pierrat, A. Henkel, M. Tarantola, D. Schneider, E. Sunnick, A. Janshoff, C. Sönnichsen *Combined optical and TEM quantification of gold-nanoparticles uptake.* **2010**, maunscript in preparation

D. Schenider, M.Tarantola, A. Janshoff *Induced epithelial to mesenchymal transition by the cytokine TGF-ß measured via ECIS*, **2010**, manuscript in preparation

Hiermit versichere ich, dass ich die vorliegende Arbeit selbständig

 angefertigt habe und alle in Anspruch genommenen Quellen

 und Hilfsmittel durch Zitate kenntlich gemacht habe.

Marco Tarantola

Mainz, den 1. Dezember 2009